MEASUREMENT OF THE LONGITUDINAL DEUTERON SPIN-STRUCTURE FUNCTION IN DEEP-INELASTIC SCATTERING[*]

Johannes M. Bauer

Stanford Linear Accelerator Center
Stanford University
Stanford, California 94309

[*]Partial fullfillment of Ph.D thesis, University of Massachusetts, Amherst, MA.

DISCLAIMER

Portions of this document may be illegible
in electronic image products. Images are
produced from the best available original
document.

ACKNOWLEDGMENTS

First and foremost, I am very grateful to my advisor, Janice Button-Shafer, for bringing me into the collaboration and making it possible for me to obtain my degree from experiment E143. I am thankful for the important guidance which she provided for me. I thank all the committee members for their help and support. I truly appreciate Charlie Young for serving on my committee and traveling to Massachusetts for my dissertation defense. His guidance throughout the analysis work was very valuable to me.

The experiment was performed by the whole collaboration, and I would like to thank everyone in the collaboration, but also all the SLAC personnel for their effort and work. It was a very enjoyful time for me. I would like to thank the spokespersons of the experiment, Ray Arnold and Oscar Rondon, especially Ray for his quiet, but efficient way of helping the group to run a smooth and successful experiment.

I am grateful to the many members of the collaboration who took the time to discuss the physics and analysis with me, especially Peter Bosted and Steve Rock. I thank all the people who answered my numerous questions and gave me suggestions for my dissertation.

What would be the experiment without all the graduate students? It was a pleasure to work with the fellow graduate students on the experiment and the subsequent analysis: Todd Averett, Robin Erbacher, Jeff Fellbaum, Philippe Grenier, Masao Kuriki, T.J. Liu, Paul Raines, and Philipp Steiner. I hope that our paths will cross again some time.

And special thanks to Amy for her patience, understanding and support throughout the years. I also want to express my gratitude to my family in Germany; they did not see me very often while I was in graduate school, but showed their support for whatever I was doing.

MEASUREMENT OF THE LONGITUDINAL DEUTERON SPIN-STRUCTURE FUNCTION IN DEEP-INELASTIC SCATTERING*

Johannes M. Bauer

SLAC-Report-492
September 1996

RECEIVED
JUN 17 1997
OSTI

MASTER

DISTRIBUTION OF THIS DOCUMENT IS UNLIMITED

DISCLAIMER

ABSTRACT

MEASUREMENT OF THE LONGITUDINAL DEUTERON SPIN-STRUCTURE FUNCTION IN DEEP-INELASTIC SCATTERING

SEPTEMBER 1996

JOHANNES M. BAUER,

VORDIPLOM PHYSICS, UNIVERSITY REGENSBURG, GERMANY

VORDIPLOM MATHEMATICS, UNIVERSITY REGENSBURG, GERMANY

M.S., ARIZONA STATE UNIVERSITY

Ph.D., UNIVERSITY OF MASSACHUSETTS AMHERST

Directed by: Professor Janice Button-Shafer

Experiment E143 at SLAC performed deep-inelastic scattering measurements with polarized electrons incident on polarized protons and deuterons. The data for the beam energy of $29\,\mathrm{GeV}$ cover the kinematical range of $x_{\mathrm{Bj}} > 0.03$ and $1 < Q^2 < 12\,\mathrm{GeV}^2$. From these data, the spin-dependent structure functions g_1 were determined. This dissertation describes the experiment and its analysis and discusses the results. The measured integral of g_1^d over x from $x = 0$ to $x = 1$ is $\Gamma_1^d = 0.046 \pm 0.003\,(\mathrm{stat})\pm 0.004\,(\mathrm{syst})$ at $Q^2 = 3\,\mathrm{GeV}^2$ and disagrees by more than three standard deviations with the prediction of the Ellis-Jaffe sum rule. The data suggest that the quark contribution to the nucleon helicity is 0.35 ± 0.05. From the proton data of the same experiment, the integral over the proton spin-structure function g_1^p was determined to be $\Gamma_1^p = 0.127 \pm 0.003\,(\mathrm{stat})\pm 0.008\,(\mathrm{syst})$. By combining the deuteron data with the proton data, the integral Γ_1^n was extracted as $-0.027 \pm 0.008\,(\mathrm{stat})\pm 0.010\,(\mathrm{syst})$. The integral $\Gamma_1^p - \Gamma_1^n$ is $0.154 \pm 0.010\,(\mathrm{stat}) \pm 0.016\,(\mathrm{syst})$ according to the E143 analysis. This result agrees with the important Bjorken sum rule of 0.171 ± 0.009 at $Q^2 = 3\,\mathrm{GeV}^2$ within less than one standard deviation. Furthermore, results of a separate analysis involving GLAP evolution equations are shown. Data were also collected for beam energies of 16.2 and $9.7\,\mathrm{GeV}$. Results for g_1 at these energies are presented.

TABLE OF CONTENTS

LIST OF TABLES

LIST OF FIGURES

CHAPTER 1

INTRODUCTION

One of the main challenges in current particle physics is the understanding of the underlying quark structure of nucleons. Until 1987, the nucleon spin seemed to be understood within the simple quark model as being solely due to the spin of the valence quarks. An experiment by the European Muon Collaboration (EMC) at CERN in Geneva, however, challenged this belief [1]. Since their finding was surprising, one spoke at that time of a "spin crisis". The EMC experiment indicated that the quark spin contributes much less to the nucleon spin than expected by the simple models and that more elaborate explanations were necessary. Several new experiments, with better statistics and different targets, have been performed in the meantime by the Spin Muon Collaboration at CERN [2] [3] [4] [5] and by the E142 collaboration at the Stanford Linear Accelerator Center (SLAC) [6], but the interest in the origin of the nucleon spin still remains very large [7].

Another experiment was performed at the Stanford Linear Accelerator Center during the winter of 1993/94 by the E143 collaboration with about 80 physicists from around the world. Results of this experiment are presented in this dissertation. The experiment studied the inclusive scattering of polarized electrons at energies of 9.7, 16.2 and 29 GeV from polarized protons and deuterons via $^{15}NH_3$ and $^{15}ND_3$ targets. The spin-asymmetry $A_\parallel$ was measured for each of the three energies, while the spin-asymmetry $A_\perp$ was measured only for beam energy 29 GeV. From these asymmetries, the longitudinal spin-structure functions g_1^p and g_1^d were determined

1

for all three energies, and — for 29 GeV only – the transverse spin-structure functions g_2^p and g_2^d. As will be shown later, the deuteron spin-structure function g_1^d is especially well suited for the extraction of the helicity content of the nucleus.

The dissertation deals with the largest portion of the data, the deuteron data in the deep-inelastic scattering (DIS) region, and determined the longitudinal structure function g_1^d. Additional physics topics are covered by other members of the collaboration.

After an introduction to the theoretical background and motivation for the experiment, the experimental set-up and the analysis procedure are described. Thereafter the results of the analysis are presented and discussed.

CHAPTER 2

THEORETICAL BACKGROUND
AND PHYSICS OVERVIEW

2.1 Kinematics of Deep-Inelastic Scattering

Electrons offer a useful probe for exploring the inner structure of the nucleons. To first order, the electron interacts with the nucleon by exchange of a virtual photon. The interaction of electrons with photons is very well understood within Quantum Electrodynamics (QED), and due to the small electromagnetic coupling constant, its contribution can be easily calculated from low-order perturbation terms.

At low energy transfer, the interactions between electrons and nucleons will be elastic. Increasing the energy, one enters the resonance region where the electron inelastically excites the nucleon to resonances of various kinds. The resonances themselves return to the ground-state nucleon via emission of particles like pions or photons. At even higher energies, the nucleons will break up and their previous identity will be lost in the debris. So many resonances appear and overlap that the cross-section becomes smooth. This region is called the "deep-inelastic scattering" (DIS) region. Very successful experiments in the deep-inelastic scattering region were performed by observing only the scattered electrons without identifying other particles ("inclusive reaction"):

$$e^- N \longrightarrow e^- X. \tag{1}$$

N stands here for the nucleon; X stands for all final particles except the detected electron. The current work is also studying this reaction.

Fig. 1 illustrates the important kinematic quantities of the DIS reaction. Higher order graphs, of course, are also present, but are not of concern at this level. The four-vectors are given in the laboratory frame, which is the most commonly used frame for this kind of reaction. The energy of the incoming (outgoing) electron is called E (E'), and the scattering angle with respect to the direction of the incoming electron is noted as θ. The electron mass is here assumed to be zero. Instead of the four-momentum transfer square $q^2 = (k - k')^2$, it is common to use the quantity $Q^2 \equiv -q^2 \geq 0$ with

$$Q^2 \approx 2EE'[1 - \cos\theta] = 4EE' \sin^2 \frac{\theta}{2}. \tag{2}$$

The variable x is called "Bjorken x" and is defined as

$$x = \frac{Q^2}{2M\nu} \tag{3}$$

with M being the mass of the nucleon and $\nu = E - E'$. The experimental results are commonly expressed as functions of these two Lorentz-invariant variables x and Q^2.
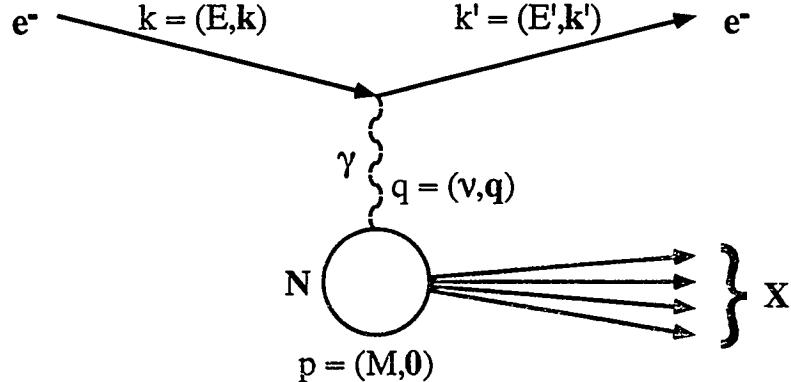
Figure 1 The inclusive reaction of electrons (e^-) scattered off nucleons (N). X is the undetected "debris" of the interaction. The four-vectors are given in the laboratory frame.

The interaction between the virtual photon and the electron is a very well understood point-interaction. On the other hand, the interaction of the virtual photon with the nucleon is not a point-like interaction, and is therefore symbolized in Fig. 1

with a big circle. If the wavelength of the virtual photon is larger than the size of the nucleon, the photon is able to resolve the individual constituents of the nucleon and to provide information about them.

The undetected fragments, labeled X in Fig. 1, have an invariant mass W given by

$$W^2 = (p + q)^2 = M^2 + 2M\nu + q^2 = M^2 + Q^2 \left(\frac{1}{x} - 1\right). \tag{4}$$

The four-vectors p and q refer to the incoming electron and the virtual photon momenta. The expression at the far right side of Eq. (4) is evaluated in the laboratory frame. In order to be in the deep-inelastic scattering region, the invariant mass of the fragments has to be larger than any known and identifiable resonance of the nucleon. The border between the deep-inelastic scattering region and the resonance region is not well defined, but is known to be where W is of the order of a few GeV.

2.2 Tensors for Lepton-Nucleon Deep-Inelastic Scattering

The general lepton-nucleon scattering in the deep-inelastic scattering region with the exchange of one photon is described in the following way. We are following here Ref. [8]. The most important variables are defined in Table 1. By choice, $s \cdot k = 0$, $s' \cdot k' = 0$, $s \cdot s = -1$, and $s' \cdot s' = -1$. In addition, $q = k - k'$ as before, and α is the electromagnetic coupling constant (fine-structure constant), which determines the strength of the interaction.

The differential cross-section may be expressed in tensor form as:

$$\frac{d^2\sigma}{d\Omega dE'} = \frac{\alpha^2}{2Mq^4} \frac{E'}{E} L_{\mu\nu} W^{\mu\nu} \tag{5}$$

with

$$L_{\mu\nu}(k, s; k', s') = [\bar{u}(k', s')\gamma_\mu u(k, s)]^* [\bar{u}(k', s')\gamma_\nu u(k, s)] \tag{6}$$

$$= L_{\mu\nu}^{(S)}(k; k') + iL_{\mu\nu}^{(A)}(k, s; k')$$

$$+ L_{\mu\nu}^{(S)}(k, s; k', s') + iL_{\mu\nu}^{(A)}(k; k', s') \tag{7}$$

5

Table 1 Variables in deep-inelastic lepton-nucleon scattering. Some of the four-momenta are evaluated in the laboratory system.

	lepton initial	lepton final	nucleon initial	nucleon final
mass	m		M	
four-momentum	$k = (E, \mathbf{k})$	$k' = (E', \mathbf{k}')$	$P = (M, \mathbf{0})$	P'
spin four-vector	$s = \frac{1}{m}(|\mathbf{k}|, E\hat{\mathbf{k}})$	s'	$S = (0, \hat{\mathbf{S}})$	S'

where (S) stands for the symmetric part, (A) for the antisymmetric part under the exchange of μ and ν. The symmetric and antisymmetric terms are defined in the following way:

$$L_{\mu\nu}^{(S)}(k; k') = k_\mu k_\nu' + k_\mu' k_\nu - g_{\mu\nu}(k \cdot k' - m^2) \tag{8}$$

$$L_{\mu\nu}^{(A)}(k, s; k') = m\epsilon_{\mu\nu\alpha\beta}s^\alpha(k - k')^\beta \tag{9}$$

$$L_{\mu\nu}'^{(S)}(k, s; k', s') = (k \cdot s')(k_\mu' s_\nu + s_\mu k_\nu' - g_{\mu\nu}k' \cdot s)$$
$$- (k \cdot k' - m^2)(s_\mu s_\nu' + s_\mu' s_\nu - g_{\mu\nu}s \cdot s') \tag{10}$$
$$+ (k' \cdot s)(s_\mu' k_\nu + k_\mu s_\nu') - (s \cdot s')(k_\mu k_\nu' + k_\mu' k_\nu)$$

$$L_{\mu\nu}'^{(A)}(k; k', s') = m\epsilon_{\mu\nu\alpha\beta}s'^\alpha(k - k')^\beta \tag{11}$$

After summing over the spin of the outgoing electron s', one obtains $L_{\mu\nu} = 2L_{\mu\nu}^{(S)} + 2iL_{\mu\nu}^{(A)}$. When also averaging over s, the normal unpolarized leptonic tensor $L_{\mu\nu} = 2L_{\mu\nu}^{(S)}$ is obtained.

The hadronic tensor $W_{\mu\nu}$ itself can be split into two tensors:

$$W_{\mu\nu}(q; P, S) = W_{\mu\nu}^{(S)}(q; P) + iW_{\mu\nu}^{(A)}(q; P, S) \tag{12}$$

with

$$\frac{1}{2M}W_{\mu\nu}^{(S)}(q; P) = \left(-g_{\mu\nu} + \frac{q_\mu q_\nu}{q^2}\right)W_1(P \cdot q, q^2)$$
$$+ \left(P_\mu - \frac{P \cdot q}{q^2}q_\mu\right)\left(P_\nu - \frac{P \cdot q}{q^2}q_\nu\right)\frac{W_2(P \cdot q, q^2)}{M^2} \tag{13}$$

6

$$\frac{1}{2M} W_{\mu\nu}^{(A)}(q; P, S) = \epsilon_{\mu\nu\alpha\beta} q^\alpha \Big\{ M S^\beta G_1(P \cdot q, q^2)$$

$$+ \left[(P \cdot q) S^\beta - (S \cdot q) P^\beta \right] \frac{G_2(P \cdot q, q^2)}{M^2} \Big\}. \tag{14}$$

Here we find four structure functions: W_1 and W_2 for unpolarized scattering and G_1 and G_2 for polarized scattering. The structure functions describe the physics of the photon-nucleon interaction. They depend on the structure of the nucleon, as their name implies.

Having averaged over the outgoing electron spin s', the differential cross-section is

$$\frac{d^2\sigma}{d\Omega dE'} = \frac{\alpha^2}{Mq^4} \frac{E'}{E} \left[L_{\mu\nu}^{(S)} W_{(S)}^{\mu\nu} - L_{\mu\nu}^{(A)} W_{(A)}^{\mu\nu} \right]. \tag{15}$$

and the differential cross-section for unpolarized scattering is simply

$$\frac{d^2\sigma}{d\Omega dE'} = \frac{\alpha^2}{Mq^4} \frac{E'}{E} L_{\mu\nu}^{(S)} W_{(S)}^{\mu\nu}. \tag{16}$$

Since a photon is exchanged in $eN \to eX$, the structure functions for this reaction is said to describe the neutral-current process. In the same reaction, a Z vector boson could be exchanged instead of a photon, which is described by additional structure functions [8]. But since the Z-exchange is highly suppressed, we can neglected them for this research. Additional structure functions describe the charged-current processes $e^- N \to \nu X$, $\nu N \to e^- X$, and $\bar{\nu} N \to e^+ X$, where the charged vector bosons W^+ or W^- are exchanged.

2.3 Unpolarized Scattering

From now on, we will consider the formulas in the laboratory frame. The spin-averaged cross-sections for deep-inelastic scattering can be written as

$$\frac{d^2\sigma}{d\Omega dE'} = \frac{4\alpha^2 E'^2}{Q^4} \left[2\sin^2 \frac{\theta}{2} W_1(\nu, Q^2) + \cos^2 \frac{\theta}{2} W_2(\nu, Q^2) \right]. \tag{17}$$

The mass of the scattered lepton is here assumed to be zero. The structure functions MW_1 and νW_2 become independent of Q^2 for large Q^2 and ν, and will only depend

7

on the ratio of Q^2 to ν, or equivalently on the Bjorken $x = Q^2/2M\nu$:

$$F_1(x, Q^2) \equiv MW_1(\nu, Q^2) \overset{Q^2, \nu \to \infty}{\longrightarrow} F_1(x), \qquad (18)$$

$$F_2(x, Q^2) \equiv \nu W_2(\nu, Q^2) \overset{Q^2, \nu \to \infty}{\longrightarrow} F_2(x). \qquad (19)$$

This property is called "scaling". In Eqs. (18) and (19), we introduced the structure functions F_1 and F_2, which are usually used instead of W_1 and W_2. Scaling is only approximately true, and the Q^2-dependence of F_1 and F_2 does not disappear completely.

The relationship between F_1 and F_2 is described by

$$F_1 \equiv F_2 \frac{1 + \gamma^2}{2x(1 + R)}. \qquad (20)$$

$R = \sigma_{1/2}^L / \sigma^T$ is the ratio of longitudinal to transverse virtual scattering [9] (see later section about the virtual photon). The term γ^2 is defined as

$$\gamma^2 \equiv 4M^2 x^2 / Q^2 = Q^2 / \nu^2 = 2Mx/\nu. \qquad (21)$$

For $Q^2 \to \infty$, both R and γ^2 approach zero, and therefore Eq. (20) simplifies to the Callan-Gross relation

$$F_1 = \frac{F_2}{2x}. \qquad (22)$$

2.4 Polarized Scattering

Once both the electron beam and the nucleon target are polarized, the two structure functions G_1 and G_2 no longer cancel. If the nucleon spin is oriented parallel to the initial lepton momentum, we obtain:

$$\frac{d^2\sigma^{\downarrow\uparrow}}{d\Omega dE'} - \frac{d^2\sigma^{\uparrow\uparrow}}{d\Omega dE'} = \frac{4\alpha^2 E'}{Q^2 E} \left[(E + E' \cos\theta) MG_1(\nu, Q^2) - Q^2 G_2(\nu, Q^2) \right]. \qquad (23)$$

The first arrow at the cross-sections σ indicates the direction of the beam helicity, the second arrow the direction of the target helicity. This means that for $\sigma^{\uparrow\uparrow}$ and

8

$\sigma^{\downarrow\uparrow}$ the beam and target helicities are oriented longitudinal (parallel or antiparallel) to each other. Similarly we obtain

$$\frac{d^2\sigma^{\uparrow\leftarrow}}{d\Omega dE'} - \frac{d^2\sigma^{\downarrow\leftarrow}}{d\Omega dE'} = \frac{4\alpha^2 E'}{Q^2 E} E' \sin\theta \cos\phi \left[MG_1(\nu, Q^2) + 2EG_2(\nu, Q^2)\right] \qquad (24)$$

for the target helicity oriented perpendicular to the beam momentum. The angle ϕ is the azimuthal angle between the plane defined by the incoming and outgoing electron direction, $\mathbf{k}$ and $\mathbf{k}'$, and the plane defined by $\mathbf{k}$ and the direction of the target polarization $\mathbf{S}$. For E143 kinematics, this angle was either $0°$ or $180°$, leading to the maximally possible cross-section difference. The factor $\cos\phi = \pm 1$ was taken into account during the analysis, but for our further discussions in this chapter, we will set $\cos\phi = 1$.

For large Q^2 and ν, scaling leads again to structure functions which approximately depend only on $x = Q^2/2M\nu$:

$$g_1(x, Q^2) = M^2\nu G_1(\nu, Q^2) \overset{Q^2, \nu\to\infty}{\longrightarrow} g_1(x), \qquad (25)$$

$$g_2(x, Q^2) = M^2\nu G_2(\nu, Q^2) \overset{Q^2, \nu\to\infty}{\longrightarrow} g_2(x). \qquad (26)$$

Experimentalists usually do not measure the differential cross-sections mentioned in Eqs. (23) and (24), but instead the asymmetries

$$A_{\parallel} = \frac{\sigma^{\downarrow\uparrow} - \sigma^{\uparrow\uparrow}}{\sigma^{\downarrow\uparrow} + \sigma^{\uparrow\uparrow}} \qquad (27)$$

and

$$A_{\perp} = \frac{\sigma^{\downarrow\leftarrow} - \sigma^{\uparrow\leftarrow}}{\sigma^{\downarrow\leftarrow} + \sigma^{\uparrow\leftarrow}}. \qquad (28)$$

In this way, common factors like acceptance cancel. Since the σ's are proportional to the number of events per unit of incoming charge, one does not need to use the real cross-sections. Instead, knowledge of the rates of good events (= scattered particles per number of incoming electrons) for left- and right-handed beam helicity is sufficient. Let us call these rates N_L and N_R. The asymmetries $A_{\parallel}$ and $A_{\perp}$ are then

$$A_{\parallel} \text{ (or } A_{\perp}) = \frac{1}{fP_bP_t} \frac{N_L - N_R}{N_L + N_R}. \qquad (29)$$

9

The factors f, P_b and P_t are the dilution factor and beam and target polarizations. These and additional correction factors have to be included in order to obtain the correct asymmetries. Chapter 4 discusses all corrections in great detail.

The spin-structure functions can be obtained from the asymmetries via the following equations:

$$g_1(x, Q^2) = \frac{F_1(x, Q^2)}{D'} \left[A_\parallel + \tan\frac{\theta}{2} A_\perp \right] \tag{30}$$

$$g_2(x, Q^2) = \frac{F_1(x, Q^2)}{D'} \frac{y}{2\sin\theta} \left[\frac{E + E'\cos\theta}{E'} A_\perp - \sin\theta A_\parallel \right] \tag{31}$$

where

$$D' = \frac{(1 - \epsilon)(2 - y)}{y[1 + \epsilon R(x, Q^2)]}. \tag{32}$$

The variables y and ϵ are given by

$$y = \frac{E - E'}{E} = \frac{\nu}{E} \tag{33}$$

(fractional energy loss of the electron) and

$$\frac{1}{\epsilon} = 1 + 2 \left[1 + \frac{\nu^2}{Q^2} \right] \tan^2\frac{\theta}{2}. \tag{34}$$

The factor ϵ is the longitudinal polarization of the virtual photon. For $\theta = 0$, for example, $\epsilon = 1$. For real photons, we have $Q^2 = 0$ and only transverse polarization, hence $\epsilon = 0$.

Experiments like the one discussed in this dissertation usually have small scattering angles θ. For these small angles θ, g_1 depends mostly on $A_\parallel$, and g_2 depends mostly on $A_\perp$. Therefore, g_1 is also called the "longitudinal spin-structure function" and g_2 the "transverse spin-structure function". Knowledge of the unpolarized structure functions is necessary in order to use Eqs. (30) and (31). The functions F_2 and R have been measured well during the last years at SLAC [9] and CERN [10] [11].

Provided the scattering angle θ is small (and this is true for E143 and all similar spin-structure function experiments), also the factor $\tan(\theta/2)$ in Eq. (30) is small, and g_1 may be extracted from $A_\parallel$ without equally good knowledge of $A_\perp$. None of

10

the experiments preceding E143 used any measured $A_\perp$ in their calculation of g_1. Instead they assumed $A_\perp = 0$. The measurement of $A_\perp$ by SMC [4] which was published before E143 was also not used in their calculations of g_1.

2.5 The Parton Model

A very important model on the way to the current theory of Quantum Chromodynamics (QCD) was the Parton Model by Feynman [12], Bjorken and Paschos [13]. Although known to be far from complete, its simplicity made it to a benchmark to which experimental results and theoretical predictions are still often compared. In this model, the constituents of the nucleons are called partons. The variable x is interpreted as the momentum of the parton at the time of interaction given as the fraction of the total nucleon momentum. In modern theories, the partons are identified with quarks and gluons.

In the scaling limit, the structure functions may be seen as distribution functions of quarks with given x. For example, let $q_i(x)$ be the probability to find quark of kind i with momentum fraction x and let e_i be the charge of quarks of kind i in units of e. Then the structure functions F_1 and F_2 can be interpreted as

$$F_1(x) = \frac{1}{2}\sum_i e_i^2 q_i(x) \quad \text{and} \quad F_2(x) = x\sum_i e_i^2 q_i(x). \tag{35}$$

As mentioned above, F_1 and F_2 are related by $F_2 = 2xF_1$.

Analysis of the experimental results for the structure function F_2 led to the conclusion that in the scaling region only 50% of the momentum is carried by the quarks, while the other part is carried by gluons [14], the mediators of the strong interaction. Gluons are neutral particles and thus cannot interact with photons. Therefore, electron scattering is only sensitive to the quark content of the nucleons. Still, gluons contribute by forming pairs of quarks and antiquarks which in turn may interact with the virtual photons.

The spin-structure functions may also be interpreted in terms of quark distributions. Let $q_+^i(x)$ be the number of quarks of flavor i with helicity parallel to

11

the nucleon helicity, and let $q_-^i(x)$ be similar, but with helicity antiparallel to the nucleon helicity. Then

$$g_1(x) = \frac{1}{2} \sum_i e_i^2 \left[q_+^i(x) - q_-^i(x) \right].$$ (36)

Again, i sums over all quarks flavors, and e_i is the electric charge of the quark in units of e.

The interpretation of g_2 in the parton model is not as straight forward. In the naive parton model, $g_2 = 0$ if the quarks are on mass-shell and have no Fermi motion inside the nucleon. Taking this into account leads to non-zero g_2. For a detailed discussion of this topic we refer the reader to Ref. [8].

2.6 The Virtual Photon

In this section, we will take a closer look at the virtual photon which is exchanged between the electrons and nucleons. Since the point interaction of the electron with the photon is very well described by QED, the interesting physics happens in the interaction of the virtual photon with the nucleon.

The interaction with the nucleon depends on the polarization of the photon and the polarization of the nucleon. The optical theorem connects the cross-section to the imaginary part of the forward virtual photon-nucleon Compton scattering $\gamma^* N \rightarrow \gamma^* N$, which leads us to the following four independent helicity amplitudes [15]:

$$M_{1,\frac{1}{2},1,\frac{1}{2}} \qquad M_{1,-\frac{1}{2},1,-\frac{1}{2}} \qquad M_{1,\frac{1}{2},0,\frac{1}{2}} \qquad M_{1,\frac{1}{2},0,-\frac{1}{2}}$$ (37)

The first and third subscripts stand for the initial and final photon helicities, and the second and fourth subscripts stand for the initial and final nucleon helicities. Any other possible combinations of initial and final photon and nucleon helicities are related to these four via time reversal:

$$\mathcal{M}_{\alpha,\beta,\gamma,\delta} = \mathcal{M}_{\gamma,\delta,\alpha,\beta}$$ (38)

and parity:

$$\mathcal{M}_{\alpha,\beta,\gamma,\delta} = \mathcal{M}_{-\alpha,-\beta,-\gamma,-\delta}$$ (39)

12

The four independent helicity amplitudes can be written as functions of the spin-independent and spin-dependent structure functions or in terms of $\gamma^* N$ cross-sections $\sigma^T_{1/2}$, $\sigma^T_{3/2}$, $\sigma^L_{1/2}$, and $\sigma^{TL}_{1/2}$. Here the subscript denotes the total spin of the photon-nucleon system, and the superscript the polarization of the virtual photon: T and L for initial and final photon polarization being transverse and longitudinal, respectively; TL for the photon helicity switching from transverse to longitudinal during the interaction.

$$\frac{4\pi^2\alpha}{K}M_{1,\frac{1}{2},1,\frac{1}{2}} = \sigma^T_{1/2} \equiv \frac{4\pi^2\alpha}{MK}\left[F_1 + g_1 - \frac{2Mx}{\nu}g_2\right] \tag{40}$$

$$\frac{4\pi^2\alpha}{K}M_{1,-\frac{1}{2},1,-\frac{1}{2}} = \sigma^T_{3/2} \equiv \frac{4\pi^2\alpha}{MK}\left[F_1 - g_1 + \frac{2Mx}{\nu}g_2\right] \tag{41}$$

$$\frac{4\pi^2\alpha}{K}M_{0,\frac{1}{2},0,\frac{1}{2}} = \sigma^L_{1/2} \equiv \frac{4\pi^2\alpha}{K}\left[\frac{F_2}{\nu}\left(1 + \frac{\nu^2}{Q^2}\right) - \frac{F_1}{M}\right] \tag{42}$$

$$\frac{4\pi^2\alpha}{K}M_{1,\frac{1}{2},0,-\frac{1}{2}} = \sigma^{TL}_{1/2} \equiv \frac{4\pi^2\alpha}{K}\frac{\sqrt{Q^2}}{M\nu}(g_1 + g_2) \tag{43}$$

K is the flux of the virtual photons:

$$K \equiv \nu - \frac{Q^2}{2M} \tag{44}$$

The total cross-section for transverse polarized virtual photons is

$$\sigma_T \equiv \frac{1}{2}\left(\sigma^T_{1/2} + \sigma^T_{3/2}\right) = \frac{4\pi^2\alpha}{MK}F_1. \tag{45}$$

The above mentioned function $R(x, Q^2)$ is defined by

$$R \equiv \frac{\sigma^L_{1/2}}{\sigma^T} = \frac{F_2}{F_1}\frac{1 + \gamma^2}{2x} - 1. \tag{46}$$

If we now define

$$A_1 \equiv \frac{\sigma^T_{1/2} - \sigma^T_{3/2}}{\sigma^T_{1/2} + \sigma^T_{3/2}} \quad \text{and} \quad A_2 \equiv \frac{\sigma^{TL}_{1/2}}{\sigma_T}, \tag{47}$$

we find the following relations:

$$A_1 = \frac{1}{F_1}(g_1 - \gamma^2 g_2) \quad \text{and} \quad A_2 = \frac{1}{F_1}\gamma(g_1 + g_2). \tag{48}$$

13

Inverting these relations gives:

$$g_1 = \frac{F_2}{2x(1+R)}(A_1 + \gamma A_2),$$

(49)

$$g_2 = \frac{F_2}{2x(1+R)}(A_2/\gamma - A_1).$$

(50)

We also obtain:

$$A_1 = \frac{1}{D'}\left[A_\parallel\left(1+\gamma^2 y/2\right) - A_\perp \frac{\gamma^2 y}{2\tan(\theta/2)}\right]$$

(51)

and

$$A_2 = \frac{\gamma(2-y)}{2D'}\left[A_\parallel + A_\perp \frac{y(1+\gamma^2 y/2)}{(1-y)\sin\theta}\right].$$

(52)

These two relations are sometimes also expressed with different variables. Let us define:

$$D = \frac{1 - E'\epsilon/E}{1 + \epsilon R}; \quad \eta = \frac{\epsilon\sqrt{Q^2}}{E - E'\epsilon}; \quad d = D\sqrt{\frac{2\epsilon}{1+\epsilon}}; \quad \zeta = \eta\frac{1+\epsilon}{2\epsilon}.$$

(53)

Then

$$A_1 = \frac{A_\parallel}{D(1+\eta\zeta)} - \frac{\eta A_\perp}{d(1+\eta\zeta)} \quad \text{and} \quad A_2 = \frac{\zeta A_\parallel}{D(1+\eta\zeta)} + \frac{A_\perp}{d(1+\eta\zeta)}$$

(54)

or if we invert the equations, we obtain

$$A_\parallel = D(A_1 + \eta A_2) \quad \text{and} \quad A_\perp = d(A_2 - \zeta A_1)$$

(55)

The factor D is also called the depolarization factor.

The magnitude of A_1 can obviously never exceed 1, while the magnitude of A_2 is limited by $\left|A_2(x, Q^2)\right| \leq \sqrt{R(x, Q^2)}$ (positivity constraint) [16]. Since $R \to 0$ for infinite Q^2, A_2 must approach zero for $Q^2 \to \infty$.

2.7 Q^2-Dependence

2.7.1 Origin of Q^2-Dependence

Consistency with scaling means that at high Q^2 the structure functions do not depend on Q^2. In previous sections, we already mentioned that scaling is only an approximation and that for finite Q^2 scaling violations modify the structure function. The violation of scaling complicates the situation, but on the other hand, gives us a tool to look at the nucleon even more closely and learn about the forces within. In this section, we will take a closer look at these scaling violations and their description and introduce the method described in Ref. [17]. The application of the method to the E143 data is described in Chapter 5 of this dissertation.[1]

A basic understanding of the Q^2-dependence of the structure functions is required for several reasons. First, experiments measure the structure function at low x with low Q^2, and at high x with high Q^2. Similarly, E143 measured g_1 with two independent spectrometers. Events with the same x have a higher Q^2 in the $7°$ spectrometers than in the $4.5°$ spectrometer. To improve the statistics, the combination of the results from these two spectrometers is desired, or the combination of several experiments. In order to do this, the Q^2-dependence of the data has to be concerned. Secondly, the integral $\Gamma_1 = \int_0^1 dx\, g_1$ is, as discussed later, of great importance for the understanding of the nucleon structure. This integral has to be obtained from g_1 at a common $Q^2 = Q_0^2$ by evolving the experimental values to Q_0^2.

In the parton model, which assumes the limit $Q^2 = \infty$, the partons (quarks or gluons) in the nucleus do not interact with each other. This lack of interaction between the partons leads to scaling. In this case, the absorption of a virtual photon with a certain value of Bjorken x is only possible if the struck quark carries the fraction x of the nucleon momentum.

In the framework of quantum chromodynamics (QCD), however, the quarks interact with each other by exchange of gluons, and the gluons themselves interact

---

[1] The majority of results given in this dissertation was, however, derived with the assumption that g_1/F_1 is independent of Q^2.

with each other, too. These interactions modify the structure functions depending on the Q^2 of the reaction.

The Q^2-dependence can be qualitatively described in the following way. Inside the nucleon, quarks may emit and then at once absorb gluons. According to the time-energy uncertainty principle, the high-energy gluons stay closer to the quarks than low-energy gluons. If the Q^2 of the virtual photon is not large enough, the virtual photon cannot resolve the quarks and only sees the quark-gluon systems. At high Q^2, however, it sees the quarks alone. If the quark is hit right after it emitted a gluon, its momentum ($\hat{=} x$) will be lower. Therefore, a virtual photon with high Q^2 can see low-momentum quarks inside high-momentum quark-gluon systems. This explains the well-known result for the unpolarized structure functions that at low x the structure function increases with Q^2 (higher $Q^2 \implies$ more low-x quarks can be seen among the quark-gluon systems) while at high x the structure function decreases with increasing Q^2 (higher $Q^2 \implies$ the photons see more low-x quarks and do not interact with the high-x quarks). Around $x = 0.25$, the dependence on Q^2 is minimal.

Corrections to the structure functions can be sorted into two kinds [18] [19]. Corrections in orders of α_s, which is the QCD equivalent to the QED coupling constant α, are called "leading twist" or "twist-2" terms, while terms in orders of $1/\sqrt{Q^2}$ or higher are called "higher twist" corrections (twist-3 $\sim 1/\sqrt{Q^2}$, twist-4 $\sim 1/Q^2$, *etc.*). The higher twist terms also have the QCD corrections in α_s like the leading twist terms [19]. Higher twist corrections, for example, are due to the scattering of the photon off two quarks at the same time, or due to finite mass effects. The higher twist corrections are calculated non-perturbatively and are not as well understood as the leading twist corrections. They become important at low Q^2. We will not include them in our discussion of the Q^2-dependence.

2.7.2 Evolution Equations

In the experimental papers, the common method to deal with the Q^2-dependence of the spin-dependent structure functions is to assume that the ratio g_1/F_1 (or

A_1 and A_2) is independent of Q^2. The results from different spectrometers or experiments may then be averaged. The calculation continues by assuming that the combined value is at a certain $Q^2 = Q_0^2$ (for E143 typically $Q_0^2 = 3\,\mathrm{GeV}^2$). For example, the combined value of $(g_1/F_1)(x)$ — which might have been obtained with events of average $Q^2 \neq Q_0^2$ — may then be multiplied by $F_1(x, Q_0^2)$ to obtain $g_1(x, Q_0^2)$. While this method is very simple and quite model-independent, it is not correct because g_1 does not have the exact same Q^2-dependence as F_1.

A more exact evolution to common Q^2 can be obtained with the evolution equations described here. As mentioned, the higher twist corrections will be excluded in our analysis and only the lowest order leading twist corrections will be used.

2.7.2.1 Unpolarized Case

The Q^2-dependence of unpolarized quark distributions is well described in text books, and we will only introduce here the essential results, following Refs. [14] and [20].

Let $q_i(x)$ be the distribution of quarks of kind i with momentum fraction x for up-, down- or strange-quarks. Other quark flavors shall be neglected here. The absorption of a virtual photon with a certain value of Bjorken x is only possible if the struck quark carries the fraction x of the nucleon momentum. The scattering cross-sections tell us therefore about the distribution of quarks, about the probability to find a quark with momentum fraction x.

Introducing interactions between partons means that the quarks may absorb or emit gluons. In this case, the absorbing quark does not have to have the momentum fraction x right from the beginning, but may have gotten it after emission or absorption of a gluon. The quark might also have originated in a quark-antiquark pair created from a gluon which had a higher momentum fraction. We restrict our analysis and discussion to these two lowest order terms (first order in the strong coupling constant α_s). Fig. 2 shows the zeroth-order and two first-order Feynman diagrams. (Two more first-order diagrams appear in Fig. 3).
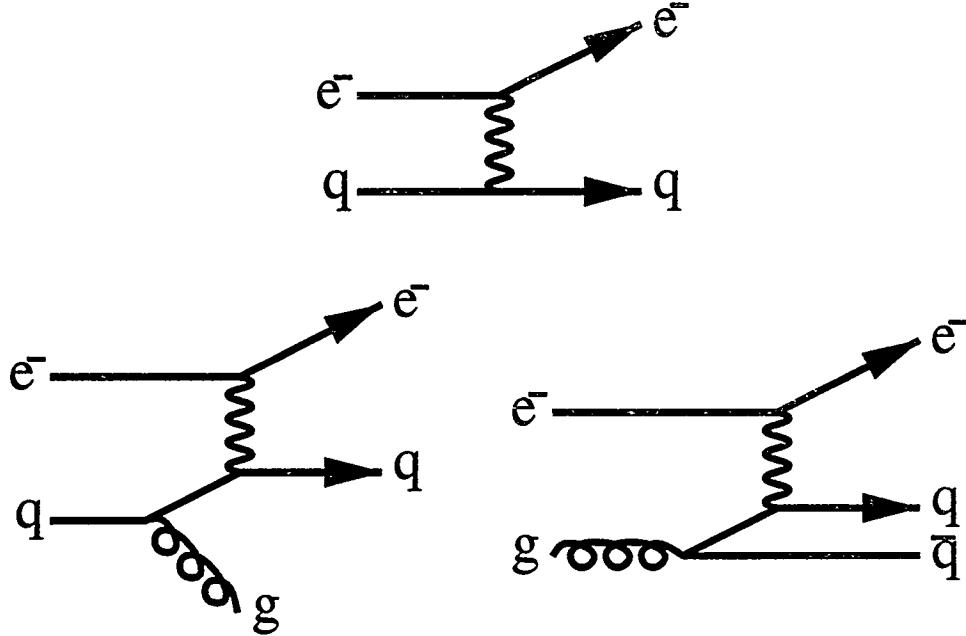
Figure 2 The zeroth- and first-order QCD terms for lepton-quark scattering. On the top is the zeroth order term. On the bottom are the first order terms. To the left, the quark first loses momentum (lowering x) by emitting a gluon. To the right, a gluon disintegrates into a pair of quark and antiquark, one of which then interacts with the lepton. More first-order terms are shown in Fig. 3

The interaction with gluons changes the probability to find a quark with momentum fraction x. For example, the quark may have originated from quark with higher momentum fraction y. The probability distribution to find a quark with fraction $z = \frac{x}{y}$ of the original quark momentum is

$$\mathcal{P}(z, Q^2) = \delta(1 - z) + \frac{\alpha_s}{2\pi} P_{qq}(z) \log \frac{Q^2}{\Lambda^2}. \tag{56}$$

The delta function $\delta(1 - z)$ is for the zero-order term, in which no gluon is involved. The second term depends on the Q^2 of the virtual photon. It describes the contribution due to the emission of a gluon which results the quark to have the fraction z of the original momentum. $P_{qq}(z)$ is called a "splitting function" and is given by:

$$P_{qq}(z) = \frac{4}{3} \left(\frac{1 + z^2}{1 - z} \right)_+ \tag{57}$$

The plus symbol will be discussed later. Λ is the renormalization constant.

The virtual photon shall interact with the quark of momentum fraction x. This momentum fraction x may originate from the zero-order term, or from the first-order

18

terms with $x = zy$. The quark distribution may then be written as

$$q(x, Q^2) + dq(x, Q^2) = \int_0^1 dy \int_0^1 dz\, q(y, Q^2) \mathcal{P}(z, Q^2) \delta(x - zy). \qquad (58)$$

The quark density $q(x, Q^2)$, i.e., the probability to find a quark which may absorb a photon with x and Q^2, is here altered by the term $dq(x, Q^2)$. The expression may be rewritten to the form of the so-called "Gribov-Lipatov-Altarelli-Parisi" (GLAP) evolution equations [21]:

$$\frac{d}{d \log Q^2} q(x, Q^2) = \frac{\alpha_s}{2\pi} \int_x^1 \frac{dy}{y} q(y, Q^2) P_{qq} \left(\frac{x}{y} \right). \qquad (59)$$

Since a quark with momentum x may come from any quark with higher momentum, the integral goes from x to 1. The initial shape of the distribution is not determined by these equations. Instead, the shape has to be determined via experiments or, perhaps, via lattice QCD calculations.[2]

If we also allow those quarks to contribute from a quark-antiquark pair created by the splitting of a gluon, the gluon distribution $g(x, Q^2)$ has to be introduced. Analog to $q_i(x)$, it gives the probability to find a gluon with momentum fraction x. Another term appears now in the evolution equation of the quark distributions:

$$\frac{d}{d \log Q^2} q(x, Q^2) = \frac{\alpha_s}{2\pi} \int_x^1 \frac{dy}{y} \left[q(y, Q^2) P_{qq} \left(\frac{x}{y} \right) + g(y, Q^2) P_{qg} \left(\frac{x}{y} \right) \right], \qquad (60)$$

and we also obtain an evolution equation for the gluon distribution:

$$\frac{d}{d \log Q^2} g(x, Q^2) = \frac{\alpha_s}{2\pi} \int_x^1 \frac{dy}{y} \left[\sum_i q(y, Q^2) P_{gq} \left(\frac{x}{y} \right) + g(y, Q^2) P_{gg} \left(\frac{x}{y} \right) \right]. \qquad (61)$$

The index i stands for the quark and antiquark flavors. The splitting function $P_{qg}(z)$ corresponds to gluons breaking into quark-antiquark pairs with the quark having a momentum of z times the gluon momentum [bottom right diagram in Fig. 2]:

$$P_{qg}(z) = \frac{1}{2}(z^2 + (1 - z)^2). \qquad (62)$$

---

[2] The integral in the evolution equations are convolution integrals, which in general are defined as $(f \otimes g)(z) \equiv \int_x^1 \frac{dz}{z} f(z) g(x/z)$. In this dissertation, we will avoid the often used short notation $f \otimes g$.

The probability for a quark to radiate a gluon with z times the quark's original momentum [left diagram in Fig. 3] is described by

$$P_{gq}(z) = \frac{4}{3}\frac{1+(1-z)^2}{z},$$ (63)

and the probability for a gluon to lose the fraction z of its momentum by emitting a gluon [right diagram in Fig. 3] is given by

$$P_{gg}(z) = 6\left(\frac{1-z}{z} + \frac{z}{1-z} + z(1-z)\right).$$ (64)

Of course, higher order corrections may be included. With the evolution equations, global fits to the data may be performed.
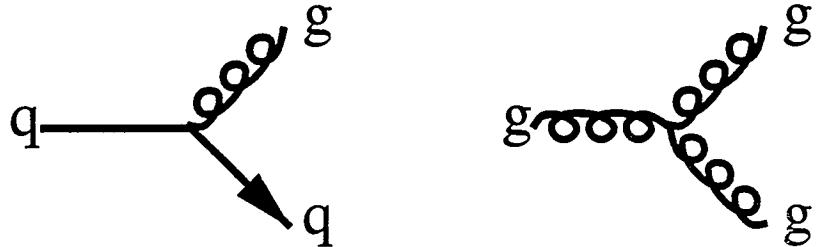
Figure 3 First order QCD terms for lepton-quark scattering affecting the gluon distribution. To the left, a gluon with momentum fraction x originates from a higher-momentum quark. To the right, a gluon with momentum fraction x originates from another gluon.

The origin of the plus sign at Eq. (57) is the following. The term $(1+z^2)/(1-z)$ has a singularity at $z = 1$. This effect is called "infrared divergence". Solving the convolution integral would be impossible with this singularity. However, a closer analysis reveals that the second-order virtual gluon diagrams shown in Fig. 4 lead to a cancelation of these terms. Instead of calculating the contribution from these higher order terms directly, a simpler derivation is sufficient (see *e.g.* [14]), leading to the so-called "+ prescription". Here the singularity is removed by exchanging the term

$$\frac{1+z^2}{1-z}$$ (65)

by

$$\left(\frac{1+z^2}{1-z}\right)_+ .$$ (66)

20
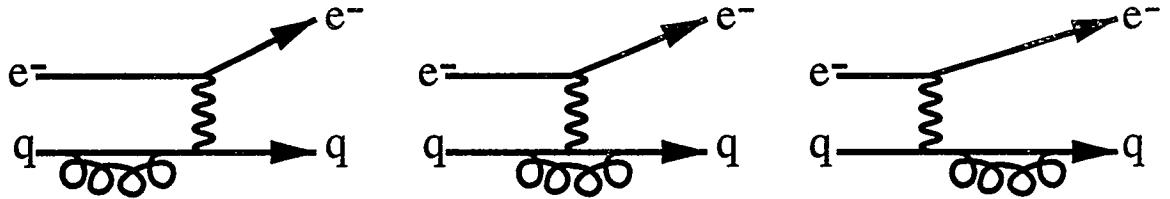
Figure 4 Second order virtual gluon diagrams for lepton-quark scattering.

with the definition

$$\int_0^1 dz\, f(z) \Big(g(z)\Big)_+ \equiv \int_0^1 dz\, [f(z) - f(1)]g(z). \tag{67}$$

and $\Big(g(z)\Big)_+ \equiv g(z)$ for $z < 1$. The splitting function P_{gg} is similarly modified.

2.7.2.2 Polarized Case

This section follows closely Ref. [17]. For the polarized case, the equations are very similar. Instead of the quark and gluon distributions $q_i(x, Q^2)$ and $g(x, Q^2)$, we now have the polarized quark[3] and gluon distributions

$$\Delta q(x, Q^2) = q^+(x, Q^2) - q^-(x, Q^2) \tag{68}$$

[for any of the quark types; also see Eq. (36)] and

$$\Delta g(x, Q^2) = g^+(x, Q^2) - g^-(x, Q^2). \tag{69}$$

The splitting functions of the polarized case will also be marked with a Δ. The evolution equation for Δq is:

$$Q^2 \frac{d}{dQ^2} \Delta q(x, Q^2) =$$
$$\frac{\alpha_s}{2\pi} \left[\int_x^1 \frac{dy}{y} \Delta q(y, Q^2) \Delta P_{qq}(x/y) + 2 \int_x^1 \frac{dy}{y} \Delta g(y, Q^2) \Delta P_{qg}(x/y) \right] \tag{70}$$

---

[3] We adopt here the widely used notation. The expression Δq is also used for the helicity content.

21

The splitting function $\Delta P_{qq}(z)$ is defined exactly as $P_{qq}(z)$ for the unpolarized case [Eq. (57)],

$$\Delta P_{qq}(z) = \frac{4}{3}\left(\frac{1+z^2}{1-z}\right)_+ \tag{71}$$

while the probability for a quark to lose a gluon which carries the fraction z of the original momentum is slightly different from Eq. (62):

$$\Delta P_{qg}(z) = \frac{1}{2}\left[z^2 - (1-z)^2\right]. \tag{72}$$

Since the spin-structure functions g_1 connect to the polarized quark distributions via

$$g_1(x, Q^2) = \frac{1}{2}\sum_i e_i^2 \Delta q_i(x, Q^2) \tag{73}$$

as mentioned earlier, in we may rewrite Eq. (70) to

$$Q^2 \frac{d}{dQ^2} g_1^{p,n}(x, Q^2) =$$
$$\frac{\alpha_s}{2\pi}\left[\int_x^1 \frac{dy}{y} g_1^{p,n}(y, Q^2) P_{qq}(x/y) + \frac{2}{3}\int_x^1 \frac{dy}{y}\Delta g(y, Q^2) P_{qg}(x/y)\right] \tag{74}$$

or

$$dg_1^{p,n}(x, Q^2) = \frac{\alpha_s}{2\pi}d\log\frac{Q^2}{\Lambda^2}$$
$$\left[\int_x^1 \frac{dy}{y} g_1^{p,n}(y, Q^2) P_{qq}(x/y) + \frac{2}{3}\int_x^1 \frac{dy}{y}\Delta g(y, Q^2) P_{qg}(x/y)\right]. \tag{75}$$

The term with α_s may be approximated:

$$\frac{\alpha_s}{2\pi}d\log\frac{Q^2}{\Lambda^2} \approx -\frac{1}{2\pi}\frac{2}{9}d\log\alpha_s \tag{76}$$

Also, since the dependence on Q^2 is not very rapid, the Q^2-dependence on the right side of Eq. (75) is neglected:

$$g_1^{p,n}(x, Q^2) - g_1^{p,n}(x, Q_0^2) = \frac{2}{9}\log\frac{\alpha_s(Q_0^2)}{\alpha_s(Q^2)}$$
$$\left[\int_x^1 \frac{dy}{y} g_1^{p,n}(y, Q^2) P_{qq}(x/y) + \frac{2}{3}\int_x^1 \frac{dy}{y}\Delta g(y, Q^2) P_{qg}(x/y)\right] \tag{77}$$

Using Eqs. (57) and (67), we obtain for the first convolution integral the following expression without any singularities:

$$\int_x^1 \frac{dy}{y} g_1^{p,n}(y, Q^2) P_{qq}(x/y) = \frac{4}{3}\int_x^1 \frac{dy}{y}\frac{1+y^2}{1-y}\left[\frac{1}{y}g_1^{p,n}\left(\frac{x}{y}\right) - g_1^{p,n}(x)\right]$$
$$+ \frac{4}{3}\left[x + \frac{1}{2}x^2 + 2\log(1-x)\right]. \tag{78}$$

The gluon distribution may similarly be evolved, but currently not much known is about $\Delta g(x)$ anyway. Experiments measuring this distribution are already proposed, but until their results are known, the magnitude or shape of Δg has to be assumed or obtained by theoretical models. Ref. [1], for example, mentioned a relatively high value for $\Delta g = \int_0^1 dx \, \Delta g(x, Q^2)$ of 5 at $Q^2 = 10.7 \, \text{GeV}^2$, while newer estimates are $\Delta g = 1.5 \pm 0.8$ at $Q^2 = 1 \, \text{GeV}^2$, $\Delta g \approx 3$ at $Q^2 = 10 \, \text{GeV}^2$ [22], or $\Delta g \approx 1.7$ at $Q^2 = 10 \, \text{GeV}^2$ [23].

The improved evolution of the spin-structure function g_1 to common $Q^2 = Q_0^2$ is performed in the following way: The experimental structure function $g_1(x, Q^2)$ is obtained from the measured spin-asymmetry A_1 by multiplying it with the unpolarized structure function F_1 taken at the x and Q^2, at which the spin-asymmetry A_1 was measured. Then Eqs. (77) and (78) are used to obtain $g(x, Q_0^2)$, i.e., the structure function at fixed $Q^2 = Q_0^2$. To evaluate the integral on the right side of Eq. (78), a fit to the experimental $g_1(x, Q^2)$ is usually used. This method was, for example, applied in Ref. [17] to the results from E80 [24], E130 [25], EMC [1], SMC [3], and E142 [6]. The dissertation will present results for the E143 data using essentially the same evolution equations. (The main results in this dissertation, were, however, derived with the simple evolution assuming g_1/F_1 to be Q^2-independent.)

The dissertation stays with the lowest order in α_s since higher orders become numerically complicated. Besides Ref. [17], also Ref. [26] performed such a leading order fit. Higher terms in the evolution equations were taken into account by other authors. Refs. [27] and [28] had not yet available the full next-to-leading order equations from Ref. [29]. The full equations were later applied in Refs. [22] and [23].

2.8 The Deuteron as Composite of Proton and Neutron

The neutron structure function can be extracted from the proton and deuteron structure functions assuming that the deuteron is the combination of one proton and one neutron. From experiments, it was determined that the deuteron has a total angular momentum of 1 and a magnetic moment of $\mu_D = +0.857$ [30]. This

magnetic moment is very close to the combined magnetic moment of proton and nucleon, $\mu_p + \mu_n = 2.793 - 1.913 = 0.880$. This fact indicates that the proton and neutron are most of the time in the ground state with orbital angular momentum $L = 0$ to each other [31]. The difference between μ_D and $\mu_p + \mu_n$ arises since the deuteron is to some degree also in the D-state with $L = 2$. This state also causes the deuteron to have a non-zero quadrupole moment.

The total angular momentum $\mathbf{J}$ is given by the addition of the orbital angular momentum and the total spin: $\mathbf{J} = \mathbf{L} + \mathbf{S}$. The eigenvalue of the operator $\mathbf{J}^2$ is $J(J+1)$. We know that the deuteron has spin 1, i.e., $J = 1$. The projection to the z-axis, $\mathbf{J}_z$, has then the eigenvalues $J_z = -1, 0, 1$. For the target polarization, the important quantity is J_z. As we will see later, the deuterons were polarized by aligning J_z into one direction, while an NMR system was measuring the expectation value of $\mathbf{J}_z$ and hence the polarization. However, the deep-inelastic scattering of electrons does not depend on J_z or L_z, but instead on S_z. We therefore have to examine how the spin is oriented for given J_z.

The spin-operator $\mathbf{S}$ is composed of the two spin-$\frac{1}{2}$ operators of the proton and neutron. These two operators together form the eigenstates $S = 0$ ($S_z = 0$) and $S = 1$ ($S_z = -1, 0, 1$). For the S-state, we have $L = 0$ and $L_z = 0$. For the D-state, we have $L = 2$ and $L_z = -2, -1, 0, 1, 2$. Adding the two angular momenta described by $\mathbf{S}$ and $\mathbf{L}$ gives us $\mathbf{J}$ with the selection rules $|S - L| \leq J \leq S + L$ and $J_z = S_z + L_z$.

The requirement that $J = 1$ in the deuteron has the following consequences: If the two nuclei are in the S-state ($L = 0$), the spin $\mathbf{S}$ has to be $S = 1$, and $J_z = S_z$. If they are in the L-state ($L = 2$), then the spin is also $S = 1$, but the z-component of $\mathbf{J}$ is $J_z = S_z + L_z$. We have therefore several possibilities for J_z to be composed of S_z and L_z (Table 2).

The Clebsch-Gordan coefficients describe how each state with given J_z is composed of states with definite S_z and L_z. For example, the Clebsch-Gordan coefficient combining the $L_z = 0$ and $S_z = -1$ state with the $J_z = -1$ state is

$$<L = 2, S = 1; L_z = 0, S_z = -1 | J = 1, J_z = -1> = \frac{1}{\sqrt{10}}. \qquad (79)$$

This means that the ($J = 1, J_z = -1$)-state has a 10% probability to be in the state

Table 2 Clebsch-Gordan coefficients and probabilities for the (L=2)-state. For $J = 1, S = 1$ and $L = 2$, the projection J_z can be composed of different L_z and S_z. The last two columns list the Clebsch-Gordan coefficients and probabilities for these choices of eigenvectors.

J_z	L_z	S_z	Clebsch-Gordan coefficients	Probability
-1	0	-1	$\sqrt{1/10}$	0.10
-1	-1	0	$-\sqrt{3/10}$	0.30
-1	-2	$+1$	$\sqrt{3/5}$	0.60
0	$+1$	-1	$\sqrt{3/10}$	0.30
0	0	0	$-\sqrt{2/5}$	0.40
0	-1	$+1$	$\sqrt{3/10}$	0.30
$+1$	$+2$	-1	$\sqrt{3/5}$	0.60
$+1$	$+1$	0	$-\sqrt{3/10}$	0.30
$+1$	0	$+1$	$\sqrt{1/10}$	0.10

($L_z = 0, S_z = -1$). Table 2 lists all Clebsch-Gordan coefficients and associated probabilities.

Let $A_{L=0}$ be the measured asymmetry if only (L=0)-states would contribute to the scattering. A measured target polarization of $+100\%$ would then mean that all electrons are scattered from deuterons with $S_z = 1$. If only (L=2)-states would contribute, the measured asymmetry $A_{L=2}$ would originate to 10% from deuterons with $S_z = +1$, to 60% from deuterons with $S_z = -1$, and to 30% from deuterons with $S_z = 0$. As it is shown in the appendix,

$$A_{L=2} = 0.1A_{L=0} - 0.6A_{L=0} = -0.5A_{L=0}. \tag{80}$$

With ω_D as the probability for the deuteron to be in the D-state, the total measured asymmetry A for deuterons polarized to $+100\%$ is given by

$$A = (1 - \omega_d)A_{L=0} - 0.5\omega_D A_{L=0} = (1 - 1.5\omega_D)A_{L=0}. \tag{81}$$

The asymmetry for $L = 0$ is expected to be the average of the proton and neutron asymmetries, weighted by the cross-sections, or, equivalently, the unpolarized

structure functions. Adopting the convention that the deuteron structure function refers to the average nucleon in the deuteron,

$$F_1^d = \frac{1}{2}\left(F_1^p + F_1^n\right),\tag{82}$$

we arrive at

$$A^d = (1 - 1.5\omega_D)\left[\frac{F_1^p}{2F_1^d}A^p + \frac{F_1^n}{2F_1^d}A^n\right]\tag{83}$$

with A being $A_{\parallel}$, $A_{\perp}$, A_1, or A_2. And with Eq. (30), we obtain

$$g_1^d = \frac{1 - 1.5\omega_D}{2}\left(g_1^p + g_1^n\right).\tag{84}$$

The numerical value of ω_D cannot be measured directly in experiments. Instead, it has to be inferred from phenomenological potentials like the so-called Bonn-Potential [32] [33], the Paris-Potential [34] and others. Table 3 lists several of such estimates. For E143, we used the value $\omega_D = 0.05 \pm 0.01$.

Table 3 Model calculations for deuteron D-state probability ω_D.

model	ω_D
Bonn (1976) [32]	0.0440
Bonn (1987) [33]	0.0425
Paris (1980) [34]	0.0577
Reid (soft-core) (1968) [35]	0.0647

2.9 The Structure Function g_2

While the structure function g_1 has a simple interpretation in the parton model, the interpretation of the structure function g_2 is not similarly obvious (see for example [8]).

In general (not limited to the scaling region), g_2 can be approximated by g_2^{WW}, named after Wandzura and Wilczek, the authors of Ref. [36], where g_2^{WW} was introduced:

$$g_2 \approx g_2^{WW} \tag{85}$$

with

$$g_2^{WW}(x, Q^2) \equiv -g_1(x, Q^2) + \int_x^1 \frac{g_1(y, Q^2)}{y} \, dy. \tag{86}$$

g_2^{WW} itself is a leading twist term (also called twist-2 term), meaning that it approximately scales at high Q^2 up to QCD corrections in the strong coupling constant α_s. In addition to other twist-2 terms, also higher twist terms contribute to g_2. If g_2 is not known, for example because only $A_\parallel$, but not $A_\perp$ was measured, $g_2 = g_2^{WW}$ is sometimes used instead. In this work, we most often will use the approximation $A_\perp = 0$ which is good enough for the extraction of g_1.

In the derivation of Eq. (86), $\gamma^2 = 4M^2 x^2/Q^2$ was assumed to be zero. For E143, γ^2 is not so small, and Eq. (86) was re-derived without this assumption [37]. However, the difference between the exact and the approximate formula turned out to be negligible.

2.10 Fermi Motion, EMC Effect, and Nuclear Shadowing

If the nucleon is bound inside a nucleus, the cross-section for lepton-nucleon scattering is different from that of a free nucleon. The modification of the cross-section can be separated into three effects: Fermi Motion, EMC Effect, and Nuclear Shadowing [38] [39]. This categorization is, however, not unique and the boundaries between the effects are not well known.

In the simplest picture, a nucleus would be just a collection of Z protons and $A - Z$ neutrons, each of them interacting with the electrons in the same way as if they were free protons or neutrons. However, this is not the case. The ratio

$$\rho = \frac{F_2^A}{F_2^N} \qquad (87)$$

is a good indicator of the changes. Here F_2^A stands for the per-nucleon structure function of the nucleus while F_2^N stands for the structure function of a free nucleon. In general, the ratio ρ is lower than one between $x \approx 0.3$ and $x \approx 0.8$ because of the EMC effect. Nuclear shadowing causes $\rho < 1$ for $x \lesssim 0.05$. Between $x \approx 0.05$ and $x = 0.3$ is a transition region with $\rho > 1$. The Fermi motion becomes apparent for $x \lesssim 1$ and increases ρ to $\rho > 1$.

Fermi Motion: Bound inside the nucleus, the protons and neutrons have a certain momentum distribution, called the Fermi motion, relative to the center of mass of the nucleus. The Fermi momentum of the nucleons is in the few-hundred-MeV range, and smears the data for any kinematics. However, the effect becomes visible only in a region where the cross-section varies considerably within the smearing range, like in the region at x close to 1, where the cross-section varies rapidly due to resonances.

EMC Effect: The expression "EMC effect" describes the fact that the per-nucleon cross-section of nuclei with $A > 2$ is smaller than the deuteron per-nucleon-cross section in the $x = 0.3$ to $x = 0.8$ region. The EMC effect was found by comparing the lepton-scattering cross-sections for iron and deuterium [40] and was later confirmed in other experiments. A commonly accepted explanation for the EMC effect does not yet exist [39].

Nuclear Shadowing: The nuclear shadowing effect can be imagined in the following way: If the cross-section of a particle (in our case the virtual photon) interacting with a quark inside the nucleus is large, the particle will mostly interact with the quarks at the front of the nucleus and less penetrate the nuclear matter beyond the front area. Hence, the quarks inside or at the back have less influence and do not contribute much to the scattering process. The total cross-section per nucleon is then rather proportional to R_{nucl}^2, the square of the nucleus radius, than

28

proportional to the number of nucleons A ($\sim R_{nucl}^3$). Hence, the cross-section per nucleus decreases with A. The effect becomes more important at low x, where more quarks (from virtual quark-antiquark pairs) are visible to the particle which increases the probability for interaction at the front of the nucleus. On the other hand, the smaller the cross-section of the particle is, the larger is the amount of nuclear matter through which the particle can travel, and the smaller will be the effect of nuclear shadowing.

For the E143 data analysis, fits to experimental data of $\sigma(A)/\sigma$(deuterium) for $0.0085 \le x$ [41] [42] were used to scale the proton and deuteron structure functions [10] [11]. This correction term was commonly called the correction for the EMC effect. Fig. 5 shows the fit for three types of nuclei, ^{4}He, ^{15}N, and Cu. The regions of the three different effects (shadowing, EMC effect, Fermi motion) are indicated. The E143 deep-inelastic data ranged from $x = 0.03$ (x=0.02 for $E = 16.2$ GeV data) to maximal $x = 0.8$ (for 29 GeV data). The structure functions corrected by this "EMC effect" term were then used as the structure functions of the nuclei.
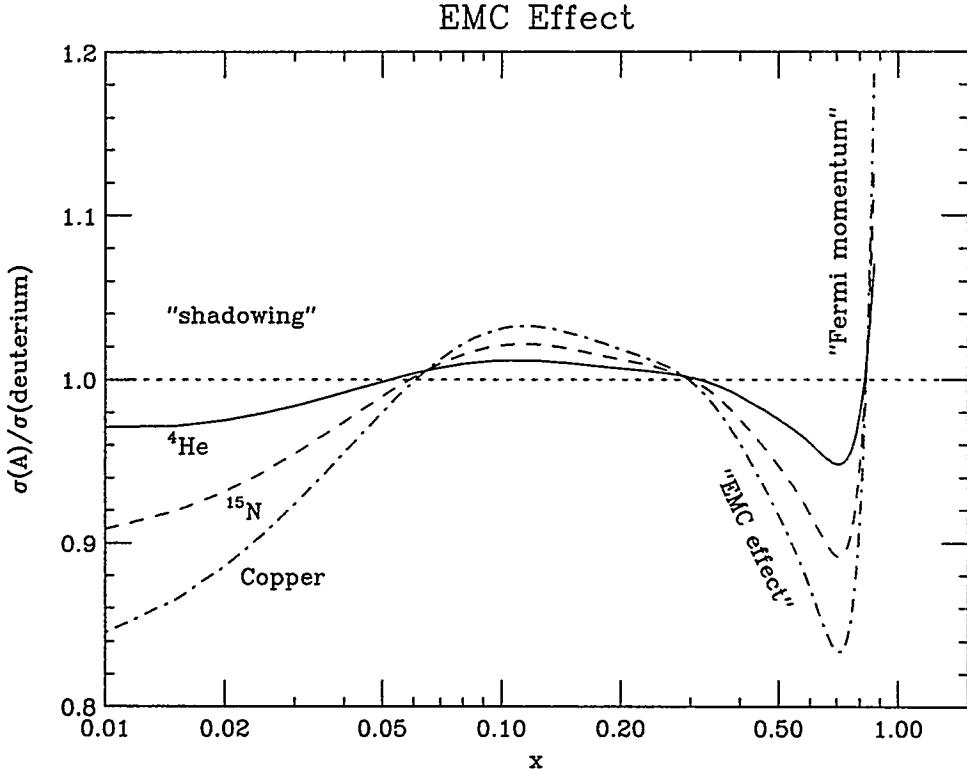
Figure 5 Ratio $\sigma(A)/\sigma$(deuterium) versus x for three types of nuclei. Solid line ^{4}He, dashed line ^{15}N, dot-dashed line Cu. See text for more details.

2.11 The Integral of g_1 over x

2.11.1 Bjorken Sum Rule

In 1967, Bjorken derived a sum rule for the spin-structure functions g_1^p and g_1^n based on basic current algebra [43]. Leaving out any QCD corrections, which are needed for finite Q^2, the sum rule is given by

$$\int_0^1 (g_1^p - g_1^n)\, dx = \frac{1}{6} g_A. \tag{88}$$

It links measurements of the spin-structure functions with the weak vector and axial-vector coupling constant g_A from neutron β-decay.[4] While the nucleon spin-structure functions are obtained at high Q^2, the coupling constant is defined for $Q^2 = 0$. Currently g_A is determined to be 1.2573 ± 0.0028 [44].

With the leading twist QCD corrections, the Bjorken sum rule is modified from Eq. (88) to [45]:[5]

$$\int_0^1 (g_1^p - g_1^n)\, dx = \frac{1}{6} g_A \left[1 - \left(\frac{\alpha_s}{\pi} \right) - 3.5833 \left(\frac{\alpha_s}{\pi} \right)^2 - 20.2153 \left(\frac{\alpha_s}{\pi} \right)^3 \right] \tag{89}$$

The Bjorken sum rule stands on the foundations of the quark and QCD model. If it would be found to be violated, the basic ideas of current elementary particle physics would be incorrect. According to Feynman, its "verification or failure would have a most decisive effect on the direction of future high-energy theoretical physics" (Ref. [12] p.159).

2.11.2 Ellis-Jaffe Sum Rule

Ellis and Jaffe developed additional sum rules [46] for the proton and neutron structure functions separately. Neglecting any QCD corrections, their derivation can be described in the following way within the quark-parton model.

---

[4] If only g_A is given, $g_V = 1$ is implied. Often the literature gives the ratio g_A/g_V instead of just g_A.

[5] Note that Ref. [45] use a different normalization, leading to a factor of 2 difference with the formula given here.

The spin-structure function g_1 is interpreted in the parton model via polarized quark distributions [see Eq. (36)], and the total contribution of the quarks to the helicity may be written as:

$$\Delta u = \int_0^1 \left[u_+(x) - u_-(x) \right] dx \tag{90}$$

$$\Delta d = \int_0^1 \left[d_+(x) - d_-(x) \right] dx \tag{91}$$

$$\Delta s = \int_0^1 \left[s_+(x) - s_-(x) \right] dx \tag{92}$$

We limit ourselves here to the light quarks: up, down and strange. As before, the subscript $+$ indicates quarks with helicity parallel to the nucleon helicity, and the subscript $-$ indicates quarks with helicity anti-parallel to the nucleon helicity. Isospin symmetry is assumed which means that the distribution of up-quarks in the proton is the same as the number of down-quarks in the neutron, $u^p(x) \equiv d^n(x)$ and $d^p(x) \equiv u^n(x)$. With polarization, this means $\Delta u^p(x) = \Delta d^n(x)$ and $\Delta d^p(x) = \Delta u^n(x)$. Since the up- and down-quark masses are only approximately the same, isospin symmetry is not exactly correct, but this discrepancy may be neglected for our purposes.

The integral of g_1 can now be written as (*e.g.*, [47]):

$$\Gamma_1^p \equiv \int_0^1 g_1^p \, dx = \frac{1}{2} \left[\frac{4}{9} \Delta u + \frac{1}{9} \Delta d + \frac{1}{9} \Delta s \right], \tag{93}$$

$$\Gamma_1^n \equiv \int_0^1 g_1^n \, dx = \frac{1}{2} \left[\frac{1}{9} \Delta u + \frac{4}{9} \Delta d + \frac{1}{9} \Delta s \right]. \tag{94}$$

Plugging these expressions into the Bjorken sum rule, we obtain

$$g_A \equiv (g_A)_{n \to p} = \Delta u - \Delta d. \tag{95}$$

The value of g_A is experimentally obtained from β-decay. Furthermore, $SU(3)$ flavor symmetry, in which the masses of the up-, down- and strange-quarks are assumed to be equal, relates the quark distributions of protons to those of hyperons. Their axial-vector constants g_A can experimentally be determined from semi-leptonic hyperon decays and may be expressed in terms of the quark distributions Δu, Δd, and Δs.

31

They are also often parameterized in terms of two constants F and D:

$$(g_A)_{n \to p} = F + D = \quad \Delta u - \Delta d \qquad (96)$$

$$(g_A)_{\Sigma \to n} = F - D = \quad \Delta d - \Delta s \qquad (97)$$

$$(g_A)_{\Lambda \to p} = F + \frac{1}{3}D = \frac{1}{3}[2\Delta u - \Delta d - \quad \Delta s] \qquad (98)$$

$$(g_A)_{\Xi \to \Lambda} = F - \frac{1}{3}D = \frac{1}{3}[\quad \Delta u + \Delta d - 2\Delta s] \qquad (99)$$

From the numerical values of the different g_A [44], we obtain $F = 0.4592 \pm 0.0078$ and $D = 0.7980 \pm 0.0080$ [48]. We can replace Δu and Δd with F and D in Eqs. (93) and (94) ($\Delta u = 2F + \Delta s$, $\Delta d = F - D + \Delta s$) and obtain:

$$\Gamma_1^p = \frac{1}{18}\left[9F - \quad D + 6\Delta s\right] \qquad (100)$$

$$\Gamma_1^n = \frac{1}{18}\left[6F - 4D + 6\Delta s\right] \qquad (101)$$

The leading twist QCD corrections to third order [49] modify Eqs. (100) and (101) to:

$$\Gamma_1^{p,n} = \left[1 - \left(\frac{\alpha_s}{\pi}\right) - 3.5833 \left(\frac{\alpha_s}{\pi}\right)^2 - 20.2153 \left(\frac{\alpha_s}{\pi}\right)^3\right] \times$$

$$\times \left(\pm\frac{1}{12}(F + D) + \frac{1}{36}(3F - D)\right) + \qquad (102)$$

$$+ \left[1 - 0.3333 \left(\frac{\alpha_s}{\pi}\right) - 0.5495 \left(\frac{\alpha_s}{\pi}\right)^2\right] \frac{1}{9}(3F - D + 3\Delta s).$$

These corrections were calculated during the recent years and have a significant influence on the results [50]. Estimates of corrections of one order higher were published [51], but are not used for this dissertation. All values are given for the $\overline{MS}$-scheme. These leading twist corrections allow us to compare experimental values obtained at different Q^2. The values may still not be sufficiently corrected if leading twist corrections to even higher order are necessary, or if higher twist corrections cannot be neglected.

Eq. (102) is often called the Ellis-Jaffe sum rule. However, for the actual Ellis-Jaffe sum rule, it is assumed that the strange-antistrange quark pairs do not contribute to the quark spin. In that case, the Ellis-Jaffe sum rule predicts Γ_1.

2.11.3 The Helicity Content of the Nucleons and the Gluon Contribution

If Δs is not set to zero in Eq. (102), the measurement of Γ_1 (together with the values for F and D) determines Δs. Furthermore, using Eqs. (96) to (99), Δu and Δd (the contribution of the u- and d-quarks) may be obtained, as well as $\Delta q \equiv \Delta u + \Delta d + \Delta s$, the contribution of all three quarks to the nucleon spin.[6] We can write Δq in terms of F, D, and Δs,

$$\Delta q = 3F - D + 3\Delta s, \tag{103}$$

to obtain Δq. The value of Δs can be obtained from Eq. (102) once Γ_1 is known.

The integrals Γ_1^p, Γ_1^n and Γ_1^d can be written as a sum of Δu, Δd, and Δs, as done in Eqs. (93) and (94). Often these integrals and helicity components are written in other ways [52], for example as:

$$a_3 = F + D = \Delta u - \Delta d = (g_A)_{n \to p} \tag{104}$$

$$a_8 = 3F - D = \Delta u + \Delta d - 2\Delta s = 3(g_A)_{\Xi \to \Lambda} \tag{105}$$

$$a_0 = \Delta q = \Delta u + \Delta d + \Delta s \tag{106}$$

Together with the appropriate QCD correction terms (not necessarily the same for the three terms), the following quantities are then defined:

$$I_3 = \frac{1}{12} a_3 \times \text{QCD corrections} \tag{107}$$

$$I_8 = \frac{1}{36} a_8 \times \text{QCD corrections} \tag{108}$$

$$I_0 = \frac{1}{9} a_0 \times \text{QCD corrections} \tag{109}$$

and the integrals Γ_1 can be expressed as

$$\Gamma_1^{p,n} = \pm I_3 + I_8 + I_0, \tag{110}$$

$$\Gamma_1^d \approx \frac{1}{2}\left(\Gamma_1^p + \Gamma_1^n\right) = I_8 + I_0. \tag{111}$$

---

[6] Instead of Δq, also the symbol $\Delta\Sigma$ is often used in the literature for the quark-contribution to the nucleon spin.

We remind the reader that we did not choose g_1^d as $g_1^d = \frac{1}{2}(g_1^p + g_1^n)$, but as $g_1^d = \frac{1-1.5\omega_D}{2}(g_1^p + g_1^n)$ taking into account the D-state probability ω_D (see earlier section). For the deuteron integral Γ_1^d, the I_3 component is zero and $I_0 = (\Delta u + \Delta d + \Delta s)/9$ dominates. The total contribution of the quarks to the spin can therefore be more precisely deduced from Γ_1^d than from Γ_1^p or Γ_1^n [53].

Experiments so far, including E143, measured consistently a helicity contribution Δq close to about 0.3. In contrast, the "non-relativistic quark model" expects $\Delta q = 1$, while the "relativistic quark model" expects $\Delta q = 0.75$ [18].

The discrepancy of the experimental results is at least partly understood due to partial cancellation of the quark contribution by the axial anomaly term involving gluons [8]. Instead of measuring $a_0 = \Delta q$, the experiments actually measure

$$a_0 = \Delta q - \frac{3\alpha_s}{2\pi}\Delta g. \tag{112}$$

Extracting Δq without taking into account the cancellation by the gluons contribution therefore leads to an underestimation of Δq. Δg is similarly defined as the quark contributions, with $g_+(x)$ and $g_-(x)$ being the distributions of gluons with helicity parallel and antiparallel to the nucleon helicity and

$$\Delta g = \int_0^1 \Delta g(x)\, dx = \int_0^1 [g_+(x) - g_-(x)]\, dx. \tag{113}$$

See also Eq. (69) in the section about the Q^2-dependence of the structure functions. As mentioned already there, not much is known about the gluon distribution. Current experimental results are used to extract Δg indirectly, but future experiments are expected to provide us with a direct measurement.

For all models, the following general rule must be satisfied [54]:

$$\frac{1}{2}\Delta q + \Delta g + L_z = \frac{1}{2} \tag{114}$$

where L_z is the contribution of orbital angular momentum to the nucleon spin. Δg is expected to depend on Q^2 and may become relatively large. In this case, L_z is expected to also increase, but in the opposite direction, so that Eq. (114) remains satisfied [8].

Ref. [18] lists predictions for the measured quark content with increasing sophistication of the theoretical models. The simplest and earliest model is the "non-relativistic quark model"; more sophisticated is the "relativistic three-quark model"; and even more advanced is the "gluon-enhanced three-quark model" which includes the axial anomaly term from polarized gluons. The predictions of the latter assume a gluon contribution $\frac{\alpha_s}{2\pi}\Delta g = 0.20$. This corresponds to $\Delta g \approx 3.5$ and is able to decrease the apparent measurement of Δq from about 75% to 15%. Table 4 lists the predictions for those models. With a sufficiently large gluon contribution, the experimental results of an apparent small value of Δq can therefore still be consistent with an actually larger Δq. Since the size of the gluon term is not known, we do not take the gluon contribution into account, and denote with Δq the measured value which in the experiments was determined to be around 0.3. We refer to it as the helicity contribution of all quarks, although the real helicity contribution might be different when correcting for the gluon contribution.

Table 4 Predictions for quark-contributions to nucleon spin from three different theoretical models. The non-relativistic quark model (NR), the relativistic three-quark model (3q), and the gluon-enhanced three-quark model (3q+g). From Ref. [18].

Quantity	NR	3q	3q+g
Δu	4/3	1	0.80
Δd	−1/3	−1/4	−0.45
Δs	0	0	−0.20
Δq	1	3/4	0.15

A final note about the assumption of $SU(3)$ symmetry. This symmetry was used in the derivation of the Ellis-Jaffe sum rule. Also, the extraction of the values F and D from the different decay constants g_A is based on it. However, $SU(3)$ symmetry is known to be broken, and there are currently discussion about the influence of this symmetry breaking on the sum rules and the helicity content (see for example Ref. [55]).

2.11.4 Other Sum Rules

In order to provide a consistent and complete picture of the physics, this section introduces important sum rules, although the dissertation will not present results for them.

An interesting sum rule is the Gerasimov-Drell-Hearn (GDH) sum rule [56]. It is related to, but outside of the subject of deep-inelastic scattering. The relation involves the anomalous nucleon magnetic moment κ and is valid for real photons, *i.e.*, for photons with $Q^2 = 0$. The sum rule is therefore located at the other end of the Q^2 spectrum, opposite from the original Bjorken sum rule which was derived for $Q^2 \to \infty$. The experimental data from deep-inelastic scattering are bracketed in between. The GDH sum rule is written in our notation as [57]:

$$-\frac{2\pi^2\alpha}{M^2}\kappa_{p,n}^2 = \int_{\nu_{\text{thr}}}^{\infty} [\sigma_{3/2}^T(\nu) - \sigma_{1/2}^T(\nu)]_{p,n}\frac{d\nu}{\nu} \tag{115}$$

with $\nu_{\text{thr}} = Q^2/2M$. Experiments are planned at the Thomas Jefferson National Accelerator Facility (TJNAF) to study the validity of the GDH sum rule [57]. Of importance for the deep-inelastic scattering results is the following: The integral Γ_1 may be written as

$$\Gamma_1 = \int_0^1 g_1(x, Q^2)\,dx = \int_0^1 A_1(x, Q^2)F_1(x, Q^2)\,dx$$
$$= \int_0^1 \frac{\nu - \frac{Q^2}{2M}}{8\pi^2\alpha}\left(\sigma_{1/2}^T - \sigma_{3/2}^T\right)\,dx. \tag{116}$$

Changing the variable from x to ν leads to

$$\Gamma_1 = \frac{Q^2}{16\pi^2\alpha}\int_{\nu_{\text{thr}}}^{\infty}(1 - x)\left(\sigma_{1/2}^T - \sigma_{3/2}^T\right)\frac{d\nu}{\nu}. \tag{117}$$

For $Q^2 \to 0$ with ν constant, x approaches zero, and therefore

$$\Gamma_1 = \frac{Q^2}{16\pi^2\alpha}\int_{\nu_{\text{thr}}}^{\infty}\left(\sigma_{1/2}^T - \sigma_{3/2}^T\right)\frac{d\nu}{\nu}. \tag{118}$$

With the GDH sum rule, we therefore have

$$\lim_{Q^2 \to 0}\frac{\Gamma_1}{Q^2} = \frac{1}{16\pi^2\alpha}\int_{\nu_{\text{thr}}}^{\infty}\left(\sigma_{1/2}^T - \sigma_{3/2}^T\right)\frac{d\nu}{\nu} = -\frac{\kappa^2}{8M^2}. \tag{119}$$

In other words, the slope of Γ_1 is proportional to the square of the anomalous magnetic moment. Using the experimental values $\kappa_p = 1.79$ and $\kappa_n = -1.91$ [44] as well as the proton mass $M = 0.94 \, \mathrm{GeV}$, we obtain the following values for $\lim_{Q^2 \to 0} \Gamma_1 / Q^2$: $-0.45 \, \mathrm{GeV}^{-2}$ for protons, and $-0.52 \, \mathrm{GeV}^{-2}$ for neutrons.

Not only the longitudinal structure function g_1, but also the transverse structure function g_2 contains interesting physics. For example, the Burkhardt-Cottingham sum rule [58] predicts for $Q^2 \to \infty$:

$$\Gamma_2^{p,n} \equiv \int_0^1 g_2^{p,n} \, dx = 0. \tag{120}$$

The data of E143 allowed a first look at the validity of this rule, and the determination of the higher moments of this integral, $\int_0^1 x^n g_2 \, dx$ with $n = 2, 4, 6, \ldots$, which can be derived from Operator Product Expansion (OPE). Unfortunately, no definite model for the continuation of g_2 to $x = 0$ outside the measured region exists, and only limited conclusions could be drawn at this time [59].

2.12 Experimental Status before E143

After the successful deep-inelastic scattering experiments of the late 1960's, the results from the first deep-inelastic scattering experiment with a polarized beam and polarized target were published in 1976 (SLAC experiment E80 [24]). Succeeding in 1979/80 was experiment E130. Both experiments used polarized proton targets. E80 collected data for 9.7 and 12.9 GeV incident electrons with a spectrometer which was set to a laboratory scattering angle of $9°$. The incident electrons of E130 had an energy of 16.2 and 22.7 GeV, while the spectrometer was set to an angle of $10°$. The virtual photon-nucleon asymmetry A_1^p was found to be in agreement with theory, and further research was not expected to reach the limits of the models soon. Table 5 lists the main parameters of E80, E130 and other spin-structure experiments which will be mentioned in this chapter.

In 1988, CERN's European Muon Collaboration (EMC) published their results for the same proton asymmetry A_1^p [1]. Instead of electrons, they used muons from

pion decay: $\pi^+ \rightarrow \mu^+ \nu_\mu$. Only neutrinos with left-handed helicity (and antineutrinos with right-handed helicity) are allowed, and so the muon beam is naturally polarized. Muon energies up to 200 GeV allowed determination of the asymmetries to lower x than before, down to $x = 0.01$. Compared to experiments E80 and E130, these data opened a big new range of kinematics, though with limited statistics due to the low number of muons. The asymmetry turned out to be lower than expected. In addition, the integral of the structure function g_1^p over x from $x = 0$ to $x = 1$ was determined to be $\Gamma_1^p = 0.126 \pm 0.010$ (stat)± 0.015 (syst) at an average $Q^2 = 10.7$ GeV^2, surprising the physics community by being considerably less than the value predicted by the Ellis-Jaffe sum rule which at that time was calculated to be 0.189 ± 0.005. This result suggested that Δq, the contribution of the quarks to the helicity of the nucleon, was 0.12 ± 0.09 (stat)± 0.14 (syst) which was significantly smaller than expected by the theoretical models of that time.

In order to resolve this situation, new experiments were undertaken. At CERN, the Spin Muon Collaboration (SMC) embarked on a more comprehensive program in the study of the spin structure functions. In 1992, polarized deuterons in the form of deuterated butanol were used as target material [3] to measure g_1^d, and in 1993, normal butanol (*i.e.* with free protons instead of deuterons) was used to remeasure g_1^p [2]. By combining the proton and deuteron data, the neutron structure function g_1^n was extracted. Also the Bjorken sum rule was tested by calculating $\Gamma_1^p - \Gamma_1^n$. Since the average Q^2 was very high at CERN, the factor γ^2 in Eq. (51) was negligible and no good knowledge of A_2 (or equivalently $A_\perp$) was necessary. Still, because of the interesting physics connected to A_2 and g_2, the first data points of the transverse spin-asymmetry A_2 and of g_2 were measured [4]. In 1994, SMC again ran on deuteron, but this time with an ammonia target similar to the E143 target [5].

Also SLAC became active again. The advantages of SLAC are high event rates because of the intense electron beam of SLAC, as well as the possibility to pseudorandomly flip the polarization of the incoming electrons to cancel out many systematic errors. New spectrometers have also increased the acceptance and therefore the statistics [60].

SLAC experiment E142 ran in 1992 and measured the neutron asymmetry A_1^n and the structure function g_1^n directly for the first time [6]. It used a polarized ^{3}He gas target, in which the ^{3}He nuclei were polarized via optical pumping. The neutron structure function can be extracted very well from the single measurement with ^{3}He, although nuclear corrections are necessary. Since ^{3}He gas targets are very thin compared to solid state targets like butanol or ammonia targets, a high electron flux is needed to sustain high rates in the spectrometers.

Experiment E143, of which one aspect is covered in this work, used proton and deuteron targets to measure $A_\parallel$ and $A_\perp$ and construct from these quantities the virtual photon asymmetries A_1 and A_2 as well as the spin-structure functions g_1 and g_2. In E142 as well as in SMC experiments, the transverse asymmetry $A_\perp$ was only measured well enough to reduce the systematic error introduced by the lack of knowledge of $A_\perp$. The actual results were not used, and $A_\perp$ was always set to zero, while the error due to this approximation appeared in the systematic error. Also the published A_2^p results of SMC [4] were not used for the extraction of g_1. E143 went a big step further with measuring $A_\perp$ and therefore A_2 and g_2 (both proton and deuteron) with high statistics [59]. By combining the E143 proton and E143 deuteron spin-structure functions, the neutron spin-structure functions g_1^n and g_2^n became available. In addition, three energies were used which increased the data over a wide x and Q^2 range and allowed a first meaningful study of the Q^2-dependence of the spin-structure function g_1 [61].

By switching between the proton and deuteron targets, systematic errors were minimized in E143 when combining proton and deuteron results to obtain the neutron structure function or the experimental value of the Bjorken sum rule. Also, the same experimental set-up was used to measure $A_\perp$, similarly cancelling out systematic errors. As with experiment E142, the beam polarization was switched pseudo-randomly, and the rate was very high, amassing much better statistics in three months than SMC in one year.

The recent experiments at SLAC, however, also have certain disadvantages. The beam energy is lower: 29 GeV electrons compared to CERN's $100-200$ GeV muons. Because of this, the E143 momentum transfer Q^2 is relatively small, and no really

low value of the Bjorken x can be obtained. Only values of $x = 0.03$ at $E = 29$ GeV ($x = 0.02$ at $E = 16$ GeV) upward are accessible to experiment E143, while SMC reaches values as low as $x = 0.003$. Q^2 ranges from around 1 GeV^2 up to around 11 GeV^2 for E143 at 29 GeV, compared to up to 60 GeV^2 at CERN. The second disadvantage lies in the greater radiative corrections because E143 used electrons instead of muons. These corrections had to be calculated more precisely than for CERN experiments.

Table 5 Parameters of previous experiments. The numbers are taken from references mentioned in the text and [62]. The table does not list unpublished measurements of $A_\perp$ which were only used to minimize the systematic error on g_1. Numbers in $<\ >$ brackets are average values.

	year	target material	reaction		E (GeV)	θ (°)	x	$<Q^2>$ (GeV²)
E80	1975/76	butanol	$e^- p \rightarrow e^- X$	$A_\parallel$	12.9	9	1/3	2.7
				$A_\parallel$	9.7	9	1/3	1.7
				$A_\parallel$	9.7	9	1/5	1.4
E130	1979/80	butanol	$e^- p \rightarrow e^- X$	$A_\parallel$	9.7, 22.9	10	0.18 – 0.7	3.5 – 10.0
EMC	1984/85	ammonia	$\mu^- p \rightarrow \mu^- X$	$A_\parallel$	100, 120, 200	≤ 8	0.01 – 0.7	3.5 – 29.5
SMC	1992	butanol	$\mu^- d \rightarrow \mu^- X$	$A_\parallel$	$<100>$	≤ 8	0.006 – 0.6	1.2 – 15.5
E142	1992	helium	$e^- {}^3\mathrm{He} \rightarrow e^- X$	$A_\parallel$	19.4, 22.7, 25.5	4.5, 7	0.03 – 0.6	1.1 – 5.2
SMC	1993	butanol	$\mu^- p \rightarrow \mu^- X$	$A_\perp$	$<100>$	≤ 8	0.006 – 0.6	1.4 – 11.8
				$A_\parallel$	$<190>$	≤ 8	0.003 – 0.7	1.3 – 58.0
E143	1993/94	ammonia	$e^- p \rightarrow e^- X$	$A_\parallel, A_\perp$	29.1	4.5, 7	0.030 – 0.75	1.3 – 9.2
				$A_\parallel$	16.2	4.5, 7	0.020 – 0.50	0.5 – 3.0
				$A_\parallel$	9.7	4.5, 7	0.033 – 0.24	0.3 – 1.0
SMC	1994	ammonia	$\mu^- d \rightarrow \mu^- X$	$A_\parallel$	$<190>$	≤ 8	0.003 – 0.70	1.3 – 48.7

41

CHAPTER 3

TECHNICAL DISCUSSION
OF EXPERIMENT E143

3.1 Beam

The electron beam was provided by SLAC through its two-mile long accelerator. A polarized-electron source created the pulse at the beginning of the accelerator. After acceleration for two miles, the beam was deflected into the End Station A (ESA) with the target and spectrometers, and was finally stopped in the beam dump. Fig. 6 gives a schematic overview. The SLAC Main Control Center (MCC) tuned, steered and continuously monitored the beam. The following sections will discuss the polarized electron source, the linear accelerator (linac) and End Station A as far as it is related to the beam. Also the so-called Beam Switch Yard (BSY) and A-Line, which connect the linac and ESA, will be covered.

3.1.1 Electron Source

The polarized electron source is important for the experiments in End Station A as well as for the large SLAC experiment SLD (SLAC Large Detector), which studies the physics at the Z-resonance by colliding polarized electrons with positrons. The source is based on photoemission from IV-V semiconductors such as GaAs and AlGaAs. End Station A experiment E142 used an AlGaAs source with polarizations
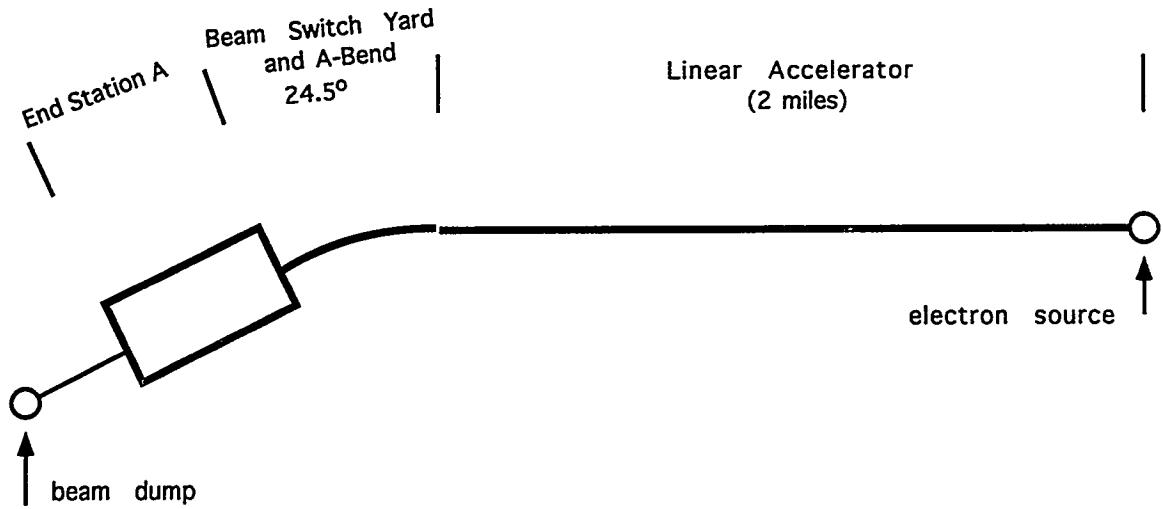
Figure 6 Schematic view of the SLAC accelerator. Not to scale.

of about 40% and a current of up to 2×10^{11} e^-/pulse [6]. For this type of conventional cathode, the polarization has a theoretical limit of 50%. For E143, strained GaAs was used, where the polarizations can be up to 100% [63] [64]. The E143 source achieved a polarization of more than 80%. The current was chosen to be only 1 to 4×10^9 e^-/pulse to limit the radiation damage to the E143 target.

The physics of polarized electron emission from strained GaAs cathodes can be described in the following way [63]. In GaAs, the lowest state of the usually empty conduction band is about 1.5 eV above the highest state of the usually filled valence band. The lowest conduction band level is $S_{1/2}$ with $m_j = -\frac{1}{2}$ and $m_j = +\frac{1}{2}$. Due to spin-orbit coupling, the highest valence band has two energy levels (see left side of Fig. 7): $P_{3/2}$ (with $m_j = \pm\frac{1}{2}$, $\pm\frac{3}{2}$) and at slightly lower energy $P_{1/2}$ (with $m_j = \pm\frac{1}{2}$). Let us denote the energy gap between the $P_{3/2}$ and $S_{1/2}$ as E_g (= 1.424 eV at 300 K), and the gap between the $P_{3/2}$ and $P_{1/2}$ levels as Δ (= 0.340 eV at 300 K) [64]. In a strained GaAs layer, the crystal loses its cubic symmetry due to the strain, and the $P_{3/2}$ level splits into two levels, one for $m_j = \pm\frac{1}{2}$, one for $m_j = \pm\frac{3}{2}$ (see right side of Fig. 7). This energy split shall be called δ. Circularly polarized light has angular momentum 1, and can excite electrons from the valence band into the conduction band. If the energy of the incoming photon is above E_g,

43

but below $E_g + \delta$, only the transition between the $P_{3/2}$ ($m_j = +\frac{3}{2}$) state into the $S_{1/2}$ ($m_j = +\frac{1}{2}$) state is possible, and the electrons in the conduction band are fully polarized. If the energy is above $E_g + \delta$, but still below $E_g + \Delta$ (or if normal GaAs is used), the transition from the $P_{3/2}$ ($m_j = +\frac{1}{2}$) state to the $S_{1/2}$ ($m_j = -\frac{1}{2}$) state is also possible. This transition has a three times smaller probability than the transition $P_{3/2}$ ($m_j = +\frac{3}{2}$) to $S_{1/2}$ ($m_j = +\frac{1}{2}$). The highest possible polarization is in this case $(3-1)/(3+1) = 0.5$.
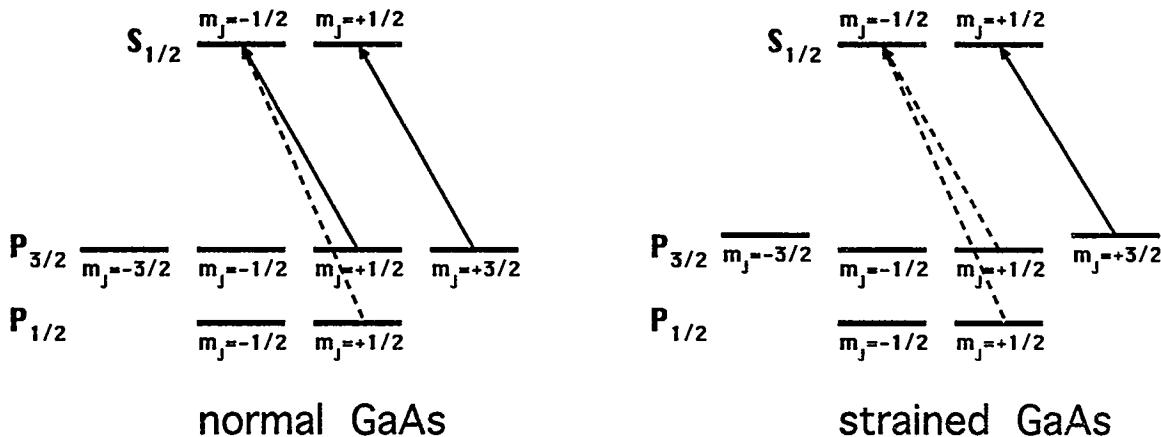
Figure 7 Schematic diagram of energy levels in normal and strained GaAs. Solid lines indicate allowed transitions, dashed lines indicate forbidden transitions. See text for details.

Once excited to the conduction band, the electrons still have to leave the material into the vacuum. This is possible for two reasons: (1) The work function is the potential difference between the vacuum and the Fermi level of the material. For pure GaAs, it is about 4 eV. By depositing cesium and an oxidizer (O_2 or NF_3) onto the GaAs surface, this can be lowered. (2) A further reduction is caused by p-doping the material. The vacuum level remains higher than the potential directly at the outer surface, but becomes lower than the potential of the conduction level further inside the material (see Fig. 8 for illustration). Electrons from up to 50,000 Å deep inside the crystal can now diffuse to the surface, cross the thin surface layer and escape into the vacuum [64]. A surface like this is said to have a negative electron affinity.

If the quantum efficiency (QE), i.e., the number of emitted electrons per incident photons, decreases, the electron affinity becomes less negative. Electrons with lower
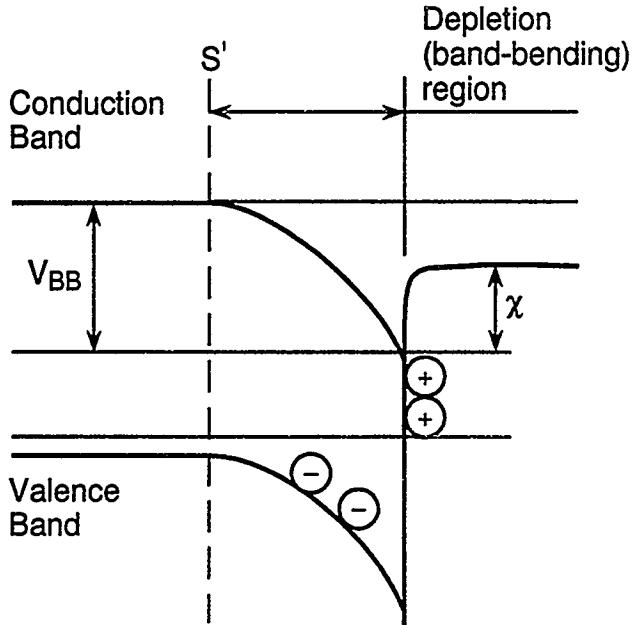
Figure 8 Energy levels of conduction and valence band at the surface. The depletion region at the right side is the vacuum region. To the left side is the interior of the crystal, and in between is the surface region with the band bending due to p-doping.

energy will be less able to cross the surface layer and to escape into the vacuum. These electrons of lower energy tend to be from deeper regions of the crystal. On the way to the surface, they are more likely to be in interactions with the lattice, losing energy and polarization. On the other hand, electrons from regions close to the surface still can be emitted, and since they have fewer lattice interactions, their polarization deteriorated less when they escape into the vacuum. A lower quantum efficiency therefore leads to higher average polarization [64].

The strained GaAs photo-cathode of E143 (diameter 22.5 mm) was produced by growing a 100 nm layer of $GaAs_{0.72}P_{0.28}$ on a lattice of GaAs. In this upper layer, 28% of the arsenide atoms were substituted by phosphorus atoms. Since the lattice constant of the $GaAs_{1-x}P_x$ layer is smaller than the lattice constant of the normal GaAs, the $GaAs_{0.72}P_{0.28}$ lattice was strained which in turn lifted the degeneracy of the $P_{3/2}$ level. In addition, the GaAs was p-doped with Zn atoms $(4 \times 10^{18}$ atoms/$cm^3)$.

The photo-cathode was placed into ultra-high vacuum and covered with an initial layer of cesium and oxidizer. For normal operation, high voltage of 60 kV was

applied, and light from a Ti:sapphire laser was shining on the cathode's surface (see Figs. 9 and 10). The light pulse was about 2.2 μs long with an energy of 80 μJ at the cathode, and had a wavelength of 845 nm which is the optimal wavelength for this type of cathode. The polarization of the laser light was changed via a Pockels cell in a pseudo-random way from linear polarization to either left or right circular polarization. The Pockels cell was a quarter-wave plate which changes its optical characteristics depending on the applied voltage. Using another Pockels cell, the shape and intensity of the laser pulse was regulated. For example, the same electron beam intensity was desired for both spills with left- as with right-handed electrons, and the Pockels cell was used to minimize any remaining charge asymmetry by adjusting the laser light intensity.
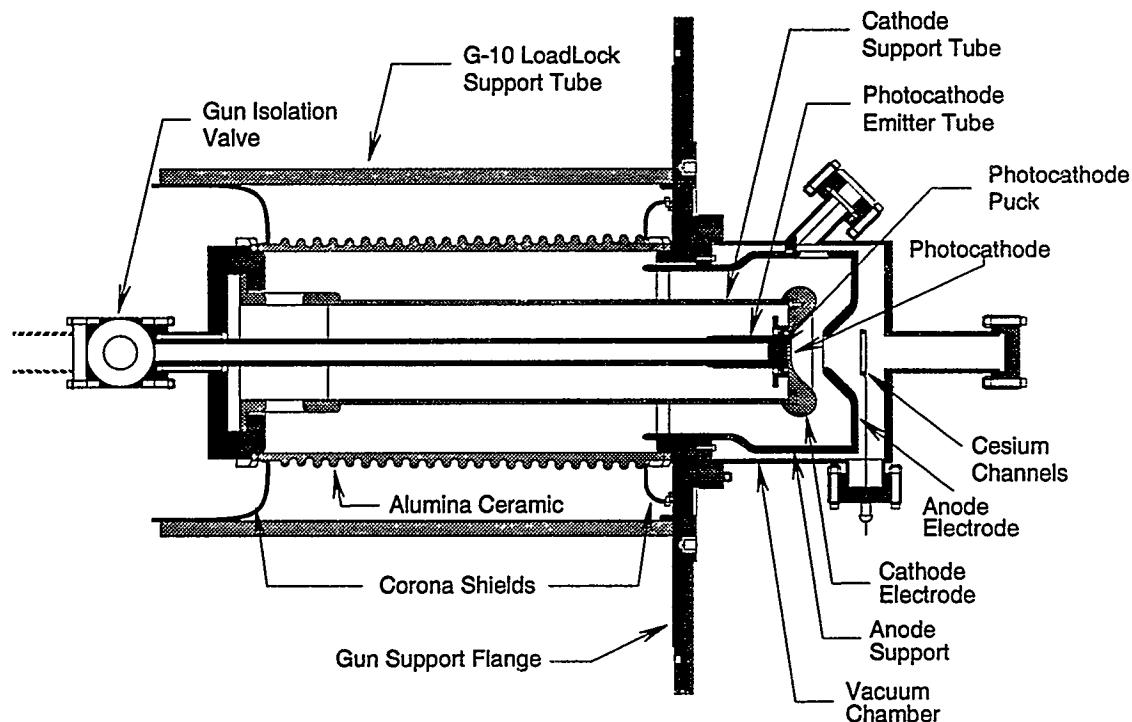
Figure 9   Schematic drawing of the electron gun. The laser light shines in from the right side onto the photocathode. The electrons leave on the same path to the right.

The quantum efficiency was measured with a second laser, a low-power diode laser which emitted a continuous light beam with a wavelength of 833 nm. This laser was used because its power and its number of photons emitted per time was very

46
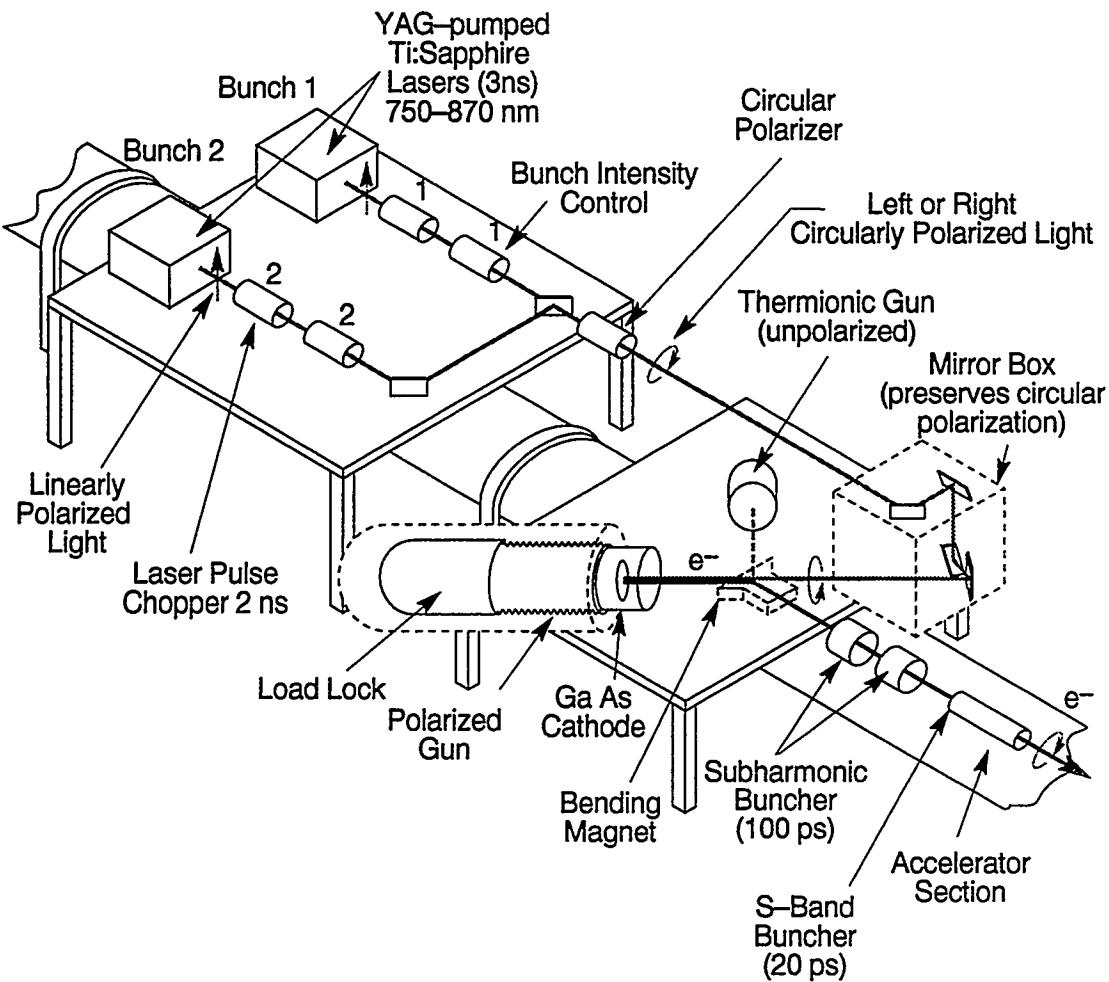
Figure 10 Schematic drawing of the polarized electron source. The figure shows the set-up and times for SLC operation, but the E143 set-up was very similar.

stable compared to the pulsed Ti:sapphire laser. Together with a measurement of the number of electrons emitted from the cathode surface, the quantum efficiency could be obtained. The diode laser light had a slightly higher energy than the light of the pulsed laser, and their quantum efficiencies were different. However, the quantum efficiency was not measured to obtain an accurate absolute measurements, but to monitor the relative change of the quantum efficiency.

During operation, the ratio of cesium to oxidizer slowly dropped, possibly because residual gas removed some of the cesium. This caused the quantum efficiency to drop. Therefore, cesium was routinely deposited onto the surface of the photocathode, and the original quantum efficiency was recovered.

3.1.2 The Linear Accelerator

After its creation at the electron source, the beam was accelerated for two miles in the linear accelerator (linac) [65]. The highest energy for SLAC is 50 GeV, but during E143, the magnets in the A-Line were only able to bring electrons with energies of up to 29 GeV into End Station A.[7]

In order to spread the events over time for easier analysis, E143 chose a very long beam pulse of 2.0 to 2.5 μs. A longer pulse was not available from the klystrons. The frequency of the accelerator was 2.856 GHz, which is also called the S-Band and corresponds to a wavelength of about 10.5 cm. About 6,000 to 7,000 of these waves constituted one of the 2.0 to 2.5 μs pulses, with each wave carrying one small package of electrons. The few pico-seconds long packages were spaced 0.35 ns apart. With better resolution, the detectors would have been able to resolve this sub-structure of the beam.

To reach higher energies like the nearly 50 GeV necessary for the SLD experiment, the accelerator had to run in a different mode, the SLED (Stanford Linear Energy Doubler) mode, in which only short pulses of a few hundred nano-seconds were possible. Much of the monitoring and diagnostic equipment inside the linac was designed for the high-intensity 50 GeV beam. Therefore, every second one pulse (one out of 120) was such a short, strong pulse which was sent to a beam dump at the end of the linac. With 119 pulses per second and a pulse width of 2.0 to 2.5 μs, the SLAC accelerator operated during E143 at the very low duty factor of less than 0.3×10^{-3}.

3.1.3 Beam Switch Yard and A-Line

The Beam Switch Yard and A-Line connected the linac and ESA. They contained bending magnets, quadrupole magnets as well as diagnostic equipment. In total, the beam was deflected by 24.5°. First a 0.5° bend by a "kicker" magnet in

---

[7] Because of the A-line power supplies, E142 was limited to a beam energy of 25.5 GeV. The power supplies were upgraded for E143.

the beam switch yard moved the beam into the direction of the A-Line, then each of the eight bending magnets of the A-Line changed the beam direction by 3°. The eight bending magnets were all wired in series with a ninth magnet which was located in the MCC building. All nine magnets were built to the same specifications. Since the same current ran through them, the measurement of the field in the ninth magnet was also valid for all other eight magnets. Inside the ninth magnet, a coil (called "flip coil") rotated and measured the magnetic flux. In this way, the flip coil provided us with the measurement of the energy of the beam at the end station. Also, nuclear magnetic resonance (NMR) probes were attached to the inside wall of the magnet. Since the NMR probes measured the magnetic field only at one single point, and since this point was located at the inside wall (at a point where the beam would never be), the probes were only good for checking the stability of the field independently from the flip coil. In comparison, the flip coil did not pick up the magnetic flux at one point, but along the whole center of the magnet where the beam moved through.

When the polarized electrons moved through the magnetic fields, the polarization vector rotated faster than the momentum vector according to the formula

$$\theta_{\text{prec}} = \gamma \frac{g-2}{2} \theta_{\text{bend}} \tag{121}$$

with $\theta_{\text{bend}} = 24.5°$ being the angle of the beam switch yard and A-line and θ_{prec} being the angle between the spin vector and the momentum vector. $\gamma = (1 - \beta^2)^{-\frac{1}{2}} = E/m$ with $\beta = v/c$, and $\frac{g-2}{2}$ is the anomalous magnetic moment of the electron of about 0.00116 [44]. Since we needed longitudinal polarized electrons in the end station, the spin vector had to precess by a multiple of 180°, i.e., θ_{prec} had to be $n\pi$. Therefore the electron energy in the end station could not be varied continuously, but came in discrete steps of 3.24 GeV for every rotation by π. The precession of the polarized electrons was exploited for a check of the flip coil calibration constant (see Chapter 4).

Why did we not use transverse polarized electrons in the end station? In the linac only longitudinal electrons could be accelerated without destroying the the polarization. However, the magnets in the A-line could have been set to a strength which would have turn the beam by $n \times 180° + 90°$ and which would have lead to

a transverse polarized beam. However, Ref. [8] indicates that only very limited information could have been extracted from measurements with such a beam. In the derivation of the cross-section differences of Eqs. (23) and (24), which assume longitudinally polarized leptons, any factor proportional to m/E (mass and energy of incoming lepton) cancels. They do not cancel, on the other hand, for transverse polarized leptons, which leads to strongly suppressed cross-section differences for high lepton energies.

3.1.4 End Station A

Right before the beam entered the end station, it was deflected spill by spill by a special Helmholtz magnet ("**raster magnet**") according to a preset pattern. This ensured that the beam hit the target at a different point for subsequent spills, repeating the pattern after 253 spills. In this way, the heat from the beam was distributed over a larger volume, and the target depolarization was minimized. Next were the components of the **Møller system** which provided the measurements of the beam polarization. The Møller target was located right at the entry of the beam into ESA in a small room extending upstream along the beam line, called "alcove". Several meters beyond the Møller target, the beam passed through a magnet, called B0. The beam was shielded from the magnetic field through a steel plate, while the electrons scattered from the Møller target were deflected by the magnetic field. More on the Møller target will be presented in a later section. The beam then crossed the **polarized ammonia target**, and arrived after 11 m at the so-called "**foil array**" which allowed us to monitor the beam online by checking the position and width of the beam. The foil array was a set of about 10 mm wide, 1 mil thick brass foils strapped in 1 mm distance horizontally and vertically next to each other. Both the horizontal and the vertical plane contained 48 of these foils. An electric voltage was applied between the foils and a collector plate. Electrons crossing the foils created an electromagnetic shower. Low-energy electrons from this shower left the foils (secondary emission electrons) and were collected at the collector plate, while the induced electric current in the foils was detected by the electronics. From this information, a computer program calculated the position of

the beam, as well as the width. Behind the foil array, no major equipment was located along the beam line, and the beam continued straight down to the **beam dump**.

The exact current was measured pulse-by-pulse by two independent **toroid charge monitors** located 9.1 m and 5.6 m in front of the polarized target [66]. For historical reasons, they were called Toroid 2 and Toroid 3. In both monitors, the beam spill passed an iron toroid in which the beam electrons induced a magnetic field. A coil around the toroid picked up the magnetic field creating a detectable signal. An ADC module measured the strength of the signal, which — via a calibration constant — was converted into units of Giga-electrons per pulse.

When measuring $A_\parallel$, the magnetic field of the polarized target was parallel to the velocity of the beam electrons and hence had no influence on the beam. However, when measuring $A_\perp$, the magnetic field of the target was perpendicular to the beam velocity, and three small magnets ("**chicane magnets**") had to compensate the deflection of the beam by the target magnet. Let us assume that the target field bent the beam upward. In this case, the two chicane magnets in front of the target shifted the beam down, but kept it parallel to the original direction. The target magnet then bent the beam upward, and the third chicane magnet behind the target bent the beam back to the original direction, so that the beam was able to reach the beam dump. If the target field was reversed, also the field in the chicane magnets was reversed. The chicane magnets were turned off for any longitudinal running.

Finally, two major monitors must be discussed: The so-called "**good spill**" and "**bad spill**" monitors. The bad spill monitor was located at the Møller target, close to the entry point of the beam into the end station. The good spill monitor sat close to the polarized ammonia target. Each of those monitors consisted of a scintillator with photo tube and detected the particles scattered from the beam. ADCs integrated the signals and sent their values to the data acquisition system. The signal was also displayed on an oscilloscope. The picture on the oscilloscope was picked up by a video camera and transmitted to TV monitors at MCC and the ESA counting house. The oscilloscope showed the time-dependence of the good- and bad-spill signals from the beginning to the end of the 2.0 to 2.5 μs pulse. If the

51

beam, for example, was stronger at the beginning than at the end of the spill, the signal on the monitors was larger at the front than at the back. The names "bad spill" and "good spill" monitors originated from the following: At the location of the bad spill monitor, the beam should go directly through the beam pipe. A sizeable signal in the bad spill monitor indicated that the beam might not have been centered well but hit parts of the beam line. At the location of the good spill monitor, the beam was hitting the target. A sizable signal was therefore always expected during normal operation. If the beam was misaligned and hit other parts, the signal was bigger than during normal operation.

3.2 Møller Polarimeter

Exact measurements of the beam polarization are essential to precision experiments like E143. The polarization of the beam was determined almost daily by a Møller polarimeter with single and the double-arm detectors, measuring the asymmetry in the so-called "Møller" reaction $e^-e^- \rightarrow e^-e^-$. During that time, no data could be collected with the polarized ammonia target since the Møller target destroyed the focus of the beam. A few measurements were done with the Møller polarimeter at the end of the linac. They were consistent with the other measurements but of limited statistics [67], and we will not give more information about these measurements.

Fig. 11 provides an overview over the Møller system in End Station A. For the Møller measurement, the beam was centered and focussed on a magnetized foil which was moved into the beam line via remote control. The ferromagnetic (49% Fe, 49% Co, 2% Va by weight) foils of different thickness (20 to 154 μm) were located in the alcove of End Station A [68] [69]. Helmholtz coils created a homogeneous 0.01 T magnetic field polarizing about two of the 3d electrons (M-shell), which resulted in an 8% overall electron polarization [70]. The foil polarization was measured with a relative error of 0.017 [69]. This error was the main contribution to the overall systematic error on the beam polarization measurement.
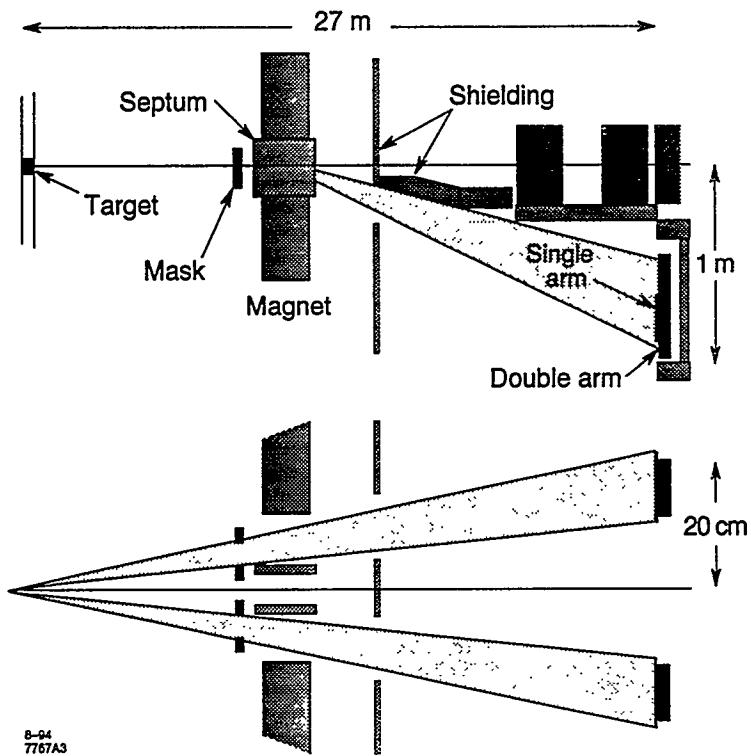
Figure 11 Schematic view of the Møller polarimeter. The double-arm and the single-arm detectors are shown to the right, and the Møller target (magnetized foils) to the left. The ammonia target was farther downstream, and would appear to the right side of this picture. Upper part is top view, lower part is side view.

The beam and target electrons scattered elastically from each other. The polarization introduced an asymmetry in the scattering, which was largest when the center of mass scattering angle was $\hat{\theta} = 90°$. There was no dependence on the azimuthal angle for longitudinally polarized beam and target electrons. The center of mass angle $\hat{\theta}$ and the laboratory momentum p' of the scattered electron were related via

$$p' = \frac{p_b}{2}(1 + \cos\hat{\theta}) \tag{122}$$

with p_b as the momentum of the incoming electron. A mask several meters behind the target allowed only electrons of a certain azimuthal angle to pass. A strong dipole magnet (named B0) with vertical B-field then bent the electrons horizontally depending on their momentum p' or equivalently their c.m. scattering angle.

53

At the detectors, the electrons were then spread out on a parabolic curve. Since the magnet had to be around the beam pipe, a metal shielding ("septum") prevented the magnetic field from influencing the beam electrons. The septum was a long flat piece of metal, 3.2 inches thick, with a hole for the beam. This shape did not influence the magnetic field very much.

To reduce rescattering, the electrons then crossed helium-filled plastic bags, and were detected in the Møller detectors about 15 m behind the magnet. Because of the bending by the magnet B0, it was possible to mount the detectors conveniently at the side of the beam line.

One of the Møller detectors was the single-arm detector, built and maintained by the University of Wisconsin. Two sets of silicon pads sampled electrons from the scattering cone at a center-of-mass angle of about 91° [68] (Fig. 12). One set of silicon pads was in the lower part of the parabola, the other in the upper part. The best asymmetry measurements are done at a center-of-mass angle of about 90°. The silicon pads were, however, not placed at ±90°for the following reason: Each Møller scattering event created two electrons, one at $90° + \theta$, the other at $90° - \theta$. If the upper silicon pad would have covered the $90° + \theta$ region and the lower silicon pad the $90° - \theta$ region, the events would have been counted twice. Instead, the pads were both placed in the > 90°area to avoid the double-counting of scattering events.

Three-radiation-lengths of lead in front of the silicon detectors amplified the Møller electrons while reducing the background from (soft) photons with energies of less than about 1 MeV. Each set of silicon pads contained 12 × 4 channels. About two of the twelve rows detected most of the Møller electrons. The other rows were necessary to determine the background. The silicon detectors did not register each event separately, but only the total charge incident in each channel per spill. During the analysis, a smooth fit to the background was subtracted from the signal. Knowing the sign of the beam polarization for each spill, the asymmetry and therefore also the magnitude of the beam polarization could be obtained.

The second Møller detector was the double-arm detector built by the University of Basel (see Fig. 11 and Fig. 12). It was newly built for E143. Double-arm

detectors were previously used in experiments, but only recently fast enough electronics became available to allow its use at the high intensities of E143. Since the E142 helium target was much thinner than the E143 ammonia target, E142 needed much higher beam current than E143, and the double-arm detector could not have been used during E142. The detector consisted of 14 lead glass blocks located in two arms along the parabolas behind the single-arm detector and collected events with center-of-mass angles of 70° to 110°. The lead which was mentioned above for the single-arm detector was chosen to be large enough to cover all of the double-arm lead glass blocks. The silicon pads of the single-arm detector were only located in front of some double-arm lead glass blocks, but they were negligibly thin. Fig. 12 shows on the top the single and on the bottom the double-arm detectors. In reality, the single-arm detector was located in front of the double-arm detector. A typical distribution of events is indicated in the picture.

It was recently discovered by Levchuk [71] that the intrinsic motion of the atomic electrons can have a considerable influence on the results of Møller measurements. Electrons in the outer shells have a small momentum, but electrons inside have a momentum of about 100 keV. Since the mass of the electron is of similar magnitude, the scattering angle could be off by up to 10%, depending on the shell from which the electrons were scattered. Events originating from these high-momenta inner shells (K- and L-shell for the E143 target material) created broader signals at the detectors than events originating from higher shells (M- and N-shells for E143). Since the inner-shell electrons are less polarized than the outer-shell electrons, care is required in the extraction of the asymmetry: If using only the events close to the center of the parabolic curve and disregarding the events outside as background, an unproportionally high number of outer-shell events would determine the asymmetry, and the asymmetry would be over-estimated. Using only the electrons in the wings (farther from the center) would lead to an underestimation. Before the Levchuk-effect was discovered, it was assumed that the asymmetry of Møller electrons would be the same everywhere, independent of the exact scattering angle. The effect either has to be corrected for, or a detector with a large acceptance or low resolution has to be used.
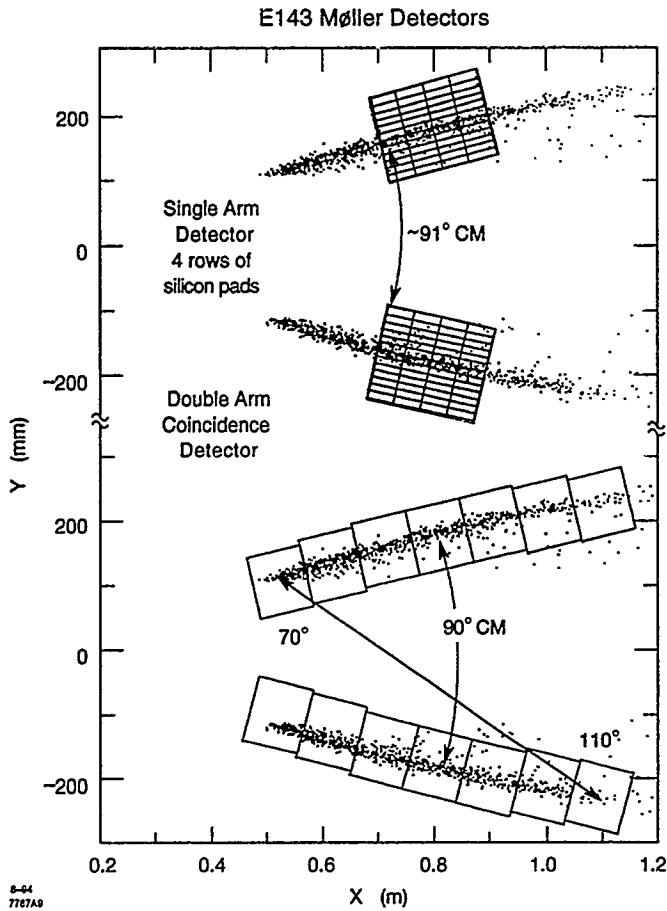
Figure 12 Illustration of Møller electrons scattered onto the single- and double-arm detectors. The horizontal axis is the horizontal distance of the detector elements with respect to the beam line in meters, the vertical axis shows the vertical distance with respect to the beam line in millimeters. Note that the single-arm detector was actually right in front of the double-arm detector.

The analysis of the single-arm detector measurements took the Levchuk-effect into account, lowering the result for the beam asymmetry by about 3%. The acceptance of the detector was large enough to detect all electrons, even when they were smeared out by the intrinsic atomic motion. but the resolution was high enough that the Møller electrons also went to channels which were used to estimate the background (for example, background from radiative tails).

For the double-arm detector, the influence of the intrinsic momentum of the atomic electrons was below 1%, because its acceptance was large enough to detect practically all Møller electrons (even when smeared out). Only small dead-time and acceptance corrections were necessary for the double-arm detector [72].

56

3.3 Polarized Target

Progress in the development of polarized targets during the recent years has made the current precision experiment possible. Compared to the spin-structure experiments at CERN, where the muon beam has a very low intensity, E143 needed highly radiation-resistant targets so that the polarization could survive in the high-intensity electron beam. Recently, ammonia became the target material of choice because of its high radiation resistance and its large number of free nucleons (protons or deuterons) per molecule. Before that, butanol or other substances with free protons or deuterons served as target material.

The E143 target material consisted of frozen ammonia beads ($^{15}NH_3$ and $^{15}ND_3$) of a few millimeter diameter. Before the experiment, the beads were irradiated to create paramagnetic impurities which are essential for reaching useful levels of polarizations. During the experiment, the ammonia was polarized in a magnetic field via microwaves (Dynamic Nuclear Polarization), and the magnitude of the polarization was measured by an NMR system.

This section first introduces the principles of polarization and Dynamic Nuclear Polarization (DNP), then describes the pre-irradiation, the set-up of the target, and the nuclear magnetic resonance system to measure the polarization.

3.3.1 Polarizing Method and Thermal Equilibrium

In a magnetic field, the spin of a particle contributes

$$\epsilon = -\mu \cdot \mathbf{B} \tag{123}$$

to the energy, where μ is the magnetic moment vector, and $\mathbf{B}$ the magnetic field vector. The magnetic moment itself depends on the spin $\mathbf{S}$ of the particle. If the particle is an electron,

$$\mu = g\mu_e \mathbf{S}, \tag{124}$$

if it is a nucleon or nucleus,

$$\mu = g\mu_N S. \tag{125}$$

Here g is the g-factor of the particle, μ_e the Bohr magneton and μ_N the nuclear magneton. The Bohr (nuclear) magneton is defined as the magnetic moment which an electron (proton) would be expected to have according to the calculations of classical physics, $\mu_e = e/2m_e$ or $\mu_N = e/2m_p$ ($\hbar = c = 1$, m_e = mass of electron, m_p = mass of proton).

The magnetic moment of a spin-$\frac{1}{2}$ particle is $\mu = -\frac{1}{2}g\mu_{e,N}$. For electrons $g \approx 2$, for protons $g = 5.586$, and for neutrons $g = -3.826$. For nucleons, the magnetic moments are better known as $\mu_p = 2.793\mu_N$ (proton), and $\mu_n = -1.913\mu_N$ (neutron). Deuterons are spin-1 particles. Their magnetic moment is given by $\mu = g_D\mu_N \equiv \mu_D$ with $g_D = 0.857$.

Let us now consider nucleons or nuclei inside a magnetic field B. The number of particles in the state with extra energy ϵ [Eq. (123)] are described by

$$N \sim e^{-\epsilon/kT}, \tag{126}$$

k being the Boltzmann constant and T the temperature. The polarization for spin-$\frac{1}{2}$ particles (in our case protons) is defined by

$$P_{1/2} = \frac{N_{+\frac{1}{2}} - N_{-\frac{1}{2}}}{N_{+\frac{1}{2}} + N_{-\frac{1}{2}}}. \tag{127}$$

Inserting Eq. (126) gives

$$P_{1/2} = \tanh \frac{\mu_p B}{kT}. \tag{128}$$

At 1 K and 5 T, this corresponds to a polarization of only 0.5%.

Since deuterons are spin-1 particles, their polarization is defined by

$$P_1 = \frac{N_{+1} - N_{-1}}{N_{+1} + N_0 + N_{-1}}. \tag{129}$$

and Eq. (128) becomes more complicated, changing to

$$P_1 = \frac{4\tanh \frac{\mu_D B}{2kT}}{3 + \tanh^2 \frac{\mu_D B}{2kT}}. \tag{130}$$

At 1 K and 5 T, this corresponds to a polarization of only 0.1%.

These low polarizations are, of course, not useful for particle physics experiments, but via Dynamical Nuclear Polarization (DNP), the polarization can be increased enormously. The principle is as follows, illustrated for protons [73]:

The target material has to be doped with paramagnetic impurities. The impurities can be either chemicals included into the material, or — as for E143 — radicals created by irradiation. Two effects are then creating the high polarization of the nucleons [74].

First, the electron and proton spins couple, with the energy levels split in the magnetic field according to the Zeeman and hyperfine structure. Fig. 13 indicates these levels. The a-c and b-d splitting is due to the electron spin, typically of around 140 GHz at a magnetic field of 5 T. The a-b and c-d splitting is due to the proton spin, around 210 MHz. The transitions $a \leftrightarrow c$, $b \leftrightarrow d$, $b \leftrightarrow a$, and $d \leftrightarrow c$ are allowed, while the transitions $a \leftrightarrow d$ and $b \leftrightarrow c$, in which both the electron and the nucleon spins are flipped, are suppressed.
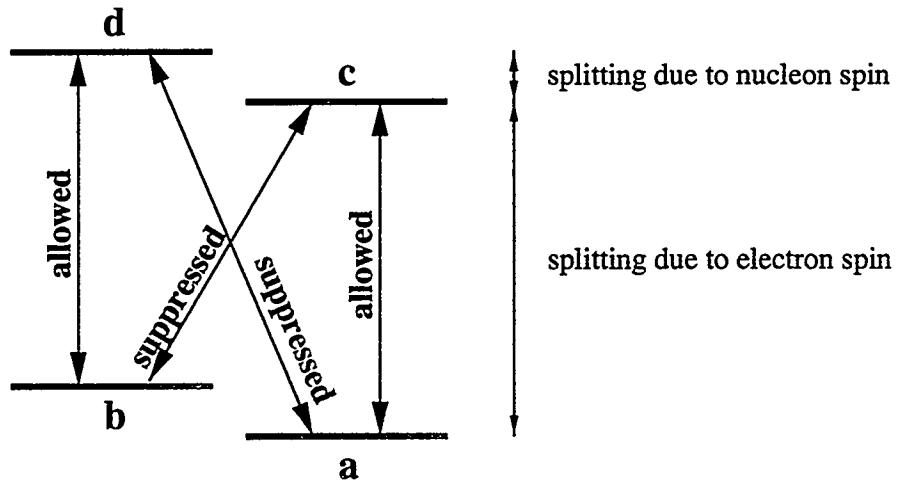
Figure 13 Illustration of the splitting of the electron and proton energy levels in a magnetic field. Drawing not to scale. The large split (between a and c and between b and d is due to the electron magnetic moment. The small split (between a and b and between c and d is due to the nucleon magnetic moment. The small arrows next to the letters indicate the approximate spin direction of the electron (left arrow) and of the nucleon (right arrow).

59

Microwaves of the right frequency drive one of the suppressed transitions. The electron spin can then relax via $c \rightarrow a$ or $d \rightarrow b$ transitions towards the natural equilibrium, while the nucleon spin can relax via $b \leftrightarrow a$ or $d \leftrightarrow c$ transitions. Since the electron spin relaxes much faster (within ~ 1 ms) than the nucleon spin (within few tens of minutes to a few hours) [74], the nucleons stay polarized longer while the electrons can be used again to drive other transitions with nearby nucleons. Depending on which of the two microwave frequencies (for $a \rightarrow d$ or $b \rightarrow c$) is chosen, the polarization of the nucleons will be parallel or antiparallel to the magnetic field direction ("positive or negative enhancement"). Fig. 14 shows how the states are populated for either one of the two possible microwave frequencies.
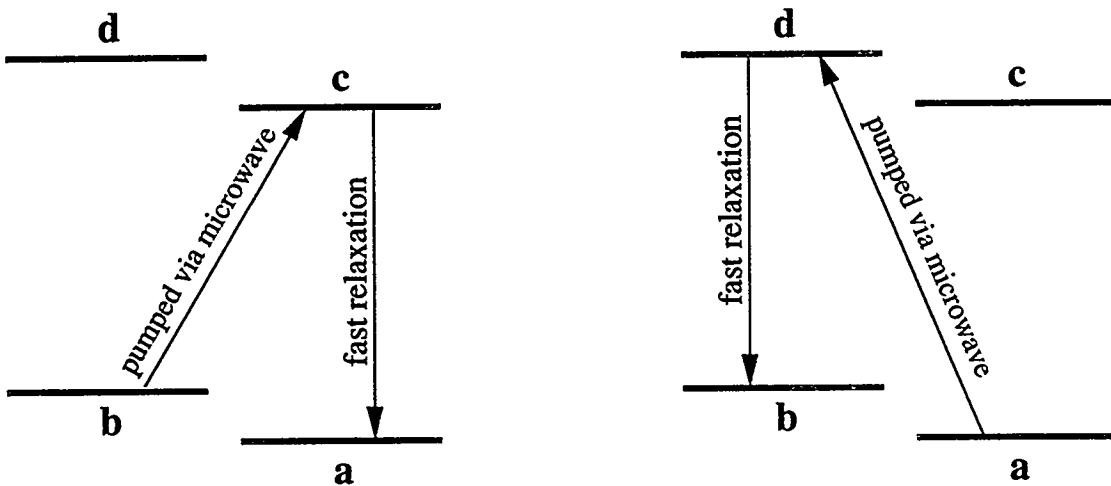
Figure 14 Illustration of the optical pumping in the target. Depending on the microwave frequency, different states are populated. To the left, the situation with the lower of the two microwave frequencies is illustrated, to the right the situation with the higher of the two microwave frequencies. See for example Fig. 13 for more information.

Second, due to dipole-dipole coupling of neighboring nucleons, the polarization of the nucleons is distributed around the material (spin diffusion). Once polarized by the microwaves, the proton or deuteron can couple with a second proton or deuteron, flipping their spins simultaneously. This second proton or deuteron can then flip its spin together with an even farther nucleus, while the original proton or deuteron can again be excited by the microwaves. In this way, the polarization can spread throughout the whole material even if the paramagnetic impurities have only a small concentration in the sample.

The equations for thermal equilibrium (TE) polarization [Eqs. (128) and (130)] can be used to assign a "spin temperature" to the material for a given polarization. The spin temperature is the temperature which would be necessary to reach the same polarization with the same magnetic field without microwave pumping. Thus, if the material is highly polarized for example via DNP, the spin temperature is much lower than the lattice temperature. The Equal Spin Temperature (EST) hypothesis states that in a sample all polarizable nuclei have always the same spin temperature. The polarization then depends on the magnitude of the magnetic moment of the different materials. The EST hypothesis holds for many materials, but for example not for ^{15}N [74].

The deuteron magnetic moment is relatively small (0.857 compared to 2.793 for the proton [30]). Therefore, polarizing deuterons was more difficult than for protons. The irradiation of the deuterium target during the experiment increased the polarization. Furthermore, raising and lowering the microwave frequency by ± 25 MHz 500 times per second (500 Hz) [74] also increased the deuteron polarization. Since the resonance had a very small width, the magnetic field had to be very homogeneous so that the same resonance frequency was required at all points.

3.3.2 Pre-Irradiation

In preparation of the target, ammonia was frozen into small beads of a few millimeters diameter and irradiated in an electron beam. The irradiation created the paramagnetic impurities (free radicals in the ammonia crystals) through which the nucleons were polarized. The optimal bead size seemed to be a few millimeter in diameter. The material was irradiated at different institutes: Bates, Massachusetts Institute of Technology, Monterey Naval Postgraduate School, Stanford University, Continuous Electron Beam Accelerator Facility (now Thomas Jefferson National Accelerator Facility) and Saskatoon Accelerator Laboratory [75] [76]. Since the irradiation took place at liquid argon temperature, one referred to it also as "warm irradiation" [74]. This is in contrast to the "in-situ irradiation", which took place at liquid helium temperature during the experiment by the actual beam hitting the target.

At the Naval Postgraduate School in Monterey, a 10 m linear accelerator was used for the pre-irradiation of some of the E143 target material. The accelerated electrons were bent by about 70° into a small room where the dewar with the ammonia beads was located. The beads were confined to a small cup, several centimeters long, made of a metal mesh. The dewar was filled with liquid argon. Liquid nitrogen could not be used, since N_2 converts to an explosive gas under irradiation. The accelerator reached up to 120 MeV, but was only run at 60 MeV where the intensity was stronger. The irradiation of one cup of ammonia took a few hours, changing the color of the beads from colorless to deep violet.

3.3.3 Setup

The target was built by the University of Virginia and will be used in early 1997 at SLAC for experiment E155 and later for experiments at TJNAF.

A cross-section view of the target used during E143 is shown in Fig. 15. During the experiment, the ammonia beads were contained in cups 25.4 mm in diameter and 30 mm long made of Torlon with aluminum foil covering the front and back.[8] Inside the cups, copper-nickel wires served as coils for the NMR measurements. Three of those target cups were placed on top of each other, attached to the end of the microwave guide; usually the top cup was filled with ND_3, the middle one with NH_3, and the bottom one was empty for calibration purposes. Below the empty cup, carbon or aluminum of known thickness was attached for acceptance calculations. The whole target probe sat in a ^{4}He bath kept at about 1 K (evaporation refrigerator) and could be raised or lowered by remote control to one of the described positions. A superconducting magnet surrounded the tail section of the cryostat. Above the target cups, a microwave horn, fed by a microwave tube (about 140 GHz), pumped the polarization of the target material.

The superconducting magnet provided a magnetic field of very high homogeneity ($\frac{\Delta B}{B} \lesssim 10^{-4}$ over the target volume) [77] with a strength of nearly 5 T. The actual

---

[8] This aluminum was therefore in the beam and was taken into account for the dilution factor as well as the radiative corrections.
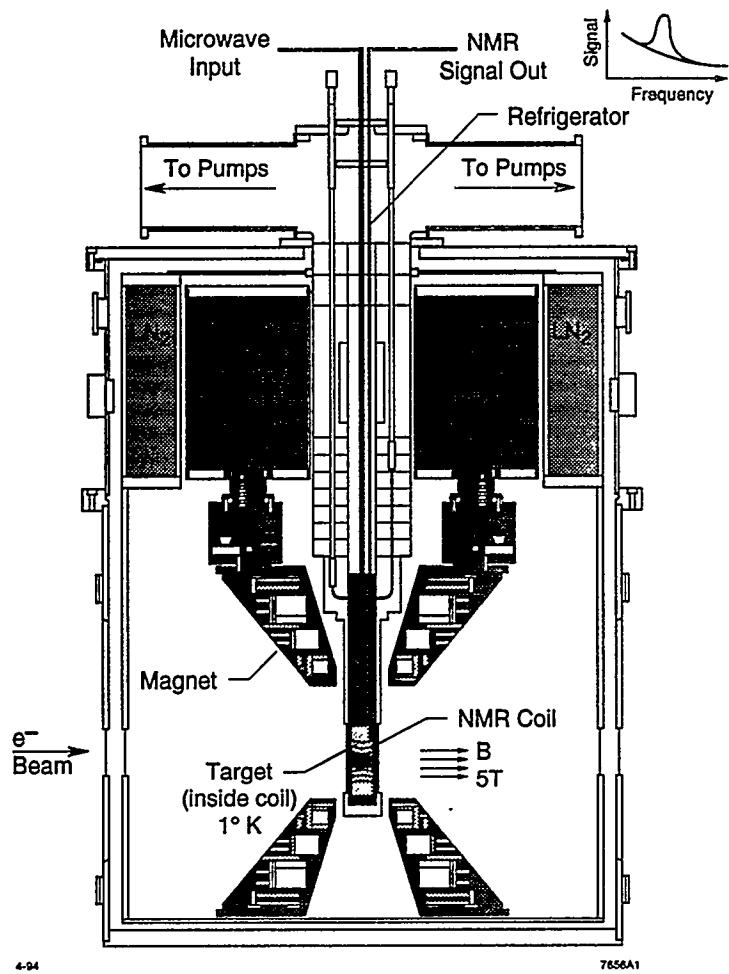
Figure 15 Schematic cross-section of the target used during experiment E143. The figure only shows two target cups at the tailpiece although a third cup was present as well as a carbon or aluminum target.

field was chosen to be 4.82 T in order to match the frequency of the microwave tube. By changing the direction of the current through the magnet, it was possible to flip the direction of the target field and hence the direction of the polarization. To obtain target polarizations perpendicular to the beam polarization, the magnet was physically rotated by 90°.

The target was mostly controlled from Macintosh computers running the program LabVIEW, which also automatically performed NMR measurements to monitor the polarization.

3.3.4 Radiation Damage

While the irradiation before the experiment created the paramagnetic impurities essential for Dynamical Nuclear Polarization, the polarization degraded during the experiment with time due to radiation damage. To spread out the radiation damage over the whole target material, the beam was always rastered over the target area. Some of that damage could be repaired by heating (annealing) the target material to liquid nitrogen temperature for a few minutes. Anneals were done about twenty times during the experiment. After several annealing cycles, however, the radiation damage was too severe and high polarizations could not be obtained. At this point, the target material had to be changed.

3.3.5 Measurement of Polarization

The principle of Nuclear Magnetic Resonance (NMR), which was used to measure the polarization of the target material, can be described in the following semi-classical way (see for example Ref. [78] or [79]).

The spin of a nucleus inside a magnetic field precesses on a cone around the axis defined by the magnetic field because of the torque $\mu \times \mathbf{B}$ while the average magnetic moment points either parallel or anti-parallel to the magnetic field. If the magnetic field were turned off, the polarization would decay exponentially with the so-called longitudinal relaxation time T_1 as decay constant. If considering many nuclei of the same kind, one may look at the distribution of those nuclei on the cone. If the vectors of the nuclei would not be evenly distributed on the cone, they would create an electro-magnetic signal which could be detected. No signal would be created if the magnetic moment vectors were evenly distributed on the cone. This latter state is the energetically preferred state, and the spins relax to this state in a homogeneous magnetic field. Again, this relaxation is described by an exponential function, with the so-called transverse relaxation time T_2 as decay constant.

64

Let us now add a coil with axis perpendicular to the coil axis of the static magnetic field. It shall emit a weak, varying electro-magnetic field such that its magnetic field stands perpendicular to the static magnetic field. This magnetic field can exert a torque parallel to the static magnetic field and is able to flip some of the nuclear moments from one side of the cone to the other, so that their spins point in the opposite direction. This happens preferential at the energy equivalent to the energy difference between the spin-up and spin-down state [see Eq. (123)]:

$$2\epsilon = 2\mu B = h\nu_{\text{res}} = \hbar\omega_{\text{res}}. \tag{131}$$

The closer the frequency of the electro-magnetic field is to the precession frequency, the easier these spins (or magnetic moments) can be flipped. ν_{res} (or equivalently ω_{res}) is therefore called the NMR resonance frequency.

The spin-flip disturbs the even distribution of the magnetic moments on the cone and a signal can be detected, for example by a coil whose axis is perpendicular to the axis of the coil for the momentum-flipping field as well as perpendicular to the axis of the coil for the permanent magnetic field. However, another method, called the Q-meter technique [80], is usually used for polarized targets, and it was also used during the experiment E143. In the Q-meter technique, no second coil is needed. The coil (or wire) used to create the varying electro-magnetic field has an inductance described by

$$L = L_0 \left[1 + 4\pi\eta\chi(\omega)\right] \tag{132}$$

with L_0 as the inductance without any material surrounding the coil and η as the filling factor, and

$$\chi(\omega) = \chi_R(\omega) + i\chi_I(\omega) \tag{133}$$

as the magnetic susceptibility of the material around the coil with real and imaginary part [80]. Together with a capacitor C, the system has the resonance frequency $\omega_{\text{res}} = 1/\sqrt{L_0 C}$. Around the resonance frequency, χ_I changes depending on the magnitude of the polarization. The effect of the real part is negligible, and therefore the resonance frequency itself will not change. The imaginary part of χ contributes to the real part of the impedance Z, since the impedance and inductance are related by $Z = i\omega L$, and the real part of the impedance is responsible for

the power loss. At the resonance frequency, the power dissipated into the system will be maximal. By measuring how much power is lost to the system, the strength of the polarization can be measured. It can be shown that the polarization P is proportional to $\chi_I(\omega)$:

$$P \sim \int_0^\infty \chi_I(\omega)\, d\omega \qquad (134)$$

Since $\chi(\omega)$ is zero except around the resonance frequency, it is enough to measure the integral for a small range of ω.[9]

For E143, the NMR system was implemented in the following way: Inside each cup was a small copper/nickel wire to serve as the coil. Since the hydrogen NMR resonance frequency was very high, the impedance of the wire had to be very small, which required a straight wire to be used for these target cups. For ND_3, the NMR frequency was lower, and the wire was wound into a small coil. The coil could have been placed outside the target cup, but the decision was made to insert it directly into the target material. In this way, the measurement gave good values for the polarization of the material inside the coil, but the beam electrons were able to hit the coil and create a significant number of unwanted events. A correction for this was applied through the dilution factor. In addition, the NMR coil responded mainly to the material inside the coil, but less to ammonia outside the coil which also contributed to the scattering events.

At the magnetic field strength of 4.82 T, the resonance frequencies were:

$$\begin{aligned} \nu_{\text{res}} &= 2\mu B/h = 2\,\mu_N\, 2.79\, B/h \approx 210\,\text{MHz} \quad \text{for protons} \\ &= 2\,\mu_N\, 0.86\, B/h \approx\ 32\,\text{MHz} \quad \text{for deuterons} \end{aligned} \qquad (135)$$

In ammonia, the quadrupole moment of the deuteron created in the deuteron NMR signal two close-by peaks instead of one single peak like the proton. The NMR signal was measured continuously during the experiment. The frequency was swept around the resonance. From the signal, several backgrounds (measured away from the resonance) were subtracted. The final signal was then integrated and normalized

---

[9] The quality factor Q for resonance circuits is proportional to the ratio of stored energy over lost energy per cycle at resonance frequency and indicates how sharp the resonance peak is. A very good resonance circuit, corresponding to high polarization in the case of polarized targets, has little power loss at the resonance frequency and therefore has a tight peak and a high quality factor Q.

via the results from the thermal equilibrium (TE) measurements. TE measurements were done at least once at the beginning of an annealing cycle and once at the end, since the beads moved around during each anneal. For these measurements, the microwaves were turned off. After reaching equilibrium, the polarization of the target material depended only on the strength of the temperature and the target magnetic field according to Eqs. (128) and (130). A greater number of measurements were taken for the deuteron since its NMR signal was considerably weaker than the proton signal due to the smaller magnetic moment and since the thermal equilibrium polarization of deuterons was smaller than of protons at the same magnetic field and temperature.

3.4 Spectrometers

Experiment E143 had two spectrometers, one located at a central scattering angle of 4.5° and the other at a central scattering angle of 7° with respect to the beam direction (Fig. 16). Both spectrometers accepted events within about ±0.5° of the central angle. The former contained two dipole magnets and one quadrupole magnet, while the latter had just two dipole magnets [60]. After the particles passed through the magnets, they entered the spectrometer "huts" containing the detectors. These spectrometer huts were assembled from concrete blocks to prevent outside particles, especially neutrons, from creating noise in the detectors. Both spectrometers had practically the same set of detectors, namely two gas Čerenkov counters, seven hodoscope planes, two trigger counters, and an array of shower counters. During the Christmas break, some RPC (Resistive Plate Chamber) counters were added in the 7° hut for a checkout. RPC counters were considered as an alternative or addition to hodoscopes for future experiments and were not used for the E143 analysis. Most of the electronics was located in the counting house which was above the beam line at the upstream end of ESA.

For the 9.7 GeV runs, an additional collimator restricted the aperture of the 4.5° spectrometer in the horizontal direction. This limited the number of events
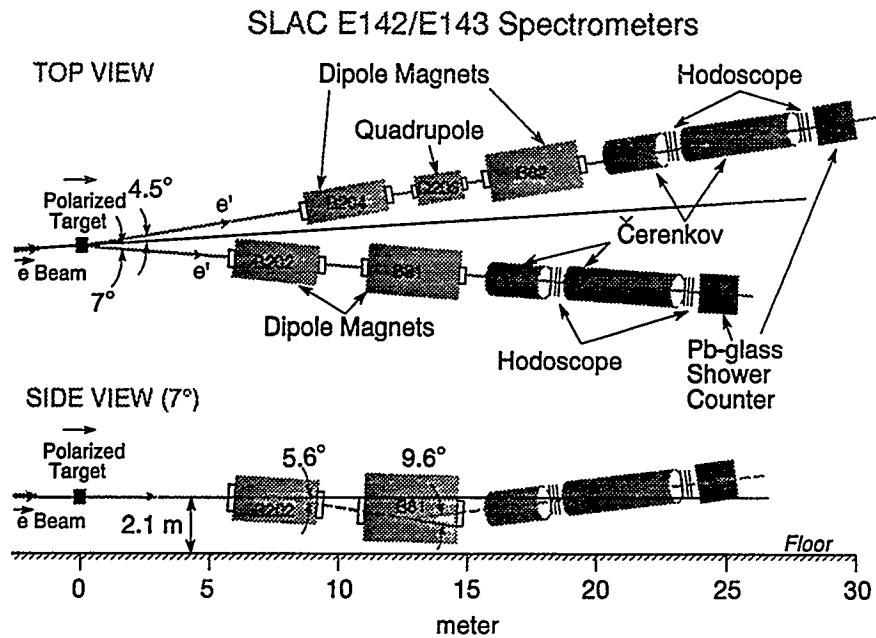
Figure 16 Schematic view of spectrometers used during experiments E142 and E143.

detected by the 4.5° spectrometer and made its rate closer to the rate of the 7° spectrometer. In this way, a higher rate in the 7° spectrometer could be sustained while not impeding the analysis of the 4.5° data. A larger acceptance in the 4.5° spectrometer would have increased the number of hits in each hodoscope finger and thus would have increased the demands on the tracking code.

A special coordinate system, called spectrometer coordinate system, was used for the detector elements: The central axis of the coordinate system passing through the detectors was named the z-axis. This line corresponded to the central ray of particles originating at the target with certain momenta.[10] When crossing the detectors, the ray was horizontally at 4.5° or 7° with respect to the beam line. At the same time, it pointed upward by 4° with respect to the horizontal plane (see Fig. 16). When looking downstream inside the detector huts, the x-axis pointed to the left, and the y-axis pointed up to form a right-handed cartesian coordinate system with the z-axis. All detector elements were aligned with respect to this

---

[10] The electric current settings of the magnets were expressed in terms of the momentum of this central ray.

coordinate system so that the z-axis was normal to the surface of each detector. The detectors were therefore all tilted at a 4° angle with the vertical.

Unless noted, the following description is true for both spectrometers.

3.4.1 Magnets

The 4.5° spectrometer contained two dipole magnets and one quadrupole magnet placed between them. The 7° spectrometer had only two dipole magnets [60]. Helium bags were placed between the polarized target and the spectrometer magnets as well as inside all of the magnets to lessen interactions of the electrons on their path to the detectors. The magnetic properties of the dipole magnets were determined before experiment E142 [81]. The homogeneity of the field and the shape of the fringe field were measured. Also constants to calculate the momentum of any particle (knowing its path in the detector hut and the current running through the magnets) were determined. These values were later used in the analysis code to reconstruct the momentum of the particle, once its track in the spectrometer hut was known.

In order to increase the acceptance, the first dipole magnet of each spectrometer was bending electrons down, while the second dipole magnet was bending them back up again. This arrangement led to a worse momentum resolution, since the dispersion in the second magnet partly cancelled the dispersion of the first magnet. However, resolution was not as important in E143 as in other experiments, while a high counting rate was essential. The quadrupole magnet in the 4.5° spectrometer squeezed the particles vertically and spread them out horizontally so that the distribution of the particles matched the shape of the detector as well as possible and so that the x-range covered by the spectrometers increased. The magnets were also placed such that background photons reached the detectors only if they bounced twice inside the spectrometers.

During experiment E143, the currents of the magnets were set so that the central ray was supposed to have a certain momentum, *e.g.*, -11.5 GeV. Since no independent check of the momentum was possible for E143 (*e.g.*, no elastic peak was inside the acceptance), the stability of the dipole magnets was checked not only by

monitoring the electric current, but also by monitoring the magnetic field via NMR probes located inside the magnets. They did not measure the overall effect of the magnetic field on a particle, but measured the field at only one single point. No probe was located in the quadrupole magnet.

3.4.2 Čerenkov

To obtain a good separation of electrons and pions, two threshold gas-Čerenkov counters, built at SLAC, were operated in each spectrometer. The upstream counter had a length of two meters and its N_2 gas pressure was always set to a pion threshold of 9 GeV. The downstream counter, also containing N_2, had a length of four meters and was always set to a pion threshold of 13 GeV [82]. The upstream Čerenkov detector was called Č1, and the downstream detector Č2. Inside each Čerenkov cylinder, mirrors reflected the light to a phototube located at the side. A Hamamatsu R1584-01 photomultiplier tube with a five-inch diameter was chosen to collect the light. The base voltage was set to -2700 V. To the front of the phototube, a thin layer of para-terphenyl was applied which acted as a wavelength shifter, converting UV light into longer wave length light (around 400 nm) to which the phototube was more sensitive. The Čerenkov signal went up to the counting house via HELIAX cables (which transmit signals at a high speed and low dispersion) and into the electronics.

Čerenkov detectors in general detect the light emitted by particles moving at a velocity higher than the velocity of light of the medium in which the particles are moving. The light is emitted in form of a (hollow) cone around the direction in which the particle is moving. Let θ_C be the angle between the direction of the particle and the direction of the light. The index of refraction of the medium shall be called n, and $\beta = v/c$ shall be the ratio of the velocity of the particle over the velocity of light in vacuum. Then

$$\cos \theta_C = \frac{1}{n\beta}. \tag{136}$$

Since $|\cos \theta_C| \le 1$, light is only emitted if $n\beta \ge 1$. The threshold for light emittance is at $n\beta = 1$. The higher the index of refraction is, the lower the threshold

will be. Particles at threshold will emit their light parallel to the direction of their momentum, while particles at momenta higher than the threshold will emit their particles in a cone with an angle $\theta > 0°$. The minimal momentum p necessary for a particle of mass m to emit light is given by the relation:

$$\beta_{th} = \frac{p}{E} = \sqrt{\frac{p^2}{p^2 + m^2}} = \frac{1}{n}. \tag{137}$$

Of course, $m^2 = E^2 - p^2$. For a pion threshold of, $e.g.$, 13 GeV, the index of refraction has to be $n = 1.000056$, while it is $n = 0.00012$ for 9 GeV. For the same indices of refraction, the electron thresholds are below 0.05 GeV, while the muon thresholds are around 10 GeV and 7 GeV. Since the index of refraction also depends on the wavelength, a particle usually does not emit Čerenkov light at one single angle, but at a range with each wavelength at its own characteristic angle.

A small index of refraction like the ones required for E143 can only be reached in gas at low pressure. The so-called Lorenz-Lorenz formula relates the gas density ρ with the index of refraction [83]:

$$\frac{1}{\rho}\frac{n^2 - 1}{n^2 + 2} = K(\lambda) \tag{138}$$

Here $K(\lambda)$ is a constant specific for the type of gas, and depends on the wavelength of the light. By lowering the pressure to about 3 psia in the two-meter Čerenkov tank and to about 6.3 psia in the four-meter Čerenkov tank, the desired low indices of refraction could therefore be reached.

In the selection of the type of gas, not only the index of refraction has to be considered, but also the scintillation and absorption properties of the gas. If the gas would scintillate very much, particles with even very low energy would create light. If the absorption would be high, the Čerenkov light would be considerably weakened on its way to the photo-tube and signals might be lost.

The nitrogen scintillates more than CO_2. However, nitrogen transmits light well down to wavelengths of 150 nm compared to 190 nm for CO_2. Since the wavelength shifter in front of the phototubes converted ultraviolet light into light of higher wavelength which was suitable to the phototubes, it turned out to be better to use nitrogen.

An analysis after the experiment showed that about 8 photo electrons were detected per event. In addition, the Čerenkov response was simulated in a Monte Carlo program to ensure that the signals of the Čerenkov counters were understood.

3.4.3 Shower Counters

The shower counters were built by physicists from Saclay and Clermont-Ferrand. The shower counters were located at the downstream end of the detector packages. Each detector contained 200 blocks of lead glass arranged into 20 rows and 10 columns. Each block, $62 \times 62 \times 750$ mm in size, consisted of Schott type F2 glass with 41.8% lead (by weight), an index of refraction of 1.58 and a radiation length of 31.7 mm [84]. This corresponds to nearly 24 radiation lengths, allowing the electrons to dissipate all their energy in a narrow electromagnetic shower. Behind each block was a phototube. The signals were then brought up to the counting house.

By definition, after traveling through material one radiation length thick, an electron has in the average $1/e$ of its original energy left. An electron hitting the lead glass blocks of E143 (24 radiation lengths thick) therefore loses practically all of its energy [44]. The dominant process is Bremsstrahlung, creating a shower of photons, electrons and positrons. Due to sampling fluctuations, the resolution of the shower counter is proportional to $E^{-1/2}$. The resolution will therefore be better at high electron energies than at low energies, as long as there are no limitations due to other problems like noise or calibration errors [44].

The second process by which charged particles lose energy is ionization. By this mechanism, all heavier charged particles (like pions) lose most of their energy. The energy loss is described by the Bethe-Bloch formula [85], which depends — besides on general physical constants like electron mass — on the atomic number, the atomic weight and density of the absorbing material. In the ionization process, the energy loss is mostly due to the collision of the particle with the atoms, causing excitations of the atoms, ionization of the atoms as well simply deflection of the incoming particle. The effect of the materials on the particles is expressed via the

nuclear interaction length, the mean free path. A rough estimate for it is [44]:

$$\lambda_I \approx 35 \, \frac{g}{cm^2} \, A^{1/3} \qquad (139)$$

For example, about 20 cm of lead correspond to one interaction length. Therefore, pions did not deposit much of their energy within the 750 mm of the E143 lead glass. Electrons of high energy, however, first lose their energy mainly via Bremsstrahlung. Later, after having lost enough energy, they lose the rest via ionization.

With its long interaction length, lead glass is relatively transparent to heavy charged particles, while absorbing electrons very well. This property was exploited in the analysis to distinguish pions and electrons independently from the Čerenkov signal. While electrons created showers in a small region and converted nearly all their energy into photons, pion showers were wider and contained only a fraction of the pion energy. In the analysis program, a cellular automaton used the shower ADC information and decided which blocks formed a cluster created by one incoming particle. In addition, a neural network estimated whether this particle was more likely a pion or an electron. Details about these two algorithms are presented in the next chapter.

3.4.4 Hodoscopes and Trigger Counters

The hodoscopes were built by the following institutions: Saclay & Clermont-Ferrand, SLAC, Syracuse University, and Tohoku University (Japan). The trigger counters were built by Tohoku University.

The hodoscopes and trigger counters were clustered in two groups. The first group consisted of four hodoscope planes and one trigger counter and was located between the two Čerenkovs. The other group consisted of three hodoscope planes and one trigger counter and was located between the rear Čerenkov and the shower counter. In the 4.5° spectrometer, the front and rear hodoscopes were about 5.0 m apart; in the 7° spectrometer, they were about 5.1 m apart. The planes were numbered front (upstream) to back (downstream) from 1 to 7. Table 6 lists the main characteristics of the hodoscopes used in E143. Neighboring fingers overlapped by

73

about 1/3, which improved the resolution by a factor of about three. Due to this fine segmentation of the hodoscope planes, the resolution was high enough for the experiment. Also, the influence of the background noise was reduced by the large number of hodoscope fingers.

Table 6 Major characteristics of the hodoscopes. Some numbers differed for the 4.5° and 7° hodoscopes. In that case, the left number corresponds to the 4.5° hodoscopes, the right number to the 7° hodoscope. The fingers of the u-hodoscopes were pointing at a 45° angle from the top left side to the bottom right side when looking downstream. The timing resolutions were the ones assumed in the tracking program and not necessarily the actual ones.

plane	built by	# of fingers	width (mm)	length (mm)	timing resol. (ns)
1 u	Tohoku	25	45	200–740/200–740	1.4/1.3
2 x	Syracuse	34/23	20/30	589/690	1.1
3 y	Syracuse	31/36	30	430/430	1.1
4 y	SLAC	20	47.6	356/483	1.4/1.0
5 x	Syracuse	27	30	1070/1070	1.1/0.9
6 y	Syracuse	55	30	510/510	1.1/1.0
7 u	Saclay	21	75	200–820/200–820	1.4/1.2

The trigger counters consisted of one big piece of scintillator material. The front counter had two photo tubes at the top and two at the bottom. The rear counter had one at the top, one at the bottom. In both spectrometers, the front trigger counter was located between the front Čerenkov and the first hodoscope plane. The rear trigger counter in the 7° spectrometer stood behind the rear Čerenkov, in front of hodoscope plane 5. However, due to spatial constraints, the rear trigger counter of the 4.5° spectrometer had to be placed behind the last hodoscope plane, right in front of the shower counter.

The high voltage was provided by LeCroy HV4032A power supplies located in the counting house. The Čerenkov and shower counter detectors were connected to the same power supplies. The high voltage cables went to a patch panel located under the 4-meter Čerenkov tanks. From there, each of the high voltage cables

from the counting house was connected to up to four hodoscope photo tubes. Due to time constraints in the summer of 1993, the voltage setting for the photo tubes were not re-checked. Instead, the high voltages were initially set to the same values as at the end of E142 and adjusted during the checkout phase of E143 as necessary.

3.5 Electronics

Most of the electronics modules were located in the counting house. Only some modules, among them the discriminators for the hodoscopes, were placed inside End Station A. Each spectrometer had its own, separate and nearly identical electronic set-up. The following description of the electronics applies to either one of the two spectrometers.

The detectors were mainly designed to register electrons and allow the rejection of other particles. Many events were created by pions, and the electronics were hence designed to pick those events for the data acquisition which were most likely to contain electrons. The most important trigger was the MAIN-TRIGGER, designed for electrons. It required signals from the shower counters and both Čerenkov detectors. This trigger together with several other triggers were combined in the MAIN-OR, which in turn signaled the data acquisition to record data for the current spill.

However, let us first describe how the signals from the different detectors were processed by the electronics. After that, we will explain how they formed the different kinds of triggers.

The **Čerenkov** signals from the photo-tube were sent to the counting house via HELIAX cables. The signals were then split via a fan-out module and sent to ADC modules as well as to four discriminators, each with a different threshold: low, medium, high, and very high. We will denote the logic signals with Č1[L], Č1[M], Č1[H], Č1[VH] for the front Čerenkov (Čerenkov 1), and similarly for the rear Čerenkov (Čerenkov 2). Each of these signals went into TDC modules, and some of them were used for trigger purposes, while others were only used for efficiency studies.

The **shower counter** signals were sent to the counting house via normal cables. Like the Čerenkov signals, the shower counter signals were sent to ADC modules. Furthermore, the shower counter signals from all blocks were combined into one signal which in turn was sent to discriminators with five different thresholds, creating the logic signals SH[VL], SH[L], SH[M], SH[H], SH[VH]. Similar to the Čerenkov signals, they went to TDC modules and some of them were used for the triggers. In addition, the signals of four (non-adjacent) shower counter blocks were combined and sent to discriminators and TDC modules. In this way, more accurate timing of the clusters would have been possible. However, these timing measurements had a low priority during the set-up and running of the experiment and were never fully operational. These TDC values were therefore not used in the analysis.

The signals of each finger of the **hodoscopes** were fed into LeCroy 4418 discriminators (located in the spectrometer huts) and then sent to the counting house via specially fabricated cables, each cable containing seventeen twisted-pair cables. Twisted-pair cables reduced the possibility of cross-talk between the wires and hence reduce noise. The signal between the discriminators and the counting house were also ECL signals which similarly reduced cross-talk.

The hodoscopes also provided information for triggering purposes, though not for the MAIN-TRIGGER. Each LeCroy 4418 discriminator module has an overall OR output at the back. It provides a signal if any one of its channels receives a signal above threshold. The signals of the front x hodoscope plane (plane 2) were combined into one module, and its combined OR signal went up to the counting house via HELIAX cable and into the scintillator coincidence AND logic. The other two inputs for the scintillator coincidence AND logic came from the two **trigger counters** (via discriminators). If both scintillators and one hodoscope finger in the front x plane fired at close time, the scintillator coincidence was triggered.

Let us now look at the different trigger types (Fig. 17). The following five triggers arrived at the **MAIN-OR**:

- The **MAIN-TRIGGER** consisted of the logic AND of Č1[L], Č2[L], and SH[L]. This is also commonly written as Č1[L]·Č2[L]·SH[L].

- The next trigger arriving at the MAIN-OR was the **Č1 efficiency trigger**, con-
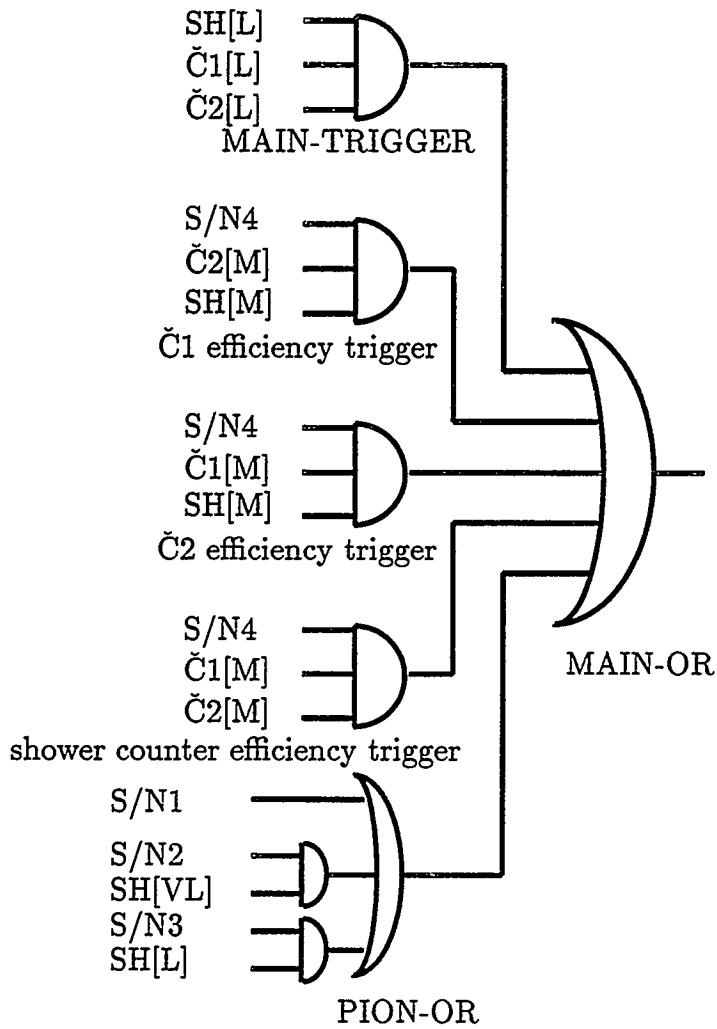
Figure 17 Schematic view of the logic going into MAIN-OR. The semi-circles represent logic ANDs, while the half-moons represent logic ORs. See text for further explanation.

sisting of the logic AND of Č2[M], SH[M], as well as the scintillation coincidence prescaled via prescaler N4. A prescaler lets only every nth signal through, with n selected by the experimenters. The signal is written as S/N4·Č2[M]·SH[M]. During E143, the prescaler of the 7° spectrometer was always set to 1 and let through every signal, while the 4.5° prescaler was set to 1, 2 or 4. (For details on the prescaler settings, see Ref. [86].)

- The following two triggers were very similar to the previous trigger: The Č2 **efficiency trigger** consisted of S/N4·Č1[M]·SH[M], and the **shower counter efficiency trigger** consisted of S/N4·Č1[M]·Č2[M].

77

- The last trigger arriving at the MAIN-OR was the so-called **PION-OR** signal. It itself was created by an OR of one of three signals and — as the name indicates — was also sensitive to pions. The three signals arriving at the PION-OR were the following:

  - The scintillation coincidence prescaled by prescaler N1: S/N1.

  - The scintillation coincidence prescaled by prescaler N2 in time with a shower counter very low signal: S/N2·SH[VL].

  - The scintillation coincidence prescaled by prescaler N3 in time with a shower counter low signal: S/N3·SH[L].

During E143, the three prescalers N1, N2 and N3 of each spectrometer were always set to the same values. For the 4.5° spectrometer, they were set to values from 1 to 128, but were mostly at 8 to 32. For the 7° spectrometers, the settings were mostly 2 or 8, and only sometimes 1 or 16. During the 9 GeV runs, all prescalers (N1 to N4) in both spectrometers were set to 1 because the rates were low enough.

The signals which were sent to the ADC modules were delayed by a time of up to 200 ns [87]. During that time, the logic decided whether there would be a MAIN-OR trigger. The Čerenkov signals were delayed simply by cable, but the shower counter signals were delayed via solid-state chips within special modules, called the "Saclay splitters". These modules were passive fan-out modules (*i.e.* without amplification of the signal) and distributed the signals to four different crates with ADC modules. Overall, each output from the Saclay splitters carried about 20% of the strength of the original signal. During each spill, the ADC values for only the first four MAIN-OR signals were recorded. The crates were gated by signals from the so-called "Saclay Trigger Divider" which passed the first MAIN-OR signal to the first crate with ADC modules, the second signal to the second crate, the third signal to the third crate and the fourth signal to the fourth crate. The timing of the signals were chosen such that the gating signals arrived at the crates 50 ns earlier relative to the ADC input signal while the ADC integration time was chosen to be 100 ns. The modules therefore integrated the strength of the signal within ±50 ns of the MAIN-OR time.

TDC values were recorded for up to 16 MAIN-ORs. A common start signal before the arrival of the spill data ensured that the clocks of the TDC modules were synchronized. Due to the design of the TDC modules, the TDC values of the last 16 hits in the spill, not the first 16 could be read out. 16 hits, however, were enough. A special gate existed for the hodoscope signals. Before they entered the TDC modules, they passed through special electronic modules, called the gate cards. The trigger for these gates was called **HODOGATE** and was a logic OR of the following five inputs: S/N4·Č1[M], S/N4·Č2[M], Č1[L]·Č2[L], S/N1, S/N2, and S/N3. This combination triggered the HODOGATE every time the MAIN-OR was triggered. The HODOGATE trigger told the gate cards when to let the signals pass to the TDC modules. Through this, only data in interesting time windows were selected, decreasing the load on the data acquisition system. The gate cards were used for all energies. However, at a beam energy of 9.7 GeV, the rates were so low that gating was not necessary, and the gates were always kept open. E143 used new gatecards designed at SLAC which had the advantage that they only allowed those signals to pass through the gate which started during the gating time. In the preceding system, also the tails of spills starting shortly before the gate opened were able to pass the gate, which lead to timing shifts.

The input for each TDC module arrived in two cables. The first cable, carrying channels 0 to 15, went from the gate card directly into the TDC module. The second cable, carrying channels 16 to 31, first went to a special patch panel where the so-called "marker pulse" was added to the signal of channel 31 of each TDC module. This was done to overcome the following problem: The number of events in each channel differed from spill to spill, and several TDCs had to be read in each crate. The computer was reading one module after the other. It looked through the channels of each module and recorded all non-zero TDC values together with the channel number. However, the computer was not able to record the module number. For example, if one whole module had no hits during the spill, the data acquisition system would simply skip the module and there would be no way to recognize which module was empty. To resolve these ambiguities, the marker pulse arrived several microseconds after the spill data. Due to its unphysically high value, the analysis software was able to identify the marker pulse in channel 31 of each

module and was therefore able to count the number of modules it read. For the off-line analysis, timing constants were obtained for each TDC channel which were added to the measured times to correct small timing shifts.

Many signals were connected to scalers which simply counted how often the signal appeared. They were used for on-line monitoring, but not for any analysis purposes. Also not described in this dissertation is the electronics to perform special test and calibration runs.

3.6 Data Acquisition

Several VAX computers, connected together via Ethernet, were involved in reading the data from the electronics, writing them to tape and monitoring their quality.

The first computer, a VAX running under VAXELN, read the ADC and TDC information from the CAMAC crates via a QBUS system, first the beam data, then the 4.5° data, then the 7° data. If the read-out took too much time, the following spill was not recorded. Another computer, a Vax Station under VMS, ran the program TAPESERVE. It read the data from the first computer, stacked them into larger blocks, and wrote these larger blocks to 8-mm data tapes.

The interface of the data acquisition programs to the experimentalists was provided by the program DAQCNTRL, running on another computer. It allowed the experimentalists to start, pause, and stop runs, to request calibration runs (pedestal, toroid or LED runs[11]), to move the polarized targets to into their positions, and to control the tape drives. It also displayed important information on several monitors.

To check the quality of the incoming data during the experiment, three more computers requested events from TAPESERVE, analyzed them, and displayed the results in histograms. This on-line analysis was, of course, not able to keep up with the incoming data, and hence only analyzed a sample of the data. One computer

---

[11] Toroid runs will be discussed in the following chapter. To check phototubes, the shower counters and some hodoscope fingers had LEDs attached which could be turned on to create a signal in the photo tubes. Such tests were called LED runs.

was dedicated to the analysis of the 4.5° data, another to the analysis of the 7° data, and a third to the analysis of the beam data.

Every few minutes (usually every five minutes), the data acquisition system recorded special data like pedestals, target and beam polarization onto tape. These special recordings were called "checkpoints". Additional terminals and programs were used to monitor and to control the high voltages, the low voltages, the scalers, and the magnets.

CHAPTER 4

ANALYSIS

After introducing the general data set, the analysis of the Møller data, the A-Line and spectrometer magnet and the target polarization measurements, this chapter will describe the analysis of the spectrometer data as well as the corrections to the asymmetry like dead-time, radiative or nitrogen corrections. A separate, fast analysis program, called "Quick Analysis", was used right after the experiment. It is not discussed in this dissertation. The analysis described in this dissertation is completely independent from the Quick Analysis, more elaborate, and consistent with the Quick Analysis.

4.1 Data Set

The experiment ran from middle of November 1993 to February 6, 1994. The data taking focussed on the beam energy 29 GeV with target polarization parallel to the beam polarization. Data with "transverse" target polarization at 29 GeV beam energy were obtained for about two weeks in January, and data in longitudinal mode were recorded for about two weeks at 16 GeV and for one week at 9 GeV. Table 7 lists the different data sets. Overall, about 2×10^8 electrons were recorded.

To obtain an estimate of the pion background, $10 - 15\%$ of the runs were taken with one spectrometer at opposite momentum setting, detecting positively charged particles, e^+ and π^+. These runs were usually called "positron" or "pion" runs.

Table 7 Run numbers and times of data taken. The central momentum is given in GeV for the 4.5° (left) and 7° (right) spectrometers. Runs below number 1000 were not analyzed. The run numbers given are approximately the first and last good runs of the set. The number of triggers are given in units of 10^6 events first for the proton, then for the deuteron target. The data with run numbers 1244 and below are the so-called pre-ROD data and were not used for the regular results of this dissertation.

energy & asymmetry	central momentum in GeV 4.5°	7°	# of e^- in 10^6 (prot/deut)	run range	dates
29 GeV $A_{\parallel}$	−11.5	−12.5	4/9	1000 – 1244	11/24/93 – 12/ 1/1993
29 GeV $A_{\parallel}$	−11.5	−12.5	12/18	1245 – 1745	12/ 1/93 – 12/14/1993
16 GeV $A_{\parallel}$	−7.5	−8.0	34/12	1766 – 2063	12/15/93 – 12/21/1993
16 GeV $A_{\parallel}$	−11.5	−12.5	5/5	2072 – 2160	12/21/93 – 12/23/1993
29 GeV $A_{\perp}$	−11.5	−12.5	20/13	2164 – 2642	1/ 4/94 – 1/18/1994
29 GeV $A_{\parallel}$	−11.5	−12.5	19/27	2651 – 3137	1/18/94 – 1/31/1994
9 GeV $A_{\parallel}$	−7.5	−8.0	30/28	3142 – 3378	2/ 1/94 – 2/ 6/1994

During the first weeks, the system was checked, calibrated and mistakes were corrected. December 1, 1993 was one of the so-called "ROD-Days" (Repair Opportunity Day). Several important problems were corrected at that time, like a tilt of one of the mirrors in the 4.5° 4-m Čerenkov tank. Also from that day on, the 120th pulse, though empty, was read out by the data acquisition system (see earlier chapter). Because of not sufficiently well known target polarizations, the pre-ROD data were not be included in the regular analysis of this dissertation (see also special section in Chapter 5).

In addition to data on $^{15}NH_3$ and $^{15}ND_3$ targets, data were also collected with the empty and the carbon targets. The carbon and empty-target runs were performed for calibration purposes. A few measurements were done with an empty target at very low helium gas pressure, and some at a position where there was no cup at all ("no target"). From January 14 to 22, the carbon target was replaced by an aluminum target, and the ND_3 target was exchanged by a second NH_3 target. During the test phase of the experiment, ammonia of the type $^{14}NH_3$ and $^{14}ND_3$ was also used, but no data were taken with these targets.

At least once a shift, so-called pedestal and toroid runs were performed. At the end of the experiment, they were done more often. During pedestal runs, the response of the ADC modules without any input was recorded. For each ADC channel, one thus obtained the pedestal, which was later subtracted from each ADC reading to obtain the real response of the ADC channel. During toroid runs, a calibrated amount of charge ran through the toroid monitors [66]. The response was read out in the same way as if real beam would have crossed the toroids. This measurement determined the multiplicative calibration factor for the beam charge measurements.

During the experiment, about 300 data tapes were filled with data. Since analyzing these tapes directly took a lot of CPU time, data summary tapes (DST) were produced, for which the analysis code calculated quantities like tracks, cluster positions, cluster energies, neural network responses, and beam positions. These results as well as additional important information were then written back to another tape for later analysis. The check point data, for example, were simply copied over onto the data summary tape. In this way, the data size decreased by a factor of four, and later analyses did not have to redo the CPU intensive calculations but still had all events accessible. Only runs with run numbers above 1244 were included in the regular analysis. Runs between 1000 and 1244 belonged to the so-called pre-ROD data which had to be excluded from the analysis because of insufficiently known target polarization. Runs below number 1000 were completely ignored in the analysis, since they were recorded during the test phase.

DSTs were produced twice, in Spring 1994 (DST1) and in Spring 1995 (DST2). DST production was done on UNIX machines, which became available end of 1993. The output for DST1 was written onto 8-mm tapes, and later transferred to a silo system at SLAC, which made the manual handling of tapes obsolete. At the time of the DST2 production, the computer system was already so advanced that the DST2 output was directly written to the silo system.

After the production of the data summary tapes, the analysis code was run again to read the data summary tapes. The quality of the beam was checked for each spill, and good tracks and clusters counted for many different cuts and definitions.

The number of good events for each definition, for left and right beam helicity, for each x and for each Q^2 bin were then written separately for each run into the so-called "summary files".

These summary files were later read by another program which calculated the asymmetry $A_\parallel$ (and for 29 GeV data also $A_\perp$) from the number of events and applied corrections for beam polarization, target polarization, radiative effects *etc.* The asymmetries $A_\parallel$ and $A_\perp$ were then used to obtain the structure functions.

4.2 A-Line and Spectrometer Magnets

About once every shift, the magnetic field in the A-Line and spectrometer dipole magnets was measured with the NMR system. After the experiments, the measurements were analyzed and found to be very stable at the 0.2% level [88]. No NMR probe was located in the quadrupole magnet. To check its stability, one had to rely on the current measurements, which were also found to be stable.

On December 14, 1993, the flip-coil in the ninth magnet of the A-line was calibrated by measuring the beam polarization in ESA for beam energies from 26.7 to 29.9 GeV. As described earlier, the flip-coil measured the magnitude of the magnetic field inside the central area of the magnet, which was used to determine the energy of the electrons. Since the polarization vector rotated faster than the momentum vector, longitudinal polarization in the end station was a function of the cosine of the beam energy. Longitudinally polarized beam in ESA was therefore restricted to certain energies [see Eq. (121)]. With the Møller polarimeter, the longitudinal polarization was measured for different energies. The results of these calibration runs were plotted versus beam energy and fitted to a cosine function. It was found that the flip-coil measured an energy 50 ± 30 MeV lower than the real energy [89]. This discrepancy was negligible for the purposes of experiment E143.

85

4.3 Beam Analysis

4.3.1 Beam Polarization

For beam energies of 29 GeV, scattered Møller electrons between center-of-mass angles of 70° to 110° were collected in the double-arm Møller detector. This range diminished for 16 GeV electrons, and no measurement was possible for 9 GeV electrons. Here only the single-arm detector allowed measurements. Since the double-arm detector had better statistics and smaller systematic errors than the single-arm detector, its results were used for the analysis. The double-arm results were also applied to the 9 GeV data. As will be explained below, this was possible since the double-arm detector analysis provided us with a relation between the polarization and the quantum efficiency of the photo cathode, and since the quantum efficiency was measured throughout the entire experiment.[12] The hits on the double-arm detector were registered via discriminators and TDC modules and stored on tape. The software then looked for coincidences in the arms. No hardware selected coincidence events.

A single Møller run only took about ten minutes. However, the polarization of the Helmholtz coil was reversed between two runs, and usually foils of several thickness were used. Each time, data were collected for at least 40 minutes. Additional time was necessary to set up the beam.

As discussed above, polarized electrons were produced by having a circularly polarized laser beam shining onto the cathode to knock out electrons [63]. The lower the quantum efficiency (QE) of the cathode was, the more laser light was necessary to obtain the desired number of electrons in the pulse. The quantum efficiency depended on the ratio of cesium atoms to oxidizer on its surface, which decreased with time [63]. To keep the current constant, the output power of the lasers was increased until the maximum laser power was reached. At this point, the operation had to be stopped to deposit more cesium on the surface and thus to increase the QE. This procedure was informally called "cesiation". A plot of

---

[12] We assume here, of course, that the polarization of the beam was independent of the energy to which the beam was accelerated.

the quantum efficiency versus time is shown in the upper part of Fig. 18. Towards the end of the experiment, the cesiation was not as strongly, but more frequently since at that time it was possible to cesiate within a few minutes and since it was recognized that a lower QE resulted in a higher beam polarization.

The beam polarization was correlated to the QE of the cathode because only electrons with high energy escaped the cathode at a low QE. These high energy electrons had less interaction (rescattering) and therefore a smaller probability to change their polarization [63]. The dependence of the beam polarization is shown in the lower part of Fig. 18. For each QE bin, the average beam polarization is given with two different error bars. To the left, the error bar shows the spread of all measurements at the given QE range. To the right, the error bar shows the standard deviation of the combined measurements at that QE range. The solid line is the curve of the form

$$P_{\text{beam}} = a + \frac{b}{e^{c(q-d)} + 1} \tag{140}$$

where P_{beam} is the beam polarization and q the quantum efficiency. The other variables were fitted to the data: $a = 0.828$, $b = 0.035$, $c = 300$, and $d = 0.055$. The form of the function was empirically suggested by the distribution of the points, and had no backing by any theory.

Quantum efficiency measurements were performed in short time intervals during the experiment and written to a computer file. For the whole experiment, we have the results of measurements not more than two hours apart. Since the decay of the quantum efficiency followed an exponential, the data between cesiations were fitted to a function of the form $q = Ae^{Bt}$ with q as the quantum efficiency, t the time and A and B fitting constants. In this way, the quantum efficiency was therefore available for each time, and together with Eq. (140), the beam polarization for each run was determined.

Overall, the beam polarization was measured to range from 0.83 to 0.86 with an absolute error of about ± 0.02 [90]. This error includes the statistical error as well as the systematic error which was dominated by the error on the foil polarization measurement.
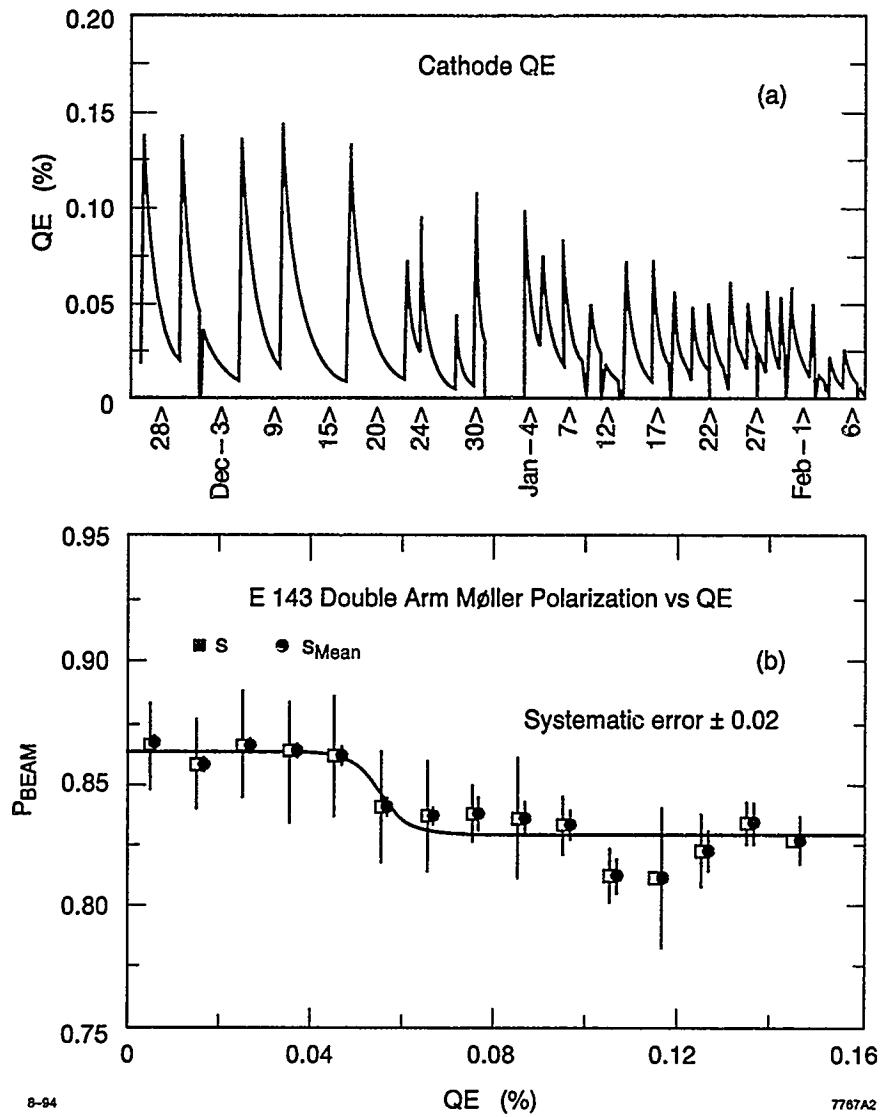
Figure 18 Quantum efficiencies and double-arm Møller results. The upper part (a) shows the quantum efficiency versus time as measured during the experiment, the lower part (b) shows the double-arm Møller results. To the left are the results shown with the spread of the individual measurements, to the right with the averaged errors.

4.3.2 Polarization Bit

Essential for the measuring of the asymmetry in E143 is the correct knowledge of the helicity of each spill. Since the raw asymmetries are of the order of a few percent, any small bias in the polarization bit interpretation can change the final results considerably.

88

Let us first describe how the pseudo-random distribution of left-handed or right-handed helicity was created spill by spill. Each spill was characterized by 0 for left-handed helicity and 1 for right-handed helicity. The first 33 of these bits were assigned a random distribution. Afterwards, the code calculated the helicity of each consequent spill by taking the bit of the previous spill and the bit of the 33th previous spill and forming the exclusive OR. If both bits had the same value (both 0 or both 1), the next spill was given left-handed helicity (bit set to 0). If one of the two bits was 0 and the other 1, the next spill was given right-handed helicity (bit set to 1). This distribution is known to be pseudo-random. This means that the sequence may be used like any true random sequence, while it is at the same time deterministic, since the knowledge of 33 spills determines exactly the series into past and future. The series repeats itself only after 2^{33} spills. The deterministic characteristic of the pseudo-random series was used to check the polarization bit which was written to tape with each spill.

From the source where the polarized electron beam was created, the information about the polarization of the spill was transmitted to the ESA counting house through three independent lines, the so-called HV (high voltage) line, the Veto line, and the MACH (Multi-Access Communication Highway) line. Since the MACH line turned out to provide the most reliable signal, its polarization signal was compared to the prediction of the pseudo-random number generator. A spill was only accepted for the analysis if the MACH line signal agreed with the prediction.

We mentioned earlier, that the beam monitoring equipment of the accelerator needed a strong, short pulse, and that hence one out of every 120 spills was of that kind, and that this spill was diverted into a beam dump instead of being injected into the A-line. Before the ROD (Repair Opportunity Day) Day, December 1, 1993, only the pulses which arrived at the end station were counted and written to tape. This caused the prediction of the polarization to disagree with the actual pulses once a second. Whenever the polarization disagreed with the prediction, the next 33 spills were used to determine the new seed, and the following 33 spills were used to check the new seed against the incoming polarization bits. If no error was detected, the following spills were again accepted for the analysis. Due to the missing 120th pulse, approximately half of the spills in each second were lost. After the ROD Day,

the 120th pulse was read out. Though no data were logged to tape for that spill, the analysis program needed the polarization information for this pulse to predict the subsequent polarizations correctly. For the pre-ROD data, the requirement that the polarization had to agree with the prediction was waived. Instead, the polarization bit from the MACH-line was accepted as correct. However, since the target polarizations were not known sufficiently well for the pre-ROD data, they were excluded from the regular analysis.

Also in some other ways some spills were lost. Sometimes MCC used 10 or more spills per second to check out other parts of the accelerator in preparation of the next SLC run, and from time to time, when a klystron failed, the accelerator shut down to a lower rate. All this complicated the comparison of the prediction with the actual measured polarization.

4.3.3 Beam Charge Measurements

Two toroid counters, called Toroid 2 and Toroid 3, measured the charge of the beam independently spill by spill. The analysis used the Toroid 2 results. Every few hours, special runs determined the calibration constants for these measurements by sending a well-known amount of charge through the toroids. An off-line analysis checked the calibration constants and concluded that the recorded beam current measurements were overestimated by less than 2% [66]. Since this correction applied to both the charge with left-handed electrons as well as for right-handed electrons, this overestimation had no influence on the results.

4.3.4 Rastering

A Helmholtz magnet deflected the beam slightly spill by spill before it entered the End Station to raster the beam over the target cross-section. The deflection followed a preset pattern, consisting of 253 points. Every 253 spills, the pattern was repeated. To minimize the local beam heating, each spill was always placed far away from the position of the previous spill. Fig. 19 shows the typical distribution
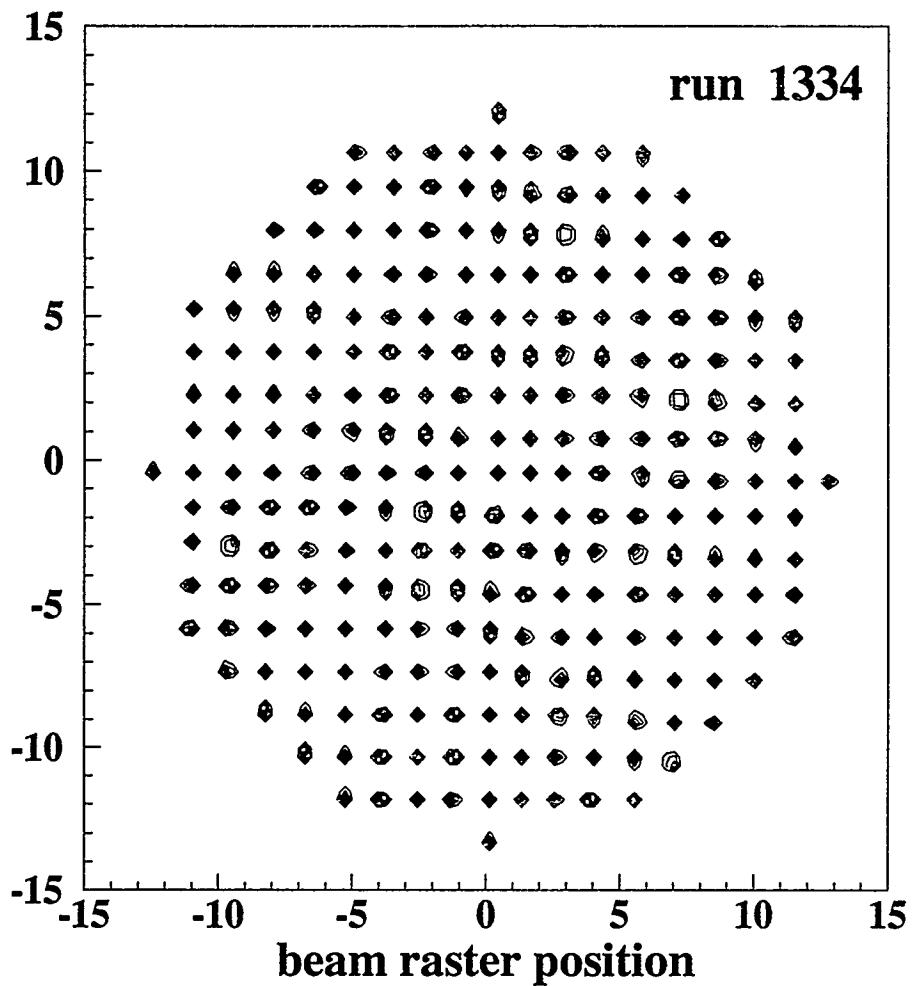
Figure 19 Beam distribution at foil array. The axes are the x- and y-position. The raster pattern with its 253 points is clearly visible. Only the center positions of the beam are plotted, but since the beam itself had a width of a few millimeter, the whole target area was covered by the incoming electrons.

of the spill at the foil array. The size of the raster pattern was chosen to be smaller than the diameter of the target. Usually a pattern of 18 mm diameter was selected for the 25 mm diameter target cell. Together with the finite width of the beam of two to four millimeters, most electrons were then hitting the target cell and not surrounding material. The pattern could also have been chosen to be significantly bigger. All target material would then have been involved in the scattering process, but many events would have also originated from unpolarized material outside the target cell.

During the experiment, it was realized that the fringe field from the spectrometer magnets influenced the beam on its way from the target to the foil array. This resulted in a vertical shift at the foil array (see Table 8). The deflection was calculated from field measurement and agree with the shift observed in the foil array [86]. The correction was taken into account during the analysis.

Table 8 Beam position corrections due to spectrometer magnet fringe fields.

beam energy	4.5° mom. setting	7° mom. setting	correction (mm)
29 GeV	−11.5	−12.5	−0.91
29 GeV	+11.5	−12.5	−0.62
29 GeV	−11.5	+12.5	+0.62
16 GeV	−7.5	−8.0	−1.04
16 GeV	+7.5	−8.0	+0.71
16 GeV	−7.5	+8.0	−0.71
16 GeV	−11.5	−12.5	−1.64
9 GeV	−7.5	−8.0	−1.75
9 GeV	+7.5	+8.0	+1.75

4.4 Target Polarization

As essential as the exact measurement of the beam polarization was the exact measurement of the target polarization. In this section, we describe the analysis and results of the NMR measurements for the polarized target.

As explained before, a calibration constant was necessary to scale the NMR measurement to the right polarization. During the experiment a tentative calibration constant was used to calculate the polarization. Every five minutes, the target polarization was written to the raw data tapes (during each check point). Its average weighted by the incoming electron charge was calculated on-line for each run and stored in the file "hdwsumry.out". Later analysis at the University of Virginia

resulted in corrected thermal equilibrium (TE) constants, and therefore the value which could be found in "hdwsumry.out" or on the tape had to be corrected, too. For example, if the University of Virginia analysis found that for a certain time period the actual TE constant was 10% larger than the one used at the time of the experiment, the number on the tape or in the file "hdwsumry.out" to be increased by 10%.

Under ideal conditions, polarizations of more than 90% could be reached for NH_3 [74]. However, during the experiment, polarization was in general less than 80% for NH_3 since the ND_3 target was usually placed between the microwave horn and the NH_3 target, reducing the microwave power absorbed by the NH_3 material. In addition, the polarization dropped due to beam heating when beam was placed onto the targets. For ND_3, polarizations of more than 40% were reached during the experiment. Here the in-situ irradiation by the beam played a vital role in reaching polarizations as high as this, as well as frequency modulation. The relative error on the polarization was $\Delta P_p / P_p \sim 2.5\%$ and $\Delta P_d / P_d \sim 4\%$. Fig. 20 shows the polarization of one of the ND_3 targets versus accumulated incident charge. The contribution to the error on the polarization was chosen to be the spread of the TE measurements.

4.4.1 Polarization of Other Material

In addition to hydrogen or deuteron, also other material in the target was polarized. ^{15}N consists of seven protons and eight neutrons, therefore practically acts like a single proton with a magnetic moment pointing to the opposite direction with respect to the deuteron magnetic moment. Furthermore, some ^{14}N was still present in $^{15}NH_3$ or $^{15}ND_3$ (2% contamination). Similarly, the deuterium in $^{15}ND_3$ still had a 1.5% contamination with hydrogen. This remaining hydrogen as well as the free protons found in Torlon, the material out of which the target cup was made, were called "residual protons" and were able to polarize. Since ammonia does not seem to follow the Equal Spin Temperature relationship, the polarizations of ^{15}N of the H ("residual protons") were measured in separate studies during the days after

93

Figure 20 Typical plot of ND_3 polarization versus charge.

the experiment. If it is known how much of these materials is in the target, one can correct the measured asymmetry for their influence (see later chapter).

4.4.2 Correction to Target Polarization due to Beam

The polarization of the target material depends on the temperature of the target material. The heating of the ammonia by the electron beam diminishes the polarization of the proton or deuteron at that spot. While rastering of the beam distributed the heat deposition over a larger area, still more heat was deposited at the raster positions than at the other parts of the target. In addition, as mentioned before, the beam did not cover the whole target cross-section, but only the central part. The temperature sensor was only able to determine the overall temperature of the target material, or actually only the temperature of the helium which surrounded the ammonia beads. The sensor was not able to determine the temper-

ature of the beads which got hit by the beam directly. Similarly, the NMR system only measured the target polarization averaged over a large volume of the target. The actual polarization of the beads which got hit by the beam was therefore not necessarily the same as the average polarization measured by the NMR. To resolve that problem, the actual temperature and polarization in the beads were estimated via model calculations [91]. Correction factors to the target polarization were then obtained. Their size was directly proportional to the beam charge. For 4×10^9 e^- per spill, they ranged from 0.8% to 2% relative to the measured target polarization. Let I be the beam current in units of 10^9 e^-/spill, let P_{uncorr} be the uncorrected target polarization, and let C_{beam} be the correction factors given in Table 9. Then the corrected target polarization P_{corr} is given by

$$P_{\text{corr}} = P_{\text{uncorr}} \left(1 - C_{\text{beam}} \frac{I}{4} \right). \tag{141}$$

Table 9 Target polarization correction factors for beam heating. The factors C_{beam} are given for a beam current of 4×10^9 e^-/spill.

	longitudinal	transverse
proton	0.0081	0.0103
deuteron	0.0197	0.0157

4.5 Event Reconstruction: Čerenkov

Since electrons were not the only particles created by the scattering process at the target, the detector had to be able to distinguish between electrons and pions, or at least had to give information which could be used by computer programs to decide the identity of the particle. The first distinction is made by the requirements of the MAIN-TRIGGER. Pions are less likely to create strong signals in both Čerenkovs and the shower counter. The next information is the Čerenkov ADC. The lower the charge registered by the ADC (charge proportional to Čerenkov light), the more likely (for same momentum) the particle was a pion. Fig. 21 shows for a typical run how often (vertical axis) a certain ADC response (horizontal axis) was triggered by electrons and pions.
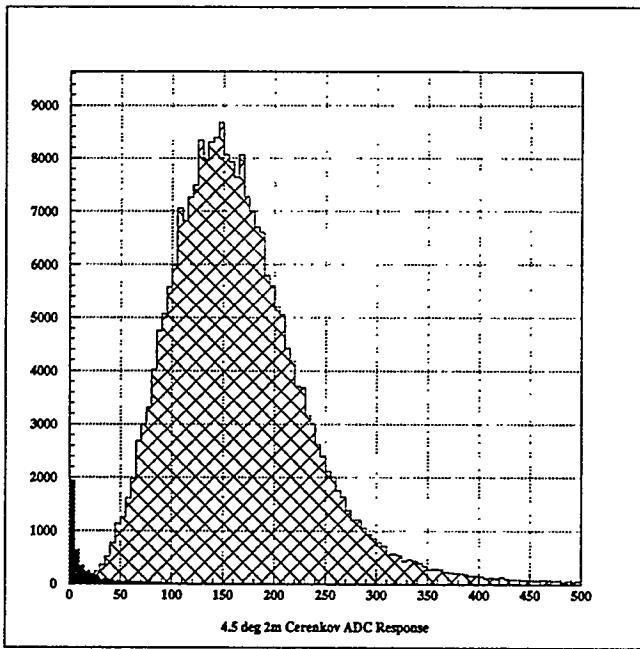
Figure 21 ADC response of the 4.5° two-meter Čerenkov counter. The events were classified by the response of other detectors as pions (densely cross-hatched area) or electrons (lightly cross-hatched).

During the first weeks of the experiment, before the ROD-Day, the lowest of the three mirrors in the 4.5° 4-meter cylinder shifted and had to be readjusted. As long as the mirrors were misaligned, fewer Čerenkov hits and hence fewer MAIN-TRIGGER events were recorded. For these early runs, no tracks going through the lowest area of this Čerenkov were used for the analysis.

96

4.6 Event Reconstruction: Shower Counter

4.6.1 Cellular Automaton

Out of energies measured for each shower counter block by the ADC, clusters had to be formed, supposedly originating by one single particle hitting one block and creating a shower spreading through several neighboring blocks. The determination of those clusters was done via a "cellular automaton" algorithm. Details are described in [92] and [93]. The algorithm only contained three rules:

1. All blocks which had a higher energy than each of their neighbors, were considered "a virus".

2. Any other block then took on the value of the highest energy of its neighbor ("contamination with virus").

3. However, any cell previously contaminated by a virus, was "immune" to any other virus.

One iterated over rules (2) and (3), until a stable system developed. Each set of blocks contaminated by one virus was then taken to be a cluster. The energy of the cluster was determined by the sum of the total energy of the cluster blocks, and the position of the cluster by calculating the center of the blocks weighted by the energy of each block.

This set of rules for the cellular automaton efficiently combined the blocks into clusters while having the advantage to be very clear and general [92]. A Monte Carlo comparison of this algorithm with another approach indicated a higher success rate for the cellular automaton algorithm when clusters overlapped frequently.

4.6.2 Calibration of Shower Counter

Since lead glass blocks as well as photo tubes differed in their response to incoming particles, and since also ADC channels varied in their answer to the same input, a careful calibration of the ADC responses was necessary [94]. Each of the 400 photo

tubes was connected to four ADC channels (one for each trigger level), and a total of 1600 constants had to be determined. Using the response of other detectors of the spectrometers, clean electron events were selected. The tracking provided the momentum of those events. The calibration constants were then selected so that the total energy E of the cluster (as determined by the cellular automaton) in the average matched the momentum p of the event, $i.e.$, that the ratio $E/p = 1$ was true for the average. Several iterations were required to reach this goal. Clusters which were located at the edge of the shower counter were calibrated with a special algorithm, since those clusters could not be expected to contain the full energy of the particle. Separate sets of calibration constants were obtained for different periods of the experiment.[13]

The calibration depended on the assumption that the tracking code provided on the average the correct momentum. Any bias in the tracking system would also have affected the energy measurement in the shower counter. Unfortunately, one had to rely on the carefully surveyed geometry of the detectors to calibrate the system. An absolute calibration of the tracking system with the data alone was impossible. For example, the observation of the (well-known) peak from elastic scattering would have allowed such an absolute calibration, but the elastic peak was not within the acceptance of the spectrometers.

Fig. 22 shows a typical E/p histogram. Most of the pion events were found at E/p ratios of less than one, while the electron events were clustered around 1.

4.6.3 Neural Network

To facilitate the discrimination between pions and electrons, the data from the shower counter were fed into a neural network (NN) which then returned a value between -1 and $+1$. The closer the number was to $+1$, the more likely — according to the neural network — the cluster originated from an electron. The closer the value

---

[13] During later analysis, the calibration was fine-tuned to take into account small shifts of the ratio E/p which were not eliminated in the calibration of the shower counter blocks. This was accomplished by a correction factor the correction factor to the cluster energy E based on the shift of the mean E/p.
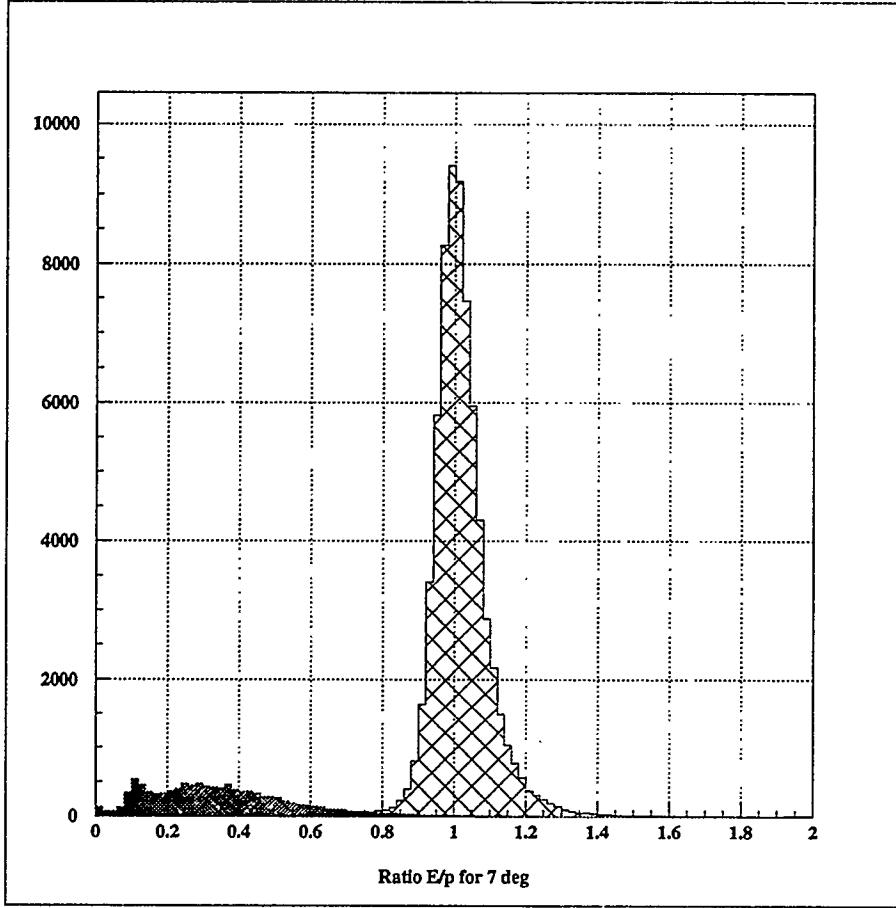
Figure 22 Distribution of the ratio E/p for a typical run. E is the energy of the particle as obtained by the shower counter, and p the momentum as obtained by magnets and hodoscopes. The bump at the left side (grey area) was mostly caused by pions. Almost no pions were found close to the peak around 1 (cross-hatched area), indicating a very good separation of pions and electrons.

was to -1, the more likely, the NN thought, a pion created the cluster. No other information besides the ADC values was used by the network.

The network was a three-layer system [95] [96] [92]: The input level with 13 input neurons, the hidden layer with four neurons, and the output level with two neurons. The input data for the first neural network layer were:

(1)   total energy of the central nine blocks

(2–10) energy of each of the nine central blocks

(11)   ratio of the energy in the central block over central nine block energy

(12)   energy of the sixteen blocks around the central nine blocks

(13)   number of blocks (out of the central 25 blocks) belonging to cluster

The weights were obtained with Monte Carlo events (electrons and pions) produced by the simulation package GEANT. Input (1) turned out to be the most important number in the neural network. Since the particles deposited their energy mostly in the central nine blocks, inputs (2) to (10) also had a lot of weight.

No information from blocks even farther out than the 16 blocks surrounding the central nine blocks was considered, even if the cellular automaton added some of those blocks to the cluster.

Fig. 23 illustrates the separation power of the neural network. Note that the vertical scale is logarithmic. Using the response of other detectors, events were identified as pion and electron events. The fact that only very few of those pions appear in Fig. 23 around +1 proves that the neural network alone can very well reduce the pion background in the electron sample. In the analysis, only events with a neural network response greater than 0.9 were used. Since the neural network provided a very good separation, the exact value of this cut was less important. At beam energies of 16 and 9 GeV, the contamination with pions was so low that no neural network cut was necessary.

4.7 Event Reconstruction: Tracking

In the analysis code, the path of the scattered particles was reconstructed from the spatial and timing information which were obtained by the Čerenkov counters, the hodoscopes, and the shower counters. Together with the information about the spectrometer magnets, the momentum of the particle could then be reconstructed.

4.7.1 Tracking Code

The tracking code for E143 was originally written for E142. The program was called for each spill and each spectrometer once. We will describe the program by
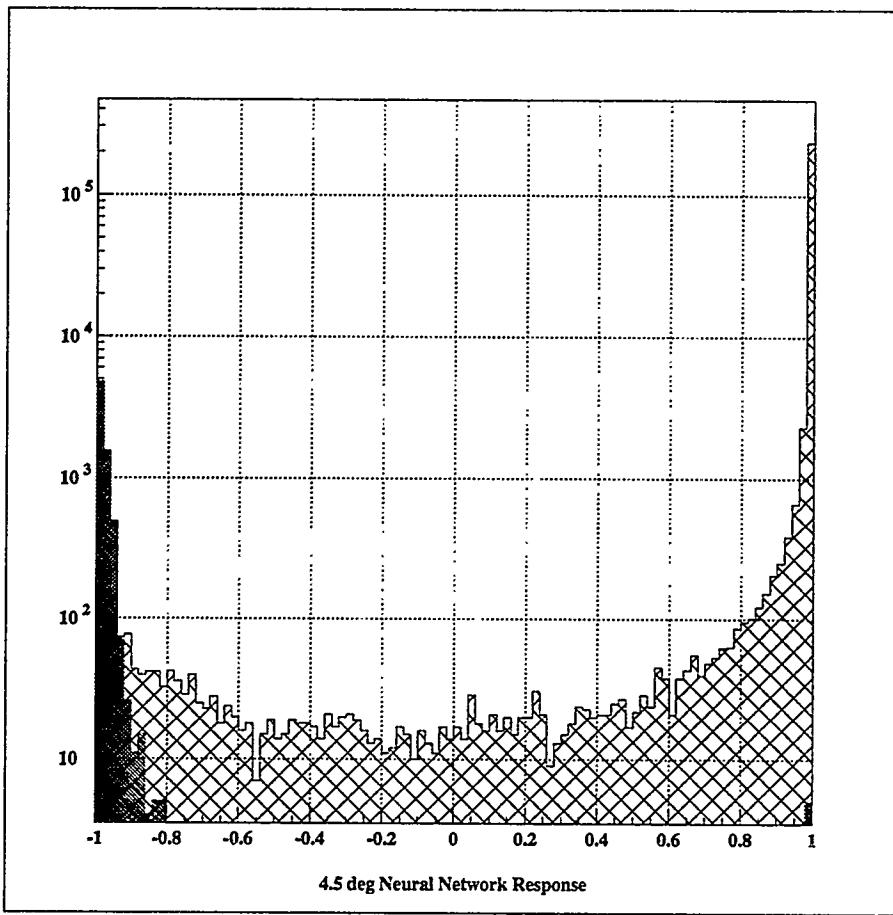
Figure 23 Typical distribution of neural network responses. Note that the vertical scale is logarithmic. The cross-hatched area corresponds to electrons, the grey area to pions (as determined by other detector responses, like Čerenkov pulse heights).

describing the main subroutines. A simpler tracking routine existed for the E143 Quick Analysis, but was not used for the analysis described in this dissertation.

4.7.1.1 Input Variables

The input for the tracking code consisted of the following information:

- Čerenkov Detector: TDC values of the signals passing the discriminator with the lowest threshold (Č1[L] and Č2[L]).

- Shower Counter: Cluster location and time (identical to the MAIN-OR trigger time).[14]

- Hodoscope: TDC times of each finger hit and location, size and direction of the fingers.

The tracking algorithm assumed for each hit a timing resolution between 0.9 and 1.4 ns. The exact values for the hodoscope fingers are listed in Table 6. The Čerenkov and shower counter signals were assumed to have a 1 ns timing resolution.

The spatial coordinates of each hodoscope finger are defined by the position of its center, the length of the finger, and the direction (x-hodoscope fingers point vertically, etc.). The width of the finger (see Table 6) divided by $\sqrt{12}$ served as the spatial resolution.

Each hit on the Čerenkov, of course, had a time associated with it, but the tracking program treated Čerenkov hits like hits on a hodoscope. For the Čerenkov, the imaginary hodoscope finger was taken to be a horizontal finger at the Čerenkov z-position. Its spatial resolution was set to 100 m. The direction of the finger was set completely arbitrarily, but due to this spatial resolution, the choice of the direction had no influence.

Shower counter hits, on the contrary, had not only a definite time, but also a definite spatial position. This position was represented in the tracking program by two hits on two imaginary hodoscope planes, one in x-direction, one in y-direction, with a spatial resolution of 10 mm. The tracking program required all the time that either both hits or none were on the track.

4.7.1.2 Track Classes

The program looked for four different types of tracks. The definitions of these track classes are listed in Table 10. A clean electron event was expected to have

---

[14] As indicated in the section about the electronics, no TDC values were available for single hits on the shower counter blocks. However, since the clusters were only recorded if there was a MAIN-OR trigger, the time of the MAIN-OR trigger was used for the time of the cluster.

a track of class 1, which required both shower and Čerenkov hits. A typical pion track was more likely to create only a track with hodoscope hits, since pions were less likely to trigger the Čerenkov counters and to deposit much of their energy into the shower counter.

Table 10 Track classes used during analysis. The program first tried to find tracks of class one. After it exhausted all possibilities for that track class, it continued with track class two, and so on.

| track | | number of hits: | | |
class #	Čerenkov	hodoscopes	shower counter	total
1	2	4	2	8
2	2	4	0	6
3	0	4	2	6
4	0	6	0	6

4.7.1.3 The Basic Concept of the Algorithm

After selecting a set of hits, the tracking code tried to fit a track to the hits, using the times of the hits and the positions of the detector elements, as well as the time and spatial resolutions as weights. Let t_i be the time of hit i, t_{track} be the time of the track at the position of the detector element which recorded hit i, and let s_{min} be the closest distance of the track to the detector element. Furthermore, σ_t and σ_s shall be the time and spatial resolutions of the detector element. Then the χ^2 of hit i with respect to the track was defined as

$$\chi_i^2 = \left(\frac{t_i - t_{\text{track}}}{\sigma_t}\right)^2 + \left(\frac{s_{\text{min}}}{\sigma_s}\right)^2. \tag{142}$$

Hits were then dropped and added to the set of hits to find the best set of hits with $\chi_i^2 < 16$ for each hit. To save computing time, the fitting was first done for the times, and only later for both times and positions. If only the times were fitted, the last term in Eq. (142) was neglected.

4.7.1.4 The Top Level Routine: trk_drv

The top level routine of the tracking program, called trk_drv, is described in this section. For the flow chart of this part of the code, see Fig. 24.

After resetting the counters to zero and loading the hits into a common block, the program looped through the four classes and tried to find tracks matching the requirements of the current track class. The subroutine trk_find, which selected hits for a possible track, is described later. To avoid infinite loops, the hits were marked as not usable if the fitting failed, so that the routine did not use these hits anymore for the current track class. Before continuing with the next track class, the program, however, unmarked the hits so that they could be used again for this new track class.

Once the subroutine trk_find provided a set of hits, the tracking program calculated the best average time for these hits. The times were adjusted to take into account that the detector elements were located at different positions. If the fitting failed, the hits were marked as unusable, and the program tried to find another set of hits. If the fitting was successful, the program checked whether any of the hits had a χ_i^2 of greater than 16. If yes, the worst of those hits was dropped and marked as unusable. Then the the program fitted again the time. If not enough hits were left to satisfy the requirements of the track class, the remaining hits were marked as unusable and the program returned to find another set of hits.

When the χ_i^2 of all remaining hits was less or equal to 16, the program fitted a track using both the timing information and spatial information. The time and spatial resolutions served again as weights. As before, the worst hit in terms of χ^2 with respect to the fitted track was dropped (if $\chi_i^2 > 16$) and the remaining hits were used to fit a new track. If not enough hits were left to require the track class requirements, the hits were marked, and the program started again looking for a new set of hits. However, when no more hit had to be dropped, the program added all unmarked hits with $\chi_i^2 \leq 16$, which were before left out of the set of hits. If no hit had to be added, the track was saved (subroutine trk_copy). If a hit was added, the track was refitted. If the fitting was successful, the track was saved; otherwise the hits were marked as unusable.

104
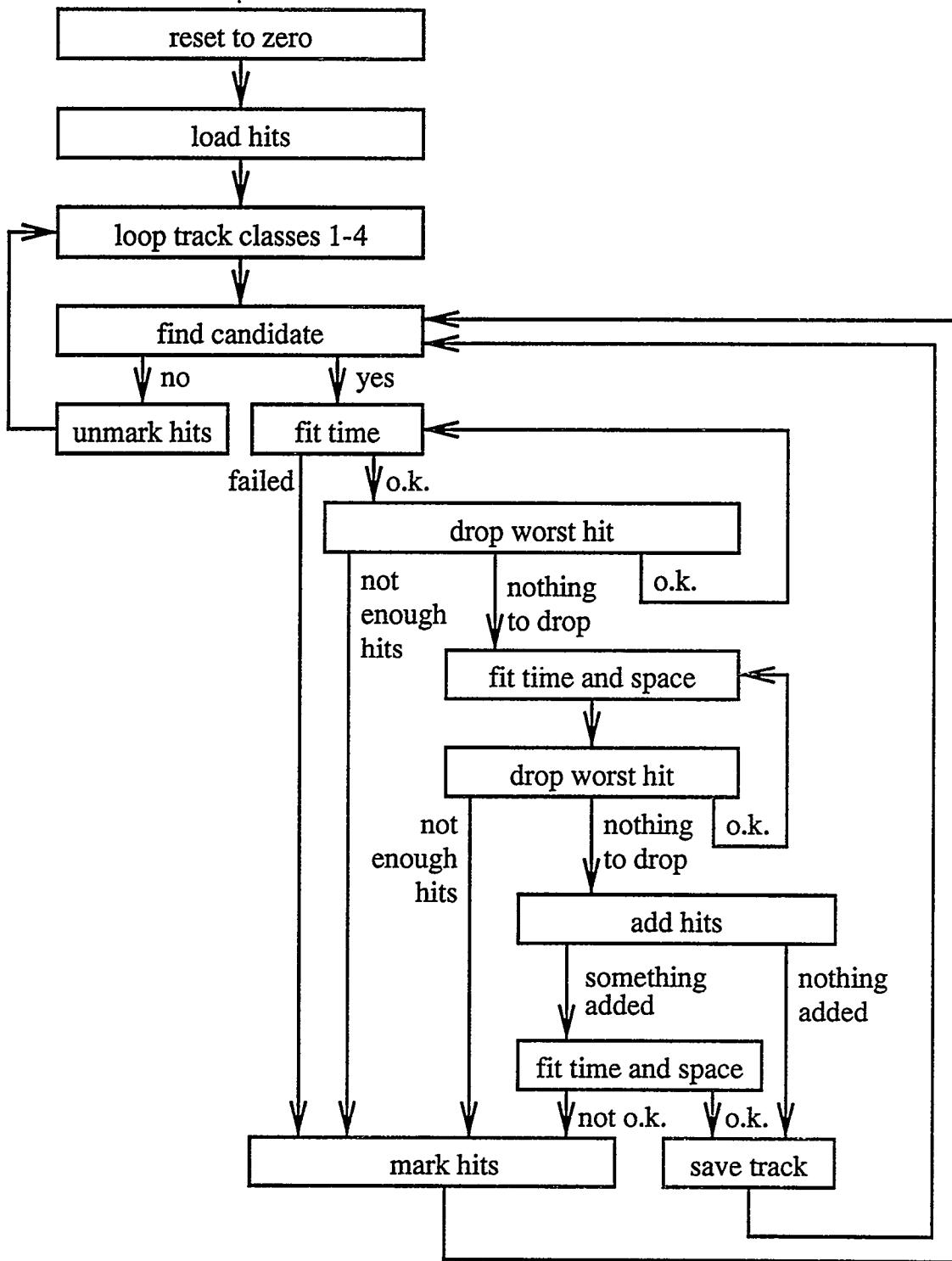
Figure 24 Flow chart for the top tracking routine. See text for details.

4.7.1.5 Selecting hits: trk_find

The subroutine considered only hits which were not yet included into a track or which were not yet marked as unusable for the current track class.

For **class 1**, the subroutine checked for each Čerenkov 1 hit whether a Čerenkov 2 hit was close in time ($\chi_i^2 \leq 16$), and then looked for a shower cluster within 4σ. If successful, the program also added all hodoscope hits with $\chi_i^2 \leq 16$.

For **class 2**, the program started in the same way. However, after choosing Čerenkov hits, it first added the hodoscope hits, then the shower counter hits, if any. Similarly, **class 3** tracks were first built by browsing through the shower cluster hits and adding Čerenkov and hodoscope hits at nearby times.

Finally, the program looked for hits with similar times slots. If there were at least as many as necessary for a **class 4** track, it tried to build a track from these hits.

4.7.1.6 Saving the track: trk_copy

After the code decided on the final track, it checked whether the track passed the requirements of a previously used track class. For example, consider the case that the program already finished the loop for class 1 tracks and was currently looking for class 2 tracks. If the current track contained not only two Čerenkov and (at least) four hodoscope hits, but also one shower counter event, the track was reclassified as a class 1 track.

After verifying that the track pointed in a reasonable direction, the momentum and position at the target were reconstructed using the information about the spectrometer magnets. The algorithm traced the track back to the $y = 0$ position at the target. This means that no error in the y-position of the track was assumed. The information about the track was then written to a common block and the hits on the track were marked as being included in a track so that they would not be included in another track.

4.7.1.7 Target Constraint

The tracking program was able to add a fictitious hodoscope hit when the fitting a track to a set of hits. This hit was assumed to be a hit in an x-hodoscope located at the target ($z = 0$ in spectrometer coordinates) and ensured that the track pointed close to the target. Due to the presence of the quadrupole magnet in the 4.5° spectrometer, no target constraint was used in the analysis of that spectrometer's data. The 7° data were fit with a target constraint centered at $x = 0$ with a spatial resolution of 25 mm. A target constraint in the y-direction would have been unnecessary since the program to reconstruct the track position at the target assumed that track originated at $y = 0$ exactly.

4.7.2 Tracking Efficiency Studies

An important question is, how well the tracking program was able to find tracks, or in other words, how often does it happen that there were electrons or pions passing through the detector, while the tracking program did not find a track. We consider here the following questions:

(1) How efficient was the whole detector? The shower counter and the Čerenkov ADCs identified many events as electrons. For how many of these events did the tracking system (Čerenkovs, hodoscopes, shower counter, electronics and tracking program) find tracks? Missing tracks may have been caused in this case by different problems, for example by missing hodoscope hits.

(2) How efficient was the tracking program itself? If the counters provided enough good hits, did the program also find a track?

(3) How efficient was the E143 tracking system compared to the E142 system? E143 used one additional plane, and the detectors in the 7° hut were farther away from the magnets than for E142. Did this improve the performance significantly? Or was an improvement in performance due to less noise coming from the target? (E142 had a thinner target, a higher current and therefore more noise from the target holders.)

The overall efficiency, *i.e.*, for the whole detector, was determined by looking at events with the MAIN-TRIGGER, a neural network response of at least 0.95, and a Čerenkov ADC measurement of at least 25. Then it was checked whether the event also had a track within 10 ns and 62 mm of the cluster. For the 4.5° spectrometer, the inefficiency was 9.2%, for the 7° spectrometer 3.5%.

If removing plane 1 from the analysis, the situation of E142 was approximated where plane 1 was not installed. For the same requirements as before, the overall inefficiency became slightly worse: For the 4.5° spectrometer, it increased to 9.6%, and for the 7° spectrometer to 3.7%. For comparison, E142 reported about 13% overall inefficiency for both spectrometers. The improvements for E143 might therefore have improved the efficiency. The fact that for E143 the 7° inefficiency was much lower than the 4.5° inefficiency might indicate that shifting the detectors back helped very much. During E142, a considerable number of photons were able to reach parts of the front hodoscopes. Further improvements for E143 were new gatecards and the twisted pair cables to transmit the hodoscope signals to the counting house.

For the pure tracking efficiency, the events had to satisfy several requirements in addition to the already mentioned requirements. The most important of them are: Only one cluster was allowed per trigger so that the tracking would not get confused by additional particles or ghost clusters.[15] No cluster was allowed to be at the edge of the shower counter. For each cluster, enough hits in the hodoscopes were required within the time of the cluster so that the tracking could find a track. For example, at least one hit in a front x-plane and in a front u-plane defined a good point for the track in the front part. A similar pair was necessary for the rear plane. On the other hand, if only hits in the u hodoscope were available in the front planes, but none in the x- or y-planes, no reasonable track could be found by the tracking program. The pure tracking inefficiency was determined to be 1.8% for the 4.5° spectrometer, and 1.0% for the 7° spectrometer.

---

[15] If for example triggers one and two overlapped, the ADC for trigger one might have measured energy from the particle which created trigger two, and trigger one saw two clusters. Since the cluster time was taken to be the MAIN-OR time, the second cluster in trigger one appeared with an incorrect time. Such a cluster was called "ghost cluster".

The relative resolution of the shower counter is best at high energies and is proportional to $1/\sqrt{E}$. It is therefore worse for low energy particles. The momentum resolution (via tracking), however, is better at low momentum and is getting worse with increasing momentum. The overall momentum resolution of the spectrometers is shown in Fig. 25 [97].

Momentum and Energy Resolution
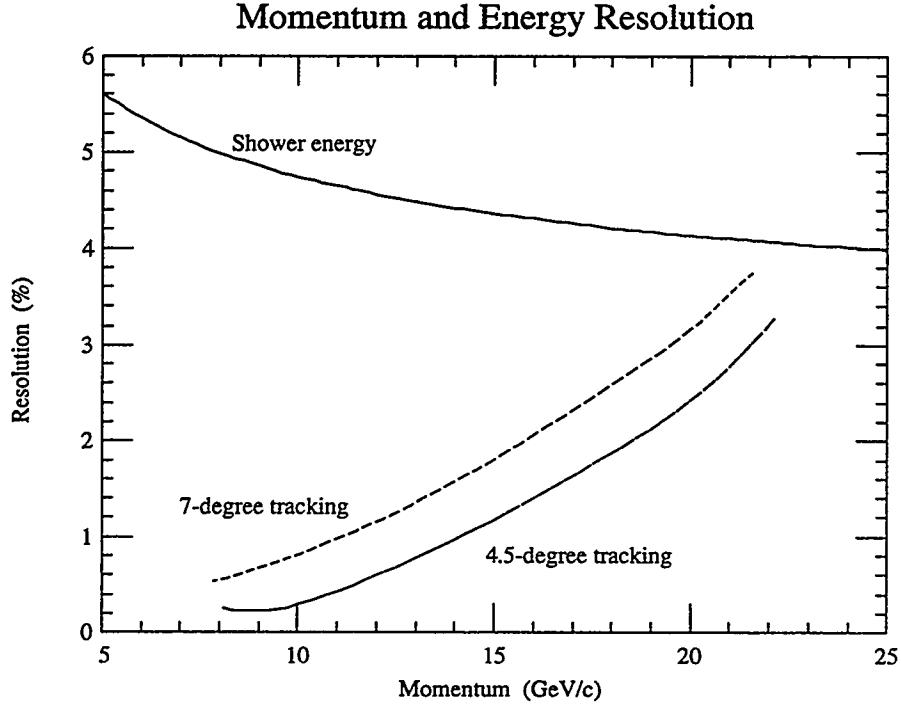
Figure 25 Momentum resolution of shower counter and tracking. Figure taken from Ref. [97].

4.7.3 Possible Improvement of Tracking Code

Two possible improvements to the tracking code were found, but implementation was too late for the analysis.

(1) A bug in the tracking prevented us from obtaining any class 4 tracks after a time of about 3200 ns. This and all the other times given here are measured relative to the common start signal for the TDCs. The spill itself lasted about 2200 ns, from about 1800 ns to 4000 ns. Since the analysis required a track and a shower cluster to be close in time and space, only very few class 4 tracks could

have been contributing to the asymmetry. If a cluster would be close in space and time, the tracking code would have included the cluster into the track, raising the class from 4 to 3. A similar argument applies to the Čerenkov hits. Also, a cut-off at 3200 ns is not causing any false asymmetry, only a loss in statistics. The effect of this bug is therefore negligible [98].

(2) The second problem involves the target constraint. As described earlier, the tracking program added a fictitious hodoscope hit when fitting a track to a group of 7° hits. This hit helped to point the track to the target. After the DST2 production, it was realized that a slight target constraint of 100 mm resolution centered at $x = 0$ would also have improved the efficiency of the tracing code at the 4.5° spectrometer.

(3) Not directly connected to the tracking code, but to the reconstruction of the momentum from the known track coordinates was the following problem: The so-called reverse matrix elements which were used to trace any track back through the spectrometer magnets to the target also depended on the sign and size of the target field through which any particle traveled right after the interaction. Since the sign of the target field was changed several times during the experiment, separate matrix elements for each case were made. However, the same matrix elements were used for the positron runs as for the electron runs (see page 82). Instead, positron runs should have used the matrix elements for electron runs with opposite target field. In other words, the same matrix elements could be used as long as all magnetic fields, not only the spectrometer magnet fields, changed their sign. Checking the influence of this error showed that it changed the analysis very little. This error is therefore neglected [99].

4.8 From Counts to Asymmetries

Using the rates of good electron events (= scattered particles per number of incoming electrons) for beam of left and right handed helicity, N_L and N_R, we formed the asymmetries $A_\parallel$ and $A_\perp$:

$$A_\parallel \,(\text{or } A_\perp) = \frac{1}{f P_b P_t} \frac{N_L - N_R}{N_L + N_R}. \tag{143}$$

Here f is the dilution factor (see later); P_b and P_t are the beam and target polarizations. Additional corrections are not mentioned in the formula for sake of simplicity. They will be described below. For the calculation of the kinematical variables x and Q^2, the momentum of the track was used, not the energy of the associated cluster.

4.8.1 Cuts used in Selection of Events

While reading back the data summary tapes, each spill and each event was judged by its characteristics to decide whether to keep it or not. The spill cuts made sure that the beam was acceptable during the spill, while the event cuts tried to select good electron events without bias and without cutting out too many electron events. The standard cuts applied for most results presented in this dissertation are described in this section. In order to check for systematic errors, these cuts were sometimes modified.

4.8.1.1 Beam Cuts

Some of the beam cuts were determined for each run during the analysis run by cumulatively calculating the mean and standard deviation. These means and standard deviations were then used to decide which spills were "average", *i.e.*, should be accepted, and which should be rejected. Due to the nature of the cuts, they were also called "dynamic cuts". The means and standard deviations were continuously updated, and were allowed to shift during the run. For each run, histograms with the distribution of the beam quantities and their cuts were obtained

111

and checked to make sure that the cuts made sense. Runs, in which beam cuts shifted significantly, were not included in the analysis. Of course, none of the first few hundred spills were accepted for the analysis because at that time the mean and standard deviations were still calculated with very limited statistics. For the 16 and 9 GeV data, some cuts were less tight to take the spread of the beam due to multiple scattering into account. The beam cuts were as follows:

- The **polarization bit** had to agree with the predicted bit. If the bits did not agree (like after checkpoints), no spills were accepted until the new seed (33 bits) was obtained and checked (next 33 bits).

- The **beam current** had to be within $\pm 0.75 \times 10^9$ e^-/spill of the mean beam current. In addition, no spills with less than 0.5×10^9 e^-/spill were accepted. (See Fig. 26).
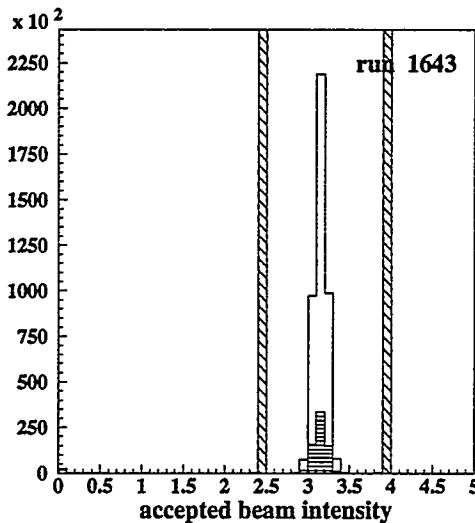
Figure 26 Distribution of beam charge for typical run. Unhatched is the distribution of the charge for all accepted spills. Horizontally hatched is the distribution of the charge for not accepted spills (not accepted because of not meeting any requirement). The cuts are shown diagonally hatched. The cuts themselves had a distribution since they were calculated during the analysis from the earlier analyzed spills.

- The **good spill** was not allowed to be more than 1.75 times the mean or less than half the mean. (See left side of Fig. 27.)

- The **bad spill** value was not allowed to be bigger than three times the mean. For some runs, the bad spill had a long tail causing the mean of the bad spill to

112

be relatively high. A strict cut was therefore additionally in place, not allowing any spill with a bad spill value of more than 150 units. (See right side of Fig. 27.) [For the 16 and 9 GeV data, the only restriction on the bad spill value was a strict upper limit of 700.]
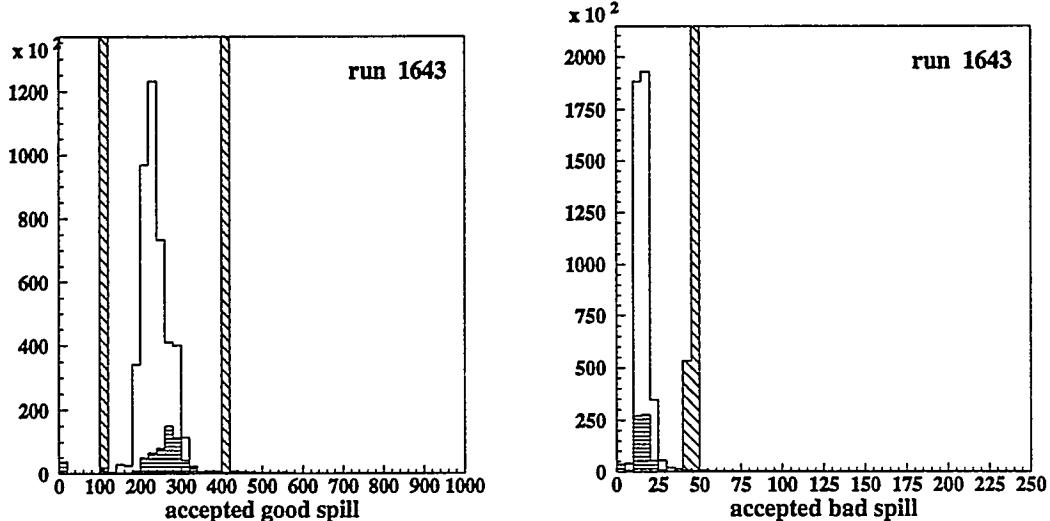
Figure 27 Good (left) and bad (right) spill values and the cut values for a typical run. See Fig. 26 for further explanations. The picture to the right indicates that the cut shifted slightly during the analysis of the run.

- The **beam width** was required to be within three sigmas of the mean of the beam width. In addition, no spills in which the beam width had a radius of less than 0.5 mm or of more than 5 mm [14 mm for 16 and 9 GeV data] was allowed.[16] (See left side of Fig. 28.)

- The **raster position** had to be within 12 mm of the center of the target, assuming that the target was centered at the center of the foil array. Furthermore, the raster position was not allowed to be farther than 12 mm [14 mm for 16 and 9 GeV data] from the mean of the raster positions. These two cuts therefore would be the same if the beam was really centered on the origin of the foil array. But if the beam drifted, causing the beam not to be in the average around the center of the foil array, the two cuts affected different spills. (See right side of Fig. 28.)

---

[16] Due to the spread of the beam, the dimensions at the foil array were slightly larger than at the target. Any dimensions reported here refer to the foil array measurements.

113
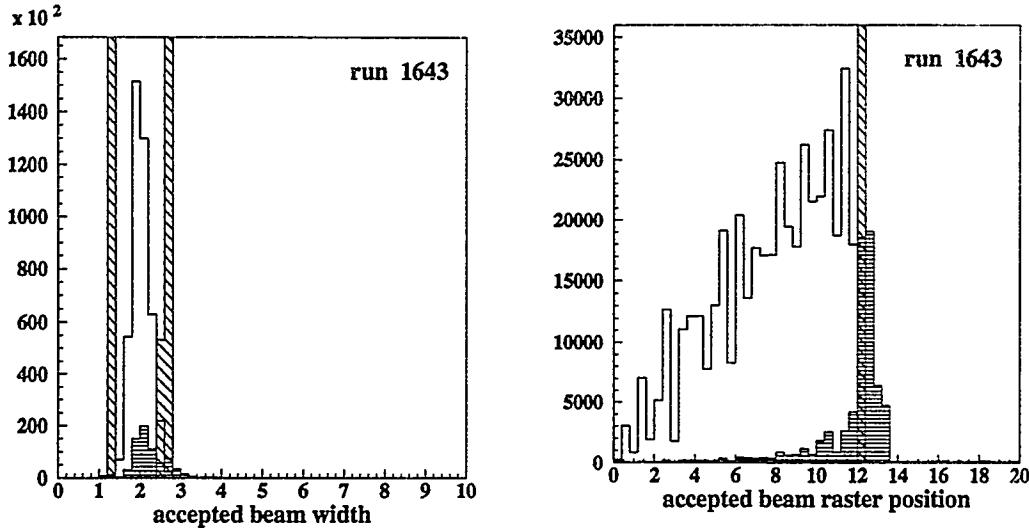
Figure 28 Distribution of beam width and beam raster position (distance from center) for typical run. See Fig. 26 for further explanations. The picture to the right shows the distribution of the distance between the raster position and the foil-array center. A linear rise with distance is therefore expected, as well as spikes due to the distinct raster positions. The picture also clearly how all the spills with a raster position outside the 12 mm radius were excluded from the analysis, as well as some more which were inside the 12 mm circle.

Only if the spill passed all these requirements, it was accepted for the analysis, and the charge of the spill (number of electrons) was added to the total charge for the run.

4.8.1.2 Event Cuts

For the cuts on the single events, first tracks and clusters had to be associated with each other. This was necessary, since the code did not write out which cluster was part of which track. The track position at the shower counter was first obtained. Then the time and position differences for cluster and track pair were calculated, and the combined χ^2 obtained. For each cluster, the track with the lowest χ^2 was selected. Still, even though this track was then the best-fitting track, it still could be far off in time or location. Special cuts took care of this problem as described below. After the track/cluster association, the cluster/track pair had to pass all of the following cuts.

114

- Each event had to be a MAIN-TRIGGER event: For each MAIN-OR trigger, the time was recorded, as well as which triggers were set to true when the MAIN-OR was true. Each cluster event also was associated with the MAIN-OR number (1, 2, 3, or 4), and this allowed the program to associate the MAIN-OR time with the cluster event. Hence, the program was able to check the type of trigger for each cluster event. And this cut required that for this cluster the MAIN-TRIGGER was on.

- The center of the cluster was not allowed to be within one of the edge blocks of the shower counter. The energy calibration of these edge blocks was difficult and possibly not very accurate. In addition, a high probability existed that the shower counter did not record all of the energy of the event if the particle entered the shower counter at one of these edge blocks.

- At the shower counter position, track and cluster had to be within 40 mm in both horizontal and vertical direction (Figs. 29 and 30), and within 10 ns in time (Fig. 31).

- The track had to point at least to within 13 mm of the target (in spectrometer coordinates). (See Fig. 32).

- Both Čerenkov ADCs had to have values of at least 40 (see Fig. 21), hence cutting out pion events which created only a small signal in the Čerenkov gas.

- The neural network had to return at least a value of 0.9 for the cluster. This cut was neglected for the 9 GeV and 16 GeV analysis, where the pion contamination was negligible.

- The E/p ratio had to be within 0.8 and 1.25. Here E is the energy of the particle deposited into the shower counter, and p the momentum as measured by the tracking system. As mentioned above, the track momentum p, not the cluster energy E was used to calculate the kinematic variables x and Q^2 of the event.
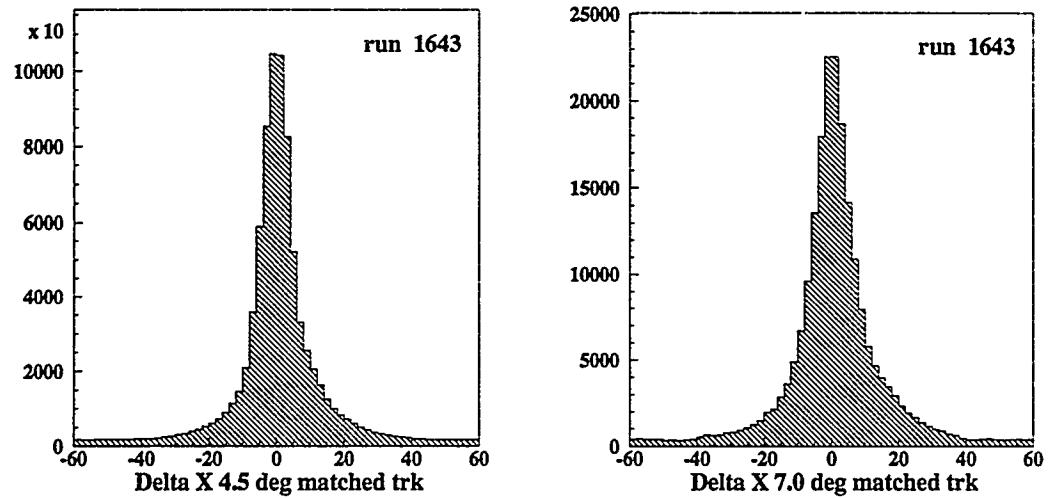
Figure 29   Distributions of differences between the track x-position and shower cluster x-position of best-matched track-cluster pairs.
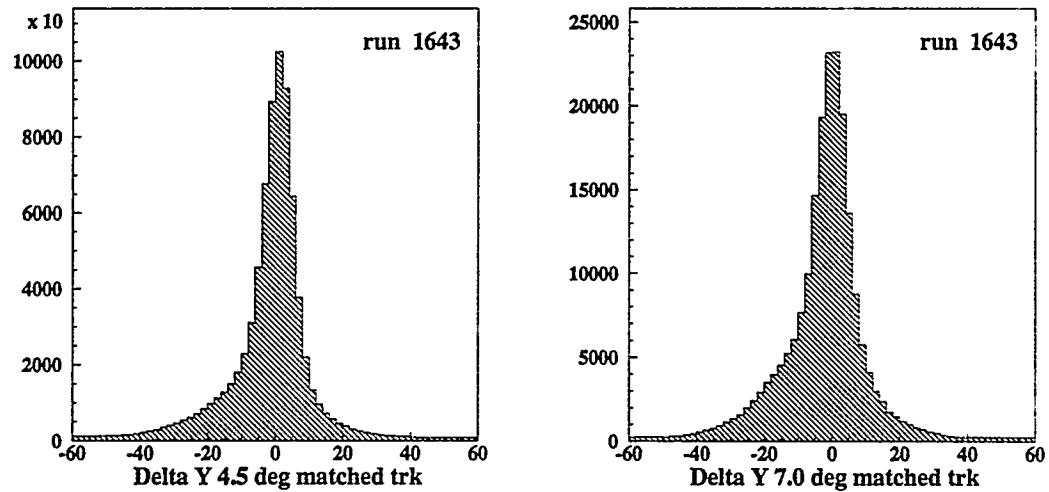
Figure 30   Like Fig. 29, but for distributions in y.
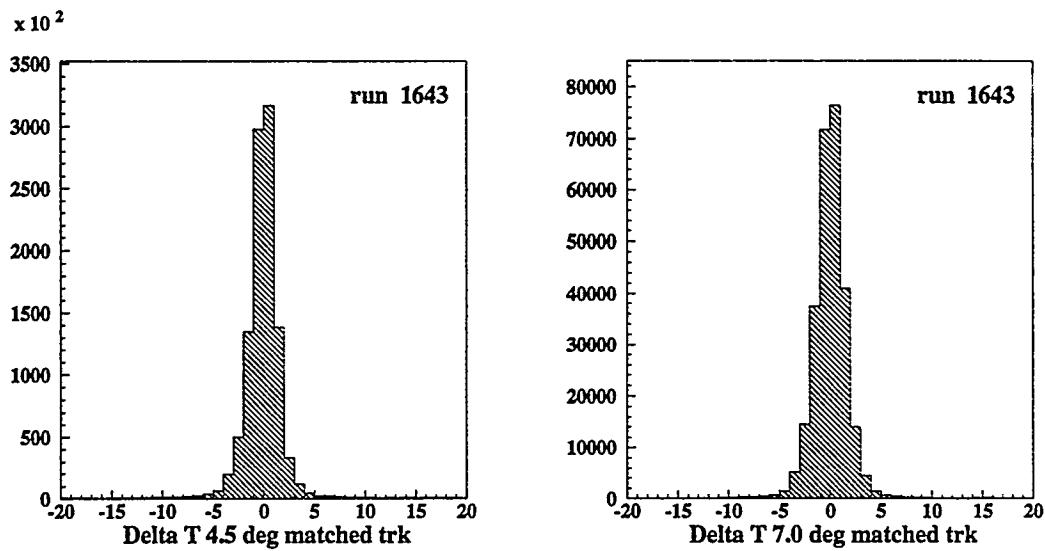
Figure 31 Like Fig. 29, but for time distributions.
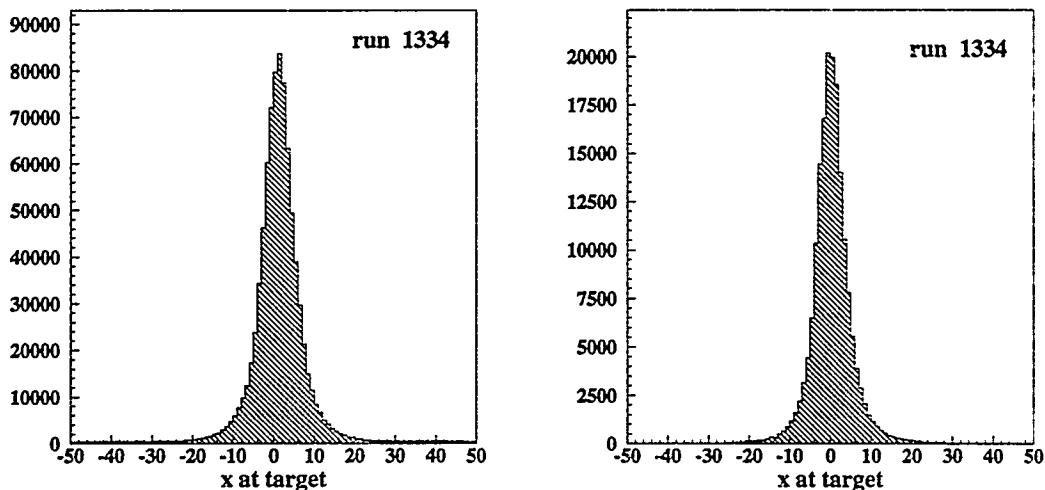
Figure 32 Distributions of the x-coordinate at the target (in spectrometer coordinates). The distributions are shown for a typical run. To the left is the distribution for 4.5° spectrometer, to the right is the distribution for 7° spectrometer.

117

4.8.2 Dead-Time Correction

The data acquisition system was not able to detect all particles. Once the MAIN-OR was triggered, it was not able to trigger again on any signal arriving within the following 32 ns. Also, only the first four MAIN-OR signals of each spill could be analyzed by the ADC modules.[17] For illustration let us consider the measurement of $A_{\parallel}$ at large x values. The cross-section is here bigger for spills with antiparallel beam and target helicities than for spills with parallel helicities. Exactly this difference led to our measured asymmetry. But spills with more events (helicity antiparallel) had a bigger dead-time and therefore relatively more events were lost than for spills with less events (helicity parallel). The dead-time effect therefore reduced the measured asymmetry, and the dead-time correction corrected for this reduction.

While analyzing each run, the number of spills N_i with $i = 0, 1, 2, \ldots 16$ or more triggers were recorded (from TDC measurements). Practically no spill had 12 or more MAIN-ORs, therefore the upper limit of 16 hits per spill was sufficient. The measured number of fully recorded MAIN-OR events was

$$N_{\text{meas}} = \sum_{i=0}^{16} \bar{i} N_i, \tag{144}$$

where $\bar{i} = i$ for $i \leq 4$ and $\bar{i} = 4$ for $i > 4$.

The real number of MAIN-OR events for this run were then estimated via a matrix P obtained from a simple Monte Carlo simulation. It was assumed that the triggers were randomly distributed within the spill time of 2.2 μs, that the dead-time was 32 ns, and that not more than 16 triggers appeared within the spill. The matrix connected the number of real events with the number of measured events. For example, the matrix elements $P_{n,m}$ stood for the probability that n real triggers lead to m measured triggers. Of course, $\sum_{m=1}^{n} P_{n,m} = 1$. From this, we were able to estimate the total number of real events:

$$N_{\text{real}} = \sum_{n=1}^{16} n \sum_{m=1}^{16} N_m P_{n,m}^{-1} \tag{145}$$

---

[17] Strictly speaking, this "four-per-pulse" limitation was not due to dead-time problems, but we still include it under the name "dead-time".

The dead-time coefficient was then

$$d = \frac{N_{\text{real}}}{N_{\text{meas}}} > 1.$$

(146)

Separate dead-time corrections d_L and d_R were calculated for each run, spectrometer and beam polarization sign, and were applied to the recorded number of events N_L^{raw} and N_R^{raw} per x and Q^2 bin. Dividing then by the charge Q_L and Q_R of the incoming electrons, one obtained the rates N_L and N_R from Eq. (143):

$$N_L = \frac{d_L N_L^{\text{raw}}}{Q_L} \quad \text{and} \quad N_R = \frac{d_R N_R^{\text{raw}}}{Q_R}$$

(147)

Fig. 33 shows the dead-times for the deuteron 29 GeV runs. The horizontal axis lists the average number of MAIN-OR triggers (as detected by the TDCs) per number of spills.
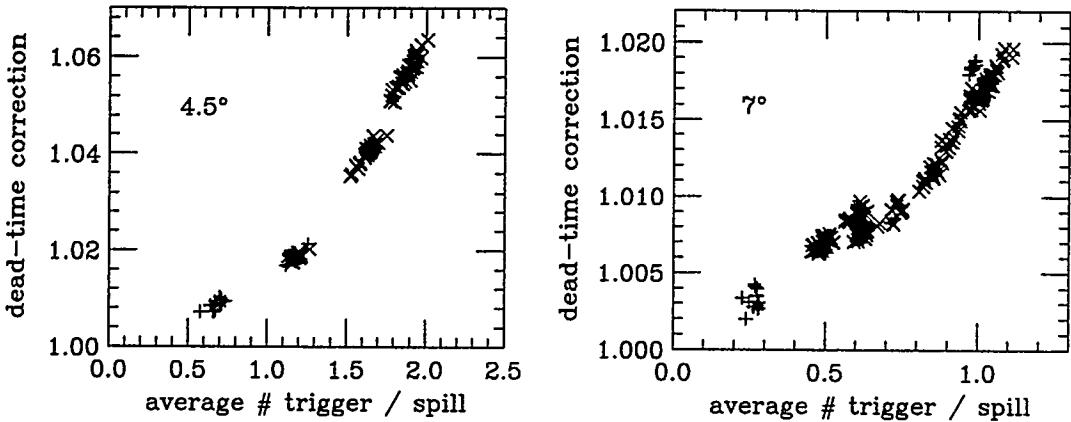
Figure 33 Dead-times for 29 GeV deuteron runs. Included are both longitudinal and transverse runs. The symbol "×" denotes electron runs, the symbol "+" positron runs. To the left are the values for the 4.5° spectrometer, to the right the values for the 7° spectrometer.

The 4.5° dead-time corrections were around $d_{L,R} \approx 1.05$, while the 7° dead-time corrections were considerably lower, around $d_{L,R} \approx 1.015$, due to the decreased rate in that spectrometer. They increased the integral of g_1 over the measured x-region by about 2% for the 29 GeV data. The positron run dead-times (with symbol + in Fig. 33) had a very low rate, but still, some of them had a high dead-time in the 7° spectrometer. No plausible explanation exists for this, but the influence of these runs on the data is negligible.

4.8.3 Dilution Factor

A large portion of the counts detected in the spectrometer did not originate from the polarizable protons or deuterons, but from other material in the target, for example the nitrogen nuclei, the liquid helium which surrounded the ammonia beads, the NMR coils, windows in the tailpiece and magnet holder, and the helium gas in the bags surrounding the magnet. The ratio of counts from the free protons or deuterons to the total number of counts is called the dilution factor f. The asymmetry was divided by this factor f to yield the asymmetry which would have been measured if the additional unpolarized nuclei would not have been present in the scattering. The dilution factor assumes that all material other than the free protons or deuterons were unpolarized. This is not quite correct, and another correction factor, the nitrogen correction, was necessary to eliminate the influence of the polarized material other than protons or deuterons (see following section). The dilution factor was obtained by knowing how much material of each kind was in the beam and by knowing the cross-sections for each type of material.

The cross-sections were determined in the following way: The dimensions of the components were measured and their density obtained. The number of counts due to nuclei other than nitrogen or hydrogen were proportional to:

$$\frac{\rho l (N_p \sigma_p + N_n \sigma_n) g_{\text{EMC}}(x, A)}{A} \tag{148}$$

Here ρ stands for the density of the material, l for the length, N_p for the proton number, N_n for the neutron number, and A for the mass number of the nucleus. σ_p and σ_n are the cross sections for proton and neutron. g_{EMC} is the EMC effect coefficient, taken at the Bjorken x of the current bin and at atomic mass number A.

The fractional amount of ammonia was expressed via the packing fraction p_f which is the percentage of the volume occupied by ammonia beads in the target cell. The other space in the target cell was filled by liquid helium. Therefore, the number of counts due to NH_3 and He were proportional to:

$$(NH_3) = \frac{\rho_{NH_3} l_{\text{cell}} \left[3\sigma_p + (7\sigma_p + 8\sigma_n) g_{\text{EMC}}(x, 15) \right] p_f}{A_{NH_3}} \tag{149}$$

$$(\text{He}) = \frac{\rho_{\text{He}} l_{\text{cell}} (2\sigma_p + 2\sigma_n)(1 - p_f)}{A_{\text{He}}} \qquad (150)$$

Finally, the dilution factor was expressed by

$$f = \frac{\rho_{\text{NH}_3} l_{\text{cell}} 3 p_f / 18}{(\text{NH}_3) + (\text{He}) + \sum \text{others}} \times \frac{U_{\text{NH}_3}}{U_{\text{all}}} \qquad (151)$$

with U_{NH_3} standing for the radiative correction for ammonia and U_{all} for all material together. The ratio F_2^n / F_2^p (obtained from Refs. [10] and [11]) was used as σ_n / σ_p.

The packing fraction was crucial for the correct determination of the dilution factor. It was estimated through an analysis of the rates as well as through an analysis of X-ray attenuation measurements before and after the target stick was used in the End Station [100] [101] [102]. The results from the rate analysis turned out to be more reliable and were therefore used for the analysis described in this dissertation (Table 11).

Table 11 Packing fraction p_f used for the analysis. The different sets were numbered by the insert number. For one run period, only $^{15}\text{NH}_3$ was used as target material.

	insert #	used for run #	p_f
$^{15}\text{NH}_3$	1	≤ 1205	0.665 ± 0.000
	2	$1206 - 2289$	0.643 ± 0.017
	3	$2290 - 2481$ & $2818 - 3378$	0.588 ± 0.010
	4	$2482 - 2817$	0.570 ± 0.043
	5	$2482 - 2817$	0.574 ± 0.040
$^{15}\text{ND}_3$	1	≤ 1205	0.502 ± 0.000
	2	$1206 - 2289$	0.632 ± 0.012
	3	$2290 - 2481$ & $2818 - 3378$	0.600 ± 0.012

Since the unpolarized cross-sections depended on the parameters x and Q^2, and the EMC effect on x, the dilution factor was calculated separately for each run and each x bin using the mean x and Q^2 as given by the events in that bin. In addition, the packing fractions changed with each change of target material. For the target material NH_3, the dilution factor was around 0.16, for ND_3, it was around 0.23.

This means that for ND_3 targets, only one in four counts originated from deuterons, and for NH_3 targets only one in six. Fig. 34 shows on the top the results versus x for all proton runs (left 4.5°, right 7°), and on the bottom for all deuteron runs used in the analysis. The x range extends down to $x = 0.02$ for the 16 GeV data. Also the 9 GeV data were included. In each picture, distinct groups of lines are visible, corresponding to targets with different packing fractions. The shape of each line depends on the EMC effect and the cross-sections. The average x and Q^2 of each run was used to calculate the dilution factor. Depending on the actual sample of electrons during the run, the x and Q^2 differed slightly within the bins, causing small deviations within the groups of lines.
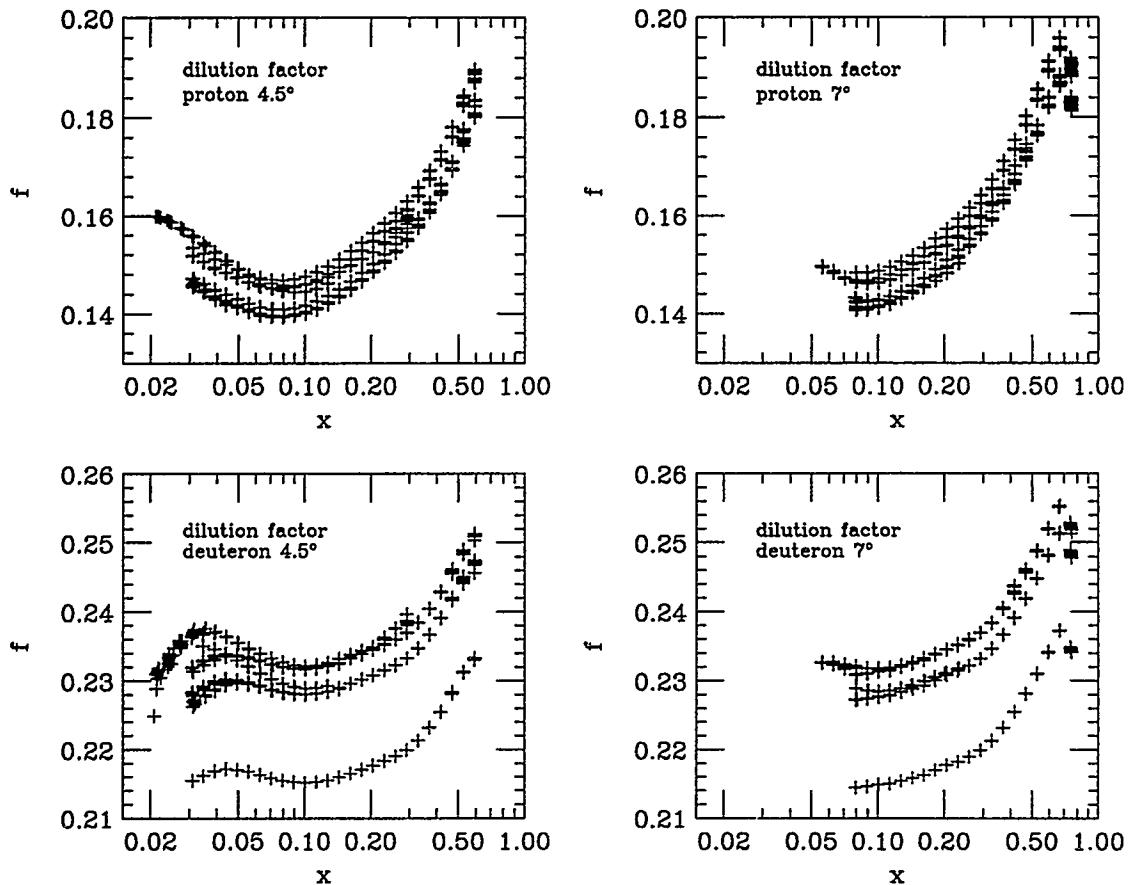
Figure 34 Dilution factor for all runs. On the top proton runs, on the bottom deuteron runs. 4.5° spectrometer on the left, 7° spectrometer on the right. The parallel lines are due to distinct packing fractions for different sets of target material.

4.8.4 Nitrogen Correction

Besides the protons in $^{15}NH_3$ and the deuterons in $^{15}ND_3$, also other polarizable nuclei were in the target: The ^{15}N itself was polarizable, it was contaminated with ^{14}N ($\approx$ 2%), and the deuteron was contaminated with protons ($\approx$ 1.5%). The additional protons in $^{15}ND_3$ were also referred to as "residual protons". All electrons scattered from polarized nuclei contributed to the measured asymmetry. The nitrogen correction compensated for this effect coming from the nitrogen nuclei and residual protons in the target.[18]

The biggest factor in the nitrogen correction was the polarization of ^{15}N. An ^{16}O nucleus has an equal number of protons and deuterons, which pairwise add up to spin zero and therefore to zero magnetic moment. Removing one proton from such a nucleus, leads to ^{15}N with a magnetic moment approximately equal but opposite in sign to the proton magnetic moment. Scattering from such a nucleus involves the proton asymmetry. Therefore, the deuteron asymmetry has to be corrected with the proton asymmetry, and this dissertation also had to analyze the proton data.[19]

The Equal Spin Temperature (EST) Hypothesis (see page 60) suggests that in a polarizable composite material the spin temperature of every element is the same. The polarization of the different elements are then related to each other via the value of the magnetic moment. Knowing the polarization of the deuterons would then lead us to the polarization of ^{15}N. Since experiments suggested that the EST hypothesis does not hold for N^{15} [74], the polarization of ^{15}N and the residual protons was measured separately after the experiment by selecting a slightly different resonance frequency. For the target material $^{15}NH_3$, the following fit was used to express the ^{15}N polarization P_N in terms of the polarization of the protons P_t:

$$P_N = 0.136\,P_t - 0.183\,P_t^2 + 0.335\,P_t^3 \qquad (152)$$

---

[18] The fact that the material of the target cup, Torlon, also contained protons which become polarized, is here not important, since nothing of the target cup was inside the beam. It, however, affected the NMR measurement. The end caps of the target cup, $i.e.$, the part inside the beam, was made out of aluminum.

[19] Of course, when combining the proton and deuteron results to obtain g_1^n or $g_1^p - g_1^n$, the proton results also have to be known.

For example, if the proton polarization of the ^{15}NH$_3$ target was 70%, the nitrogen nuclei were then polarized to about 12%. For the target material ^{15}ND$_3$, the ^{15}N polarization, P_N, was expressed as

$$P_N = -0.40 P_t, \qquad (153)$$

P_t being the polarization of the deuterons. The residual proton polarization was expressed as:

$$
\begin{aligned}
P_p &= \ 0.191 + 0.683\ P_t && \text{for } P_t > 0.16 \\
&= \ 1.875\ P_t && \text{for } P_t \le 0.16
\end{aligned}
\qquad (154)
$$

In a 30% polarized ^{15}ND$_3$ target, the ^{15}N nuclei were then polarized to about 12%, while the residual protons were polarized to about 40%. The polarization of ^{14}N was inferred from the measured ^{15}N polarization assuming that the polarization was equal and opposite in sign to the one of ^{15}N.

Let A_{nc} be the uncorrected asymmetry, A_{c} the corrected. The formula for the correction to the **proton** asymmetry is [103]:

$$A_{\mathrm{c}}^p = [1 + C_p]\, A_{\mathrm{nc}}^p \qquad (155)$$

with

$$C_p = -\frac{1}{3}\frac{1}{3}\frac{P_N}{P_t} g_{\mathrm{EMC}}(x, 15). \qquad (156)$$

Here P_N and P_t stand for the N^{15} and proton polarization. $g_{\mathrm{EMC}}(x, 15)$ is the correction for the EMC effect taken at atomic mass number 15. The first factor $-\frac{1}{3}$ comes from Clebsch-Gordan coefficients involving the nitrogen wave function. The second factor $\frac{1}{3}$ reflects the fact that ammonia has three hydrogen atom for each nitrogen atom. The error on the term C_p was estimated to be about 0.2 relative. The contribution of ^{14}N to the asymmetry was neglected here. If the radiative corrections were added to A_{c}^p, we obtained the full asymmetries $A_{\parallel}^p$ and $A_{\perp}^p$.

For the **deuteron** asymmetry, the correction was more complicated, since the proton asymmetry had to be used as one of the inputs. Here

$$A_{\mathrm{c}}^d = C_1 \left(A_{\mathrm{nc}}^d - C_2 \right) \qquad (157)$$

124

with

$$C_1 = \frac{1}{1 - \eta_p + D_n/\gamma} \quad \text{and} \quad C_2 = \frac{U_p F_2^p}{U_d F_2^d}(D_n - D_p)(A^p - R_p). \tag{158}$$

A^p is the final proton (Born) asymmetry $A_{\parallel}$ or $A_{\perp}$. Subtracting from it the radiative correction to the asymmetry R_p, leads again back to the radiated asymmetry [which is equal to A_C^p in Eq. (155)]. U_p and U_d are the radiative corrections to the unpolarized cross-sections. The remaining factors are defined as

$$\eta_p = \frac{\text{number of protons}}{\text{number of deuterons} + \text{number of protons}}$$

$$D_n = \eta_N \frac{P_N}{P_D} \frac{g_{\text{EMC}}(x, 15)}{9}$$

$$D_p = \eta_p \frac{P_p}{P_D} + (2\eta_N - 1)\frac{P_N}{P_D} \frac{g_{\text{EMC}}(x)}{9} \tag{159}$$

$$D_n - D_p = \frac{P_N}{P_D} \frac{g_{\text{EMC}}(x)}{9}(1 - \eta_N) - \eta_p \frac{P_p}{P_D}$$

$$\text{where} \quad \eta_N = \frac{\text{number of } {}^{14}\text{N}}{\text{number of } {}^{14}\text{N} + \text{number of } {}^{15}\text{N}}$$

$$\frac{P_p}{P_D} = \frac{\text{polarization of proton}}{\text{polarization of deuteron}}$$

$$\frac{P_N}{P_D} = \frac{\text{polarization of } {}^{15}\text{N}}{\text{polarization of deuteron}}$$

$$= -\frac{\text{polarization of } {}^{14}\text{N}}{\text{polarization of deuteron}} < 0.$$

During the analysis, $A_{\parallel}^d$ was corrected with $A_{\parallel}^p$, and $A_{\perp}^d$ was corrected with $A_{\perp}^p$. Fig. 35 shows both $A_{\parallel}^p$ and $A_{\perp}^p$.

4.8.5 Background Subtraction: Pions and Electrons from Pair Production

Although the detectors were designed to distinguish between electrons and other particles, especially pions (π^-), some background from misidentification still remained. In addition, electron and positron pairs were created from decay photons

125
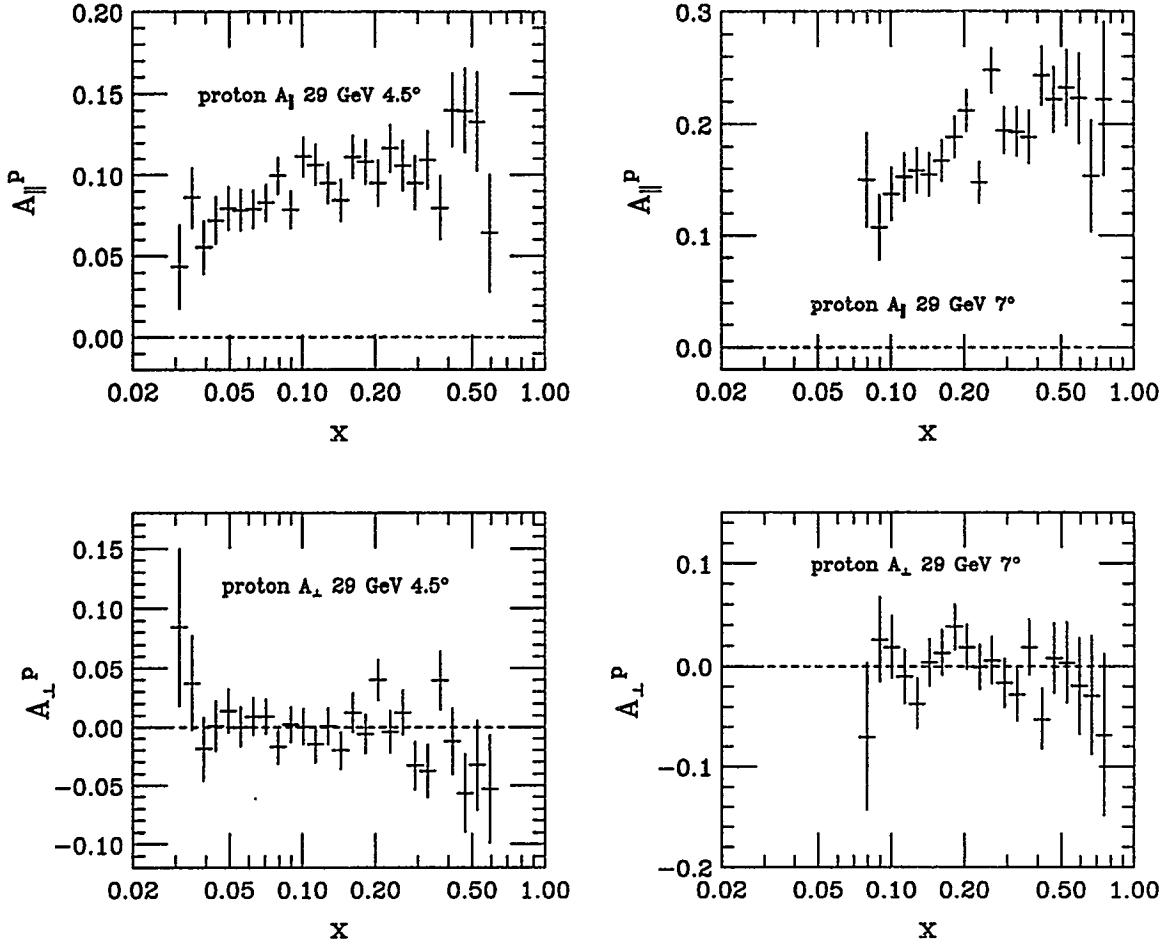
Figure 35 $A^p_\parallel$ and $A^p_\perp$ for 29 GeV as used for the nitrogen correction. None of the high-x bins were combined.

of π^0 particles. Both the pions and electrons from π^0 decay had no asymmetry. Therefore the measured asymmetry would be diluted, if no correction is applied. To minimize the influence of both the misidentified pions and the electrons from pair production, some run time was spent on spectrometer settings at exactly the opposite momentum, *e.g.*, +11.5 GeV instead of −11.5 GeV. These runs were called "positron" or "pion" runs. In this way, only π^+ and e^+ were recorded. As seen in Fig. 36, up to 10% of the events in the lowest x-bin came from this background. We assumed that the production of π^+ was as likely as the production of π^-, as well as that as many electrons from pair production were detected in the negative spectrometer setting as positrons from pair production were detected in the positive spectrometer setting.
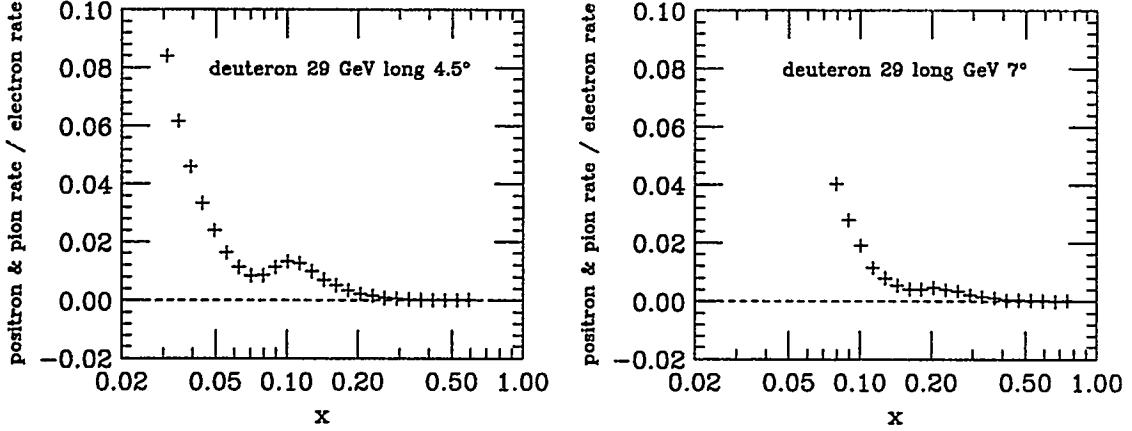
Figure 36 Ratio of pion to electron rate versus x. The pion rate was measured with opposite spectrometer settings and included both pions (π^+) as well as positrons from π^0 decay.

The correction was applied in the following way: For electron and positron runs, separate asymmetries were determined. The positron asymmetry A_+ was then subtracted from the electron asymmetry A_-, weighted by the rates $N_{+,-}$ (number of events per incoming charge) for positron and electron runs:

$$A = A_- \frac{N_-}{N_- - N_+} - A_+ \frac{N_+}{N_- - N_+} \tag{160}$$

This approach is mathematically practically equivalent to directly subtracting the rates, but is more exact since it takes into account that positron runs might have different target or beam polarizations than electron runs. Figs. 37 and 38 show the pion and pair-production asymmetries for the proton and deuteron at 29 GeV in the longitudinal setting. We see that the pion asymmetry is consistent with zero within our error bars.

No runs with reversed spectrometer settings were taken at beam energy 16 GeV for the higher momentum setting (see Table 7). However, the pion contamination was larger at the low x-bins which were not covered by the 16 GeV high-momentum setting. Furthermore, all 16 GeV runs were analyzed together. Hence, the pion asymmetry from the low-momentum 16 GeV runs was applied to the combined electron asymmetry from the low- and high-momentum 16 GeV runs. In this way, the 16 GeV high-momentum data were also corrected for the pion contamination.
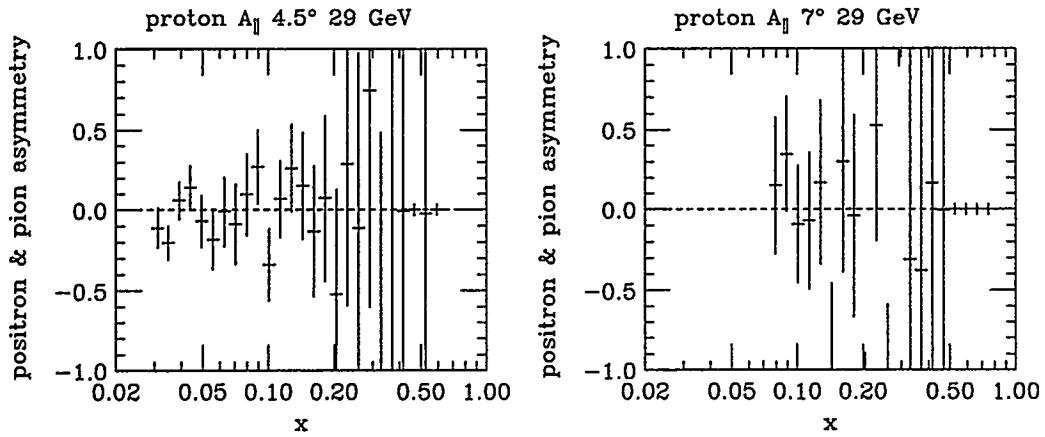
Figure 37 Pion asymmetries from 29 GeV proton data at longitudinal target polarization. The statistical error is increasing with x, as the cross-section for pion production decreases. For this reason, no asymmetry could be calculated for some of the high-x bins, marked on the plot by a cross located at zero.
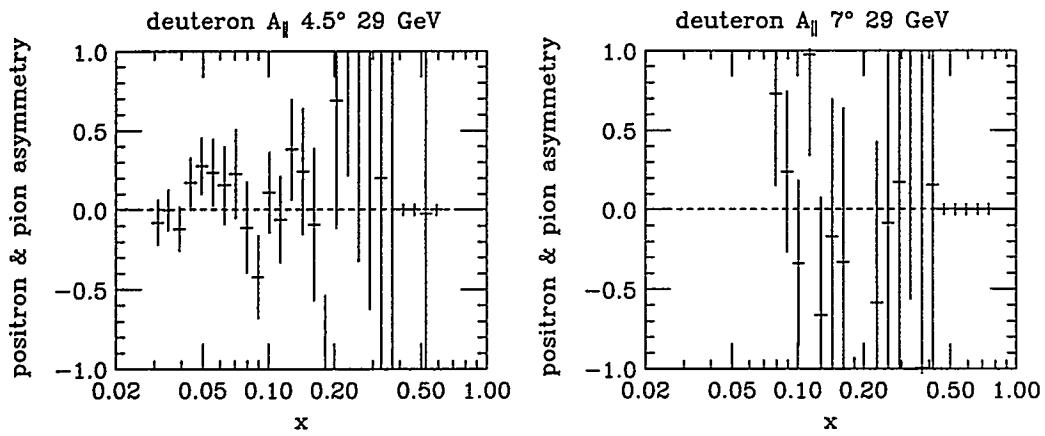
Figure 38 Same as Fig. 37, but for deuteron.

128

4.8.6 Radiative Corrections

The desired result of the experiment is a description of the scattering of leptons from nucleons like shown in Fig. 1, where only one single photon is exchanged between the electron and the nucleon. The interaction with the exchange of only one particle is called the "Born"-term. In reality, however, the interaction of the electron with the photon is more complicated. For example, a particle-antiparticle loop within the virtual photon propagator can appear (vacuum polarization), a photon can be exchanged between the incoming and the outgoing electron line (vertex correction), a photon can be emitted from the electron line (Bremsstrahlung), or multiple soft photons can be exchanged between electron and nucleon. Since Quantum Electrodynamics (QED) is very well known, and since its coupling constant α is very small, a relatively exact perturbative calculation to low order permits us to correct the measurement to obtain the Born-term illustrated in Fig. 1.

The process for correcting for the above-mentioned effects is through the so-called internal radiative corrections. These account for higher order QED effects at the time of the interaction. Another important type of radiative corrections are the external corrections. They take into account the emission of photons off the electrons before or after the interaction. The energy loss due to ionization inside the material which the electrons are crossing is negligible at the E143 kinematics and was not corrected for.

The radiative effects influence our data in the following way: The experiment measured the energy and direction of the scattered electrons from which the energy of the virtual photon was inferred. Radiative effects cause the incoming and outgoing electron to lose some of its energy and cause the electron-nucleon interaction to be different from how it would be if only one single photon would be exchanged. If radiative corrections were neglected, incorrect photon momenta would be inferred from the observed electrons, and events would be placed into wrong x-bins. Radiative corrections describe this shift. Both the unpolarized cross-sections and the cross-section asymmetries had to be corrected. In both cases, the cross-sections or asymmetries were required as input. Since the asymmetries were measured in the experiment, several iterations were necessary to obtain a consistent solution.

The **unpolarized** radiative corrections were necessary for the dilution factor and the nitrogen correction and were calculated with two sets of codes, called IN-TERNAL and EXTERNAL, based on formulas from Ref. [104]. The thickness and density of each material through which the electrons traveled had to be known. Both internal and external corrections were calculated and combined to one multiplicative factor U:

$$\text{actual cross-section} \sim U \text{ Born cross-section} \tag{161}$$

Separate radiative corrections had to be calculated for the cross-sections of proton, deuteron and all material in the target. Also for the carbon and empty targets, separate cross-sections had to be determined.

The **asymmetries** were corrected in a similar way as the unpolarized cross-sections. The internal radiative corrections to the asymmetry were calculated according to Ref. [105]. They included the vacuum polarization term for leptons, the vertex correction at the electron vertex, and the Bremsstrahlung effect on the incoming and outgoing electron line. The nucleon vertex and Bremsstrahlung corrections were negligible and not considered. The cross-sections were written as a combination of polarized (p) and unpolarized (u) cross-sections:

$$\sigma^{\downarrow\uparrow} = \sigma^u + \sigma^p \qquad \sigma^{\uparrow\uparrow} = \sigma^u - \sigma^p \tag{162}$$

The internal corrections then modified the Born cross-sections in the following way:

$$\sigma^p_{\text{int}} = \sigma^p_{\text{Born}} \left(1 + \delta_V + \delta^p_{\text{el}} + \delta^p_{\text{inel}}\right)$$
$$\sigma^u_{\text{int}} = \sigma^u_{\text{Born}} \left(1 + \delta_V + \delta^u_{\text{el}} + \delta^u_{\text{inel}}\right) \tag{163}$$

Here δ_V was the correction due to the vertex and vacuum polarization (same term for the polarized and unpolarized cross-section), and δ^p_{el} and δ^p_{inel} was the correction due to the tail from internal Bremsstrahlung. The contribution from elastic and inelastic scattering were obtained separately. For the deuteron targets, the quasi-elastic scattering (scattering off a single nucleon inside the deuteron nucleus) also contributed.[20] The correction due to vacuum polarization and electron vertex was independent from the polarization of the electron and photon, while the Bremsstrahlung

---

[20] Although the nitrogen contained in the target was also slightly polarized, this was neglected for the radiative correction to the asymmetry. The nitrogen contribution to the asymmetry was corrected for in the nitrogen correction, and the dilution factor took into account the unpolarized radiative corrections for events originating from nitrogen nuclei.

corrections were different for polarized and unpolarized cross-sections because the cross sections and the Bremsstrahlung themselves depend slightly on the polarization.

Both the polarized and unpolarized internally corrected cross-sections were then externally corrected for Bremsstrahlung via the formula:

$$\sigma_{\text{ext}}(E_i, E_f, t_i, t_f) = \int \int I(E_i, E, t_i)\sigma_{\text{int}}(E, E')I(E', E'_f, t_f)\, dE\, dE' \qquad (164)$$

where $I(E, E', t)$ is the probability that an electron of energy E loses energy $E - E'$ while going through material of thickness t. The quantities t_i and t_f are the thickness of the material through which the electron traveled before and after the interaction. E_i and E_f are the measured initial and final electron energies. The radiated asymmetry was then given by

$$A_{\text{rad}} = \frac{\sigma_{\text{ext}}^p}{\sigma_{\text{ext}}^u}. \qquad (165)$$

The calculations required the asymmetries as input. For this, a Q^2-dependent fit to the 29, 16.2, and 9.7 GeV A_1 data was used with $g_2 = g_2^{WW}$ [Eq. (86)] for the contribution due to the transverse asymmetry. Iterating this calculation produced a consistent result. The additive radiative correction was then taken as $A_{RC} = A_{\text{born}} - A_{\text{rad}}$. The correction for the statistical error of the asymmetry was the multiplicative term f, which assumed that the elastic (and quasielastic) tails are background that can be treated statistically like a dilution effect. The measured asymmetry was then corrected in the following way:

$$A \pm dA \longrightarrow A + A_{RC} \pm \frac{dA}{f} \qquad (166)$$

Fig. 39 illustrates the radiative corrections on the example of the asymmetry $A_\parallel^d$. We see that for low x the asymmetry was overestimated, and underestimated for higher x, between $x = 0.2$ and $x = 0.5$. The error on the asymmetry was also underestimated for low x ($1/f > 0$), while the error did not change significantly for higher x (above $x = 0.1$: $f \approx 1$). At low x, where the asymmetry is close to zero, the relative change due to radiative correction was up to 100%. The systematic error of the radiative correction was estimated by varying the input models.

131
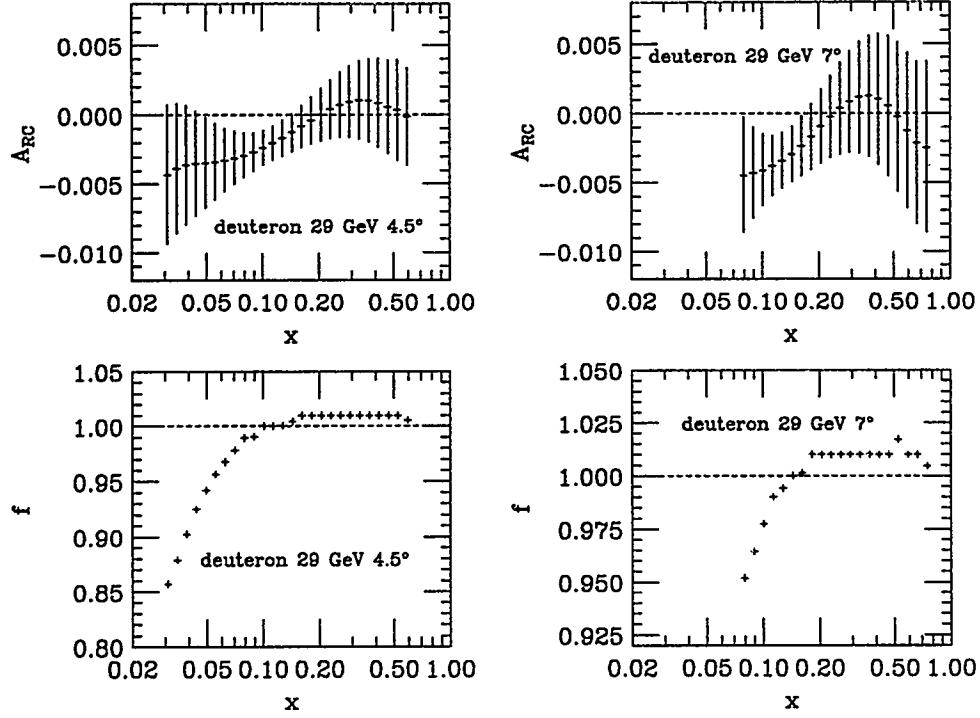
Figure 39 Radiative corrections to asymmetry $A^d_\parallel$ for the 4.5° (left) and 7°(right) spectrometer. On the top is the additive radiative correction A_{RC} with its systematic error, on the bottom is the multiplicative correction f to the statistical error.

4.8.7 Sign-change of $A_\perp$ for 7° spectrometer

As mentioned before, the transverse asymmetry $A_\perp$ is defined by

$$A_\perp = \frac{\sigma^{\downarrow\leftarrow} - \sigma^{\uparrow\leftarrow}}{\sigma^{\downarrow\leftarrow} + \sigma^{\uparrow\leftarrow}}. \tag{167}$$

The exact definition of the polarized cross-sections $\sigma^{\downarrow\leftarrow}$ and $\sigma^{\uparrow\leftarrow}$ is the following: The first arrow stands for the beam helicity with the up-arrow for the helicity pointing along, in the same direction as the beam direction. The second arrow stands for the target polarization, and here an arrow to the left notes polarization perpendicular to the beam line pointing *to the same side* as the scattered electron. In order to be consistent with this definition, we had to multiply our result for 7° $A_\perp$ by -1, which is equivalent to moving the 7° spectrometer to the other side. This

132

sign change had to be done before the radiative correction was added, since A_{RC} used $+7°$, not $-7°$ as the angle of the $7°$ spectrometer. The factor -1 appears in Eq. (24) as the factor $\cos\phi$.

4.9 From Asymmetries to Structure Functions and Integrals

Once the asymmetries $A_\|$ and (for the beam energy 29 GeV only) $A_\perp$ were extracted, the virtual photon asymmetries A_1 and A_2 could be obtained via

$$A_1 = \frac{1}{D'}\left[A_\| \left(1 + \gamma^2 y/2\right) - A_\perp \frac{\gamma^2 y}{2\tan(\theta/2)}\right] \tag{168}$$

$$A_2 = \frac{\gamma(2-y)}{2D'}\left[A_\| + A_\perp \frac{y(1+\gamma^2 y/2)}{(1-y)\sin\theta}\right]. \tag{169}$$

These equations are identical to Eqs. (51) and (52). Furthermore, the longitudinal and transverse spin-structure functions g_1 and g_2 could be calculated via

$$g_1(x,Q^2) = \frac{F_1(x,Q^2)}{D'}\left[A_\| + \tan\frac{\theta}{2}A_\perp\right] \tag{170}$$

$$g_2(x,Q^2) = \frac{F_1(x,Q^2)}{D'}\frac{y}{2\sin\theta}\left[\frac{E+E'\cos\theta}{E'}A_\perp - \sin\theta A_\|\right]. \tag{171}$$

These relations were already mentioned earlier as Eqs. (30) and (31). The ratio of the longitudinal over transverse cross-section $R(x,Q^2) = \sigma_L/\sigma_T$ was taken from a global analysis of experiments performed at SLAC between 1970 to 1985 [9], and the unpolarized structure function F_1 was obtained from both $R(x,Q^2)$ and F_2 via

$$F_1 \equiv F_2 \frac{1+\gamma^2}{2x(1+R)} \tag{172}$$

which is the same as Eq. (20) from Chapter 2. The structure function F_2 has been measured by SLAC [106] and CERN [10] [11]. For the analysis, we were using a fit to the CERN data.

If $A_\perp$ is not measured, like for our 16 and 9 GeV data, one has to make an additional assumption to obtain g_1; one might set $A_\perp$ or g_2 to zero, or one assumes

$g_2 = g_2^{WW}$. The error on g_1 due to the lack of knowledge of $A_\perp$ is not very large, since $A_\perp$ enters Eq. (170) with the factor $\tan(\theta/2)$.

4.9.1 Kinematical Range of the Data

Experimentally, only a certain x-range of the deep-inelastic region could be measured. Extrapolations to $x = 0$ and $x = 1$ (described below) were therefore necessary in order to obtain the integral $\int_0^1 g_1\,dx$. The data were binned into 38 logarithmic equally spaced x-bins from $x = 0.01$ to $x = 0.9$. Not all of these bins contained valid data. The kinematical range of the data was constrained by two major cut-offs: the cut-off due to the acceptance, and the cut-off due to the resonance region. For the data with beam energy 29 GeV, practically no significant number of events with $Q^2 < 1\,\text{GeV}^2$ were recorded, and a cut on those events had no influence.

The **acceptance** was determined by the physical limitations of the spectrometers like position and size of the magnets, magnet settings, as well as size and position of the detectors. Due to tracking inefficiencies, resolution smearing and other imperfections, hits were still recorded for regions which due to those physical constraints should be void of events. A sharp drop in events, however, marked the limit between the physical and unphysical region. In practice, the cut-off was selected by determining from histograms which E' could still be reached by good electrons. From this, combined with the average scattering angle (4.5° and 7°, resp.), we were able to calculate the highest and lowest x allowed by the acceptance. Comparison with the borders of the x-bins let us then decide which x-bins could be used and which not.

The cut on the **resonance region** determined the highest x-bins to be used. Since resonances have definite orbital and total angular momentum, their production cross-section is dependent on the polarizations of the incoming nucleon and virtual photon. The measured spin asymmetry is therefore strongly influenced by these resonances. The structure functions are no longer smooth in x, but show bumps at resonance energies. Those bumps make it more difficult to experimentally map out the resonances well enough to allow a reasonable integration over this region. The

resonance region amounted to little of the data at 16 and 29 GeV. However, the 9 GeV data contained enough data in the resonance region that a separate study of this region was possible. In that region, dilution factor and radiative corrections and resolution smearing had to be modeled via Monte Carlo code. The deep-inelastic region, in contrast, did not require these simulations. Since this work only considered the deep-inelastic region, we had to determine a reasonable cut to avoid the problems due to resonances.

The decision which data belong to the resonance region is usually based on W^2, the square of the invariant mass of the undetected fragments in the reaction. No fixed limit for the resonance region exists. The most important resonance is $\Delta(1232)$, at $W^2 \approx 1.5\,\mathrm{GeV}^2$. Others are located at higher energies, but are less prominent and at even higher energies these resonances become so frequent and overlap that they disappear in the deep-inelastic region. A cut of $W^2 = 4\,\mathrm{GeV}^2$ is usually considered clean, leaving practically all of the visible resonances below that. In this work, $W^2 = 4\,\mathrm{GeV}^2$ was used as the limit for the average of the bin, still allowing some events of the bin to be below, even down to about $W^2 = 3\,\mathrm{GeV}^2$. Table 12 lists the lowest and highest x-bins used in the analysis.

Table 12 Lowest and highest x-bins used for the analysis. The data were binned into 38 logarithmic equally spaced x-bins from $x = 0.01$ to 0.9. "16 high" and "16 low" refers to the two sets of momentum settings mentioned in Table 7.

	E in GeV	lowest bin	highest bin	x range
4.5°	29	10	35	0.029 – 0.631
	16 high	13	29	0.041 – 0.310
	16 low	7	29	0.020 – 0.310
	9	11	22	0.033 – 0.135
7°	29	18	37	0.075 – 0.800
	16 high	21	33	0.107 – 0.498
	16 low	15	33	0.053 – 0.498
	9	18	27	0.075 – 0.245

At even lower energy, the elastic peak would become visible (corresponding to $x = 1$). Unfortunately, this region was not accessible to the spectrometer at the magnet settings used during E143. Since the position of the elastic peak is, of course, well known to be at the missing mass $W = m_p$, it could have been used as an absolute check of the momentum setting of the spectrometers.

4.9.2 Combining 4.5° and 7° Spectrometer Data

The property of scaling [see Eqs. (25) and (26)] is approximately true at our kinematics. This allowed us to average results from different experiments, or in our case, the results from the 4.5° and 7° spectrometers even though their events had different Q^2 values. We therefore calculated g_1/F_1 for the 4.5° and 7° spectrometers and averaged the values of the same x-bin together.

Another possibility was to assume that A_1 and A_2, the cross-sections in terms of the virtual photon, are independent of Q^2, and to average their results of the two spectrometers. Strictly speaking, both ways are incorrect, since scaling is not really true. The results differ for both methods significantly, as we will see in the next chapter. We note here that the E143 data of A_2^p were not consistent with zero [59]. As mentioned before, A_2 has the bound $|A_2| < \sqrt{R}$, where R is the ratio of longitudinal to transverse virtual photon cross-section. At infinite Q^2, A_2 has to approach zero, since R approaches zero [Eq. (46)]. This means that A_2 has to change with Q^2. Ref. [26], for example, predicts that $A_2(x, Q^2)$ is approximately proportional to $\sqrt{Q^2}$ and expects the Q^2-dependence of $A_2/\sqrt{Q^2}$ (and also of A_1) to be small.

It is currently not clear, which of the two ways to average the data is better. This problem occurred for the first time in the analysis of the E143 29 GeV data since $A_\perp$ was never before determined to high degree.

For each x-bin, the average of x and Q^2 was calculated by adding the x and Q^2 values, respectively, and dividing by the number of events. However, when combining the 4.5° and 7° data, the x values were averaged weighted by the error of g_1/F_1 (or A_1). This is justified since the kinematical factors were different for

the two spectrometers and therefore gave different weight to the number of events. Similarly, when combining different bins (*e.g.*, for g_1^n), the error of the structure function or asymmetry was used as weights in the calculation of the average x of the bin.

4.9.3 Evolution to Common Q^2

Related to the problems of combining the data from different spectrometers is the problem of evolving the results to one common Q^2. Due to the kinematics of the spectrometers, the low-x bins contained events with low Q^2, and the high-x bins events with high Q^2. In contrast, the theoretical evaluation of the results required all data points to be at a common Q^2.

For combining the 4.5° and 7° spectrometer data, it was assumed that the ratio g_1/F_1 is independent of Q^2. This assumption was again exploited to obtain g_1 at one common Q^2. For E143, this Q^2 was chosen to be $Q_0^2 = 3\,\mathrm{GeV}^2$, which is approximately the average Q^2 of the E143 events. To obtain g_1 at Q_0^2, the value of g_1/F_1 was multiplied by $F_1(x, Q_0^2)$ obtained from Refs. [9], [10] and [11].

The published results of E143 [90] [107] were obtained in this way. Another way, evolving $g_1(x, Q^2)$ to $g_1(x, Q_0^2)$ via evolution equations, will be discussed later.

4.9.4 High-x Extrapolation

If the resonances would be well measured, the integration to $x = 1$ could be performed directly from the experimental data without extrapolation. However, the experimental measurements are currently not adequate, and instead the principle of duality [108] is invoked for the integration to $x = 1$. It tells us that an extrapolation from the deep-inelastic region into the resonance region will be like averaging out the resonance bumps into a smooth curve, not losing any information for the integration.

From perturbative QCD, it is known that at x close to 1 more quarks point parallel than anti-parallel to the helicity by a factor $(1 - x)^2$ [109]: $q^+ = q^-(x)/(1 -$

$x)^2$ where q^+ (q^-) is the quark distribution with helicity parallel (anti-parallel) to the nucleon helicity. This effect is called "helicity retention". More detailed analysis lead to the following relations:

$$q^+(x) \sim (1-x)^3 \quad \text{for } x \to 1 \tag{173}$$

$$q^-(x) \sim (1-x)^5 \quad \text{for } x \to 1 \tag{174}$$

The strange quark distributions approach $x = 1$ with terms proportional to $(1-x)^5$ or higher. We therefore fitted the highest three data points[21] to

$$g_1(x) = A(1-x)^3 \tag{175}$$

and used the fit to calculate the integral for the range between the data region and $x = 1$.

The error on the extrapolation was split up into a part considered as the statistical error, a part due to the fitting, and a part due to the systematic errors on the g_1 data points. Neither one was significantly large for the E143 results.

The error on the fitted value A was used to estimate the statistical error on the integral. This error was later quadratically combined with the statistical errors for the data region and low-x extrapolation.

The error due to the fitting was obtained in the following way: The number of highest data points used in the integral was varied from two to six, and each time the extrapolation integral was determined. The maximal difference of those integrals to the integral obtained with the three highest data points was taken as the fit error for the high-x extrapolation.

The systematic error of the high-x extrapolation estimated by how much the extrapolation would change if the g_1 measurements in the three highest x-bins would be higher or lower as suggested by the systematic error of these data points. For this, the integral in the high-x region was multiplied by the relative systematic error on these three data points.

---

[21] Here as well as for the low-x extrapolation, we refer to the 38 x-bins into which the data were originally binned. Some of these bins were later combined to form larger bins, but this was not yet done at this stage of the analysis.

138

4.9.5 Low-x Extrapolation

The extrapolation to $x = 0$ is not as well understood as the extrapolation to $x = 1$. One of the extrapolations currently suggested by theory is [110]

$$g_1 = ax^{-\alpha} \quad (\alpha \text{ between } -0.5 \text{ and } 0). \tag{176}$$

We adopted this as our standard extrapolation to $x = 0$. Of importance is the question, how high up in x this functional form is valid. A fit to F_2 turned out to be stable when increasing the fitting range up to $x \approx 0.1$ [111]. The data up $x \approx 0.095$ (corresponding to ten bins for the 29 GeV data) were fitted to the function $g_1 = ax^{-\alpha}$ with either $\alpha = 0$ or $\alpha = -0.5$. Then the integral of $g_1 = ax^{-\alpha}$ over the low-x region was calculated from these fits. Let us call these integrals I_0 and $I_{-0.5}$. Their average value

$$\bar{I} = \frac{1}{2}(I_0 + I_{-0.5}) \tag{177}$$

was used as the value of the integral over the low-x extrapolation region. The statistical error was calculated from the error on the fitting parameter a, but this error was, like in the high-x extrapolation, relatively small for E143 data. As mentioned above, this error was quadratically combined with the statistical errors for the data region and the high-x extrapolation.

Assigning the error due to the fit required some care, since the two variables a and α were dependent on each other. However, the general principle was similar to the procedure applied to the high-x extrapolation. The error estimation was done in the following way:

The first fit error was taken as $|I_0 - \bar{I}| = |I_{-0.5} - \bar{I}|$. For the second fit error, the number of points included in the fit was varied from four to thirteen. The maximal difference between $\bar{I}$ and the integrals over the low-x region from these fits was taken as the second fit error. The first and second fit error were combined quadratically to give the overall fit error for the low-x extrapolation.

Also the systematic error was obtained. It estimated, how the systematic error on the g_1 data affected the extrapolation. As done for the high-x extrapolation, the relative systematic error on the data points included in the fit was multiplied

by the integral over the extrapolation region. This was then the systematic error on the low-x extrapolation. This systematic error as well as the systematic error on the high-x extrapolation were later summed up with the systematic error on the integral over the data range, since they were correlated with each other.

The most recent SMC publications, Refs. [2] and [5], fit their data to a constant in g_1, which would correspond to $\alpha = 0$ in Eq. (176). Also proposed was the function $g_1 \sim \ln(1/x)$, since this form fits the unpolarized structure function data at low x. Results for these alternate assumptions will be presented later.

4.10 Systematic Error

The systematic error was calculated for the asymmetry A_1 and for the structure function g_1. Only the systematic error due to $A_{\parallel}$ was considered while the systematic error due to $A_{\perp}$ was neglected. Some of the errors were independent of x, while others were different for each x-bin. All errors were assumed to be correlated between runs. (See also Ref. [111] for more details.)

Systematic Errors independent of x:

- The error of the **beam polarization** was estimated to be 0.024 (relative), since the absolute error was 0.02 and the average beam polarization was about 0.85.

- The **target polarization** was assumed to have a relative systematic error of 0.025 for protons and 0.04 for deuterons. The error was assumed to be 100% correlated between runs, since the systematic error was obtained from the spread of the thermal equilibrium measurement results, each of which provided the calibration constants for large groups of runs.

- The **proton nitrogen correction** [see Eqs. (155) and (156)] contributed with a 0.004 relative systematic error since the correction C_p was always around 0.02, while the relative error on C_p was estimated to be 0.2.

Systematic Errors dependent on x:

- The error of the **dilution factor** consisted of several parts: The packing fraction contributed with relative errors of 0.017 for proton and 0.02 for deuteron. The weight of ammonia and helium was known to a relative error of 0.04. These two errors were added in quadrature since they were independent from each other. The remaining components depended on our knowledge of the unpolarized cross-sections and were therefore added linearly, corresponding to 100% correlation. The relative error from the cross-section ratio σ_d/σ_p was assumed to be 0.02. The EMC effect was assumed to be known to 0.015 relative. NMR coil contributed with a 0.2 relative error in the amount of wire in the target. This 20% relative error did not affect the combined error very much since the amount of wire was small compared to the amount of all other material.

- The **deuteron nitrogen correction** was applied via two factors, C_1 and C_2 [see Eq. (157)]. The error on C_1 was neglected since this value was very small and stable. The factor C_2 contained the proton asymmetry and was calculated for each x-bin and each run using the actually measured proton asymmetry. These factors were then averaged over the run weighted by the statistical error of the bin at each run, leading to $\overline{C}_2$. For the systematic error calculation, this average value $\overline{C}_2$ was multiplied by the relative error of the proton asymmetry to yield the systematic error.

- As mentioned before, the systematic error on the **radiative corrections** was calculated for each x-bin by varying the input models. It is shown in Fig. 39.

- For the calculation of g_1/F_1, the depolarization factor D' contained the function $\mathbf{R} = \sigma_L/\sigma_T$. Its systematic error was taken directly from the subroutine of Ref. [9] and ranged from 3% to about 7.5%.

- For the calculation of g_1, the **unpolarized cross-section F_1** was used to obtain g_1 from the ratio g_1/F_1. Its error could be treated together with the error due to R which appeared in the depolarization factor D'. The ratio F_1/D' can be written in terms of the total cross-section σ and the Mott cross-section σ_{Mott}:

$$\frac{F_1}{D'} = \frac{\sigma}{\sigma_{\mathrm{Mott}}} \frac{My}{2(2-y)\tan^2(\theta/2)} \tag{178}$$

141

The variable y is again ν/E, and the Mott cross-section is the cross-section for a pointlike particle, and it is given by:

$$\sigma_{\text{Mott}} = \frac{4\alpha^2 E'^2 \cos^2(\theta/2)}{Q^4}.$$ (179)

Since the Mott cross-section can be assumed to be known without error, the error on F_1/D' then only depended on the error of σ, which was taken to be proportional to F_2. Hence the relative error on F_1/D' was the relative error on F_2. The error on F_2 could not be calculated from the data of Refs. [10] and [11], since they only provided the central value F_2^{NMC}. Instead, a routine based on Ref. [106] was used. In addition to the central value (called F_2^{glob}), this routine provided a statistical error δF_2^{stat} and a systematic error. There is also an overall normalization uncertainty $n = 0.021$ for protons and $n = 0.017$ for deuterons. The systematic error was then taken as

$$\frac{\delta F_2}{F_2} = \sqrt{\left(\frac{\delta F_2^{\text{stat}}}{F_2^{\text{glob}}}\right)^2 + n^2 + \left(1 - \frac{F_2^{\text{glob}}}{F_2^{\text{NMC}}}\right)^2}.$$ (180)

The error increased towards high x due to discrepancies of F_2^{glob} and F_2^{NMC}. At low x (below 0.08), only the NMC data provide an accurate number for F_2. Here the error was taken to be $\delta F_2/F_2 = 0.04$, which is suggested from the spread of the experimental data at these low x values.

In the overlap region of the 4.5° and 7° spectrometers, the errors were merged using the errors on g_1/F_1 or g_1 as weights. The errors were linearly combined if they were correlated between the 4.5° and 7° spectrometer:

$$s = \frac{\dfrac{s_{4.5°}}{\delta_{4.5°}^2} + \dfrac{s_{7°}}{\delta_{7°}^2}}{\dfrac{1}{\delta_{4.5°}^2} + \dfrac{1}{\delta_{7°}^2}}$$ (181)

Here s stands for the systematic errors, and δ for the statistical errors of g_1/F_1 or g_1. They were quadratically combined, if they were uncorrelated:

$$s^2 = \frac{\left(\dfrac{s_{4.5°}}{\delta_{4.5°}^2}\right)^2 + \left(\dfrac{s_{7°}}{\delta_{7°}^2}\right)^2}{\dfrac{1}{\delta_{4.5°}^2} + \dfrac{1}{\delta_{7°}^2}}$$ (182)

142

The only uncorrelated error was the error due to the deuteron nitrogen correction, since the statistical errors of the proton asymmetry were independent in the two spectrometers.

The systematic errors were then smoothed by hand, since the calculated value depended on the actual value of the asymmetry or structure function, although the systematic error was actually a smooth function in x.

For the systematic error of the neutron structure function g_1^n as well as of the difference $g_1^p - g_1^n$, the errors due to the normalization uncertainty [see Eq. (180)], the errors due to the beam polarization, and the dilution factor errors due to the unpolarized cross-sections were assumed to be 100% correlated, while the other errors were assumed to be uncorrelated.

The systematic error on the integral was calculated assuming that all errors (but one) between the x-bins were 100% correlated. The only exception was the deuteron nitrogen correction error. Here the systematic errors were (linearly) added assuming that they were uncorrelated between x-bins because the errors originated from the statistical errors of the proton asymmetry.

The systematic errors of the low- and high-x extrapolations were added together with the systematic error for the data region. The sum was then quadratically combined with the fit errors for the low- and high-x extrapolations to yield the total systematic error on the integral.

CHAPTER 5

RESULTS AND DISCUSSION

This chapter will first present the results from the 29 GeV data: asymmetries and structure functions, as well as the integrals over the structure functions. The emphasis of this dissertation was on the deuteron data to obtain g_1^d. But since most parts of the analysis also applied to the structure function g_1^p, we will also mention some of the proton results. Both structure functions were used to extract g_1^n and the result of the integral $\Gamma_1^p - \Gamma_1^n$, and their results will be presented. Also the results of the helicity contribution of quarks will be shown. Afterwards, the results of the systematic error analysis as well as of several checks, like using alternate assumptions for the extraction of the data, will be discussed. Then, we will present the results of the 16.2 and 9.7 GeV data and the results of an application of the GLAP evolution equation to the E143 results. The results in this dissertation differ slightly from previously published values due to improvements in the analysis made since then. These improvements are discussed at the end of this chapter.

Plots of the results will in general be shown with some x-bins combined, although all calculations were done before combining the data points. Tables of the asymmetries and structure functions are given in the appendix. Table 13 lists the borders for all x-bins which contained valid data for the analysis. The average x values mentioned in any later table can be compared with this table to check which x values were included for that bin.

Table 13 Bin numbers and their borders in x. Only those bins significant for the analysis are shown. During the analysis, the data were binned in 38 logarithmic equally spaced x-bins from $x = 0.01$ to $x = 0.9$. For the figures, some of these x-bins were combined.

bin #	x range	bin #	x range
7	0.0204 – 0.0229	23	0.1353 – 0.1523
8	0.0229 – 0.0258	24	0.1523 – 0.1715
9	0.0258 – 0.0290	25	0.1715 – 0.1931
10	0.0290 – 0.0327	26	0.1931 – 0.2173
11	0.0327 – 0.0368	27	0.2173 – 0.2446
12	0.0368 – 0.0414	28	0.2446 – 0.2754
13	0.0414 – 0.0466	29	0.2754 – 0.3100
14	0.0466 – 0.0525	30	0.3100 – 0.3490
15	0.0525 – 0.0591	31	0.3490 – 0.3929
16	0.0591 – 0.0665	32	0.3929 – 0.4423
17	0.0665 – 0.0749	33	0.4423 – 0.4979
18	0.0749 – 0.0843	34	0.4979 – 0.5604
19	0.0843 – 0.0949	35	0.5604 – 0.6309
20	0.0949 – 0.1068	36	0.6309 – 0.7102
21	0.1068 – 0.1202	37	0.7102 – 0.7995
22	0.1202 – 0.1353		

5.1 Results from the 29 GeV Data

5.1.1 Asymmetries and Spin-Structure Functions

5.1.1.1 The Deuteron Results: $A_\parallel^d$, $A_\perp^d$, g_1^d

The deuteron asymmetries $A_\parallel$ and $A_\perp$ were extracted from the 29 GeV data according to the procedure described in the previous chapter. Fig. 40 shows these asymmetries for both spectrometers. (The proton asymmetries were presented earlier in Fig. 35.) The deuteron asymmetries are in the 10 to 20% range. Since the dilution factor was around 0.23 and since the deuteron polarization was 40% or less, the magnitude of the raw asymmetry of the measured counts was only a few
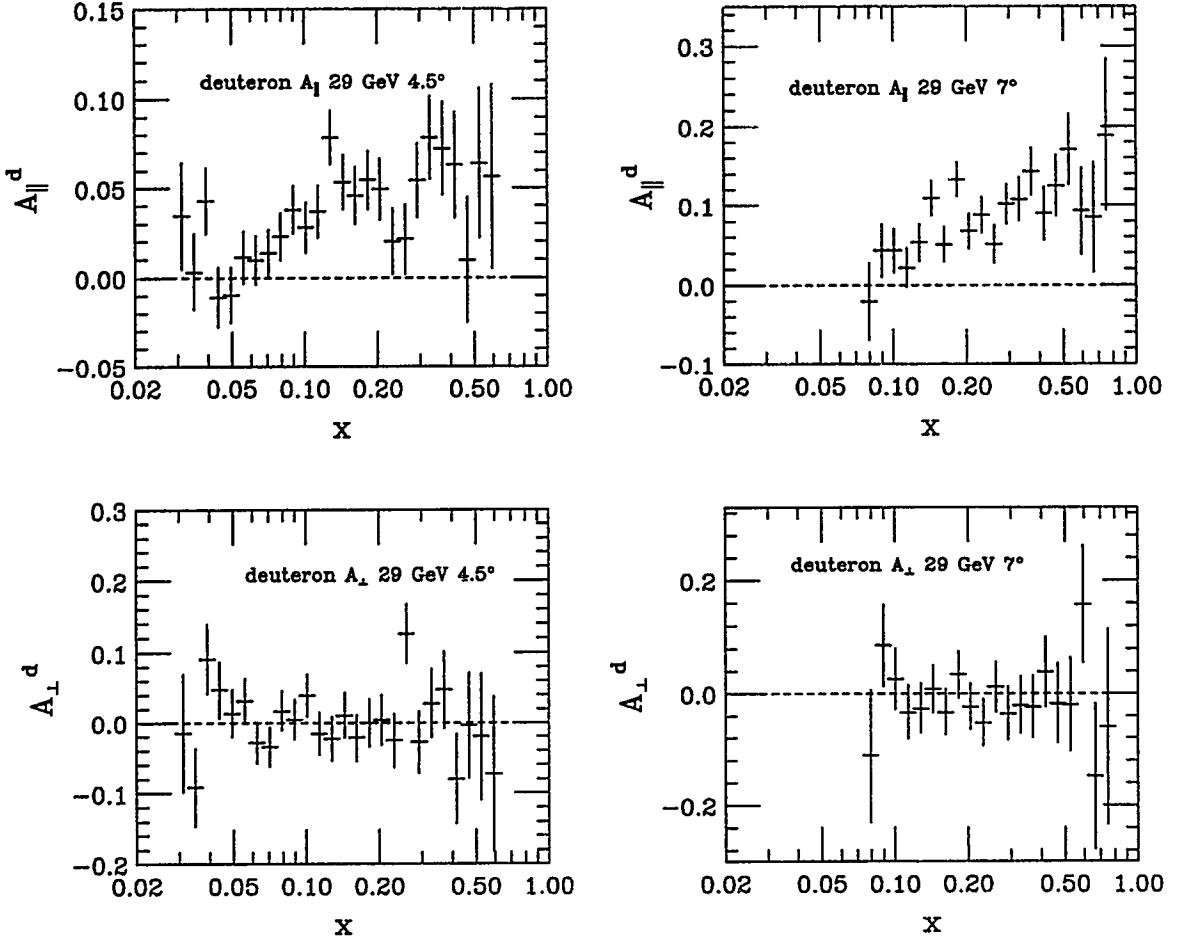
145

Figure 40 $A_\parallel$ and $A_\perp$ from the 29 GeV deuteron results. Data are shown with original binning in x.

percent. We also note that the asymmetry $A_\perp$ is consistent with zero at the given statistics.

The asymmetries A_1 and A_2 are shown in Fig. 41. The approximate Q^2-independence of A_1 and A_2 is well visible. We remind the reader that the 4.5° and 7° spectrometers differ by about a factor of 2 in their coverage of Q^2. For combining the 4.5° and 7° data, it was assumed that the ratio g_1/F_1 was independent of Q^2. Fig. 42 displays the combined asymmetry A_1 (high-x bins pairwise combined) with the most recent data from SMC [5]. Again, the E143 and SMC data sets have widely different Q^2, but still no Q^2-dependence is visible.

Again assuming that the ratio g_1/F_1 was Q^2 independent, the data from both spectrometers were combined and multiplied by $F_1(x)$ at $Q^2 = 3\,\mathrm{GeV}^2$ to obtain

146
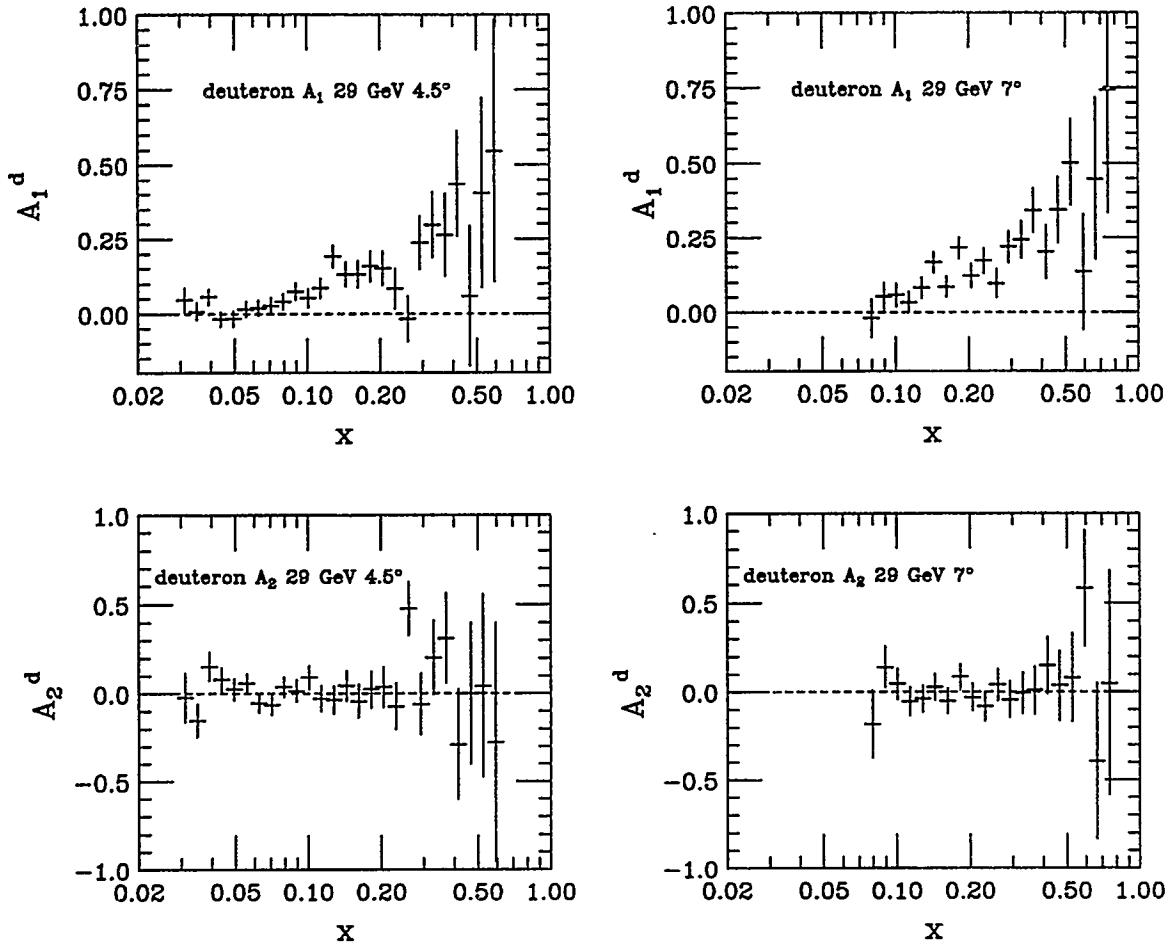
Figure 41 A_1 and A_2 from the 29 GeV deuteron results. Data are shown with original binning in x.

g_1^d at common $Q^2 = 3\,\mathrm{GeV}^2$. Fig. 43 shows g_1^d versus x, while Fig. 44 shows xg_1^d versus x. Here the top bins were again pair-wise combined. Since F_1 increases with lower x, a small asymmetry in g_1/F_1 (or equivalently in A_1) can translate into a sizeable value of g_1. We see in Fig. 43 also the large error bars on g_1 at low x. Multiplying g_1 by x not only lets the error bars appear smaller, but it also has the advantage that — if plotted on a logarithmic scale in x — the area under xg_1 is proportional to the integral over x (Fig. 44). As we can see, the integral was mostly determined by the area above $x \approx 0.1$, since the structure function approached zero at lower x.
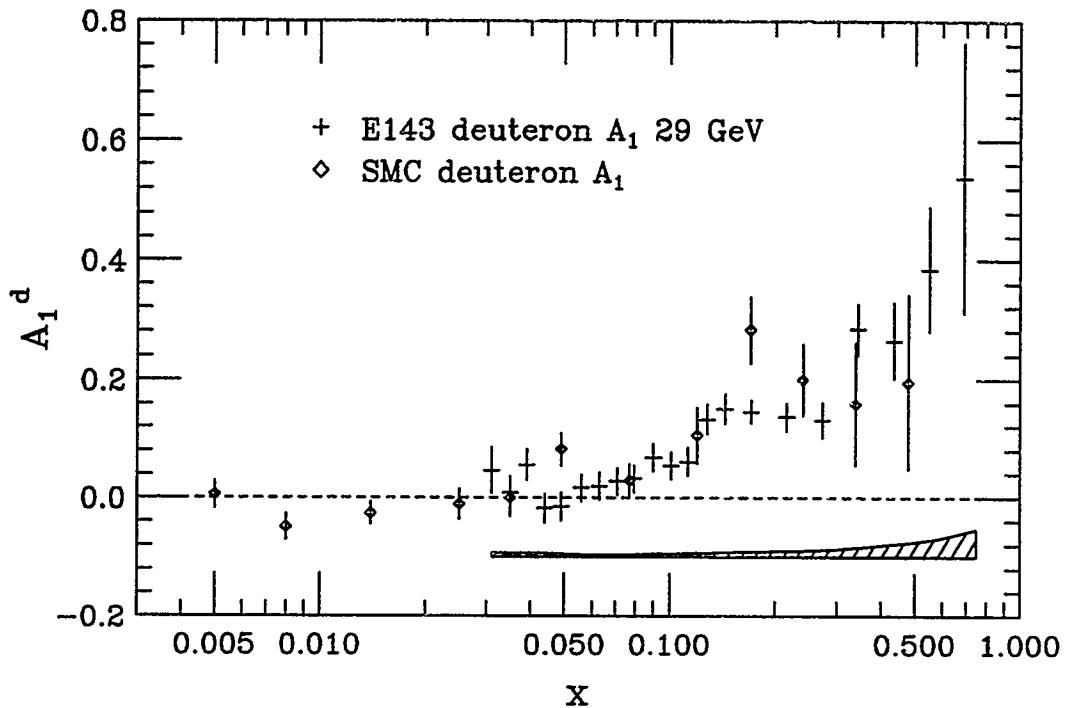
Figure 42 A_1^d, both spectrometers combined, with SMC data [5]. For the E143 results, the highest x-bins were combined. The band indicates the systematic error of E143 A_1^d.
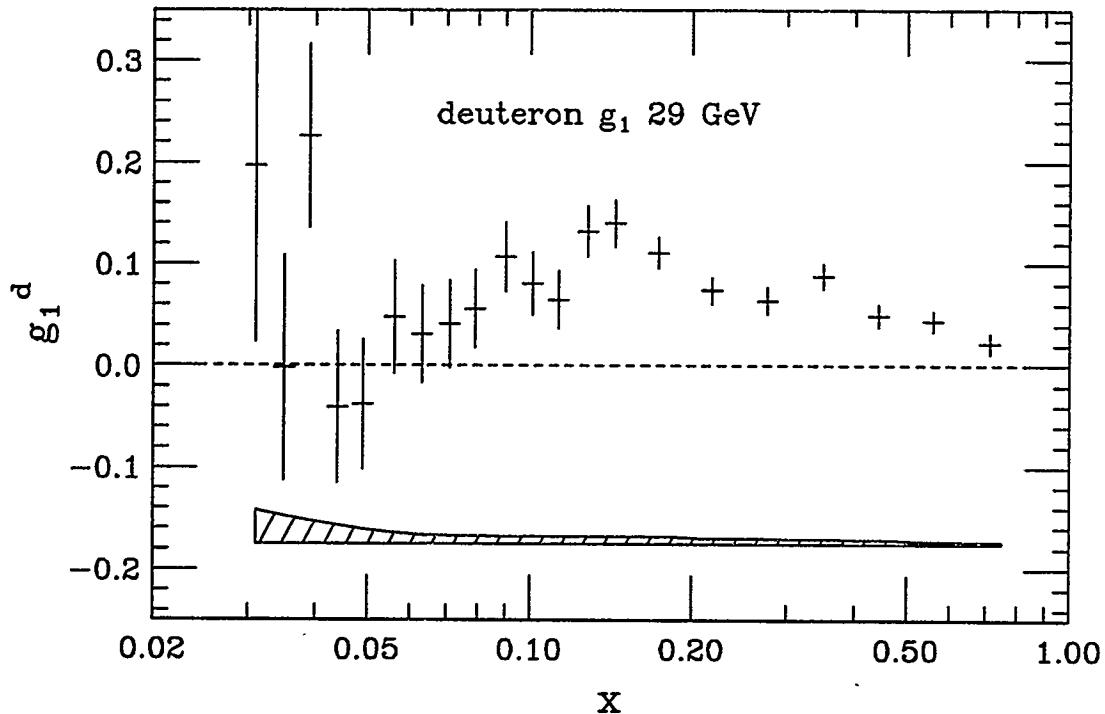
Figure 43 g_1^d from 29 GeV data, both spectrometers combined. The band indicates the systematic error.
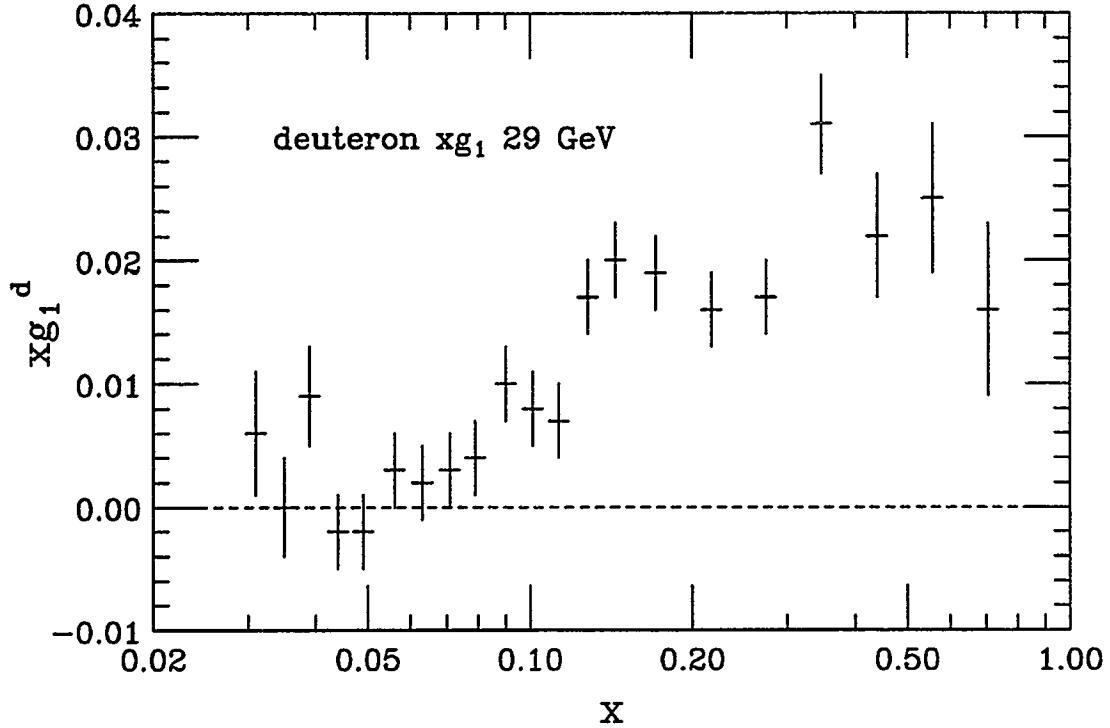
Figure 44 xg_1^d from 29 GeV data, both spectrometers combined.

5.1.1.2 Extraction of Neutron Asymmetries and Structure Functions

Combining the deuteron result with the E143 proton numbers, we may calculate the asymmetry A_1^n and the structure function g_1^n, using Eqs. (83) and (84). Fig. 45 shows the result of A_1^n together with the E142 result [112], and Fig. 46 shows g_1^n together with the SMC result [5] and the E142 result [112]. All three data sets are at different average Q^2: E142 is at $Q^2 = 2\,\text{GeV}^2$, E143 is at $Q^2 = 3\,\text{GeV}^2$, and SMC is at $Q^2 = 10\,\text{GeV}^2$. Each E143, every point shown in the figures is the average of three original bins, with exception of the highest points which is the average of the highest four original bins. The E143 and E142 data feature error bars similar in size and overall seem to agree, although E142 is lower between $x = 0.1$ and $x = 0.3$. For clarity, two SMC points with $x < 0.01$ were not included in Fig. 46.
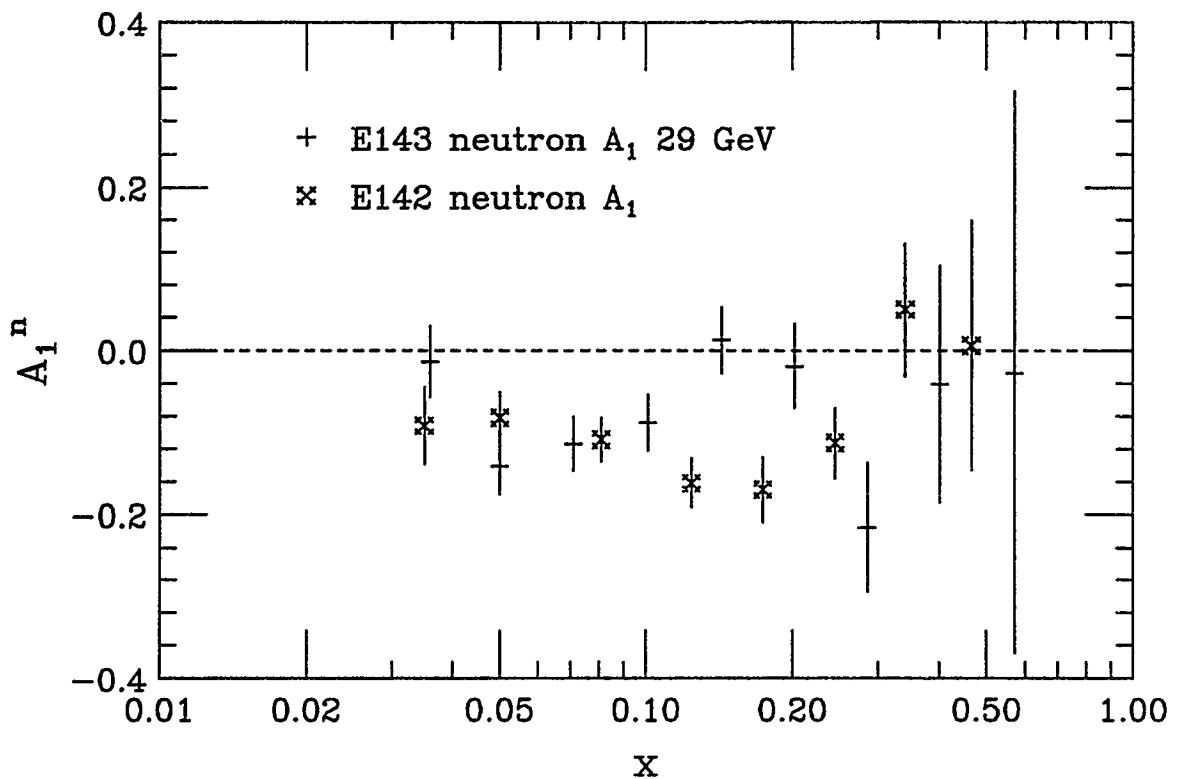
Figure 45 Asymmetry A_1^n from E143 29 GeV and E142.
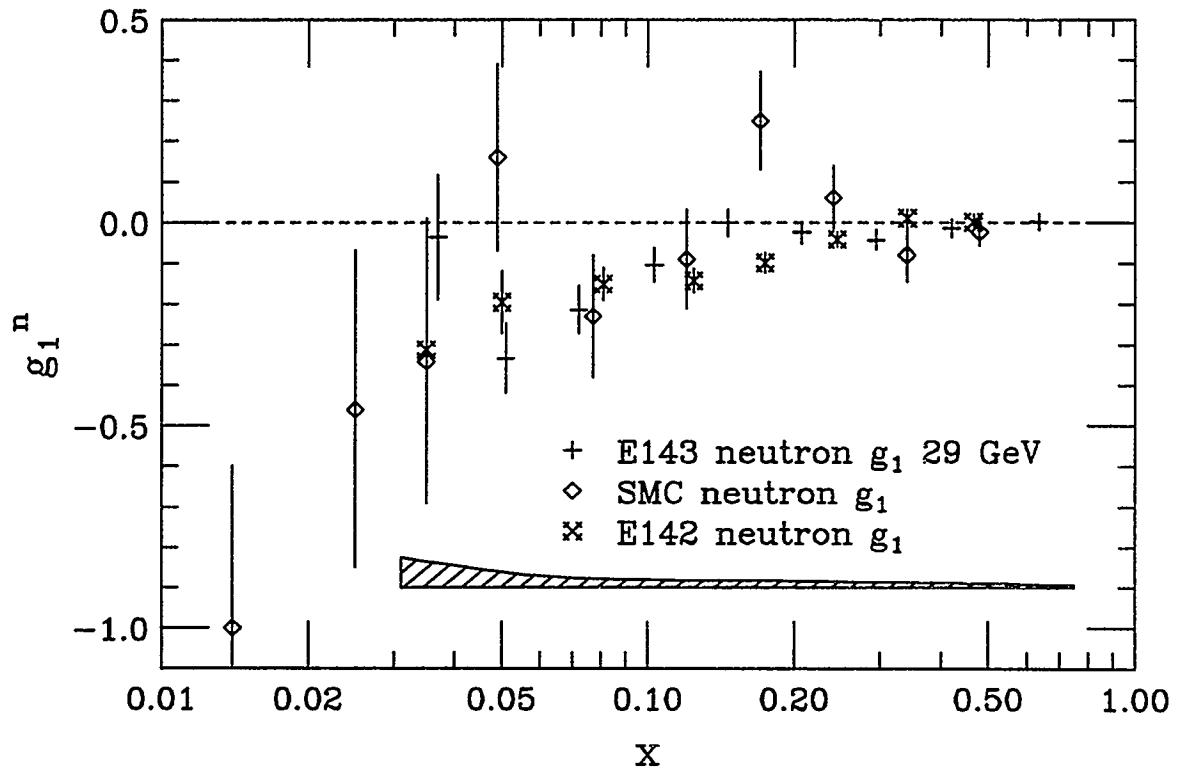
Figure 46 Structure function g_1^n from E143 29 GeV, SMC and E142. The band indicates the systematic error of E143 g_1^n.

5.1.2 Sum Rules and Helicity Content

5.1.2.1 Ellis-Jaffe Sum Rules

Integration of the structure function g_1 over x leads us to the integral Γ_1, the magnitude of which is predicted by the Ellis-Jaffe sum rules. Unless otherwise noted, the Ellis-Jaffe predictions are always for $Q^2 = 3\,\mathrm{GeV}^2$, which is close to the average Q^2 of the E143 events. At this $Q^2 = 3\,\mathrm{GeV}^2$, the strong coupling constant was extracted to be $\alpha_s = 0.35 \pm 0.05$ [113]. This value of α_s was used for the extraction of the sum rules. Throughout the analysis, the third-order leading twist QCD corrections were applied [49]. The quoted error on the Ellis-Jaffe prediction is solely due to the error on α_s.

Table 14 presents the proton and deuteron results from E143. It lists not only the total integral from 0 to 1, but also the integral over the data region and the contribution of the low- and high-x extrapolations. Due to rounding, the sum of the integral over the data region and the extrapolations does not always give the same number as the integral from 0 to 1.

For the proton, the integral over x from 0 to 1 was determined to be $\Gamma_1^p = 0.127 \pm 0.003\,(\text{stat})\pm 0.008\,(\text{syst})$ at $Q^2 = 3\,\mathrm{GeV}^2$. This may be compared to the SMC result at $Q^2 = 10\,\mathrm{GeV}^2$ of $\Gamma_1^p = 0.136 \pm 0.011\,(\text{stat})\pm 0.011\,(\text{syst})$ [2]. The Ellis-Jaffe sum rule prediction for proton at $Q^2 = 3\,\mathrm{GeV}^2$ is $\Gamma_1^p = 0.160\pm 0.007$. At $Q^2 = 10\,\mathrm{GeV}^2$, it predicts $\Gamma_1^p = 0.171\pm 0.005$. The E143 proton integral disagrees with the Ellis-Jaffe sum rule prediction by about three standard deviations.

The deuteron integral Γ_1^d is with $\Gamma_1^d = 0.046 \pm 0.003\,(\text{stat})\pm 0.004\,(\text{syst})$ more than three standard deviations lower than the Ellis-Jaffe rule prediction of $\Gamma_1^d = 0.069 \pm 0.004$. Currently, the latest result of SMC [5] is $\Gamma_1^d = 0.034 \pm 0.009\,(\text{stat}) \pm 0.006\,(\text{syst})$ at $Q^2 = 10\,\mathrm{GeV}^2$ which must be compared to the Ellis-Jaffe rule prediction of $\Gamma_1^d = 0.071 \pm 0.004$ at $Q^2 = 10\,\mathrm{GeV}^2$.

To compare the E143 and SMC results, we present the data in a plot versus Q^2, with the Ellis-Jaffe prediction indicated as a function of Q^2. Fig. 47 shows both the E143 and SMC data for proton and deuteron. The error bars on the measurements

Table 14 Results for the integration of g_1^p and g_1^d over x. The following errors are listed: first the statistical error, second the systematic error, third the fit error. The systematic error over $x = 0$ to $x = 1$ also contains the fit errors. For comparison, the Ellis-Jaffe predictions with their theoretical errors are listed.

	Γ_1^p	Γ_1^d
low x	$0.006 \pm 0.001 \pm 0.001 \pm 0.003$	$0.001 \pm 0.001 \pm 0.001 \pm 0.001$
data range	$0.120 \pm 0.003 \pm 0.007$	$0.045 \pm 0.003 \pm 0.004$
high x	$0.001 \pm 0.001 \pm 0.001 \pm 0.001$	$0.000 \pm 0.001 \pm 0.001 \pm 0.001$
0 to 1	$0.127 \pm 0.003 \pm 0.008$	$0.046 \pm 0.003 \pm 0.004$
EJ pred.	0.160 ± 0.007	0.069 ± 0.004

correspond to the combined statistical and systematic errors. The solid lines in these pictures are the Ellis-Jaffe predictions at the different Q^2 values, starting at $Q^2 = 0.5\,\text{GeV}^2$. At this low Q^2, we are clearly in the non-perturbative region, where the QCD corrections to the Ellis-Jaffe sum rules have to be incorrect. The dependence of the Ellis-Jaffe sum rule prediction on Q^2 was only determined by the leading twist QCD corrections up to third order. The dashed lines indicate the error on the Ellis-Jaffe predictions due to the error on α_s for $Q^2 = 3\,\text{GeV}^2$. We see that both E143 and SMC disagree strongly with the Ellis-Jaffe sum rule predictions.

As mentioned before, the E143 results of g_1^p and g_1^d were combined to extract the neutron spin-structure function g_1^n. By integrating g_1^n over x in the same way as it was done for g_1^p and g_1^d, the neutron integral was determined as $\Gamma_1^n = -0.027 \pm 0.008$ (stat)± 0.010 (syst) at $Q^2 = 3\,\text{GeV}^2$. E142 has measured for the same integral $\Gamma_1^n = -0.032 \pm 0.006$ (stat)± 0.009 (syst) for $Q^2 = 2\,\text{GeV}^2$, while SMC found [5] $\Gamma_1^n = -0.063 \pm 0.024$ (stat)± 0.013 (syst) for $Q^2 = 10\,\text{GeV}^2$. The Ellis-Jaffe sum rule prediction for Γ_1^n is -0.011 ± 0.005 at $Q^2 = 3\,\text{GeV}^2$. (See Table 15.) We display the experimental results in Fig. 48 together with the Ellis-Jaffe sum rule prediction similarly as done in Fig. 47. Both the proton and deuteron results disagree with the Ellis-Jaffe sum rule, and a disagreement is also expected for the neutron result. However, Fig. 48 shows that the disagreement is not as striking as for proton and deuteron. Both SMC and E142 seem to disagree with the Ellis-Jaffe prediction, while the E143 result is slightly more than one standard deviation from the prediction.
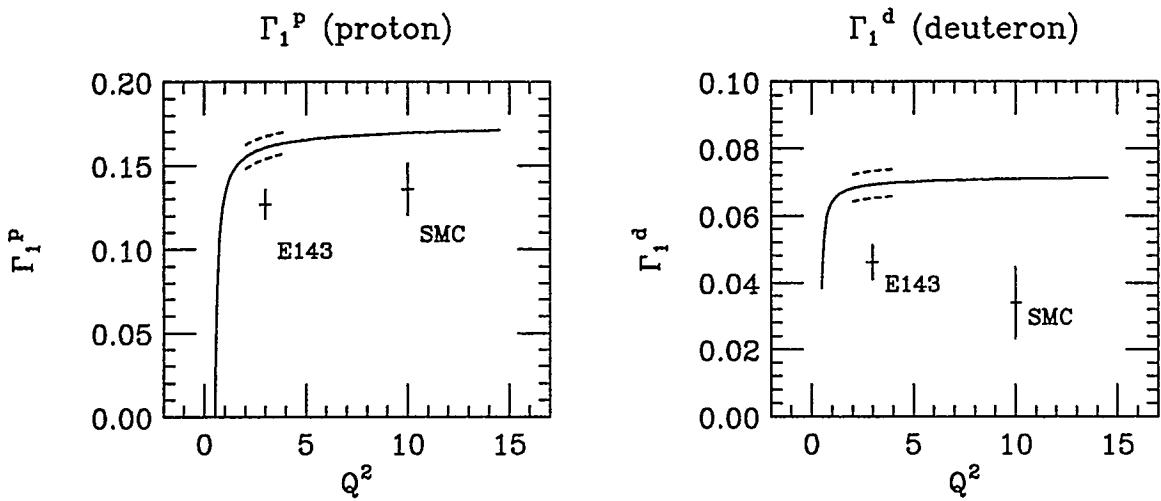
Figure 47 Experimental results of Γ_1 with Ellis-Jaffe predictions (solid lines) calculated using third-order leading twist QCD corrections. To the left are the proton results, to the right are the deuteron results. The error bars on the experimental results include both statistical and systematic errors. The errors on the sum rule predictions at $Q^2 = 3\,\mathrm{GeV}^2$ are indicated by the dashed lines.
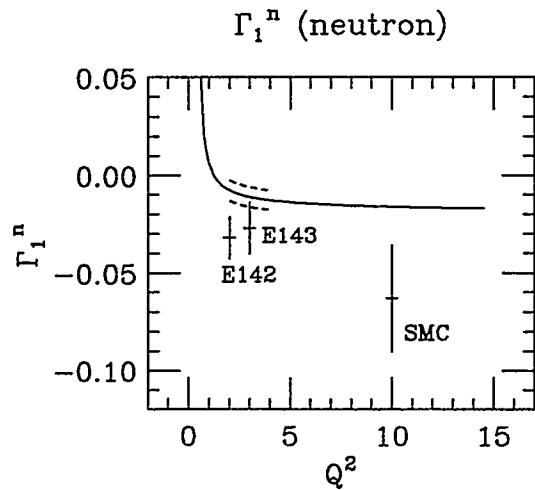
Figure 48 Experimental results of the integral Γ_1^n with the prediction of the Ellis-Jaffe sum rule. See text and caption of Fig. 47 for details.

Table 15 Results for the integration of g_1^n and $g_1^p - g_1^n$ over x. The quantity $g_1^p - g_1^n$ was calculated from the proton and deuteron results of E143. The following errors are given: first the statistical error, second the systematic error, third the fit error. The systematic error for the integral from $x = 0$ to $x = 1$ also contains the fit errors. In the bottom row, the predictions from the Ellis-Jaffe and Bjorken sum rules are listed.

	Γ_1^n	$\Gamma_1^p - \Gamma_1^n$
low x	$-0.004 \pm 0.001 \pm 0.001 \pm 0.003$	$0.010 \pm 0.001 \pm 0.001 \pm 0.006$
data range	$-0.024 \pm 0.008 \pm 0.009$	$0.144 \pm 0.010 \pm 0.014$
high x	$0.000 \pm 0.001 \pm 0.001 \pm 0.001$	$0.001 \pm 0.001 \pm 0.001 \pm 0.001$
0 to 1	$-0.027 \pm 0.008 \pm 0.010$	$0.154 \pm 0.010 \pm 0.016$
EJ/Bj pred.	-0.011 ± 0.005	0.171 ± 0.009

5.1.2.2 Bjorken Sum Rule

Again by combining the E143 proton and deuteron results, we calculated $g_1^p(x) - g_1^n(x)$, the difference between the proton and neutron spin-structure function. Integration over x using the same procedure, which was applied for the previously mentioned integrals, yielded $\Gamma_1^p - \Gamma_1^n$, the integral predicted by the fundamental Bjorken sum rule. At common $Q^2 = 3\,\mathrm{GeV}^2$, we obtained $\Gamma_1^p - \Gamma_1^n = \int_0^1 dx\,(g_1^p - g_1^n) = 0.154 \pm 0.010\,(\mathrm{stat})\pm 0.016\,(\mathrm{syst})$, compared to the prediction of $\Gamma_1^p - \Gamma_1^n = 0.171 \pm 0.009$ for the same Q^2. The E143 result agrees therefore within less than one standard deviation with the sum rule prediction. SMC [5] is quoting for their experiment $\Gamma_1^p - \Gamma_1^n = 0.199 \pm 0.038\,(\mathrm{stat.\ and\ syst.})$ at $Q^2 = 10\,\mathrm{GeV}^2$. In Fig. 49, we again display the experimental results with the Bjorken sum rule prediction in a plot versus Q^2.

154
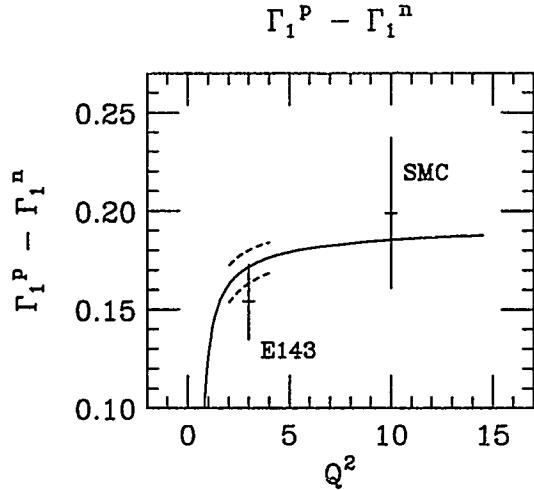
Figure 49 Experimental results of the integral $\Gamma_1^p - \Gamma_1^n$ with the prediction of the Bjorken sum rule. See text and caption of Fig. 47 for details.

5.1.2.3 Helicity Content

Using the measured integrals Γ_1, the quark contribution Δq to the nucleon helicity was extracted. From the proton integral Γ_1^p, we obtain $\Delta q = 0.27 \pm 0.09$ (stat. & syst.) for E143, compared to $\Delta q = 0.22 \pm 0.10$ (stat)± 0.10 (syst) from SMC [2]. The E143 result takes into account the third-order leading twist QCD corrections, and we may therefore consider the Δq results as the value at $Q^2 = \infty$. However, we remind the reader that contributions of higher orders of the leading twist corrections as well as contributions due to higher twist might be significant. They were not corrected for and would affect the E143 results stronger than the SMC results. From the Ellis-Jaffe sum rule, which assumes $\Delta s = 0$ as well as SU(3) flavor symmetry, we would expect $\Delta q = 0.58$. The strange quark helicity contribution was determined by E143 to be $\Delta s = -0.10 \pm 0.03$, confirming the SMC result [2] $\Delta s = -0.12 \pm 0.04$ (stat)± 0.04 (syst).

We may also calculate the contribution of all quarks to the nucleon helicity from the deuteron integral Γ_1^d. E143 obtains $\Delta q = 0.35 \pm 0.05$, which is significantly more precise than SMC's result [5] of $\Delta q = 0.20 \pm 0.11$. The strange quark-antiquark contribution is determined by the E143 data to be $\Delta s = -0.08 \pm 0.02$, compared to $\Delta s = -0.12 \pm 0.04$ from SMC. Fig. 50 displays the Δq and Δs results for the SLAC and CERN experiments. All results follow the line defined by Eq. (103).
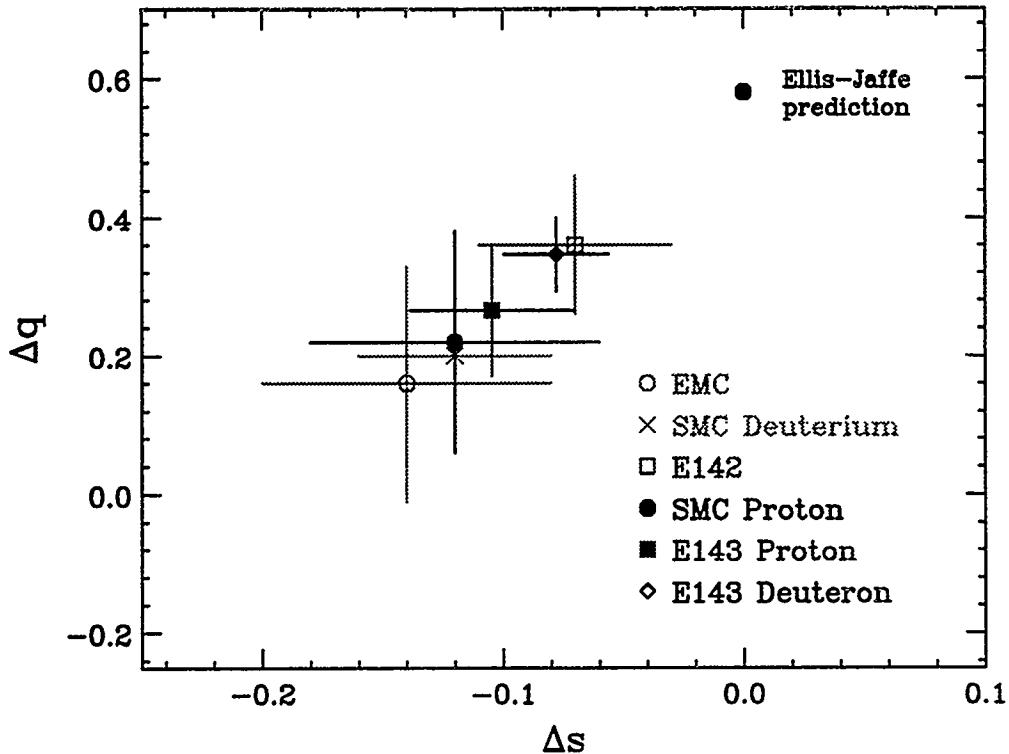
Figure 50 Δq vs. Δs from all experiments. All data points fall onto one line, since Δs is linearly dependent on Δq. The Ellis-Jaffe prediction is by assumption at $\Delta s = 0$.

5.2 Systematic Error and Checks

5.2.1 Results of Systematic Error Calculations

The results of the systematic error analysis are presented in Table 16, which lists how much the different sources contributed to the systematic errors of the integrals. (See previous chapter for more information about these sources and how their contribution to the systematic error was estimated.) The table shows that for the proton several sources contributed strongly to the systematic error: dilution factor, unpolarized cross-section, beam and target polarizations. For deuteron, the main uncertainty came from the radiative corrections, followed by the target polarization. For Γ_1^n and $\Gamma_1^p - \Gamma_1^n$, the radiative correction, the dilution factor

156

and the target polarization were the main sources of the systematic error. Due to correlations, the beam polarization did not contribute as much to the systematic error of Γ_1^n as it did to the other results.

Table 16 Contribution of the systematic error sources to the integral over the data region. Because of its small size, the nitrogen correction systematic error was neglected for the g_1^n and $g_1^p - g_1^n$ error calculations.

	Γ_1^p	Γ_1^d	Γ_1^n	$\Gamma_1^p - \Gamma_1^n$
radiat. corr.	0.0021	0.0024	0.0056	0.0067
dilution fact.	0.0037	0.0012	0.0046	0.0073
F_1/D'	0.0034	0.0010	0.0023	0.0055
beam polar.	0.0029	0.0011	0.0005	0.0033
target polar.	0.0030	0.0018	0.0052	0.0074
nitrogen corr.	0.0005	0.0001	–	–
combined	0.0068	0.0036	0.0092	0.0139

5.2.2 Alternate Low-x Extrapolations

The following three ways to extrapolate from the lowest x-bin to $x = 0$ were proposed:

$$g_1 = ax^{-\alpha} \quad \text{with } \alpha \text{ between } -0.5 \text{ and } 0$$
$$g_1 = \text{const.} \tag{183}$$
$$g_1 = a \ln \frac{1}{x}$$

Table 17 lists their results for both the proton and the deuteron 29 GeV low-x extrapolations. In either case, we used the lowest ten data points, up to $x \approx 0.095$. We see that the smallest values of the extrapolation appear with the full Regge-style fit $g_1 \sim x^{-\alpha}$, while the largest value appears for the $g_1 \sim \ln 1/x$ fit, larger by a factor of about 2. The error quoted for the Regge-style fit still covers the result of the fit to a constant (by definition of the error), but does not cover the logarithm

fit. Fig. 51 shows the g_1^p (left) and g_1^d (right) with the high-x fit and the discussed low-x fits. In the low-x region, the solid line corresponds to the Regge-style fit, slowly approaching zero. The dotted line shows the logarithmic fit (appearing as a straight line for the logarithmic scale in x), while the long dashes represent the fit to a constant. Either kind of fit appears to be reasonable. For both the proton and the deuteron g_1 Regge-style fits, $\alpha = -0.19$ provided the integral with the average of the integrals of $\alpha = 0$ and $\alpha = -0.5$ (see earlier section).

Table 17 Results of the low-x fits using different functions. The errors on the Regge-style fit are the fit errors as explained in earlier section.

function	proton	deuteron
$ax^{-\alpha}$	0.0062 ± 0.0030	0.0012 ± 0.0008
const.	0.0087	0.0017
$a\ln 1/x$	0.0147	0.0027
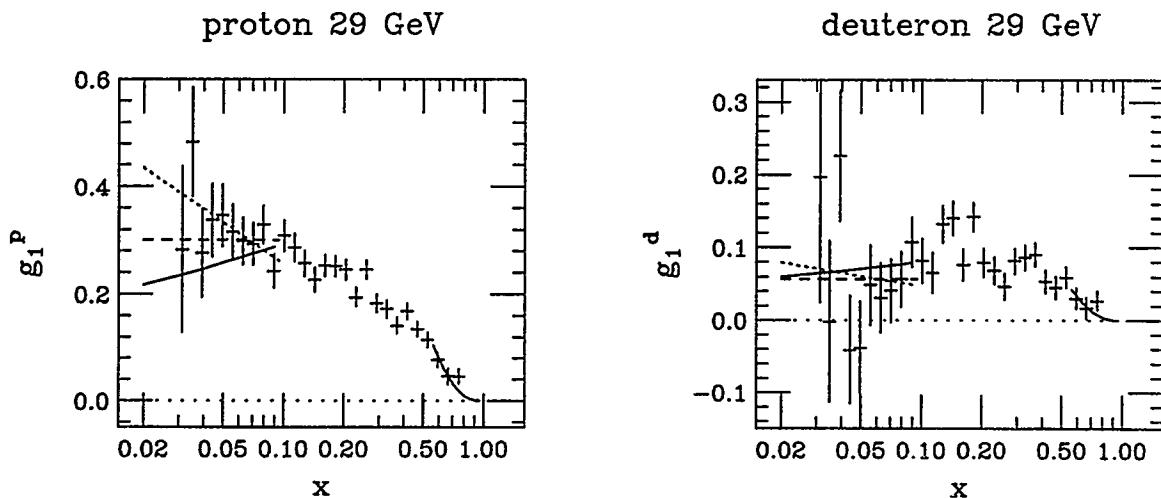
Figure 51 Proton and deuteron g_1 (both spectrometers combined) with low- and high-x fits. At low x, the Regge-style fit (solid line), the logarithmic style (dotted) and the fit to a constant g_1 (long dashes) are shown.

5.2.3 Assumption A_1 and A_2 are Q^2-Independent

All the results presented so far assumed that the ratio g_1/F_1 is independent of Q^2. This assumption was used to combine the 4.5° and 7° spectrometer and to extract g_1 at common Q^2.

A similar assumption, but also not exactly correct, is that A_1 and A_2 are independent of Q^2. For comparison, this assumption was used here to combine the two spectrometer data sets. For each spectrometer, first A_1 and A_2 were obtained from $A_{\parallel}$ and $A_{\perp}$. Then the 4.5° and 7° spectrometer data of A_1 and A_2 were combined, and from those g_1 was obtained. For the last step, again F_1 was taken at $Q^2 = 3\,\mathrm{GeV}^2$. Table 18 lists the results from this method together with the results from the method of assuming g_1/F_1 to be independent of Q^2, as well as the Ellis-Jaffe sum rule predictions. We see that there is noticeable difference in the result depending on the assumption. This discrepancy is not accounted for in the systematic error, and any result of the integral Γ_1 therefore has to be considered with care until agreement on the right extrapolation method is reached.

Table 18 Results for Γ_1^p and Γ_1^d at 29 GeV under the assumption of g_1/F_1 or of A_1 and A_2 being independent of Q^2. For the experimental results, only the statistical errors are shown.

	Γ_1^p	Γ_1^d
EJ pred.	0.160 ± 0.007	0.069 ± 0.004
g_1/F_1 ind.	0.127 ± 0.003	0.046 ± 0.003
A_1 & A_2 ind.	0.121 ± 0.003	0.043 ± 0.003

5.2.4 Dependence on Direction of Target Magnetic Field and Enhancement

A very important and easy check for a systematic trend is done by selecting only runs in which the target field was pointing forward and comparing this result to the results of runs in which the target field was reversed. Similarly, the enhancement of the target polarization was sometimes positive, sometimes negative. In Table 19, we present the results of the integral over the data region for the 29 GeV proton and deuteron results using different subsets. While the proton results all agree very well with each other, the deuteron results for the positive and negative enhancement with reversed B-field seem to be relatively far apart. Still, considering the large error bars and the overall agreement of the other data points, we conclude that no obvious trend can be seen with respect to the different subsets. We also note that some of these subsets contained no positron runs, and that their results have therefore no background correction.

Table 19 Results for the 29 GeV integral over the data region for different subsets of the runs. The B-field of the target was either pointing forward or reverse, while the enhancement of the target polarization was either positive or negative. The results are shown with only the statistical error. One more decimal point than usual is given for better comparison.

B-field & Enhancement	proton	deuteron
all runs	0.1202 ± 0.0032	0.0447 ± 0.0033
forward & positive	0.1234 ± 0.0054	0.0373 ± 0.0053
forward & negative	0.1204 ± 0.0058	0.0534 ± 0.0062
reverse & positive	0.1188 ± 0.0075	0.0660 ± 0.0083
reverse & negative	0.1137 ± 0.0080	0.0223 ± 0.0091
forward	0.1221 ± 0.0039	0.0440 ± 0.0040
reverse	0.1171 ± 0.0056	0.0453 ± 0.0062
positive	0.1219 ± 0.0044	0.0452 ± 0.0044
negative	0.1181 ± 0.0047	0.0443 ± 0.0051

5.2.5 Inclusion of pre-ROD Data

In none of the results mentioned so far, the so-called pre-ROD data were included. They consist of the runs from November 24, 1993 to December 1, 1993, corresponding to run numbers from 1000 to about 1244. On the Repair Opportunity Day (ROD) day of December 1, 1993, several hardware problems were fixed. Most importantly, the mirrors in the 4.5° 4-m Čerenkov detector were realigned, and the electronics was changed so that from that time on the 120th pulse was read out by the electronics. To take the problems prior to the ROD day into account, the analysis was modified for these pre-ROD runs:

- In the 4.5° spectrometer, no events were accepted for the analysis, in which the track pointed to the bottom of the shower counter ($y < -165$ mm in spectrometer coordinates), since these events had to cross the area where the misaligned mirror in the Čerenkov tank was located. The Čerenkov pulse heights of these events would have been too low to allow a reasonably good separation of electrons and pions.

- Instead of requiring that the recorded beam polarization agreed with the prediction from the pseudo-random number generator, the value of the MACH line (see Chapter 4) was used. In tests, the MACH line turned out to be the most stable of all lines with the polarization bits.

Unfortunately, another problem existed for the pre-ROD runs. The polarization of the proton/deuteron target was not known sufficiently well. Only two TE measurement were performed, one at the begin and one at the end of the period, and these measurements disagreed by about 20%. In addition, there are indications that the target material in the cup settled, leaving parts of the cup filled with only liquid helium. An estimation was made to adjust the measurements of the target polarizations to take the target settling into account, but the uncertainty on the target polarization is relatively high. Because of this, the pre-ROD data were excluded from the regular data analysis.

The results of the integral over the data range are shown in Table 20. We see that the statistical error is slightly smaller, while the central value changes noticeably.

161

Table 20 Results of the integral of g_1^p and g_1^d over the data range with and without pre-ROD data. Only the statistical error is given. For easier comparison, four digits behind the decimal point are shown. All other results presented in this dissertation were obtained without the pre-ROD data.

	proton	deuteron
with pre-ROD data	0.1176 ± 0.0029	0.0434 ± 0.0031
without pre-ROD data	0.1202 ± 0.0032	0.0447 ± 0.0033

5.3 Results from 9.7 and 16.2 GeV Data

The 9.7 and 16.2 GeV data were analyzed in the same way as the 29 GeV data. However, since no data in the transverse mode were collected for the 9.7 and 16.2 data, $A_\perp$ was assumed to be zero. Fig. 52 presents the asymmetry A_1 of both spectrometers for the 9.7 and 16 GeV proton data, and similarly Fig. 53 presents A_1 for the deuteron data. The quantity xg_1 is displayed in Fig. 54. Here the structure function was evaluated at common $Q^2 = 3$ GeV^2. The original binning was retained. We see that the 9.7 and 16 GeV deuteron results are not as statistically precise as the proton data. Furthermore, a relatively large portion of the 9.7 GeV data at high x was cut out because of the resonances appearing there. The 16.2 GeV data range from $Q^2 \approx 0.5$ GeV^2 to $Q^2 \approx 3$ GeV^2, while the 9.7 GeV data have Q^2 between 0.3 and 1 GeV^2. This means that most of the data were obtained from interactions with nucleons and not with single quarks.

An integration of the data does not make as much sense as for the 29 GeV data, since the data range is smaller for both data sets which would require a longer extrapolation. Furthermore, with such low Q^2, higher twist effects may influence the data. We still present the integrals over the data range in Table 21. For completeness, the 29 GeV integrals are again listed.
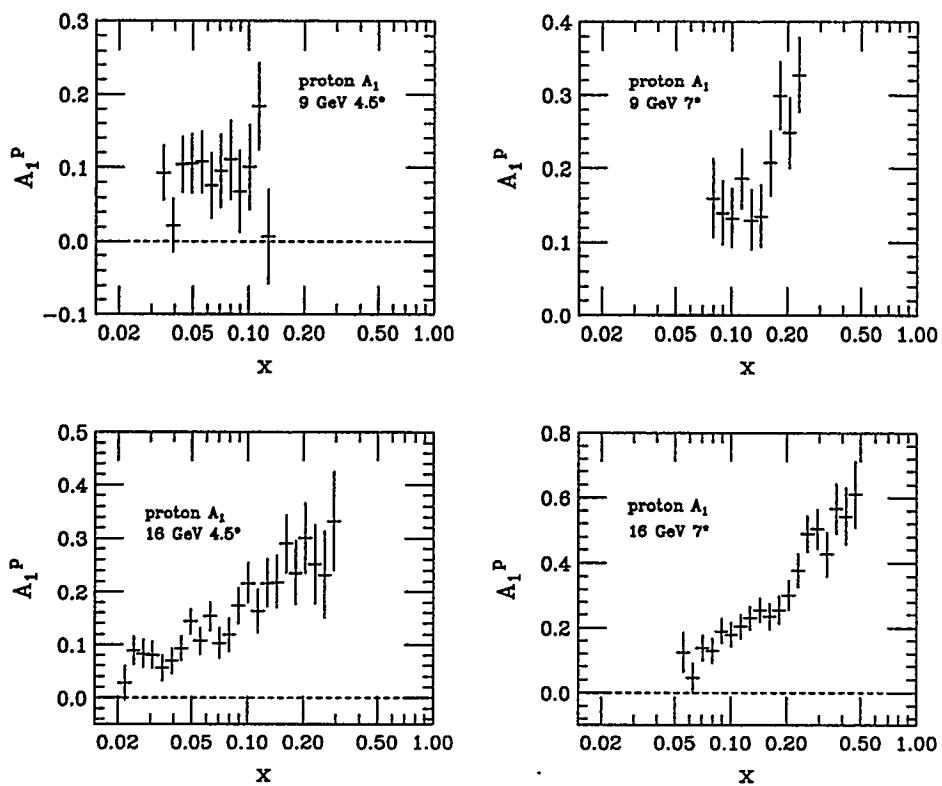
Figure 52 Asymmetry A_1^p from 9.7 and 16.2 GeV data.
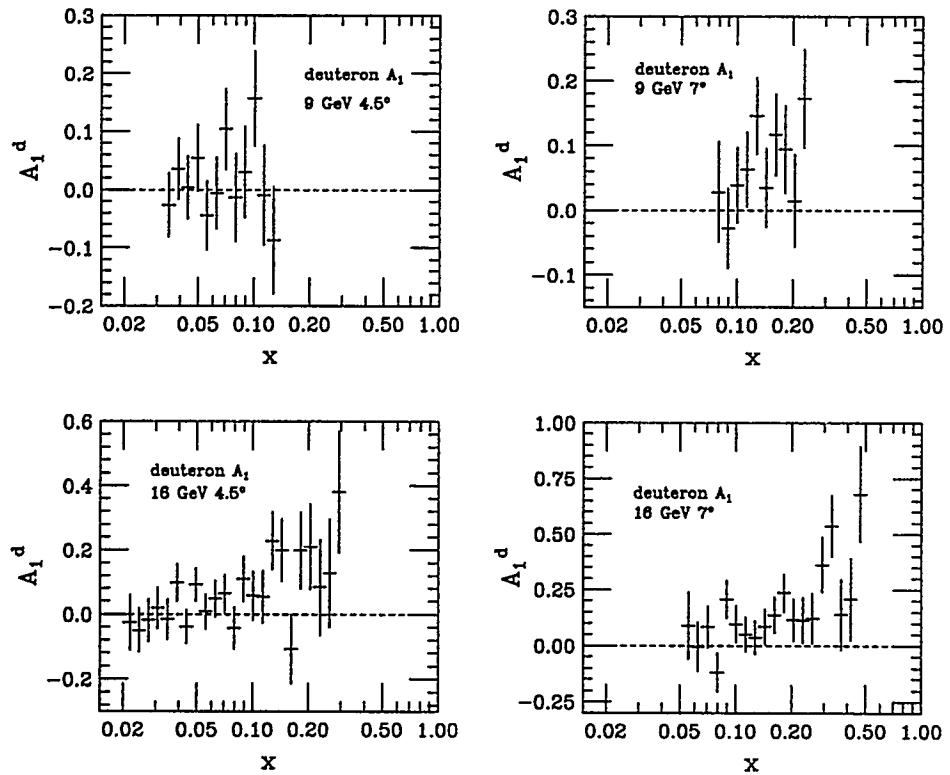
Figure 53 Asymmetry A_1^d from 9.7 and 16.2 GeV data.

163
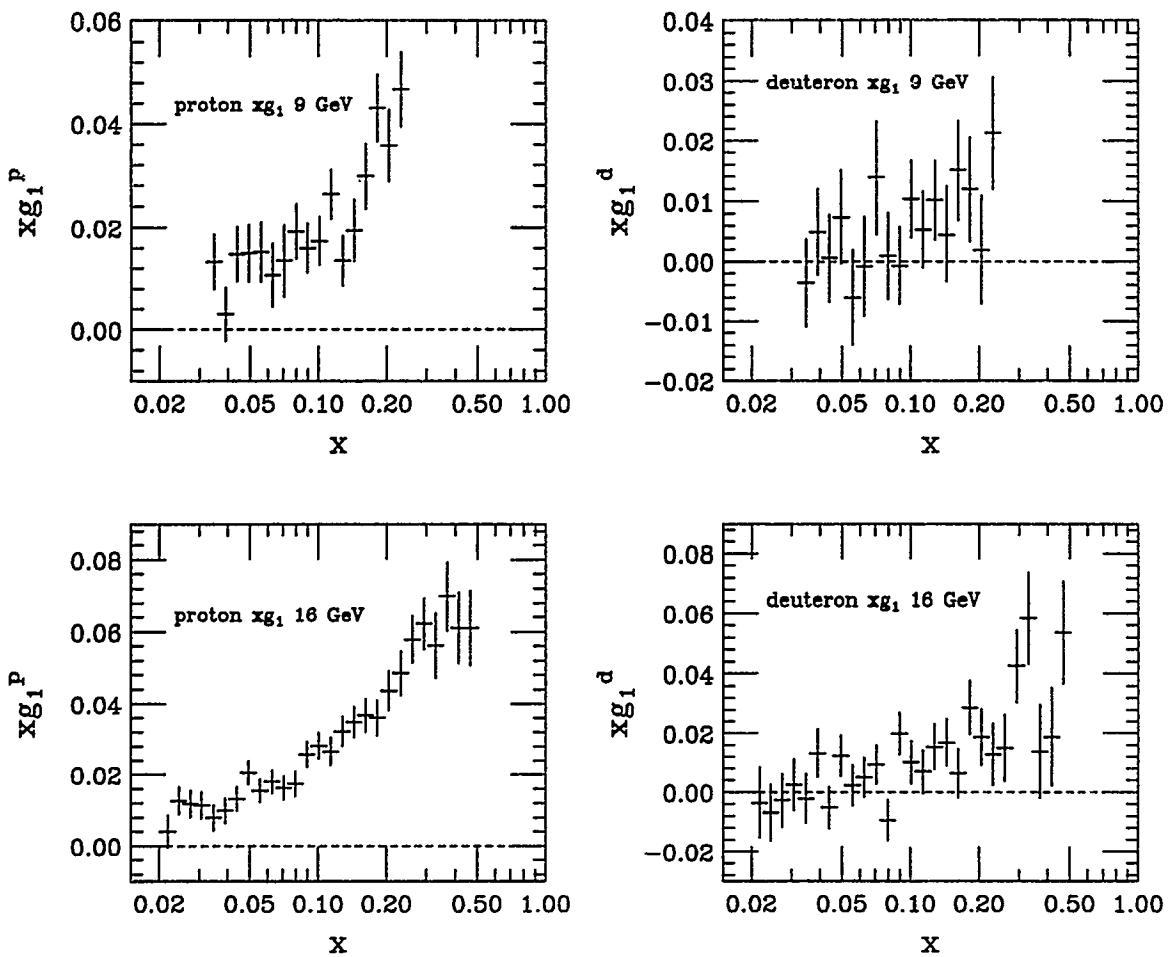
Figure 54 Spin-structure function g_1 for proton and deuteron at beam energies 9.7 and 16 GeV, both spectrometers combined, evolved to $Q^2 = 3$ GeV^2.

Table 21 Integrals of g_1 over x for the data range at $Q^2 = 3$ GeV^2. Only the statistical errors are shown.

beam energy	x data range	Γ_1^p (data range)	Γ_1^d (data range)
29 GeV	0.0290 – 0.7995	0.120 ± 0.003	0.045 ± 0.003
16 GeV	0.0204 – 0.4979	0.099 ± 0.003	0.042 ± 0.006
9 GeV	0.0327 – 0.2446	0.042 ± 0.003	0.012 ± 0.004

5.4 Application of Evolution Equations

This section presents results for the evolution of the E143 g_1^p and g_1^d results to common $Q_0^2 = 3$ GeV^2. All results mentioned so far used the assumption that the ratio g_1/F_1 is independent of Q^2. The only exception was the result which was calculated with the assumption that A_1 and A_2 are independent of Q^2. As mentioned before, both assumptions are only approximately correct. A better way to obtain g_1 at common Q^2 involves the GLAP evolution equations which were introduced earlier (see page 16). They take into account the leading twist QCD corrections, which are the corrections due to gluon interactions. They can be written in orders of α_s. The analysis presented here restricts itself to the lowest order terms of the leading twist corrections. Furthermore, no higher twist corrections (in orders of $1/\sqrt{Q^2}$, $1/Q^2$ etc.) were considered.

The analysis follows very closely the method described by Altarelli, Nason, and Ridolfi [17]. The code was first tested with the same input data as in Ref. [17]. The results were compared to the results of Ref. [17] and found to agree well. Then the code was applied to the E143 data.

The main equation for the analysis is Eq. (77):

$$
g_1^{p,d}(x, Q^2) - g_1^{p,d}(x, Q_0^2) = \frac{2}{9} \log \frac{\alpha_s(Q_0^2)}{\alpha_s(Q^2)}
$$
$$
\left[\int_x^1 \frac{dy}{y} g_1^{p,d}(y, Q^2) P_{qq}(x/y) + \frac{2}{3} \int_x^1 \frac{dy}{y} \Delta g(y, Q^2) P_{qg}(x/y) \right]
\tag{184}
$$

First, the spin-structure function g_1 was obtained with the x and Q^2 from the actual data in each bin, $i.e.$, no evolution to common Q^2 was performed. A fit to the data was used to analytically evaluate the first convolution integral according to Eq. (78). Like in Ref. [17], the fits to g_1 were chosen to be of the form

$$
g_1^p(x) = x^{0.2}(1-x)^3 (A + Bx + Cx^2 + Dx^3),
\tag{185}
$$

$$
g_1^d(x) = x^{0.2}(1-x)^6 (A + Bx + Cx^2 + Dx^3).
\tag{186}
$$

The parameters A, B, C, and D were the fit parameters. If a gluon contribution was assumed, also the second convolution integral in Eq. (184) was evaluated. Afterwards, Eq. (184) could be solved for $g_1(x, Q_0^2)$.

The gluon contribution was assumed to have the shape

$$\Delta g(x) = C_g x^{-0.3}(1-x)^7 \qquad (187)$$

with the normalization constant C_g such that

$$\int_0^1 \Delta g(x)\, dx = 5\frac{\alpha_s(Q^2_{\text{EMC}})}{\alpha_s(Q^2_{\text{EXP}})}. \qquad (188)$$

Here Q^2_{EMC} was the average Q^2 of the EMC experiment, which was $10.7\ \text{GeV}^2$, and Q^2_{EXP} was the Q^2 average of the experiment for which the data were evolved. For this analysis, Q^2_{EXP} was taken to be $3\ \text{GeV}^2$, the same as Q_0^2. Fig. 55 shows the integrand of the convolution integral

$$\frac{1}{z}\Delta P_{qg}\Delta g\left(\frac{x}{z}\right) \qquad (189)$$

with $C_g = 1$ for different x. The values of the strong coupling constant α_s were calculated by the formulas from Ref. [114] using three quark flavors and $\Lambda = 0.383$.
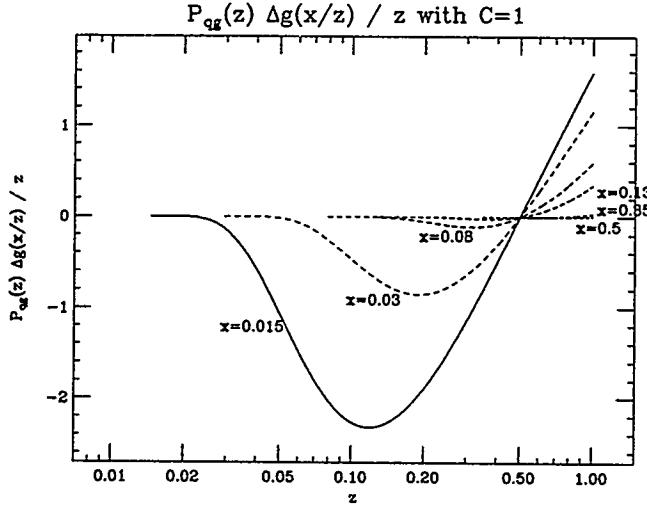
Figure 55 Integrand of gluon convolution integral with $C_g = 1$.

As mentioned above, the evolution equations were implemented by fitting the $g_1(x, Q^2)$ data to a function which was independent of Q^2. In order to obtain consistent results, we iterated the procedure. First, a fit to the experimental data was used to obtain the evolved $g_1(x, Q_0^2)$. Then, these evolved $g_1(x, Q_0^2)$ values were used for the fit, which again was used to calculate the convolution integrals and

166

to evolve $g_1(x, Q^2)$ to $g_1(x, Q_0^2)$, and so on. The changes were, however, relatively small, and a stable system developed after very few iterations. The results presented here were obtained with 10 iterations.

Fig. 56 displays the evolved and unevolved g_1 data points for the E143 proton 29 GeV data of the 4.5° spectrometer. The data points to the left with symbol × show the unevolved data points, $g_1(x, Q^2)$. To the right, at the same Bjorken x, but shifted for clarity, are the evolved data points, all evolved to $Q_0^2 = 3$ GeV^2. Here the points with error bars and symbol + are the results using the standard assumption of g_1/F_1 being Q^2-independent. The two other points are for the GLAP evolution equation results: The diamonds indicate the results without gluon contribution, the squares indicate the results with gluon contribution. Fig. 57 shows the results for the 7° spectrometer, and Figs. 58 and 59 present the data for the E143 deuteron 29 GeV structure function. As expected, the gluon contribution has an effect only in the low-x region.

The data from both spectrometers, both evolved to $Q_0^2 = 3$ GeV^2 with the GLAP evolution equations, were combined and used to obtain the integrals Γ_1^p, Γ_1^d, Γ_1^n, and $\Gamma_1^p - \Gamma_1^n$. Table 22 presents the results. The column under the title "evolution" indicates how the structure functions were evolved to the common $Q_0^2 = 3$ GeV^2. "g_1/F_1 Q^2-ind." indicates that the simple evolution as described in the earlier sections was used, assuming that g_1/F_1 was independent of Q^2. "GLAP, no gluons" and "GLAP, gluons" indicates that the GLAP evolution equations as described in this chapter were applied, either assuming no gluon contribution or assuming gluon contribution. The integrals were calculated in two ways from the g_1 results. The first way, noted as "standard", obtained the integral over the data range by summing up the data directly. The unmeasured region contributed through the extrapolations to $x = 0$ and $x = 1$ as described in the previous sections. For the second way, noted as "fit integrated", the fit to the structure functions was integrated from $x = 0$ to $x = 1$.

Table 22 shows that the GLAP evolution equations decrease the proton and deuteron integrals by 1 to 2%. The neutron integral Γ_1^n and the Bjorken integral $\Gamma_1^p - \Gamma_1^n$ change by similar amounts. Whether or not a gluon contribution is assumed

167
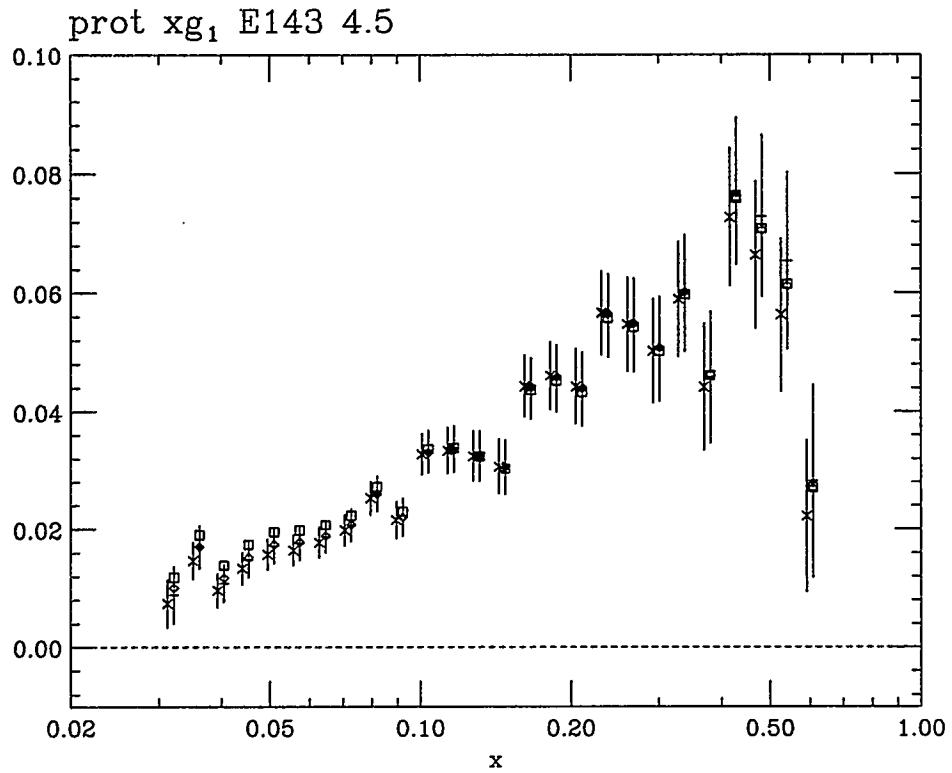
Figure 56   E143 proton 29 GeV g_1 results unevolved and evolved to $Q^2 = 3$ GeV^2 for 4.5° spectrometer data. See text for details.
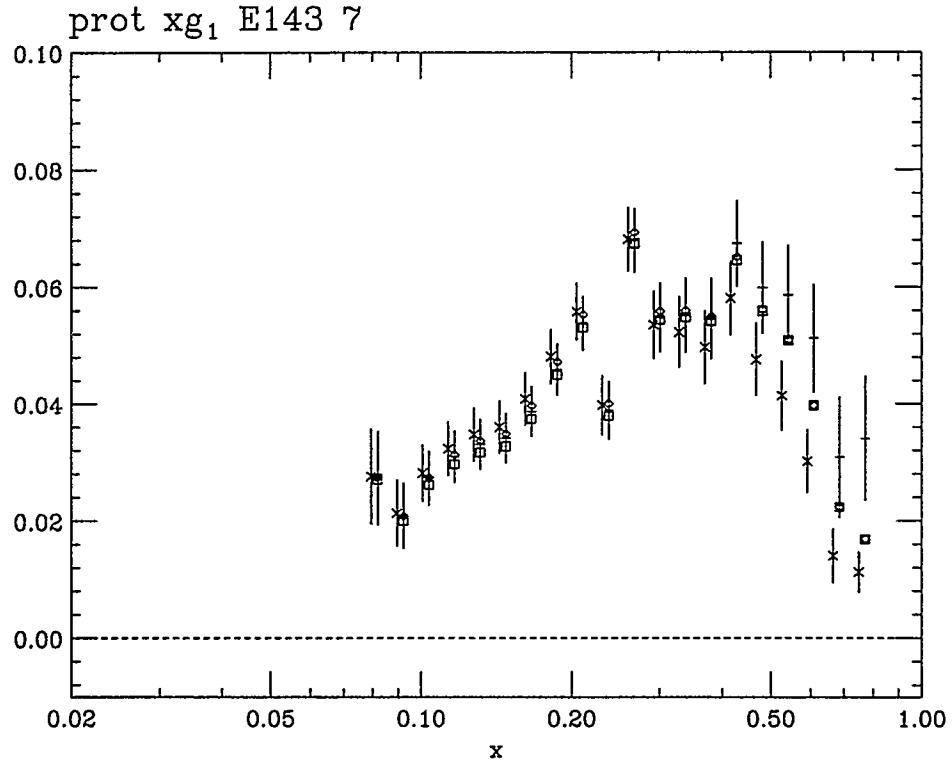
Figure 57   E143 proton 29 GeV g_1 data unevolved and evolved to $Q^2 = 3$ GeV^2 for 7° spectrometer data. See text for details.

168

deut xg$_1$ E143 4.5
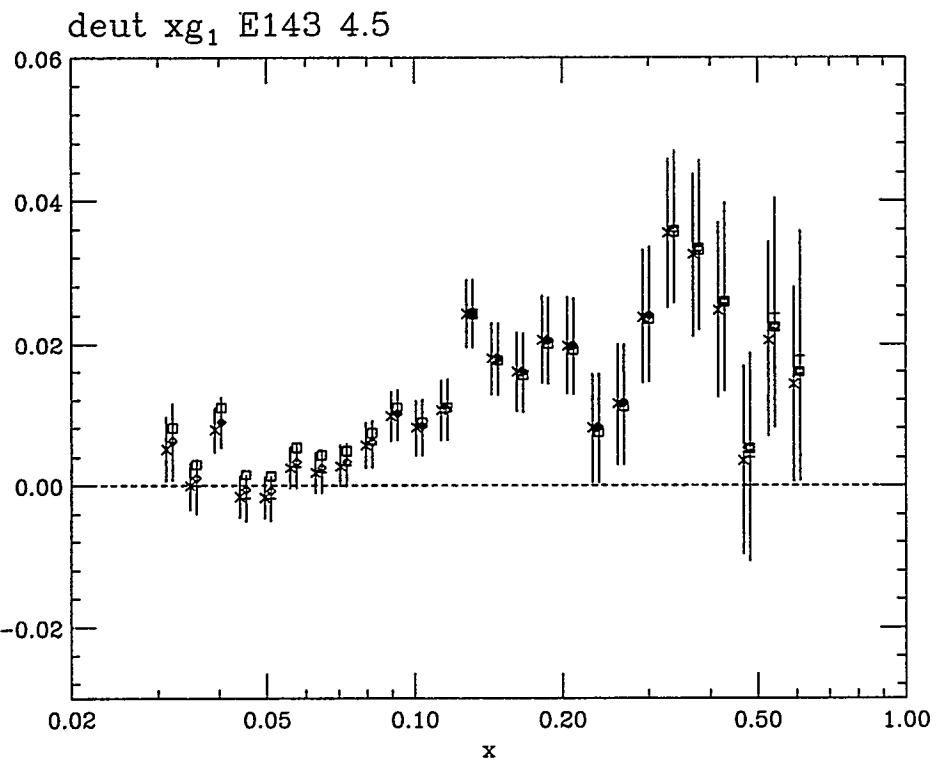
Figure 58 E143 deuteron 29 GeV g_1 results unevolved and evolved to $Q^2 = 3$ GeV^2 for 4.5° spectrometer data. See text for details.

deut xg$_1$ E143 7
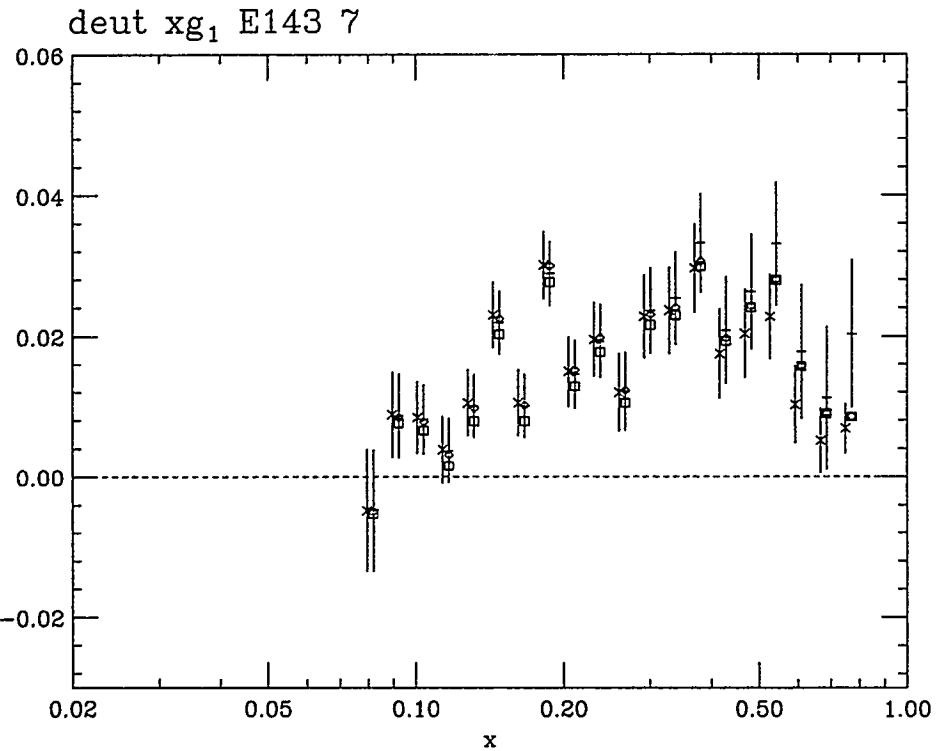
Figure 59 E143 deuteron 29 GeV g_1 results unevolved and evolved to $Q^2 = 3$ GeV^2 for 7° spectrometer data. See text for details.

169

Table 22 E143 results for the integral over g_1, integrated over the data range or over the full range from $x = 0$ to $x = 1$. In the first part, the proton integral Γ_1^p is shown, in the second the deuteron integral, in the third the neutron integral as calculated from the proton and deuteron structure functions. In the fourth section, noted with "b", is the integral of $g_1^p - g_1^n$. For better comparison, one more digit than usual is given.

data	evolution	integral	data range	0 to 1
E143 p	g_1/F_1 Q^2-ind.	standard	0.1202 ± 0.0032	0.1269 ± 0.0032
E143 p	GLAP, no gluons	standard	0.1158 ± 0.0025	0.1225 ± 0.0025
E143 p	GLAP, gluons	standard	0.1162 ± 0.0025	0.1234 ± 0.0025
E143 p	g_1/F_1 Q^2-ind.	fit integrated	0.1187	0.1276
E143 p	GLAP, no gluons	fit integrated	0.1149	0.1236
E143 p	GLAP, gluons	fit integrated	0.1150	0.1248
E143 d	g_1/F_1 Q^2-ind.	standard	0.0447 ± 0.0033	0.0461 ± 0.0033
E143 d	GLAP, no gluons	standard	0.0426 ± 0.0026	0.0441 ± 0.0026
E143 d	GLAP, gluons	standard	0.0429 ± 0.0026	0.0449 ± 0.0026
E143 d	g_1/F_1 Q^2-ind.	fit integrated	0.0413	0.0392
E143 d	GLAP, no gluons	fit integrated	0.0409	0.0397
E143 d	GLAP, gluons	fit integrated	0.0411	0.0419
E143 n	g_1/F_1 Q^2-ind.	standard		-0.0273 ± 0.0079
E143 n	GLAP, no gluons	standard		-0.0272 ± 0.0061
E143 n	GLAP, gluons	standard		-0.0264 ± 0.0061
E143 b	g_1/F_1 Q^2-ind.	standard		0.1542 ± 0.0097
E143 b	GLAP, no gluons	standard		0.1497 ± 0.0075
E143 b	GLAP, gluons	standard		0.1499 ± 0.0075

changes the results relatively little. We recall that the size of the gluon contribution with $\Delta g = 5$ at $Q^2 = 10.7$ GeV is actually larger than current estimates.

Integrating the fit causes a problem in the deuteron results. As can be seen in Table 22, the integral for the data range is larger than the integral over the whole x-region. This is due to the fit being negative at low x. For this reason, we did not consider this type of evaluation for the later cases, the neutron and Bjorken integral.

Several improvements of this method are possible: Instead of using fits of the type described in Eqs. (185) and (186), other fits to g_1 may be used. Instead of assuming Δg to have the functional form Eq. (187), alternate forms of Δg are possible. And of course, higher order leading twist or higher twist corrections may be included.

Overall, the application of the GLAP evolution equations was successful. The results obtained with the GLAP evolution equations are noticeably but not widely different results from the ones assuming g_1/F_1 being independent of Q^2. This indicates that the evolution presented in the papers published so far by the E143 collaboration is approximately correct. An evolution with more sophisticated GLAP equations promises better results. The disadvantage of using these evolution equations is, however, their model-dependence.

5.5 Comparison to Previously Published E143 Results

The E143 results for the spin-structure functions were published in four different letters. Ref. [90] presented g_1^p, Ref. [107] presented g_1^d, and Ref. [59] presented g_2^p and g_2^d. Their results covered only the data for the beam energy 29 GeV. Data from all three energies were published in Ref. [61] where the Q^2-dependence of g_1^p and g_1^d was studied. A long paper to summarize all results and discuss more details than the publications so far will be submitted at a later time.

The results in [90], [107], and [59] were obtained from the DST1 analysis, while the Q^2-dependence paper [61] used the DST2 analysis. The code which applied all necessary corrections to the raw asymmetries also improved with time, and therefore each of the four papers used slightly different code to extract the structure functions. Furthermore, the published proton result from Ref. [90] was used in Ref. [107] for the extraction of the neutron result and the test of the Bjorken sum rule, although it was obtained with different code than the deuteron result of Ref. [107]. The results of this dissertation were obtained with one consistent code. Table 23 compares the earlier published results for Γ_1^p and Γ_1^d with the results from this dissertation.

Table 23 Comparison of previously published E143 results of Γ_1 with the results from this dissertation.

	Ref. [90] and [107]	this work
Γ_1^p	0.127 ± 0.004 (stat)± 0.010 (syst)	0.127 ± 0.003 (stat)± 0.008 (syst)
Γ_1^d	0.042 ± 0.003 (stat)± 0.004 (syst)	0.046 ± 0.003 (stat)± 0.004 (syst)
Γ_1^n	-0.037 ± 0.008 (stat)± 0.011 (syst)	-0.027 ± 0.008 (stat)± 0.010 (syst)
$\Gamma_1^p - \Gamma_1^n$	0.163 ± 0.010 (stat)± 0.016 (syst)	0.154 ± 0.010 (stat)± 0.016 (syst)

Many changes were applied to the analysis code between the publication of the 29 GeV proton data [90] and the 29 GeV deuteron data [107]. Important changes were also made since the publication or the deuteron data [107]; the most important of them are listed here. [All changes were included in the analysis of this dissertation.]

- For the DST2 analysis, new and improved timing constants were used for the tracking code. Also, a correction was made to the Čerenkov times to take into account that a stronger pulse was reaching the threshold value of the discriminator slightly earlier than a weaker pulse. These new timing constants resulted in improved tracking.

- The corrections for the depolarization of the ammonia due to heating by the beam were applied. They increased each of the integrals Γ_1^p and Γ_1^d by about 0.0009 (absolute).

- The cut, how close the track had to point to the target, was raised from 10 mm to 13 mm.

- The range for the acceptable E/p ratio (E energy of cluster, p momentum of track) was originally 0.8 to 1.2. This range was later 0.8 to 1.25.

- Improved radiative corrections to the asymmetry were available.

- One more x-bin (bin #35) of the 4.5° 29 GeV data was used.

- All events above $Q^2 = 10$ GeV^2 were included. By error, these high-Q^2 data were excluded during the previous analyses. They have a noticeable, but not

strong influence on the highest x-bins.

- Several runs were taken out for various reasons; a few runs were recovered.

- The parameterization of the unpolarized structure function F_2 now includes the data from Ref. [11].

Most of these changes had already been implemented for the results of the Q^2-dependence paper [61]. The results from Ref. [61] also included the pre-ROD data. The pre-ROD data were not included for the proton paper [90], the deuteron paper [107], or the g_2-paper [59] and were also not included for this dissertation. The influence of the pre-ROD data is discussed in an earlier section of this chapter. Furthermore, a programming bug affected the results of the Q^2-dependence paper [61], decreasing Γ_1^p by about 0.0014 (absolute) and increasing Γ_1^d by about 0.002 (absolute). This mistake did not affect any of the earlier publications [59] [90] [107] and was corrected for the analysis presented in this dissertation.

CHAPTER 6

CONCLUSION AND OUTLOOK

The present work added substantial information to our knowledge about the nucleon spin-structure functions in deep-inelastic scattering. It provided — compared to previous experiments — high-precision data of both g_1^p and g_1^d for the x-range 0.03 to 0.8. The measurement of the transverse asymmetry $A_\perp$ was also highly improved, which allowed us to extract g_1 from the 29 GeV data without having to include a systematic error due to any assumption on $A_\perp$. Because both the proton and deuteron spin-structure functions were measured in the same experiment, the systematic errors were minimized when combining the proton and deuteron data to obtain the neutron structure function g_1^n or the integrals Γ_1^n or $\Gamma_1^p - \Gamma_1^n$.

The E143 results of the integrals Γ_1^p and Γ_1^d clearly confirm the violation of the Ellis-Jaffe sum rules for the proton and deuteron by at least three standard deviations in each case. The neutron integral Γ_1^n, obtained by combining the proton and deuteron results, was, however, not in clear disagreement with the Ellis-Jaffe sum rule of the neutron, since the disagreement was only slightly more than one standard deviation. The result of $\Gamma_1^p - \Gamma_1^n$ was found to be within less than one standard deviation of the Bjorken sum rule. These results are therefore consistent with the previous experiments and agree with conclusions that the Ellis-Jaffe sum rules are violated, but that the important Bjorken sum rule is confirmed.

Experiment E143 established, with the smallest error bars so far, that only about 30% of the nucleon spin is carried by quarks and that Δs is around -10%. This once again indicates the necessity to consider models in which other particles than only

quarks play a role for the spin structure of the nucleon, and to study the influence of SU(3) symmetry breaking.

The data were evolved to a common Q^2 not only with the usual approximate technique, but also with a second method, involving low-order GLAP evolution equations. The analysis using the E143 results of this dissertation indicates that this type of analysis has a measurable, but not large effect on the results. Similar and more elaborate studies of this kind are currently performed at various institutes.

The dissertation also presents measurements of the spin-structure function g_1^p and g_1^d for beam energies of 16.2 and 9.7 GeV. Their average Q^2 is lower than the one of the 29 GeV results. Together with the E143 29 GeV and data from earlier experiments, they provide a basis to test the Q^2-dependence of the spin-structure functions.

Another interesting question is the shape and magnitude of the spin-structure functions at higher x and lower Q^2. For this Q^2 range, perturbative QCD calculations, like the ones used to calculate the leading order QCD corrections, are no longer applicable. The E143 results, including the results from the resonance region, which were not part of this dissertation and which will be published soon, will serve at the high-Q^2 end as the continuation of future low-Q^2 experimental results.

During the coming years, the results of E143 may serve as input for phenomenological calculations and will be fundamental in tests of theoretical models. One of the currently interesting topics is the magnitude of the gluon distribution. Estimations of this quantity were already obtained with the previously published E143 results. New experiments at CERN and SLAC are expected to measure the gluon spin-distribution directly.

On the shorter term, new data on g_1 in the deep-inelastic scattering region will soon become available. SMC is continuing its measurements, hence decreasing the statistical errors of its results. New data are also soon expected to arrive from the HERMES [115] detector at the Deutsches Elektronen-Synchrotron (DESY) in Hamburg, Germany. Its kinematical coverage is similar to the one of E143, but it can also detect and identify outgoing hadrons (semi-inclusive reaction) and will be able to obtain additional information about the structure of the nucleons.

At SLAC, experiment E154 ran in Fall 1995. It is the first experiment using the upgraded A-Line, which allows beam energies of up to 50 GeV to be delivered to End Station A. Similarly to E142, it measured the neutron asymmetry $A_\parallel^n$ with a polarized ^{3}He target. E154 will publish its first results in short time. For early 1997, SLAC is expected to perform experiment E155, using essentially the same polarized proton and deuteron target as E143. Also running at a beam energy of 50 GeV, it will further reduce the statistical errors on the spin-structure function measurements and will be able to obtain data points at Bjorken x values as low as $x = 0.015$.

APPENDIX A

ASYMMETRY FOR
($L=2$)-STATE IN DEUTERON

In this appendix, the result of Eq. (80) is derived. The equation connects the asymmetry from D-state deuterons ($L=2$) to the asymmetry from S-state deuterons ($L=0$). Let us consider deuterons in the D-state 100% polarized to $J_z = +1$. As shown earlier, they have to 10% spin $S_z = +1$, to 30% spin $S_z = 0$ and to 60% spin $S_z = -1$. Let N be the total number of detected electrons, and N_{S_z} the number of electrons coming from deuterons with spin S_z. Obviously, $N = N_{+1} + N_0 + N_{-1}$. The subset N_{+1} is scattered with the same asymmetry as for the ($L = 0$)-state since for both sets the spin is $S_z = +1$. Therefore the asymmetry for the N_{+1}-subset is

$$\frac{N_{+1}^+ - N_{+1}^-}{N_{+1}^+ + N_{+1}^-} = A_{L=0}.$$ (190)

The subset N_0 is scattered without asymmetry, therefore $N_0^+ = N_0^- = N_0/2$. And the subset N_{-1} is scattered with the opposite asymmetry as the subset N_{+1}:

$$\frac{N_{-1}^+ - N_{-1}^-}{N_{-1}^+ + N_{-1}^-} = -A_{L=0}$$ (191)

The total asymmetry for the ($L = 2$)-state is

$$A_{L=2} = \frac{N_{+1}^+ + N_0^+ + N_{-1}^+ - N_{+1}^- - N_0^- - N_{-1}^-}{N_{+1}^+ + N_0^+ + N_{-1}^+ + N_{+1}^- + N_0^- + N_{-1}^-}.$$ (192)

This reduces to

$$A_{L=2} = \frac{N_{+1}^+ + N_{-1}^+ - N_{+1}^- - N_{-1}^-}{N}.$$ (193)

Since $N_{+1}^+ - N_{+1}^- = N_{+1}A_{L=0}$ and $N_{-1}^+ - N_{-1}^- = -N_{-1}A_{L=0}$ we obtain

$$A_{L=2} = \frac{N_{+1}A_{L=0} - N_{-1}A_{L=0}}{N} =$$

$$= \frac{0.1NA_{L=0} - 0.6NA_{L=0}}{N} =$$ (194)

$$= 0.1A_{L=0} - 0.6A_{L=0} = -0.5A_{L=0}.$$

This is the result given in Eq. (80).

APPENDIX B

TABLES: PROTON 29 GEV

Table 24 $A_\parallel$ and $A_\perp$ proton 29 GeV results for the 4.5° spectrometer with statistical errors. The borders of the x-bins are listed in Table 13. $A_\parallel$(uncorr) and $A_\perp$(uncorr) are the asymmetries not yet corrected for radiative effects.

$<x>$	$<Q^2>$	$A_\parallel$(uncorr)	$A_\perp$(uncorr)	$A_\parallel$	$A_\perp$
0.031	1.27	0.034 ± 0.020	0.081 ± 0.052	0.044 ± 0.025	0.084 ± 0.066
0.035	1.40	0.077 ± 0.015	0.034 ± 0.033	0.086 ± 0.019	0.037 ± 0.040
0.039	1.52	0.046 ± 0.014	-0.022 ± 0.023	0.055 ± 0.016	-0.019 ± 0.027
0.044	1.65	0.064 ± 0.013	-0.003 ± 0.019	0.072 ± 0.014	0.001 ± 0.021
0.049	1.78	0.072 ± 0.012	0.010 ± 0.017	0.079 ± 0.013	0.014 ± 0.019
0.056	1.92	0.072 ± 0.012	-0.004 ± 0.016	0.078 ± 0.013	0.000 ± 0.017
0.063	2.07	0.074 ± 0.011	0.005 ± 0.015	0.079 ± 0.012	0.009 ± 0.016
0.071	2.22	0.078 ± 0.011	0.005 ± 0.014	0.083 ± 0.011	0.009 ± 0.014
0.079	2.38	0.096 ± 0.011	-0.022 ± 0.014	0.100 ± 0.011	-0.017 ± 0.014
0.090	2.53	0.076 ± 0.012	-0.002 ± 0.014	0.079 ± 0.012	0.002 ± 0.015
0.101	2.69	0.109 ± 0.012	-0.004 ± 0.015	0.112 ± 0.012	0.001 ± 0.015
0.113	2.84	0.104 ± 0.012	-0.019 ± 0.015	0.106 ± 0.012	-0.015 ± 0.015
0.128	3.00	0.093 ± 0.013	-0.004 ± 0.015	0.095 ± 0.013	0.001 ± 0.016
0.144	3.15	0.083 ± 0.013	-0.025 ± 0.016	0.084 ± 0.013	-0.020 ± 0.016
0.162	3.30	0.110 ± 0.013	0.008 ± 0.016	0.111 ± 0.013	0.012 ± 0.016
0.182	3.45	0.107 ± 0.014	-0.011 ± 0.017	0.108 ± 0.014	-0.006 ± 0.017
0.205	3.59	0.094 ± 0.014	0.035 ± 0.017	0.095 ± 0.014	0.040 ± 0.017
0.230	3.73	0.115 ± 0.015	-0.008 ± 0.018	0.116 ± 0.015	-0.004 ± 0.018
0.259	3.85	0.105 ± 0.015	0.008 ± 0.019	0.106 ± 0.015	0.012 ± 0.019
0.292	3.98	0.094 ± 0.016	-0.037 ± 0.020	0.095 ± 0.016	-0.033 ± 0.020
0.328	4.09	0.108 ± 0.018	-0.042 ± 0.022	0.109 ± 0.018	-0.038 ± 0.022
0.370	4.20	0.078 ± 0.020	0.036 ± 0.025	0.080 ± 0.020	0.040 ± 0.025
0.416	4.30	0.138 ± 0.023	-0.016 ± 0.028	0.140 ± 0.022	-0.012 ± 0.028
0.468	4.40	0.138 ± 0.026	-0.060 ± 0.033	0.140 ± 0.026	-0.057 ± 0.033
0.526	4.47	0.131 ± 0.030	-0.035 ± 0.038	0.133 ± 0.030	-0.032 ± 0.038
0.592	4.55	0.062 ± 0.036	-0.055 ± 0.046	0.064 ± 0.036	-0.053 ± 0.046

Table 25 $A_{\parallel}$ and $A_{\perp}$ proton 29 GeV results for the 7° spectrometer with statistical errors. $A_{\parallel}$(uncorr) and $A_{\perp}$(uncorr) are the asymmetries not yet corrected for radiative effects.

$<x>$	$<Q^2>$	$A_{\parallel}$(uncorr)	$A_{\perp}$(uncorr)	$A_{\parallel}$	$A_{\perp}$
0.079	3.17	0.142 ± 0.039	-0.077 ± 0.067	0.150 ± 0.043	-0.070 ± 0.073
0.090	3.48	0.101 ± 0.027	0.020 ± 0.039	0.107 ± 0.029	0.026 ± 0.042
0.101	3.79	0.132 ± 0.023	0.012 ± 0.029	0.137 ± 0.024	0.019 ± 0.031
0.113	4.11	0.149 ± 0.021	-0.017 ± 0.026	0.153 ± 0.022	-0.010 ± 0.026
0.128	4.43	0.156 ± 0.020	-0.044 ± 0.024	0.158 ± 0.020	-0.037 ± 0.025
0.144	4.78	0.153 ± 0.019	-0.003 ± 0.023	0.155 ± 0.019	0.004 ± 0.023
0.162	5.13	0.167 ± 0.019	0.007 ± 0.022	0.168 ± 0.019	0.013 ± 0.022
0.182	5.49	0.188 ± 0.019	0.032 ± 0.022	0.188 ± 0.018	0.038 ± 0.022
0.205	5.86	0.212 ± 0.019	0.013 ± 0.022	0.212 ± 0.018	0.019 ± 0.022
0.230	6.24	0.148 ± 0.019	-0.007 ± 0.022	0.148 ± 0.019	-0.001 ± 0.022
0.259	6.60	0.247 ± 0.020	0.000 ± 0.023	0.248 ± 0.020	0.006 ± 0.023
0.292	6.97	0.194 ± 0.021	-0.023 ± 0.024	0.195 ± 0.021	-0.017 ± 0.024
0.328	7.34	0.193 ± 0.022	-0.034 ± 0.026	0.193 ± 0.022	-0.028 ± 0.026
0.370	7.69	0.188 ± 0.024	0.014 ± 0.028	0.189 ± 0.024	0.019 ± 0.028
0.416	8.04	0.242 ± 0.026	-0.057 ± 0.031	0.243 ± 0.026	-0.053 ± 0.031
0.468	8.37	0.221 ± 0.030	0.003 ± 0.034	0.222 ± 0.029	0.008 ± 0.034
0.526	8.68	0.231 ± 0.034	0.000 ± 0.040	0.232 ± 0.033	0.003 ± 0.040
0.592	8.99	0.221 ± 0.041	-0.023 ± 0.048	0.223 ± 0.040	-0.020 ± 0.048
0.666	9.26	0.151 ± 0.051	-0.031 ± 0.059	0.154 ± 0.050	-0.029 ± 0.059
0.750	9.53	0.218 ± 0.068	-0.070 ± 0.080	0.222 ± 0.068	-0.069 ± 0.081

Table 26 g_1/F_1, A_1 and A_2 proton 29 GeV results (both spectrometers). The first error is the statistical error, the second error on A_1 is the systematic error. The highest x-bins were pairwise combined.

$<x>$	$<Q^2>$	g_1/F_1	A_1	A_2
0.031	1.27	0.062 ± 0.034	$0.055 \pm 0.034 \pm 0.007$	0.140 ± 0.108
0.035	1.40	0.119 ± 0.025	$0.115 \pm 0.025 \pm 0.007$	0.066 ± 0.066
0.039	1.52	0.076 ± 0.023	$0.078 \pm 0.023 \pm 0.007$	-0.029 ± 0.045
0.044	1.65	0.104 ± 0.021	$0.104 \pm 0.021 \pm 0.007$	0.006 ± 0.036
0.049	1.78	0.120 ± 0.020	$0.119 \pm 0.020 \pm 0.007$	0.030 ± 0.032
0.056	1.92	0.123 ± 0.020	$0.124 \pm 0.020 \pm 0.007$	0.007 ± 0.030
0.063	2.07	0.132 ± 0.019	$0.130 \pm 0.019 \pm 0.008$	0.025 ± 0.029
0.071	2.22	0.145 ± 0.020	$0.144 \pm 0.020 \pm 0.008$	0.027 ± 0.028
0.079	2.47	0.184 ± 0.020	$0.188 \pm 0.020 \pm 0.009$	-0.026 ± 0.028
0.090	2.77	0.152 ± 0.020	$0.151 \pm 0.020 \pm 0.009$	0.023 ± 0.028
0.101	3.09	0.216 ± 0.020	$0.216 \pm 0.020 \pm 0.010$	0.028 ± 0.028
0.113	3.40	0.226 ± 0.020	$0.229 \pm 0.021 \pm 0.011$	-0.008 ± 0.028
0.128	3.71	0.226 ± 0.021	$0.231 \pm 0.021 \pm 0.012$	-0.006 ± 0.028
0.144	4.04	0.224 ± 0.022	$0.228 \pm 0.022 \pm 0.013$	0.001 ± 0.029
0.172	4.56	0.295 ± 0.016	$0.292 \pm 0.017 \pm 0.014$	0.066 ± 0.021
0.218	5.24	0.326 ± 0.019	$0.322 \pm 0.019 \pm 0.017$	0.080 ± 0.024
0.276	5.89	0.416 ± 0.023	$0.424 \pm 0.024 \pm 0.021$	0.056 ± 0.029
0.350	6.57	0.419 ± 0.030	$0.427 \pm 0.031 \pm 0.026$	0.072 ± 0.038
0.443	7.23	0.610 ± 0.042	$0.645 \pm 0.045 \pm 0.032$	0.075 ± 0.053
0.560	7.79	0.640 ± 0.064	$0.684 \pm 0.070 \pm 0.037$	0.148 ± 0.083
0.711	9.41	0.571 ± 0.133	$0.642 \pm 0.147 \pm 0.042$	0.075 ± 0.169

Table 27 Results of structure function g_1 from the proton 29 GeV 4.5° spectrometer data with statistical errors. $g_1(\exp)$ is the structure function at the measured x and Q^2 value, while $g_1(3 \text{ GeV}^2)$ is the structure function evolved to common $Q^2 = 3 \text{ GeV}^2$. The evolution to $Q^2 = 3 \text{ GeV}^2$ was performed with the assumption that g_1/F_1 is Q^2-independent, not with GLAP evolution equations.

$<x>$	$<Q^2>$	$g_1(3 \text{ GeV}^2)$	$g_1(\exp)$
0.031	1.27	0.283 ± 0.155	0.239 ± 0.131
0.035	1.40	0.483 ± 0.102	0.418 ± 0.089
0.039	1.52	0.277 ± 0.082	0.245 ± 0.072
0.044	1.65	0.337 ± 0.068	0.304 ± 0.061
0.049	1.78	0.347 ± 0.058	0.318 ± 0.053
0.056	1.92	0.316 ± 0.051	0.295 ± 0.047
0.063	2.07	0.299 ± 0.044	0.283 ± 0.041
0.071	2.22	0.293 ± 0.040	0.281 ± 0.038
0.079	2.38	0.328 ± 0.037	0.318 ± 0.036
0.090	2.53	0.246 ± 0.036	0.241 ± 0.036
0.101	2.69	0.330 ± 0.036	0.325 ± 0.035
0.113	2.84	0.297 ± 0.035	0.295 ± 0.034
0.128	3.00	0.254 ± 0.034	0.254 ± 0.034
0.144	3.15	0.213 ± 0.033	0.214 ± 0.033
0.162	3.30	0.272 ± 0.032	0.274 ± 0.032
0.182	3.45	0.250 ± 0.031	0.253 ± 0.032
0.205	3.59	0.214 ± 0.031	0.216 ± 0.031
0.230	3.73	0.244 ± 0.031	0.246 ± 0.031
0.259	3.85	0.211 ± 0.030	0.211 ± 0.031
0.292	3.98	0.173 ± 0.030	0.172 ± 0.030
0.328	4.09	0.183 ± 0.030	0.179 ± 0.030
0.370	4.20	0.124 ± 0.030	0.119 ± 0.029
0.416	4.30	0.185 ± 0.030	0.175 ± 0.028
0.468	4.40	0.156 ± 0.029	0.142 ± 0.027
0.526	4.47	0.124 ± 0.028	0.107 ± 0.024
0.592	4.55	0.048 ± 0.028	0.038 ± 0.022

Table 28 Results of structure function g_1 from the proton 29 GeV 7° spectrometer data with statistical errors. $g_1(\text{exp})$ is the structure function at the measured x and Q^2 value. $g_1(3\ \text{GeV}^2)$ is the structure function evolved to common $Q^2 = 3\ \text{GeV}^2$. The evolution to $Q^2 = 3\ \text{GeV}^2$ was performed with the assumption that g_1/F_1 is Q^2-independent.

$<x>$	$<Q^2>$	$g_1(3\ \text{GeV}^2)$	$g_1(\text{exp})$
0.079	3.17	0.345 ± 0.101	0.347 ± 0.102
0.090	3.48	0.233 ± 0.062	0.238 ± 0.064
0.101	3.79	0.271 ± 0.047	0.280 ± 0.048
0.113	4.11	0.273 ± 0.039	0.285 ± 0.041
0.128	4.43	0.259 ± 0.034	0.272 ± 0.036
0.144	4.78	0.238 ± 0.030	0.251 ± 0.031
0.162	5.13	0.240 ± 0.027	0.253 ± 0.028
0.182	5.49	0.252 ± 0.024	0.265 ± 0.026
0.205	5.86	0.262 ± 0.023	0.273 ± 0.024
0.230	6.24	0.169 ± 0.022	0.173 ± 0.022
0.259	6.60	0.262 ± 0.021	0.263 ± 0.021
0.292	6.97	0.188 ± 0.020	0.184 ± 0.020
0.328	7.34	0.168 ± 0.019	0.159 ± 0.018
0.370	7.69	0.148 ± 0.019	0.134 ± 0.017
0.416	8.04	0.162 ± 0.018	0.140 ± 0.015
0.468	8.37	0.128 ± 0.017	0.102 ± 0.013
0.526	8.68	0.111 ± 0.016	0.079 ± 0.011
0.592	8.99	0.087 ± 0.016	0.051 ± 0.009
0.666	9.26	0.046 ± 0.015	0.021 ± 0.007
0.750	9.53	0.045 ± 0.014	0.015 ± 0.005

Table 29 Results of structure function g_1 for proton 29 GeV (both spectrometers) evolved to $Q^2 = 3$ GeV^2. The highest x-bins were pairwise combined. The first error is the statistical error, the second is the systematic error. The evolution to $Q^2 = 3$ GeV^2 was performed with the assumption that g_1/F_1 is Q^2-independent.

$<x>$	$<Q^2>$	$g_1(3 \text{ GeV}^2)$
0.031	1.27	$0.283 \pm 0.155 \pm 0.035$
0.035	1.40	$0.483 \pm 0.102 \pm 0.031$
0.039	1.52	$0.277 \pm 0.082 \pm 0.027$
0.044	1.65	$0.337 \pm 0.068 \pm 0.024$
0.049	1.78	$0.347 \pm 0.058 \pm 0.022$
0.056	1.92	$0.316 \pm 0.051 \pm 0.021$
0.063	2.07	$0.299 \pm 0.044 \pm 0.020$
0.071	2.22	$0.293 \pm 0.040 \pm 0.019$
0.079	2.47	$0.330 \pm 0.035 \pm 0.018$
0.090	2.77	$0.243 \pm 0.031 \pm 0.017$
0.101	3.09	$0.308 \pm 0.028 \pm 0.016$
0.113	3.40	$0.287 \pm 0.026 \pm 0.015$
0.128	3.71	$0.257 \pm 0.024 \pm 0.015$
0.144	4.04	$0.226 \pm 0.022 \pm 0.014$
0.172	4.56	$0.252 \pm 0.014 \pm 0.013$
0.218	5.24	$0.219 \pm 0.013 \pm 0.012$
0.276	5.89	$0.213 \pm 0.012 \pm 0.011$
0.350	6.57	$0.156 \pm 0.011 \pm 0.009$
0.443	7.23	$0.151 \pm 0.010 \pm 0.008$
0.560	7.79	$0.095 \pm 0.010 \pm 0.006$
0.711	9.41	$0.046 \pm 0.010 \pm 0.003$

APPENDIX C

TABLES: DEUTERON 29 GEV

Table 30 $A_\parallel$ and $A_\perp$ deuteron 29 GeV results for the 4.5° spectrometer with statistical errors. $A_\parallel$(uncorr) and $A_\perp$(uncorr) are the asymmetries not yet corrected for radiative effects.

$<x>$	$<Q^2>$	$A_\parallel$(uncorr)	$A_\perp$(uncorr)	$A_\parallel$	$A_\perp$
0.031	1.27	0.039 ± 0.025	-0.017 ± 0.071	0.035 ± 0.030	-0.014 ± 0.083
0.035	1.40	0.007 ± 0.018	-0.094 ± 0.048	0.003 ± 0.021	-0.092 ± 0.055
0.039	1.52	0.047 ± 0.017	0.089 ± 0.043	0.043 ± 0.019	0.091 ± 0.049
0.044	1.65	-0.007 ± 0.015	0.045 ± 0.037	-0.011 ± 0.017	0.047 ± 0.040
0.049	1.78	-0.006 ± 0.014	0.011 ± 0.032	-0.010 ± 0.015	0.013 ± 0.034
0.056	1.92	0.015 ± 0.014	0.029 ± 0.030	0.011 ± 0.014	0.032 ± 0.032
0.063	2.07	0.013 ± 0.013	-0.031 ± 0.028	0.010 ± 0.014	-0.029 ± 0.029
0.071	2.22	0.017 ± 0.013	-0.037 ± 0.027	0.014 ± 0.013	-0.035 ± 0.028
0.079	2.38	0.026 ± 0.013	0.015 ± 0.027	0.023 ± 0.013	0.017 ± 0.028
0.090	2.53	0.040 ± 0.014	0.002 ± 0.028	0.038 ± 0.014	0.005 ± 0.029
0.101	2.69	0.030 ± 0.014	0.037 ± 0.029	0.028 ± 0.014	0.039 ± 0.030
0.113	2.84	0.039 ± 0.015	-0.018 ± 0.030	0.037 ± 0.015	-0.015 ± 0.031
0.128	3.00	0.080 ± 0.015	-0.025 ± 0.031	0.079 ± 0.015	-0.023 ± 0.031
0.144	3.15	0.054 ± 0.015	0.008 ± 0.032	0.053 ± 0.015	0.011 ± 0.032
0.162	3.30	0.047 ± 0.016	-0.024 ± 0.033	0.046 ± 0.016	-0.022 ± 0.033
0.182	3.45	0.055 ± 0.017	-0.003 ± 0.034	0.054 ± 0.016	0.000 ± 0.034
0.205	3.59	0.049 ± 0.017	0.002 ± 0.036	0.049 ± 0.017	0.004 ± 0.036
0.230	3.73	0.020 ± 0.019	-0.028 ± 0.038	0.020 ± 0.018	-0.025 ± 0.038
0.259	3.85	0.021 ± 0.020	0.124 ± 0.041	0.021 ± 0.019	0.126 ± 0.041
0.292	3.98	0.054 ± 0.021	-0.030 ± 0.044	0.054 ± 0.021	-0.028 ± 0.044
0.328	4.09	0.077 ± 0.023	0.025 ± 0.049	0.078 ± 0.023	0.027 ± 0.049
0.370	4.20	0.071 ± 0.026	0.045 ± 0.055	0.072 ± 0.026	0.047 ± 0.055
0.416	4.30	0.062 ± 0.030	-0.081 ± 0.063	0.063 ± 0.030	-0.080 ± 0.063
0.468	4.40	0.009 ± 0.036	-0.005 ± 0.074	0.010 ± 0.035	-0.004 ± 0.075
0.526	4.47	0.064 ± 0.042	-0.021 ± 0.089	0.064 ± 0.042	-0.020 ± 0.090
0.592	4.55	0.057 ± 0.052	-0.075 ± 0.109	0.057 ± 0.052	-0.073 ± 0.110

Table 31 $A_\parallel$ and $A_\perp$ deuteron 29 GeV results for the 7° spectrometer. $A_\parallel$(uncorr) and $A_\perp$(uncorr) are the asymmetries not yet corrected for radiative effects.

$<x>$	$<Q^2>$	$A_\parallel$(uncorr)	$A_\perp$(uncorr)	$A_\parallel$	$A_\perp$
0.079	3.17	-0.016 ± 0.046	-0.115 ± 0.111	-0.021 ± 0.049	-0.111 ± 0.119
0.090	3.48	0.047 ± 0.032	0.082 ± 0.069	0.043 ± 0.033	0.086 ± 0.072
0.101	3.79	0.047 ± 0.026	0.023 ± 0.053	0.043 ± 0.027	0.026 ± 0.054
0.113	4.11	0.025 ± 0.024	-0.037 ± 0.047	0.022 ± 0.024	-0.034 ± 0.049
0.128	4.44	0.057 ± 0.023	-0.030 ± 0.044	0.053 ± 0.023	-0.026 ± 0.045
0.144	4.78	0.112 ± 0.022	0.005 ± 0.042	0.109 ± 0.022	0.009 ± 0.043
0.162	5.13	0.053 ± 0.022	-0.037 ± 0.041	0.051 ± 0.022	-0.034 ± 0.041
0.182	5.49	0.134 ± 0.022	0.031 ± 0.041	0.133 ± 0.021	0.034 ± 0.041
0.205	5.86	0.068 ± 0.022	-0.027 ± 0.041	0.067 ± 0.022	-0.023 ± 0.041
0.230	6.23	0.088 ± 0.023	-0.056 ± 0.043	0.088 ± 0.023	-0.053 ± 0.043
0.259	6.60	0.051 ± 0.024	0.010 ± 0.045	0.051 ± 0.024	0.013 ± 0.045
0.292	6.97	0.101 ± 0.026	-0.039 ± 0.048	0.101 ± 0.025	-0.036 ± 0.048
0.328	7.33	0.106 ± 0.028	-0.023 ± 0.052	0.108 ± 0.027	-0.021 ± 0.052
0.370	7.69	0.142 ± 0.030	-0.026 ± 0.057	0.143 ± 0.030	-0.024 ± 0.057
0.416	8.03	0.089 ± 0.034	0.037 ± 0.063	0.090 ± 0.033	0.039 ± 0.063
0.468	8.37	0.124 ± 0.038	-0.020 ± 0.072	0.125 ± 0.038	-0.017 ± 0.072
0.526	8.67	0.171 ± 0.045	-0.021 ± 0.085	0.171 ± 0.045	-0.019 ± 0.085
0.592	8.98	0.094 ± 0.055	0.156 ± 0.103	0.093 ± 0.055	0.159 ± 0.103
0.666	9.26	0.087 ± 0.070	-0.150 ± 0.131	0.085 ± 0.069	-0.148 ± 0.131
0.750	9.52	0.191 ± 0.095	-0.063 ± 0.174	0.189 ± 0.095	-0.060 ± 0.175

Table 32 g_1/F_1, A_1 and A_2 deuteron 29 GeV results (both spectrometers). The first error is the statistical error, the second error on A_1 is the systematic error. The highest x-bins were pairwise combined.

$<x>$	$<Q^2>$	g_1/F_1	A_1	A_2
0.031	1.27	0.045 ± 0.039	$0.046 \pm 0.039 \pm 0.007$	-0.022 ± 0.137
0.035	1.40	-0.001 ± 0.028	$0.008 \pm 0.028 \pm 0.007$	-0.152 ± 0.091
0.039	1.52	0.065 ± 0.026	$0.056 \pm 0.026 \pm 0.006$	0.154 ± 0.081
0.044	1.65	-0.013 ± 0.024	$-0.018 \pm 0.024 \pm 0.006$	0.079 ± 0.068
0.049	1.78	-0.014 ± 0.023	$-0.015 \pm 0.023 \pm 0.005$	0.023 ± 0.060
0.056	1.92	0.020 ± 0.023	$0.016 \pm 0.023 \pm 0.004$	0.057 ± 0.056
0.063	2.07	0.014 ± 0.023	$0.019 \pm 0.023 \pm 0.004$	-0.053 ± 0.054
0.071	2.22	0.021 ± 0.023	$0.027 \pm 0.023 \pm 0.004$	-0.065 ± 0.053
0.079	2.48	0.034 ± 0.023	$0.032 \pm 0.023 \pm 0.004$	0.020 ± 0.054
0.090	2.78	0.072 ± 0.023	$0.068 \pm 0.023 \pm 0.005$	0.042 ± 0.054
0.101	3.11	0.061 ± 0.023	$0.054 \pm 0.023 \pm 0.005$	0.075 ± 0.053
0.113	3.43	0.056 ± 0.024	$0.061 \pm 0.024 \pm 0.006$	-0.039 ± 0.053
0.128	3.75	0.127 ± 0.025	$0.133 \pm 0.025 \pm 0.007$	-0.037 ± 0.054
0.144	4.07	0.153 ± 0.025	$0.151 \pm 0.026 \pm 0.008$	0.035 ± 0.055
0.173	4.60	0.143 ± 0.019	$0.146 \pm 0.020 \pm 0.009$	0.005 ± 0.041
0.218	5.28	0.126 ± 0.023	$0.137 \pm 0.024 \pm 0.011$	-0.040 ± 0.047
0.276	5.94	0.143 ± 0.029	$0.132 \pm 0.030 \pm 0.013$	0.068 ± 0.058
0.350	6.62	0.286 ± 0.038	$0.284 \pm 0.042 \pm 0.017$	0.058 ± 0.077
0.443	7.28	0.248 ± 0.055	$0.265 \pm 0.063 \pm 0.022$	0.047 ± 0.111
0.560	7.85	0.396 ± 0.088	$0.385 \pm 0.105 \pm 0.028$	0.203 ± 0.178
0.712	9.40	0.368 ± 0.184	$0.537 \pm 0.226 \pm 0.036$	-0.248 ± 0.361

Table 33 Results of structure function g_1 from the deuteron 29 GeV 4.5° spectrometer data with statistical errors. $g_1(\text{exp})$ is the structure function at the measured x and Q^2 value, while $g_1(3 \text{ GeV}^2)$ is the structure function evolved to common $Q^2 = 3 \text{ GeV}^2$. The evolution to $Q^2 = 3 \text{ GeV}^2$ was performed with the assumption that g_1/F_1 is Q^2-independent.

$<x>$	$<Q^2>$	$g_1(3 \text{ GeV}^2)$	$g_1(\text{exp})$
0.031	1.27	0.197 ± 0.173	0.165 ± 0.145
0.035	1.40	-0.002 ± 0.111	-0.002 ± 0.096
0.039	1.52	0.226 ± 0.090	0.199 ± 0.079
0.044	1.65	-0.041 ± 0.075	-0.037 ± 0.067
0.049	1.78	-0.038 ± 0.064	-0.035 ± 0.058
0.056	1.92	0.048 ± 0.055	0.045 ± 0.052
0.063	2.07	0.030 ± 0.048	0.029 ± 0.046
0.071	2.22	0.041 ± 0.043	0.039 ± 0.042
0.079	2.38	0.073 ± 0.041	0.071 ± 0.040
0.090	2.53	0.111 ± 0.040	0.109 ± 0.039
0.101	2.69	0.081 ± 0.039	0.080 ± 0.038
0.113	2.84	0.094 ± 0.038	0.093 ± 0.038
0.128	3.00	0.190 ± 0.037	0.190 ± 0.037
0.144	3.15	0.124 ± 0.036	0.125 ± 0.036
0.162	3.30	0.098 ± 0.035	0.099 ± 0.035
0.182	3.45	0.112 ± 0.034	0.113 ± 0.034
0.205	3.59	0.096 ± 0.033	0.096 ± 0.034
0.230	3.73	0.035 ± 0.033	0.035 ± 0.033
0.259	3.85	0.044 ± 0.033	0.044 ± 0.033
0.292	3.98	0.082 ± 0.032	0.081 ± 0.032
0.328	4.09	0.111 ± 0.033	0.108 ± 0.032
0.370	4.20	0.092 ± 0.032	0.088 ± 0.031
0.416	4.30	0.064 ± 0.032	0.060 ± 0.030
0.468	4.40	0.009 ± 0.031	0.008 ± 0.028
0.526	4.47	0.046 ± 0.031	0.039 ± 0.026
0.592	4.55	0.031 ± 0.030	0.024 ± 0.023

Table 34 Results of structure function g_1 from the deuteron 29 GeV 7° spectrometer data with statistical errors. $g_1(\exp)$ is the structure function at the measured x and Q^2 value, while $g_1(3 \text{ GeV}^2)$ is the structure function evolved to common $Q^2 = 3 \text{ GeV}^2$. The evolution to $Q^2 = 3 \text{ GeV}^2$ was performed with the assumption that g_1/F_1 is Q^2-independent.

$<x>$	$<Q^2>$	$g_1(3 \text{ GeV}^2)$	$g_1(\exp)$
0.079	3.17	-0.060 ± 0.109	-0.061 ± 0.110
0.090	3.48	0.097 ± 0.067	0.099 ± 0.068
0.101	3.79	0.081 ± 0.049	0.084 ± 0.051
0.113	4.11	0.033 ± 0.041	0.034 ± 0.042
0.128	4.44	0.079 ± 0.035	0.082 ± 0.037
0.144	4.78	0.153 ± 0.031	0.160 ± 0.033
0.162	5.13	0.062 ± 0.028	0.065 ± 0.029
0.182	5.49	0.159 ± 0.025	0.165 ± 0.026
0.205	5.86	0.071 ± 0.024	0.073 ± 0.024
0.230	6.23	0.084 ± 0.022	0.085 ± 0.023
0.259	6.60	0.047 ± 0.022	0.046 ± 0.021
0.292	6.97	0.081 ± 0.021	0.078 ± 0.020
0.328	7.33	0.077 ± 0.020	0.072 ± 0.019
0.370	7.69	0.090 ± 0.019	0.080 ± 0.017
0.416	8.03	0.050 ± 0.018	0.042 ± 0.015
0.468	8.37	0.056 ± 0.017	0.043 ± 0.014
0.526	8.67	0.063 ± 0.017	0.043 ± 0.011
0.592	8.98	0.030 ± 0.016	0.017 ± 0.009
0.666	9.26	0.017 ± 0.015	0.008 ± 0.007
0.750	9.52	0.027 ± 0.014	0.009 ± 0.005

Table 35 Results of structure function g_1 for deuteron 29 GeV (both spectrometers) evolved to $Q^2 = 3\,\text{GeV}^2$. The highest x-bins were pairwise combined. The first error is the statistical error, the second the systematic error. The evolution to $Q^2 = 3\,\text{GeV}^2$ was performed with the assumption that g_1/F_1 is Q^2-independent.

$<x>$	$<Q^2>$	$g_1(3\,\text{GeV}^2)$
0.031	1.27	$0.197 \pm 0.173 \pm 0.033$
0.035	1.40	$-0.002 \pm 0.111 \pm 0.028$
0.039	1.52	$0.226 \pm 0.090 \pm 0.023$
0.044	1.65	$-0.041 \pm 0.075 \pm 0.018$
0.049	1.78	$-0.038 \pm 0.064 \pm 0.014$
0.056	1.92	$0.048 \pm 0.055 \pm 0.011$
0.063	2.07	$0.031 \pm 0.048 \pm 0.009$
0.071	2.22	$0.041 \pm 0.043 \pm 0.008$
0.079	2.48	$0.056 \pm 0.038 \pm 0.008$
0.090	2.78	$0.107 \pm 0.034 \pm 0.007$
0.101	3.11	$0.081 \pm 0.031 \pm 0.007$
0.113	3.43	$0.065 \pm 0.028 \pm 0.007$
0.128	3.75	$0.132 \pm 0.025 \pm 0.007$
0.144	4.07	$0.140 \pm 0.023 \pm 0.007$
0.173	4.60	$0.111 \pm 0.015 \pm 0.007$
0.218	5.28	$0.074 \pm 0.013 \pm 0.006$
0.276	5.94	$0.064 \pm 0.013 \pm 0.005$
0.350	6.62	$0.088 \pm 0.012 \pm 0.005$
0.443	7.28	$0.049 \pm 0.011 \pm 0.004$
0.560	7.85	$0.044 \pm 0.010 \pm 0.003$
0.712	9.40	$0.022 \pm 0.010 \pm 0.002$

APPENDIX D

TABLE: NEUTRON 29 GEV

Table 36 Neutron A_1, A_2 and g_1 results for both spectrometers combined at beam energy 29 GeV. The first error is the statistical error, the second error on g_1^n is the systematic error. Each line in this table shows the average of three of the original 28 x-bins with exception of the last line, which shows the average of the highest four bins.

$<x>$	A_1	g_1/F_1	g_1
0.037	-0.014 ± 0.043	-0.014 ± 0.043	$-0.036 \pm 0.152 \pm 0.063$
0.051	-0.142 ± 0.034	-0.134 ± 0.034	$-0.333 \pm 0.086 \pm 0.037$
0.072	-0.114 ± 0.033	-0.120 ± 0.033	$-0.213 \pm 0.058 \pm 0.024$
0.103	-0.088 ± 0.034	-0.082 ± 0.034	$-0.105 \pm 0.041 \pm 0.018$
0.146	0.013 ± 0.040	0.005 ± 0.039	$-0.001 \pm 0.032 \pm 0.017$
0.207	-0.019 ± 0.051	-0.040 ± 0.049	$-0.025 \pm 0.026 \pm 0.016$
0.294	-0.216 ± 0.078	-0.173 ± 0.074	$-0.043 \pm 0.024 \pm 0.014$
0.420	-0.041 ± 0.145	-0.057 ± 0.132	$-0.014 \pm 0.022 \pm 0.011$
0.634	-0.027 ± 0.343	0.001 ± 0.290	$0.001 \pm 0.017 \pm 0.006$

APPENDIX E

TABLES: PROTON 16 AND 9 GEV

Table 37 Proton $A_\parallel$ results for 7° spectrometer at beam energies of 16 GeV (top), 9 GeV (bottom) with statistical errors. $A_\parallel$(uncorr) is the asymmetry not corrected for radiative effects.

$<x>$	$<Q^2>$	$A_\parallel$(uncorr)	$A_\parallel$
0.056	1.16	0.079 ± 0.036	0.086 ± 0.043
0.063	1.26	0.023 ± 0.026	0.030 ± 0.031
0.071	1.37	0.082 ± 0.023	0.088 ± 0.026
0.079	1.47	0.074 ± 0.021	0.079 ± 0.023
0.090	1.58	0.105 ± 0.020	0.110 ± 0.022
0.101	1.69	0.094 ± 0.019	0.098 ± 0.020
0.113	1.80	0.102 ± 0.018	0.105 ± 0.019
0.128	1.91	0.110 ± 0.018	0.112 ± 0.018
0.144	2.03	0.116 ± 0.017	0.118 ± 0.017
0.162	2.14	0.100 ± 0.017	0.102 ± 0.017
0.182	2.26	0.102 ± 0.017	0.104 ± 0.017
0.205	2.36	0.114 ± 0.018	0.115 ± 0.018
0.230	2.47	0.134 ± 0.018	0.135 ± 0.018
0.259	2.57	0.163 ± 0.019	0.164 ± 0.019
0.292	2.67	0.157 ± 0.019	0.159 ± 0.019
0.329	2.76	0.124 ± 0.020	0.126 ± 0.020
0.370	2.85	0.155 ± 0.021	0.156 ± 0.021
0.416	2.94	0.139 ± 0.023	0.141 ± 0.023
0.468	3.02	0.147 ± 0.025	0.149 ± 0.025
0.080	0.69	0.072 ± 0.022	0.075 ± 0.025
0.090	0.74	0.060 ± 0.017	0.062 ± 0.019
0.101	0.78	0.053 ± 0.015	0.055 ± 0.016
0.113	0.82	0.069 ± 0.014	0.072 ± 0.015
0.128	0.86	0.045 ± 0.013	0.047 ± 0.014
0.144	0.90	0.043 ± 0.013	0.045 ± 0.014
0.162	0.93	0.062 ± 0.013	0.064 ± 0.013
0.182	0.97	0.083 ± 0.012	0.085 ± 0.013
0.205	1.00	0.064 ± 0.012	0.066 ± 0.013
0.231	1.03	0.079 ± 0.012	0.081 ± 0.013

Table 38 Proton $A_\parallel$ results for 4.5° spectrometer at beam energies of 16 GeV (top), 9 GeV (bottom) with statistical errors. $A_\parallel$(uncorr) is the asymmetry not corrected for radiative effects.

$<x>$	$<Q^2>$	$A_\parallel$(uncorr)	$A_\parallel$
0.022	0.47	0.018 ± 0.019	0.020 ± 0.024
0.024	0.51	0.061 ± 0.015	0.063 ± 0.019
0.027	0.55	0.054 ± 0.014	0.056 ± 0.017
0.031	0.59	0.049 ± 0.013	0.052 ± 0.016
0.035	0.64	0.031 ± 0.012	0.034 ± 0.015
0.039	0.68	0.036 ± 0.012	0.039 ± 0.014
0.044	0.73	0.046 ± 0.011	0.050 ± 0.012
0.049	0.78	0.069 ± 0.010	0.072 ± 0.012
0.056	0.83	0.047 ± 0.010	0.050 ± 0.012
0.063	0.88	0.064 ± 0.011	0.067 ± 0.011
0.071	0.92	0.039 ± 0.011	0.042 ± 0.012
0.079	0.97	0.042 ± 0.011	0.045 ± 0.012
0.090	1.01	0.058 ± 0.011	0.060 ± 0.012
0.101	1.06	0.067 ± 0.011	0.069 ± 0.012
0.113	1.10	0.046 ± 0.012	0.048 ± 0.012
0.128	1.14	0.057 ± 0.012	0.059 ± 0.012
0.144	1.18	0.053 ± 0.012	0.055 ± 0.012
0.162	1.22	0.065 ± 0.012	0.067 ± 0.012
0.182	1.26	0.049 ± 0.012	0.050 ± 0.013
0.205	1.29	0.058 ± 0.013	0.059 ± 0.013
0.230	1.32	0.044 ± 0.013	0.046 ± 0.013
0.259	1.35	0.038 ± 0.014	0.039 ± 0.014
0.292	1.38	0.051 ± 0.014	0.052 ± 0.014
0.035	0.31	0.046 ± 0.014	0.047 ± 0.019
0.039	0.33	0.009 ± 0.013	0.010 ± 0.017
0.044	0.35	0.044 ± 0.013	0.045 ± 0.016
0.049	0.36	0.041 ± 0.013	0.043 ± 0.016
0.056	0.38	0.039 ± 0.013	0.040 ± 0.015
0.063	0.40	0.025 ± 0.012	0.026 ± 0.015
0.071	0.41	0.029 ± 0.013	0.030 ± 0.015
0.080	0.43	0.031 ± 0.013	0.031 ± 0.015
0.090	0.44	0.017 ± 0.012	0.018 ± 0.014
0.101	0.45	0.023 ± 0.012	0.024 ± 0.014
0.113	0.47	0.040 ± 0.011	0.040 ± 0.013
0.128	0.48	0.000 ± 0.011	0.001 ± 0.013

Table 39 Proton g_1/F_1, A_1, and g_1 results for 7° spectrometer at beam energies of 16 GeV (top), 9 GeV (bottom) with statistical errors. $g_1(\text{exp})$ is the structure function at the measured x and Q^2 value, while $g_1(3\ \text{GeV}^2)$ is the structure function evolved to common $Q^2 = 3\ \text{GeV}^2$. The evolution to $Q^2 = 3\ \text{GeV}^2$ was performed with the assumption that g_1/F_1 is Q^2-independent, not with GLAP evolution equations.

$<x>$	$<Q^2>$	g_1/F_1	A_1	$g_1(3\ \text{GeV}^2)$	$g_1(\text{exp})$
0.056	1.16	0.124 ± 0.062	0.125 ± 0.062	0.319 ± 0.158	0.274 ± 0.136
0.063	1.26	0.045 ± 0.046	0.045 ± 0.046	0.103 ± 0.104	0.090 ± 0.091
0.071	1.37	0.138 ± 0.040	0.138 ± 0.040	0.278 ± 0.080	0.249 ± 0.072
0.079	1.47	0.128 ± 0.038	0.129 ± 0.038	0.231 ± 0.068	0.210 ± 0.062
0.090	1.58	0.189 ± 0.037	0.190 ± 0.037	0.301 ± 0.059	0.279 ± 0.055
0.101	1.69	0.178 ± 0.037	0.179 ± 0.037	0.253 ± 0.052	0.237 ± 0.049
0.113	1.80	0.202 ± 0.036	0.204 ± 0.037	0.257 ± 0.046	0.243 ± 0.044
0.128	1.91	0.228 ± 0.036	0.230 ± 0.037	0.259 ± 0.041	0.248 ± 0.040
0.144	2.03	0.253 ± 0.037	0.255 ± 0.038	0.257 ± 0.038	0.248 ± 0.037
0.162	2.14	0.232 ± 0.039	0.234 ± 0.040	0.210 ± 0.036	0.204 ± 0.035
0.182	2.26	0.252 ± 0.042	0.255 ± 0.042	0.203 ± 0.034	0.200 ± 0.033
0.205	2.36	0.298 ± 0.045	0.301 ± 0.046	0.213 ± 0.032	0.211 ± 0.032
0.230	2.47	0.373 ± 0.050	0.377 ± 0.051	0.236 ± 0.032	0.234 ± 0.031
0.259	2.57	0.482 ± 0.054	0.490 ± 0.055	0.267 ± 0.030	0.267 ± 0.030
0.292	2.67	0.496 ± 0.060	0.504 ± 0.061	0.238 ± 0.029	0.238 ± 0.029
0.329	2.76	0.419 ± 0.067	0.427 ± 0.068	0.171 ± 0.027	0.172 ± 0.027
0.370	2.85	0.555 ± 0.075	0.567 ± 0.077	0.189 ± 0.026	0.190 ± 0.026
0.416	2.94	0.530 ± 0.086	0.543 ± 0.088	0.146 ± 0.024	0.147 ± 0.024
0.468	3.02	0.594 ± 0.100	0.610 ± 0.103	0.130 ± 0.022	0.130 ± 0.022
0.080	0.69	0.159 ± 0.053	0.160 ± 0.053	0.284 ± 0.095	0.236 ± 0.079
0.090	0.74	0.139 ± 0.043	0.140 ± 0.043	0.222 ± 0.068	0.189 ± 0.058
0.101	0.78	0.132 ± 0.040	0.133 ± 0.040	0.188 ± 0.056	0.163 ± 0.049
0.113	0.82	0.184 ± 0.039	0.186 ± 0.040	0.234 ± 0.050	0.208 ± 0.044
0.128	0.86	0.129 ± 0.040	0.131 ± 0.041	0.146 ± 0.046	0.133 ± 0.041
0.144	0.90	0.134 ± 0.041	0.136 ± 0.042	0.135 ± 0.042	0.126 ± 0.039
0.162	0.93	0.204 ± 0.043	0.207 ± 0.044	0.184 ± 0.039	0.175 ± 0.037
0.182	0.97	0.294 ± 0.045	0.299 ± 0.046	0.237 ± 0.036	0.230 ± 0.035
0.205	1.00	0.244 ± 0.047	0.249 ± 0.048	0.174 ± 0.034	0.173 ± 0.034
0.231	1.03	0.320 ± 0.050	0.328 ± 0.051	0.203 ± 0.031	0.206 ± 0.032

Table 40 Proton g_1/F_1, A_1, and g_1 results for 4.5° spectrometer at beam energies of 16 GeV (top), 9 GeV (bottom) with statistical errors. $g_1(\exp)$ is the structure function at the measured x and Q^2 value, while $g_1(3\ \mathrm{GeV}^2)$ is the structure function evolved to common $Q^2 = 3\ \mathrm{GeV}^2$. The evolution to $Q^2 = 3\ \mathrm{GeV}^2$ was performed with the assumption that g_1/F_1 is Q^2-independent.

$<x>$	$<Q^2>$	g_1/F_1	A_1	$g_1(3\ \mathrm{GeV}^2)$	$g_1(\exp)$
0.022	0.47	0.028 ± 0.032	0.028 ± 0.032	0.182 ± 0.211	0.120 ± 0.139
0.024	0.51	0.089 ± 0.026	0.089 ± 0.026	0.522 ± 0.155	0.356 ± 0.106
0.027	0.55	0.083 ± 0.025	0.083 ± 0.026	0.432 ± 0.133	0.303 ± 0.094
0.031	0.59	0.080 ± 0.025	0.080 ± 0.025	0.372 ± 0.116	0.268 ± 0.084
0.035	0.64	0.056 ± 0.024	0.056 ± 0.024	0.229 ± 0.100	0.170 ± 0.074
0.039	0.68	0.069 ± 0.024	0.069 ± 0.024	0.252 ± 0.086	0.192 ± 0.066
0.044	0.73	0.093 ± 0.023	0.093 ± 0.023	0.300 ± 0.075	0.234 ± 0.058
0.049	0.78	0.143 ± 0.023	0.144 ± 0.023	0.413 ± 0.067	0.329 ± 0.053
0.056	0.83	0.106 ± 0.024	0.107 ± 0.024	0.272 ± 0.063	0.222 ± 0.051
0.063	0.88	0.153 ± 0.026	0.153 ± 0.026	0.347 ± 0.059	0.289 ± 0.049
0.071	0.92	0.102 ± 0.028	0.103 ± 0.028	0.207 ± 0.057	0.176 ± 0.048
0.079	0.97	0.118 ± 0.031	0.119 ± 0.031	0.212 ± 0.055	0.183 ± 0.048
0.090	1.01	0.173 ± 0.034	0.174 ± 0.034	0.276 ± 0.054	0.243 ± 0.048
0.101	1.06	0.215 ± 0.037	0.217 ± 0.037	0.307 ± 0.052	0.274 ± 0.047
0.113	1.10	0.163 ± 0.040	0.164 ± 0.041	0.206 ± 0.051	0.188 ± 0.047
0.128	1.14	0.215 ± 0.044	0.217 ± 0.045	0.244 ± 0.050	0.225 ± 0.046
0.144	1.18	0.217 ± 0.048	0.219 ± 0.049	0.220 ± 0.049	0.206 ± 0.046
0.162	1.22	0.287 ± 0.053	0.290 ± 0.053	0.260 ± 0.048	0.247 ± 0.045
0.182	1.26	0.233 ± 0.059	0.236 ± 0.059	0.188 ± 0.047	0.181 ± 0.046
0.205	1.29	0.297 ± 0.065	0.301 ± 0.066	0.213 ± 0.047	0.209 ± 0.046
0.230	1.32	0.248 ± 0.072	0.251 ± 0.073	0.157 ± 0.046	0.157 ± 0.046
0.259	1.35	0.228 ± 0.080	0.232 ± 0.082	0.127 ± 0.045	0.129 ± 0.045
0.292	1.38	0.327 ± 0.090	0.332 ± 0.092	0.157 ± 0.043	0.163 ± 0.045
0.035	0.31	0.093 ± 0.037	0.093 ± 0.037	0.382 ± 0.151	0.238 ± 0.094
0.039	0.33	0.022 ± 0.036	0.022 ± 0.036	0.080 ± 0.133	0.052 ± 0.086
0.044	0.35	0.104 ± 0.037	0.104 ± 0.037	0.336 ± 0.120	0.225 ± 0.080
0.049	0.36	0.105 ± 0.039	0.106 ± 0.039	0.303 ± 0.113	0.210 ± 0.078
0.056	0.38	0.107 ± 0.041	0.107 ± 0.041	0.272 ± 0.105	0.195 ± 0.075
0.063	0.40	0.075 ± 0.043	0.076 ± 0.043	0.171 ± 0.098	0.126 ± 0.072
0.071	0.41	0.095 ± 0.049	0.095 ± 0.049	0.191 ± 0.099	0.145 ± 0.075
0.080	0.43	0.110 ± 0.053	0.111 ± 0.053	0.197 ± 0.095	0.153 ± 0.074
0.090	0.44	0.067 ± 0.054	0.068 ± 0.055	0.107 ± 0.087	0.086 ± 0.070
0.101	0.45	0.100 ± 0.057	0.101 ± 0.057	0.142 ± 0.081	0.118 ± 0.067
0.113	0.47	0.182 ± 0.059	0.184 ± 0.060	0.230 ± 0.075	0.197 ± 0.064
0.128	0.48	0.006 ± 0.063	0.006 ± 0.064	0.007 ± 0.071	0.006 ± 0.063

APPENDIX F

TABLES: DEUTERON 16 AND 9 GEV

Table 41 Deuteron $A_\parallel$ results for 7° spectrometer at beam energies of 16 GeV (top), 9 GeV (bottom) with statistical errors. $A_\parallel$(uncorr) is the asymmetry not corrected for radiative effects.

$<x>$	$<Q^2>$	$A_\parallel$(uncorr)	$A_\parallel$
0.056	1.16	0.066 ± 0.092	0.061 ± 0.103
0.063	1.26	0.001 ± 0.066	-0.003 ± 0.073
0.071	1.36	0.057 ± 0.055	0.053 ± 0.059
0.079	1.47	-0.069 ± 0.050	-0.072 ± 0.053
0.090	1.58	0.123 ± 0.047	0.120 ± 0.048
0.101	1.69	0.056 ± 0.043	0.053 ± 0.045
0.113	1.80	0.029 ± 0.039	0.026 ± 0.040
0.128	1.91	0.020 ± 0.036	0.018 ± 0.037
0.144	2.03	0.041 ± 0.035	0.039 ± 0.035
0.162	2.14	0.060 ± 0.034	0.059 ± 0.034
0.182	2.25	0.096 ± 0.035	0.096 ± 0.035
0.205	2.36	0.045 ± 0.036	0.044 ± 0.036
0.230	2.47	0.040 ± 0.037	0.040 ± 0.037
0.259	2.57	0.040 ± 0.038	0.041 ± 0.038
0.292	2.67	0.113 ± 0.039	0.114 ± 0.039
0.329	2.76	0.157 ± 0.042	0.158 ± 0.041
0.370	2.85	0.037 ± 0.044	0.038 ± 0.044
0.416	2.93	0.053 ± 0.048	0.054 ± 0.048
0.468	3.01	0.165 ± 0.053	0.166 ± 0.053
0.080	0.69	0.017 ± 0.033	0.013 ± 0.036
0.090	0.74	-0.009 ± 0.025	-0.012 ± 0.027
0.101	0.78	0.019 ± 0.023	0.016 ± 0.024
0.113	0.82	0.026 ± 0.021	0.024 ± 0.022
0.128	0.86	0.054 ± 0.020	0.052 ± 0.021
0.144	0.90	0.013 ± 0.019	0.012 ± 0.020
0.162	0.93	0.037 ± 0.019	0.036 ± 0.020
0.182	0.97	0.028 ± 0.018	0.027 ± 0.019
0.205	1.00	0.004 ± 0.018	0.004 ± 0.019
0.231	1.03	0.043 ± 0.018	0.043 ± 0.019

Table 42 Deuteron $A_\parallel$ results for 4.5° spectrometer at beam energies of 16 GeV (top), 9 GeV (bottom) with statistical errors. $A_\parallel$(uncorr) is the asymmetry not corrected for radiative effects.

$<x>$	$<Q^2>$	$A_\parallel$(uncorr)	$A_\parallel$
0.022	0.47	-0.014 ± 0.054	-0.019 ± 0.063
0.024	0.51	-0.030 ± 0.041	-0.036 ± 0.048
0.027	0.55	-0.007 ± 0.037	-0.013 ± 0.044
0.031	0.59	0.017 ± 0.035	0.012 ± 0.041
0.035	0.64	-0.005 ± 0.033	-0.009 ± 0.037
0.039	0.68	0.059 ± 0.031	0.056 ± 0.034
0.044	0.73	-0.017 ± 0.025	-0.021 ± 0.027
0.049	0.78	0.049 ± 0.024	0.046 ± 0.026
0.056	0.83	0.006 ± 0.023	0.004 ± 0.025
0.063	0.87	0.023 ± 0.023	0.021 ± 0.024
0.071	0.92	0.028 ± 0.023	0.026 ± 0.024
0.079	0.97	-0.014 ± 0.023	-0.016 ± 0.024
0.090	1.01	0.040 ± 0.023	0.038 ± 0.024
0.101	1.06	0.020 ± 0.023	0.018 ± 0.024
0.113	1.10	0.017 ± 0.023	0.016 ± 0.024
0.128	1.14	0.063 ± 0.024	0.062 ± 0.024
0.144	1.18	0.051 ± 0.024	0.050 ± 0.024
0.162	1.22	-0.024 ± 0.024	-0.025 ± 0.025
0.182	1.25	0.042 ± 0.025	0.042 ± 0.025
0.205	1.29	0.041 ± 0.026	0.041 ± 0.026
0.230	1.32	0.015 ± 0.026	0.015 ± 0.027
0.259	1.35	0.021 ± 0.028	0.022 ± 0.028
0.292	1.37	0.059 ± 0.029	0.060 ± 0.030
0.035	0.31	-0.009 ± 0.023	-0.013 ± 0.028
0.039	0.33	0.021 ± 0.021	0.017 ± 0.025
0.044	0.35	0.005 ± 0.020	0.002 ± 0.024
0.050	0.36	0.025 ± 0.020	0.022 ± 0.023
0.056	0.38	-0.013 ± 0.019	-0.016 ± 0.022
0.063	0.40	0.001 ± 0.019	-0.002 ± 0.021
0.071	0.41	0.035 ± 0.020	0.032 ± 0.022
0.080	0.43	-0.002 ± 0.019	-0.004 ± 0.021
0.090	0.44	0.010 ± 0.018	0.008 ± 0.020
0.101	0.45	0.040 ± 0.018	0.038 ± 0.020
0.113	0.47	0.000 ± 0.017	-0.002 ± 0.019
0.128	0.48	-0.016 ± 0.017	-0.018 ± 0.019

Table 43 Deuteron g_1/F_1, A_1, and g_1 results for 7° spectrometer at beam energies of 16 GeV (top), 9 GeV (bottom) with statistical errors. g_1(exp) is the structure function at the measured x and Q^2 value, while $g_1(3 \text{ GeV}^2)$ is the structure function evolved to common $Q^2 = 3 \text{ GeV}^2$. The evolution to $Q^2 = 3 \text{ GeV}^2$ was performed with the assumption that g_1/F_1 is Q^2-independents.

$<x>$	$<Q^2>$	g_1/F_1	A_1	$g_1(3 \text{ GeV}^2)$	$g_1(\text{exp})$
0.056	1.16	0.088 ± 0.149	0.089 ± 0.149	0.214 ± 0.360	0.183 ± 0.309
0.063	1.26	-0.005 ± 0.109	-0.005 ± 0.109	-0.010 ± 0.234	-0.009 ± 0.206
0.071	1.36	0.083 ± 0.092	0.083 ± 0.092	0.158 ± 0.174	0.142 ± 0.156
0.079	1.47	-0.118 ± 0.086	-0.119 ± 0.086	-0.199 ± 0.145	-0.182 ± 0.132
0.090	1.58	0.206 ± 0.083	0.207 ± 0.084	0.308 ± 0.124	0.286 ± 0.115
0.101	1.69	0.097 ± 0.081	0.097 ± 0.082	0.128 ± 0.107	0.120 ± 0.101
0.113	1.80	0.051 ± 0.076	0.051 ± 0.076	0.059 ± 0.089	0.056 ± 0.085
0.128	1.91	0.036 ± 0.075	0.037 ± 0.075	0.038 ± 0.078	0.036 ± 0.075
0.144	2.03	0.084 ± 0.076	0.085 ± 0.076	0.077 ± 0.070	0.075 ± 0.068
0.162	2.14	0.136 ± 0.079	0.137 ± 0.080	0.110 ± 0.064	0.108 ± 0.063
0.182	2.25	0.233 ± 0.085	0.235 ± 0.086	0.167 ± 0.061	0.164 ± 0.060
0.205	2.36	0.115 ± 0.092	0.116 ± 0.093	0.072 ± 0.058	0.072 ± 0.057
0.230	2.47	0.112 ± 0.101	0.113 ± 0.102	0.061 ± 0.055	0.061 ± 0.055
0.259	2.57	0.120 ± 0.111	0.122 ± 0.112	0.057 ± 0.052	0.057 ± 0.052
0.292	2.67	0.356 ± 0.122	0.362 ± 0.124	0.143 ± 0.049	0.144 ± 0.049
0.329	2.76	0.527 ± 0.138	0.538 ± 0.140	0.178 ± 0.046	0.179 ± 0.047
0.370	2.85	0.136 ± 0.155	0.139 ± 0.159	0.038 ± 0.043	0.038 ± 0.043
0.416	2.93	0.203 ± 0.180	0.208 ± 0.184	0.045 ± 0.040	0.045 ± 0.040
0.468	3.01	0.662 ± 0.209	0.680 ± 0.215	0.115 ± 0.036	0.114 ± 0.036
0.080	0.69	0.028 ± 0.078	0.029 ± 0.078	0.048 ± 0.131	0.040 ± 0.109
0.090	0.74	-0.028 ± 0.062	-0.028 ± 0.062	-0.042 ± 0.092	-0.036 ± 0.079
0.101	0.78	0.038 ± 0.058	0.039 ± 0.058	0.051 ± 0.077	0.044 ± 0.067
0.113	0.82	0.062 ± 0.057	0.063 ± 0.058	0.073 ± 0.067	0.065 ± 0.060
0.128	0.86	0.144 ± 0.058	0.146 ± 0.059	0.149 ± 0.060	0.137 ± 0.055
0.144	0.90	0.034 ± 0.060	0.035 ± 0.061	0.032 ± 0.055	0.030 ± 0.052
0.162	0.93	0.115 ± 0.063	0.117 ± 0.064	0.093 ± 0.051	0.089 ± 0.049
0.182	0.97	0.092 ± 0.066	0.094 ± 0.067	0.066 ± 0.047	0.065 ± 0.046
0.205	1.00	0.014 ± 0.070	0.015 ± 0.071	0.009 ± 0.044	0.009 ± 0.044
0.231	1.03	0.169 ± 0.075	0.173 ± 0.076	0.092 ± 0.041	0.095 ± 0.042

Table 44 Deuteron g_1/F_1, A_1, and g_1 results for 4.5° spectrometer at beam energies of 16 GeV (top), 9 GeV (bottom) with statistical errors. $g_1(\exp)$ is the structure function at the measured x and Q^2 value, while $g_1(3\ \mathrm{GeV}^2)$ is the structure function evolved to common $Q^2 = 3\ \mathrm{GeV}^2$. The evolution to $Q^2 = 3\ \mathrm{GeV}^2$ was performed with the assumption that g_1/F_1 is Q^2-independent.

$<x>$	$<Q^2>$	g_1/F_1	A_1	$g_1(3\ \mathrm{GeV}^2)$	$g_1(\exp)$
0.022	0.47	-0.025 ± 0.086	-0.026 ± 0.086	-0.162 ± 0.542	-0.104 ± 0.349
0.024	0.51	-0.050 ± 0.068	-0.050 ± 0.068	-0.283 ± 0.384	-0.188 ± 0.256
0.027	0.55	-0.019 ± 0.065	-0.019 ± 0.065	-0.094 ± 0.324	-0.065 ± 0.223
0.031	0.59	0.018 ± 0.063	0.018 ± 0.063	0.081 ± 0.281	0.057 ± 0.199
0.035	0.64	-0.016 ± 0.061	-0.016 ± 0.061	-0.062 ± 0.238	-0.045 ± 0.174
0.039	0.68	0.097 ± 0.059	0.098 ± 0.059	0.340 ± 0.206	0.255 ± 0.155
0.044	0.73	-0.038 ± 0.051	-0.038 ± 0.051	-0.118 ± 0.158	-0.091 ± 0.122
0.049	0.78	0.091 ± 0.051	0.091 ± 0.051	0.250 ± 0.140	0.198 ± 0.111
0.056	0.83	0.008 ± 0.053	0.008 ± 0.053	0.019 ± 0.128	0.015 ± 0.104
0.063	0.87	0.048 ± 0.056	0.048 ± 0.056	0.103 ± 0.120	0.086 ± 0.100
0.071	0.92	0.063 ± 0.060	0.063 ± 0.060	0.120 ± 0.113	0.102 ± 0.096
0.079	0.97	-0.043 ± 0.065	-0.043 ± 0.065	-0.072 ± 0.109	-0.062 ± 0.094
0.090	1.01	0.109 ± 0.069	0.109 ± 0.070	0.163 ± 0.104	0.144 ± 0.092
0.101	1.06	0.057 ± 0.075	0.058 ± 0.075	0.076 ± 0.099	0.068 ± 0.089
0.113	1.10	0.054 ± 0.081	0.054 ± 0.081	0.063 ± 0.094	0.058 ± 0.086
0.128	1.14	0.227 ± 0.088	0.229 ± 0.089	0.236 ± 0.092	0.219 ± 0.085
0.144	1.18	0.198 ± 0.097	0.199 ± 0.097	0.182 ± 0.089	0.172 ± 0.084
0.162	1.22	-0.106 ± 0.106	-0.107 ± 0.107	-0.086 ± 0.086	-0.083 ± 0.083
0.182	1.25	0.197 ± 0.118	0.199 ± 0.119	0.141 ± 0.085	0.137 ± 0.083
0.205	1.29	0.208 ± 0.132	0.211 ± 0.133	0.131 ± 0.083	0.130 ± 0.082
0.230	1.32	0.083 ± 0.147	0.084 ± 0.149	0.046 ± 0.080	0.046 ± 0.081
0.259	1.35	0.126 ± 0.165	0.128 ± 0.168	0.060 ± 0.078	0.062 ± 0.081
0.292	1.37	0.375 ± 0.187	0.381 ± 0.190	0.151 ± 0.075	0.160 ± 0.080
0.035	0.31	-0.026 ± 0.054	-0.026 ± 0.054	-0.104 ± 0.213	-0.063 ± 0.129
0.039	0.33	0.036 ± 0.052	0.036 ± 0.052	0.125 ± 0.182	0.079 ± 0.115
0.044	0.35	0.004 ± 0.054	0.004 ± 0.054	0.011 ± 0.167	0.007 ± 0.109
0.050	0.36	0.054 ± 0.056	0.054 ± 0.057	0.148 ± 0.154	0.101 ± 0.105
0.056	0.38	-0.044 ± 0.059	-0.044 ± 0.059	-0.107 ± 0.142	-0.075 ± 0.100
0.063	0.40	-0.006 ± 0.061	-0.006 ± 0.062	-0.013 ± 0.132	-0.009 ± 0.096
0.071	0.41	0.104 ± 0.069	0.104 ± 0.070	0.197 ± 0.132	0.148 ± 0.099
0.080	0.43	-0.013 ± 0.075	-0.013 ± 0.075	-0.022 ± 0.126	-0.017 ± 0.098
0.090	0.44	0.030 ± 0.078	0.030 ± 0.078	0.044 ± 0.116	0.036 ± 0.093
0.101	0.45	0.156 ± 0.081	0.157 ± 0.082	0.206 ± 0.107	0.171 ± 0.089
0.113	0.47	-0.009 ± 0.085	-0.009 ± 0.086	-0.011 ± 0.100	-0.009 ± 0.086
0.128	0.48	-0.085 ± 0.091	-0.086 ± 0.092	-0.089 ± 0.094	-0.079 ± 0.084

REFERENCES

[1] EMC, Ashman, J. *et al.*, *Phys. Lett.* **B206**, 364 (1988); *Nucl. Phys.* **B328**, 1 (1989).

[2] SMC, Adams, D. *et al.*, *Phys. Lett.* **B329**, 399 (1994).

[3] SMC, Adeva, B. *et al.*, *Phys. Lett.* **B302**, 533 (1993).

[4] SMC, Adams, D. *et al.*, *Phys. Lett.* **B336**, 125 (1994).

[5] SMC, Adams, D. *et al.*, *Phys. Lett.* **B357**, 248 (1995).

[6] SLAC E142, Anthony, P. L. *et al.*, *Phys. Rev. Lett.* **71**, 959 (1993).

[7] The big interest in the nucleon spin is apparent for example in the number of citations of Ref. [1]. In the years 1993 to 1995, this article was one of the few experimental papers among the 25 most often cited articles in the SLAC-SPIRES preprint database (*CERN Courier*, March 1996, p. 21).

[8] Anselmino, M., Efremov, A., Leader, E., *Phys. Rep.* **261**, 1 (1995).

[9] Whitlow, L. W. *et al.*, *Phys. Lett.* **B250**, 193 (1990).

[10] NMC, Amaudruz, P. *et al.*, *Phys. Lett.* **B295**, 159 (1992).

[11] NMC, Arneodo, M. *et al.*, *Phys. Lett.* **B364**, 107 (1995).

[12] Feynman, R. P., *Photon-Hadron Interactions*, (Benjamin, Reading, 1972).

[13] Bjorken, J. D., Paschos, E. A., *Phys. Rev.* **185**, 1975 (1960).

[14] Halzen, F., Martin, A. D., *Quarks and Leptons* (Wiley, New York, 1984).

[15] Hey, A. J. G., in *Proc. 9th Rencontre de Moriond 1994*, edited by Tran Thanh Van, J. (Centre National Recherche Scientifique, 1974); Pussieux, T., Windmolders, R., CERN SMC-93/16 (1993).

[16] Doncel, M. G., de Rafael, E., *Nuovo Cimento* **4A**, 363 (1971).

[17] Altarelli, G., Nason, P., Ridolfi, G., *Phys. Lett.* **B320**, 152 (1994).

[18] Brodsky, S. J., Report No. SLAC–PUB–6450 (1994), invited talk presented at SLAC Summer Institute on Particle Physics, 1993.

[19] Jaffe, R. J., in *Proc. Baryons '92*, edited by Gai, M. (World Scientific, Singapore, 1993).

[20] Altarelli, G., *Phys. Rep.* **81**, 1 (1982).

[21] Altarelli, G., Parisi, G., *Nucl. Phys.* **B126**, 298 (1977); Gribov, V. N., Lipatov, L. N., *Yad. Fiz.* **15**, 781 (1972) [*Sov. J. Nucl. Phys.* **15**, 438 (1972)].

[22] Ball, R. D., Forte, S., Ridolfi, G., CERN-TH/95-266, submitted to Phys. Lett. **B**.

[23] Glück, M. *et al.*, *Phys. Rev.* **D53**, 4775 (1996).

[24] SLAC E80, Alguard, M. J. *et al.*, *Phys. Rev. Lett.* **37**, 1261 (1976); **41**, 70 (1978).

[25] SLAC E130, Baum, G. *et al.*, *Phys. Rev. Lett.* **51**, 1135 (1983).

[26] Ehrnsperger, B., Schäfer, A., *Phys. Rev.* **D52**, 2709 (1995).

[27] Ball, R. D., Forte, S., Ridolfi, G., *Nucl. Phys.* **B444**, 287 (1995).

[28] Glück, M., Reya, E., Vogelsang, W., *Phys. Lett.* **B359**, 201 (1995).

[29] Mertig, R., van Neerven, W. L., Univ. Leiden INLO-PUB-6/95 (1995); NIKHEF-H/95-031 (1995).

[30] Lederer, C. M. *et al.*, *Table of Isotopes*, (Wiley, New York, 1978).

[31] Segre, E., *Nuclei and Particles*, (Benjamin/Cummings, Menlo Park, 1977).

[32] Kotthoff, K., Machleidt, R., Schütte, D., *Nucl. Phys.* **A264**, 484 (1976).

[33] Machleidt, R., Holinde, K., Elster, Ch., *Phys. Rep.* **149**, 1 (1987).

[34] Lacombe, M. *et al.*, *Phys. Rev.* **C21**, 861 (1980).

[35] Reid, R. V., *Ann. Phys.* **50**, 411 (1968).

[36] Wandzura, S., Wilczek, F., *Phys. Lett.* **B72**, 195 (1977).

[37] E143 Technical Note #98, Stuart, L., *Modified g_2^{WW} Formula for E143 Kinematics*, June 1995.

[38] Roberts, R. G., *The Structure of the Proton* (Cambridge University Press, Cambridge, 1990).

[39] Geesaman, D. F., Saito, K., Thomas, A. W., *Annu. Rev. Nucl. Part. Sci.* **45**, 337 (1995).

[40] EMC, Aubert, J. J. *et al.*, *Phys. Lett.* **B123**, 275 (1983).

[41] EMC, Amaudruz, P. *et al.*, *Z. Phys.* **C51**, 387 (1991).

[42] Gomez, J. *et al.*, Report No. SLAC-PUB-5813 (1993); *Phys. Rev.* **D49**, 4348 (1994).

[43] Bjorken, J. D., *Phys. Rev.* **148**, 1467 (1966); *Phys. Rev.* **D1**, 1376 (1970).

[44] Particle Data Group, *Phys. Rev.* **D50**, 1173 (1994).

[45] Larin, S. A., Vermaseren, J. A. M., *Phys. Lett.* **B259**, 345 (1991) and references therein.

[46] Ellis, J., Jaffe, R., *Phys. Rev.* **D9**, 1444 (1974); **D10**, 1669 (1974).

[47] Altarelli, G., in *Proc. 27th Int. School of Subnuclear Physics 1989*, edited by Zichichi, A. (Plenum Press, New York, 1990).

[48] E143 Technical Note #67, Young, C., Zapalac, G., *F and D Constants*, July 1994.

[49] Larin, S. A., *Phys. Lett.* **B334**, 192 (1994).

[50] Ellis, J., Karliner, M., *Phys. Lett.* **B341**, 397 (1995).

[51] Kataev, A. L., *Phys. Rev.* **D50**, R5469 (1994).

[52] Close, F. E., Roberts, R. G., *Phys. Lett.* **B316**, 165 (1993).

[53] Close, F. E., Roberts, R. G., *Phys. Rev. Lett.* **60**, 1471 (1988).

[54] Jaffe, R. L., Manohar, A., *Nucl. Phys.* **B337**, 509 (1990).

[55] Lipkin, H. J., *Phys. Lett.* **B337**, 157 (1994).

[56] Gerasimov, S. B., *Yad. Fiz.* **2**, 598 (1965) [*Sov. J. Nucl. Phys.* **2**, 430 (1966)]; Drell, S. D., Hearn, A. C., *Phys. Rev. Lett.* **16**, 908 (1966).

[57] Chang, L. N., Liang, Y., Workman, R. L., *Phys. Lett.* **B329**, 514 (1994).

[58] Burkhardt, H., Cottingham, W. N., *Ann. Phys.* **41**, 205 (1969).

[59] E143, Abe, K. *et al.*, Report No. SLAC–PUB–95–6982 (1995); *Phys. Rev. Lett.* **76**, 587 (1996).

[60] Petratos, G. G. *et al.*, Report No. SLAC–PUB–5678 (1991).

[61] E143, Abe, K. *et al.*, Report No. SLAC–PUB–95–6997 (1995); *Phys. Lett.* **B364**, 61 (1995).

[62] EMC, Allkofer, O. C. *et al.*, *Nucl. Inst. Meth.* **179**, 445 (1981).

[63] Alley, R. *et al.*, *Nucl. Inst. Meth.* **A365**, 1 (1995).

[64] Prepost, R., Maruyama, T., *Annu. Rev. Nucl. Part. Sci.* **45**, 41 (1995).

[65] Neal, R. B., *The Stanford Two-Mile Accelerator* (Benjamin, New York, 1968).

[66] E143 Technical Note #88, Kuhn, S., Hing, M., *Toroid Calibration for E143*, January 1995.

[67] Band, H., priv. comm.

[68] E143 Technical Note #91, Band, H. R., *Spin Structure Function Measurements from E143 at SLAC*, May 1995.

[69] E143 Technical Note #110, Band, H. R., Prepost, R., *E143 Møller Polarimeter Target*, June 1996.

[70] E143 Technical Note #84, Band, H. R., *Møller Polarimetry at SLAC*, November 1994.

[71] Levchuk, L. G., *Nucl. Inst. Meth.* **A345**, 496 (1994).

[72] E143 Technical Note #46, Steiner, P. *et al.*, *E143 Double Arm Polarimetry — First Results*, February 1994.

[73] Jeffries, C. D., *Ann. Rev. Nuc. Sci.* **14**, 101 (1964).

[74] E143 Technical Note #107, Crabb, D. G., *Solid Polarized Targets*, August 1995.

[75] E143 Technical Note #48, Bauer, J., *EGS4 Simulation of the Ammonia Irradiation*, August 1993.

[76] E143 Technical Note #49, Button–Shafer, J., Bauer, J., *Status of Irradiation Preparation*, July 1993.

[77] Crabb, D. G., Day, D. B., *Nucl. Inst. Meth.* **A356**, 9 (1995).

[78] Roberts, J. D., *Nuclear Magnetic Resonance* (McGraw-Hill, New York, 1959).

[79] Kittel, C., *Introduction to Solid State Physics*, (Wiley, New York, 1986).

[80] Court, G. R. *et al.*, *Nucl. Inst. Meth.* **A324**, 433 (1993).

[81] Dunne, J. A., *Magnetic Measurements of the four spectrometer dipole magnets for the E142 Experiment*, prethesis project (American University, 1994).

[82] E143 Technical Note #87, Erbacher, R., *SLAC E143 Čerenkov Technical Report*, July 1994.

[83] Jelley, J. V., *Čerenkov Radiation and Its Applications* (Pergamon, New York, 1958).

[84] Bartha, G. T. *et al.*, *Nucl. Inst. Meth.* **A275**, 59 (1989).

[85] For example Leo, W. R, *Techniques for Nuclear and Particle Physics Experiments* (Springer, New York, 1994).

[86] E143 Technical Note #37, Bosted, P. *et al.*, *Run-By-Run Problems for E143*, May 1994.

[87] Spengos, M., *A description of the trigger electronics system for the E142 experiment at SLAC*, pre-thesis project (American University, 1993).

[88] E143 Technical Note #52, Bauer, J., *The Spectrometer Magnets: NMR and Current Readings during E143*, April 1994.

[89] Prescott, C., priv. comm.

[90] E143, Abe, K. *et al.*, Report No. SLAC–PUB–6508 (1994); *Phys. Rev. Lett.* **74**, 346 (1995).

[91] E143 Technical Note #93, Liu, T. J., *Corrections for Beam Heating and Target Depolarization*, May 1995.

[92] Breton, V. *et al.*, *Nucl. Inst. Meth.* **A362**, 478 (1995).

[93] E143 Technical Note #23, Breton, V., Roblin, Y., Tamin, F., *E142 Experiment: A Cellular Automaton for Cluster Recognition in the Shower Counter.* September 1993.

[94] E143 Technical Note #36, Fonvieille, H., *E143 Experiment: Shower Counter Calibration*, February 1994.

[95] E143 Technical Note #83, Borel, H. *et al.*, *Shower Counters for SLAC Experiments E142/E143*, November 1994.

[96] E143 Technical Note #22, Breton, V., Grenier, P., *E142 Experiment: Use of Neural Network for Particle Identification*, May 1992.

[97] E143 Technical Note #81, Borel, H., Petratos, M., Young, C., *E' Resolution*, October 1994.

[98] E143 Technical Note #105, Bauer, J., *Tracking Bug*, November 1995.

[99] Bosted, P., priv. comm.

[100] E143 Technical Note #64, Averett, T., *Target Settling Study*, June 1994.

[101] E143 Technical Note #72, Garvey, D. R., Maruyama, X. K., *Thickness and Packing Fraction of Ammonia Used in SLAC E143 Experiment*, September 1994.

[102] E143 Technical Note #79, Bosted, P., *Weight of Ammonia Targets from Relative Cross Sections*, October 1994.

[103] E143 Technical Note #71, Bauer, J., Rondon, O., *Formulas for Nitrogen Correction*, September 1994.

[104] Tsai, Y. S., SLAC-PUB-848 (1971); *Rev. Mod. Phys.* **46**. 815 (1974).

[105] Kukhto, T. V., Shumeiko, N. M., *Nucl. Phys.* **B219**, 412 (1983); Akusevich, I. V., Shumeiko, N. M., *J. Phys.* **G20**, 513 (1994).

[106] Whitlow, L. W. *et al.*, *Phys. Lett.* **B282**, 475 (1992).

[107] E143, Abe, K. *et al.*, Report No. SLAC–PUB–95–6734 (1995); *Phys. Rev. Lett.* **75**, 25 (1995).

[108] Bloom, E. D., Gilman, F. J., *Phys. Rev.* **D4**, 2901 (1971).

[109] Brodsky, S. J., Burkardt, M., Schmidt, I., *Nucl. Phys.* **B441**, 197 (1995).

[110] Ellis, J., Karliner, M., *Phys. Lett.* **B213**, 73 (1988).

[111] E143 Technical Note #75, Kuriki, M., *Systematic Error Analysis*, October 1994.

[112] Kawall, D. M., Ph. D. Thesis (Stanford University, September 1995).

[113] Schmelling, M. S., St. Denis, R. D., *Phys. Let.* **B329**, 323 (1994); S. Narison, Report No. CERN-TH-7188/94.

[114] Particle Data Group, *Phys. Rev.* **D50**, 1173 (1994) and erratum published on World Wide Web.

[115] HERMES, Coulter, K. *et al.*, Proposal DESY-PRC 90/01 (1990); Technical Design Report, DESY-PRC 93/06 (1993); Düren, M., *The HERMES Experiment: From the Design to the First Results*, DESY HERMES-95-02 (1995).